Structure, Thermodynamic Stability, and Energetics of Guest-host Interactions

in Hybrid Materials: Polymer Derived Ceramics (PDCs) and Metal Organic Frameworks

(MOFs)

by

Gerson Leonel

A Dissertation Presented in Partial Fulfillment
of the Requirements for the Degree
Doctor of Philosophy

Approved October 2023 by the
Graduate Supervisory Committee:

Alexandra Navrotsky, Chair
Lenore Dai
Mary Laura Lind Thomas
Gurpreet Singh
Tomislav Friščić

ARIZONA STATE UNIVERSITY

December 2023

ABSTRACT

This work systematically investigates structure-stability relations in various polymer derived ceramic (PDC) systems and metal organic frameworks (MOFs), both of which are hybrid materials. The investigation of silicon carbides (SiC) confirms thermodynamic stabilization of PDCs with increasing mixed bonding (Si bonded to both C, O and/or N). The study of more complex silicon oxycarbide (SiOC) structures shows stabilization of SiOCs with increasing pyrolysis temperature (between 1200 and 1500 ^{o}C), and points to dissimilarities in the stabilizing effect of different mixed bonding environments (SiO_3C, SiO_2C_2, or $SiOC_3$) and their relative amounts. Analyses of quaternary silicon oxycarbonitride (SiC(N)(O)) materials suggests increased stabilization with increasing N content, and superior stabilization due to SiN_xC_{4-x} compared to SiO_xC_{4-x} mixed bonds. Investigation of the energetics of metal filler (Nb, Hf, Ta) incorporation in SiOCs shows that choice of metal filler influences the composition, structural evolution, and thermodynamic stability in PDCs. Ta fillers can stabilize otherwise unstable SiO_3C mixed bonds. Independent of metal incorporation or lack thereof, in SiOC systems, higher pyrolysis temperature (1200-1500 ^{o}C) forms more stable ceramics. The stabilizing effect of order/disorder of the free carbon phase is system-dependent. The work on (MOFs) highlights stabilization trends obtained from the investigation of zeolitic imidazolate frameworks (ZIFs) and boron imidazolate frameworks (BIFs) based on azolate linkers. Study of the energetics of metal (Co(II), Cu (II), and Zn (II)) substitution in isostructural ZIFs shows that in MOFs the stabilizing effect of metal is dependent on both framework topology (diamondoid (*dia)* > sodalite (SOD)) and dimensionality (2D > 3D). Thermodynamic analyses of metal substitution (Ag(I), Cu(I), and Li (I)) in isostructural

SOD and *dia* BIF systems confirm increase in density as a general descriptor for increased stabilization in MOFs. The study of energetics of guest-host interactions during CO_2 incorporation in azolate frameworks (i.e., ZIF-8) shows strong dependence of energetics of adsorption on choice of linker and metal. Additionally, several energetically favorable reaction pathways for the formation of CO_3-ZIF-8 have been identified. Both PDCs and MOFs show a complex energetic landscape, with identifiable system-dependent and general structural descriptors for increased thermodynamic stabilization and tunability of the energetics of guest-host interactions.

DEDICATION

This dissertation is dedicated to my loving family for their support and motivation during graduate school.

ACKNOWLEDGEMENTS

TABLE OF CONTENT

LIST OF TABLES

LIST OF FIGURES

CHAPTER 4

CHAPTER 5

CHAPTER 1

INTRODUCTION

1.1 General Remarks

Over the past century, the human population more than quadrupled to ~8 billion.[1,2] Industries now face a growing challenge of maintaining a steady supply of food, electricity, transportation, and other essential goods and services.[3] To meet the current demands of a still-growing population, industrial facilities continue to scale up their production capacity.[4] However, due to increasing concerns over climate change, industries must opt for greener production strategies.[5] These include increasing production yield by employing appropriate catalysts, utilization of porous materials for capturing evolved greenhouse gases, and other carbon-negative approaches.[6,7] This has fueled efforts in the research and development of materials with properties suitable for catalysis, molecular sieving, and high temperature applications. Current candidates with such desired properties include hybrid materials.[8,9]

The term "hybrid materials" refers to solids that contain both inorganic and organic moieties. Though their stability at high temperature is generally more limited than that of purely inorganic phases, varying their composition and dimensions by incorporating different organic functional groups opens an exciting field of properties and applications near room temperature. Structurally and compositionally, hybrid materials

can be placed mainly into three categories. The first class is metal organic frameworks (MOFs) in which metal nodes are connected by organic linkers to form open porous reticular frameworks. [8, 9] The second consists of refractory ceramics made from metal - organic polymer precursors and hence called polymer derived ceramics (PDCs). [10, 11] The third contains compounds in which large organic cations take the place of smaller inorganic cations to extend the field of conventional structures (e.g. perovskites) with predominantly ionic bonding.[12–14] This work entirely focuses on MOFs and PDCs.

To date, only few studies investigate the thermodynamic stability of these materials, which is an important consideration for their long-term application.[15] Although many hybrid materials are thermodynamically stable with respect to simpler components, others are metastable but the energetic metastability is seldom prohibitively large. [16, 17] Therefore, synthetic pathways can be designed to make the desired products and, in many cases, the materials will persist at ambient conditions until they are heated or exposed to corrosive environments.

One must distinguish thermal stability from thermodynamic stability. The former refers to decomposition on heating (often accompanied by oxidation) and the latter to formation from simpler constituents (elements or a mixture of metal oxide or halide plus organic compound). Thus, thermal and thermodynamic stability refer to different chemical reactions and their thermodynamic trends with composition are often different. Currently, knowledge of structural descriptors for increased stabilization is lacking, and that is the focus of this work.

1.2 Scope of Dissertation

Despite a wide variety of structures and compositions, hybrid organic-inorganic materials share many commonalities. Both hybrid subclasses contain carbon, present in the form of organic bridging linkers in MOFs,[9] or as carbide and/or free carbon domains in PDCs,[18, 19-21] and like pure carbon materials, both PDCs and MOFs can exist in amorphous, intermediate, or crystalline states, depending on choice of constituents and processing history.[10, 22, 23] The large and tunable porosity in PDCs and MOFs differentiates them from other hybrid materials.[24, 25] The size, shape, structure and porosity of MOFs can be tuned by employing appropriate metal-ligand combinations.[24, 26] In PDCs, tuning employs sacrificial fillers to the initial polymer blend.[27] Both MOFs and PDCs offer the possibility of constructing hierarchical porous structures, with surface areas much higher than activated carbon.[17, 24, 28, 29] Such structural modifications are accompanied by changes in macroscopic properties, including thermodynamic stability.[11, 20]

There are many opportunities for future work linking thermodynamics and structure. The increasing power of theory offers new opportunities to deal with large unit cells and, simultaneously, organic and inorganic constituents.[30] Understanding thermodynamic stability is a necessary starting point to make hybrid materials and assess their persistence and performance. To this end, this dissertation work presents a series of already published (or in press) chapters (2-9), systematically exploring structure-stability relations in various PDC systems and MOF structure types. The work has been done as different projects due to dissimilarities in the source of the samples.

Specifically, chapter 2 investigates systematics in the thermodynamic stabilization of SiC materials, including assessment of the effect of mixed bonding, resulting from addition of elemental constituents (O and/or N) to the structures. Chapter 3 expands the work on SiCs through the investigation of thermodynamic stabilization in a series of SiOC specimens. The work identifies dissimilarities in the stabilizing effect of different SiO_xC_{4-x} mixed bonding environments and studies correlation between ordering of the free carbon phase and thermodynamic stability in SiOCs. Additionally, chapter 4 explores the energetic landscape in more complex SiC(O)(N) quaternary systems, identifies differences in the stabilizing effects of SiO_xC_{4-x} and SiN_xC_{4-x} mixed bonds, and reports the energetic trend associated with ordering of the free carbon phase in these nitrogen-containing ceramics. Considering the popular use of fillers to tune the physicochemical properties in PDCs,[10] chapter 5 explores dissimilarities in the structural evolution, energetics of formation, and temperature-stability trends from choice of metal filler (Hf, Nb, Ta) incorporated in SiOC precursors.

In the same vein, the work on MOFs explores framework descriptors for increased stabilization. Specifically, chapter 6 probes the stabilizing effect of various metal atoms (Cu(II), Zn (II), Co(II)) across different ZIF topologies (SOD and *dia*) and dimensions (3D and 2D). Chapter 7 expands the work on ZIFs by exploring the energetics of metal substitution in topologically similar BIFs, and this enables confirmation of specific correlations seen in ZIFs and BIFs as general descriptors for thermodynamic stabilization in other MOF systems as well. Considering the increasing interest in the use of MOFs for CO_2 capture,[15] the work is expanded to explore the energetics of guest (CO_2)-host (frameworks) interactions in BIF and ZIF structures, and

4

this is presented in chapter 8. Lastly, MOFs can undergo decomposition by carbonation reaction during long-term exposure to CO_2 and moisture.[31] The work in chapter 9 quantitates the energetic drive for the formation of mixed linker carbonate MOF, and identifies several energetically favorable reaction pathways for the formation of carbonate MOFs. This is done through combination of experimental calorimetric techniques and theoretical prediction from atomistic models, including DFT calculations.

This work is a valuable addition to our current understanding of thermodynamic stabilization in these materials. The rest of this chapter is a brief description of MOFs and PDCs, as reported in a previous publication.[32]

1.3 Metal Organic Frameworks (MOFs)

MOFs are highly tunable, crystalline, porous, self-assembled frameworks containing metal nodes linked by organic ligands (see Figure 1 for two examples). Both linker and metal nodes are active components in MOF structures, contributing to the surface and bulk functionality of the framework and to its thermodynamic properties. Generally, longer linkers lead to larger pores. [26, 32, 33] A popular subclass of MOFs is metal azolate frameworks (MAFs). Because many MAFs have topologies (e.g. RHO, ANA, SOD, QTZ) similar to those familiar in zeolites, [16, 34] they are often called zeolitic imidazolate frameworks (ZIFs). ZIFs often employ tetrahedrally coordinated, divalent metal nodes such as Zn(II), Co(II), or Cu(II) bridged by azolate ligands such as 2-methylimidazole or 2-ethylimidazole.[16, 35] The formation of strong metal-nitrogen bonds

which tie the organic linker to the metal node results in structurally persistent ZIF frameworks, even upon removal of guest molecules used in synthesis.[16, 35]
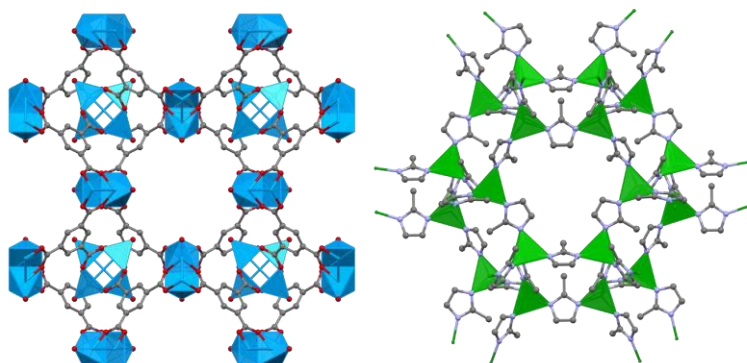
Figure 1. Examples of porous MOF structures; HKUST-1 (left) and ZIF8 (right). Color scheme: Cu is blue, O is red, N is purple, C is gray, and Zn is green.

Whereas inorganic zeolitic frameworks, sometimes called zeotypes, of a constant composition such as SiO_2 or $Al_{0.5}P_{0.5}O_2$ can be called true polymorphs (phases of different structure with the same composition), early work on MOFs emphasized making as many different structures as possible using a variety of linkers,[35] these materials do not represent true polymorphs and their thermodynamics would reflect differences in both structure and composition. A breakthrough in MOF synthesis came through the use of controlled mechanochemistry.[36] This enables synthesis of true polymorphs, and in some cases, the observation of phase transformations among several polymorphs with further grinding.[16, 34, 36]

The syntheses of a large set of MOFs has led to two fundamentally important thermodynamic questions. (1) Is there a trend in energetic stability with pore volume (or density) in MOFs similar to that seen in inorganic zeolitic materials? (2) When

mechanochemistry produces a series of denser MOF polymorphs with extended grinding time, are they more stable (grinding enables progression down an energy landscape) or are they less stable (grinding puts extra energy into the system and causes damage-driven transformation to higher points on the energy landscape). These questions inspired the Navrotsky group to perform a systematic calorimetric study of a number of ZIF polymorphs and other MOFs.[15, 16, 34, 35, 37–44]

previously Navrotsky investigated, using high temperature oxide melt solution calorimetry, the thermodynamic stability of an extensive set of zeolites with different porosities.[45–47] Zeolites are energetically metastable with respect to dense structures (e.g. quartz for SiO_2, berlinite for $AlPO_4$), thus confirming the existence of a thermodynamic penalty resulting from an increase in porosity.[45–47] The energetic metastability increases with increasing molar volume in a nonlinear fashion (see Figure 2a), with some indication that the energetics level off at high porosity, suggesting that the interior of larger pores has little effect on energetics, supporting the observation that ultraporous zeolitic frameworks are attainable.
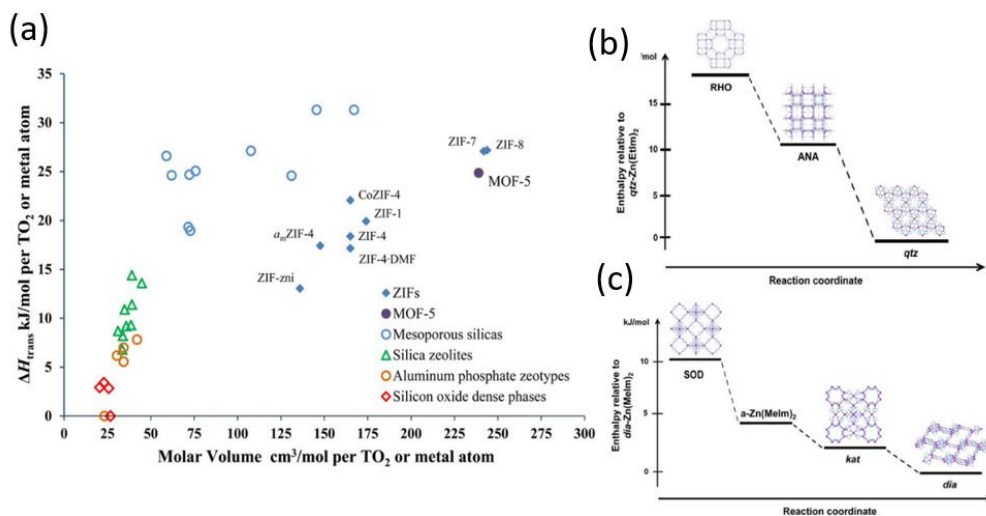
Figure 2. (a) Enthalpies of formation of zeolites, aluminum phosphate zeotypes, mesoporous silicas, ZIFs, and MOFs relative to their dense assemblages. (b) and (c) enthalpies of formation of ZIFs relative to their densest polymorphs. Reproduced with permission from references 16, 17.

The calorimetric trend for MOFs (Table 1 and Figure 2a) indeed is similar to that for zeolitic phases. The systematic offset for zeolites and MOFs seen in Figure 2a may relate to the choice of dense phase reference states but the important point is the similarity in magnitudes and slopes of the two sets of data. A firm conclusion is that although MOFs become less stable with increasing porosity, the destabilization is of the same magnitude as for zeolites.

Figure 2b gives a closer look at the energetics of true ZIF polymorphs based on zinc and 2-methyl or 2-ethylimidazole. In both cases, the calorimetric results confirm that the sequence of phases formed during mechanochemical synthesis trend downward on their energy landscapes, that is, increased grinding leads to more energetically favorable ZIFs.[16] Cryogenic heat capacity measurements on several crystalline and

8

amorphous polymorphs provide standard entropies of these ZIFs but show that details of low frequency vibrations appear to preclude a systematic variation of entropy with molar volume.[37, 38]

The pendant groups on the organic linker in a family of isostructural ZIFs seriously affect the measured enthalpy of formation (see Table 1).[34, 35] These effects can be considered as arising from changes in electron density distribution, including at the linker-node interface.[35] They can also be understood using a concept familiar to organic chemistry, namely the Hammett function.[35] In addition, theoretical calculations using dispersion-corrected periodic DFT provides energetic differences among different structures, including a fluorinated analogue of ZIF-8, in good agreement with calorimetric measurements. [34, 35] Such calculations can be used to predict the topological and energetic landscape of possible new ZIFs and suggest appropriate peripheral substituents on the organic linker to modify thermodynamic stability and tune physical properties.

The energetic effect of the nature of the metal on thermochemical stability within a given structure with the same linker has been studied by calorimetry in two systems. In "paddlewheel" MOFs, namely Cu- and Zn-HKUST-1. [39] Interaction with the solvent, dimethylformamide, greatly stabilizes both compounds, while their desolvated forms are, at best, of marginal thermodynamic and kinetic stability.[39, 42] The MOF-74 family of compounds shows promise in post-combustion CO_2 capture from coal fired power plants.[48] Unfortunately, these MOFs appear to be very sensitive to hydrolysis in the presence of water vapor, and calorimetric studies have confirmed that this instability is

driven by thermodynamically very favorable hydrolysis, probably limiting their applications [15].

Several MOF minerals have been found in nature.[43, 44, 49] These include paceite, zhemchuznikovite, and stepanovite (see Table 1).[43, 44, 49] Calorimetric measurements confirm the thermodynamic stability of these minerals in their geologic settings and enable calculation of possible corrosion and decomposition reactions. Zhemchuzhnikovite and stepanovite exhibit high proton conductivity, enabled by hydrogen-bonding networks involving interstitial water molecules, hydrated metal cation guests and the oxalate framework.[49] All the MOF minerals studied are very stable in enthalpy, and substitution of iron by aluminum improves the energetic stability of zhemchuzhnikovite.[49] Upon heating, stepanovite polymorphs lose included water guests without disrupting their 2-dimensional open framework layers.[49] Overall, these thermodynamic results are significant in the context of both geochemistry and materials chemistry, as they demonstrate that naturally occurring MOFs containing small ligands are thermodynamically stable phases that exhibit functional properties comparable to previously reported values for more complex advanced synthetic materials.[49]

The work done thus far addresses some of the fundamental questions needed for the design of thermodynamically more stable MOFs. Nevertheless, a better understanding of the free energy landscape of MOFs requires more systematic studies. Results from such work will help incorporate thermodynamic stability in the predictive design of novel MOFs.

Table 1. Enthalpies of formation of frameworks relative to endmembers: metal oxide plus linker and guest solvent (if present).

MOF compositions	Cation	Enthalpy of formation from endmembers ΔH_f (kJ/mol)	Ref
SOD-Zn(MeIm)$_2$	Zn^{+2}	-20.45 ± 0.94	[16, 35]
SOD-Zn(CHOIm)$_2$	Zn^{+2}	10.01 ± 1.03	[35]
SOD-Zn(VIm)$_2$	Zn^{+2}	-16.58 ± 1.11	[35]
SOD-Zn(AIm)$_2$	Zn^{+2}	-20.31 ± 0.90	[35]
SOD-Zn(ClIm)$_2$	Zn^{+2}	-19.48 ± 0.67	[35]
SOD-Zn(BrIm)$_2$	Zn^{+2}	-6.19 ± 0.50	[35]
SOD-Zn(IIm)$_2$	Zn^{+2}	-6.44 ± 0.79	[21,23]
SOD-Zn(CF$_3$Im)$_2$	Zn^{+2}	-3.97 ± 0.57	[35]
qtz-Zn(CF$_3$Im)$_2$	Zn^{+2}	-19.60 ± 0.27	[34]
qtz-Zn(EtIm)$_2$	Zn^{+2}	-41.25 ± 0.33	[16]
SOD-Zn(MeIm)·0.29CO$_2$	Zn^{+2}	-	[50]
SOD-Zn(MeIm)·0.56CO$_2$	Zn^{+2}	-	[50]
SOD-Zn(MeIm)·0.80CO$_2$	Zn^{+2}	-	[50]
SOD-Zn(MeIm)·0.87CO$_2$	Zn^{+2}	-	[50]
SOD-Zn(MeIm)·0.99CO$_2$	Zn^{+2}	-	[50]
ANA-Zn(EtIm)$_2$	Zn^{+2}	-31.63 ± 1.26	[16]

RHO-Zn(EtIm)$_2$	Zn^{+2}	-23.64 ± 0.85	16
dia-Zn(MeIm)$_2$	Zn^{+2}	-31.09 ± 1.17	16
kat-Zn(MeIm)$_2$	Zn^{+2}	-28.75 ± 0.62	16
Cu-HKUST-H$_2$O	Cu^{+2}	-158.11 ± 0.95	39
Cu-HKUST-dg	Cu^{+2}	49.97 ± 1.53	39
Zn-HKUST-DMF	Cu^{+2}	-162.66 ± 1.72	39
Zn-HKUST-amorph	Cu^{+2}	-10.71 ± 0.63	39
Mg-MOF-74	Mg^{+2}	303.89 ± 17.21	15
Ni-MOF-74	Ni^{+2}	264.38 ± 19.44	15
MOF-5 (DEF)	Zn^{+2}	78.64 ± 2.95	40, 41
MOF-5 (DG)	Zn^{+2}	99.47 ± 3.62	40
MOF-5·DMF	Zn^{+2}	16.69 ± 1.21	42
MOF-5	Zn^{+2}	99.47 ± 3.62	41, 42
ZIF-zni	Zn^{+2}	-33.60 ± 1.60	41
ZIF-4·DMF	Zn^{+2}	-27.60 ± 1.90	41
ZIF-4	Zn^{+2}	-24.60 ± 1.80	41
CoZIF-4	Co^{+2}	-18.40 ± 1.70	41
ZIF-1	Zn^{+2}	-26.70 ± 1.60	41
ZIF-7	Zn^{+2}	-19.50 ± 3.00	41
Cu-HK-1·H$_2$O	Cu^{+2}	-52.70 ± 0.30	41
Cu-HKUST-1	Cu^{+2}	16.70 ± 0.50	41
Zn-HK-1·DMF	Zn^{+2}	-54.20 ± 0.60	41

Zn-HK-1·amorph	Zn^{+2}	−3.60 ± 0.20	[41]
CuCa(CH$_3$COO)$_4$·6H$_2$O(s) (synthetic paceite)	Ca^{2+} and Cu^{2+}	−31.45 ± 0.25	[44]
CdCa(CH$_3$COO)$_4$·6H$_2$O(s) (synthetic paceite)	Ca^{2+} and Cd^{2+}	−20.46 ± 0.32	[44]

Abbreviation of linker ions: MeIm: 2-methylimidazolate,   CHOIm: 2-carbaldehyde: VIm: 2-vinylimidazolate; AIm: 2-acetyleneimidazolate; ClIm: 2-chloroimidazolate; BrIm: 2-bromoimidazolate; IIm: 2-iodoimidazolate: CF$_3$Im: 2-trifluoromethylimidazolate; EtIm: 2-ethylimidazolate.

1.4 Polymer Derived Ceramics (PDCs)
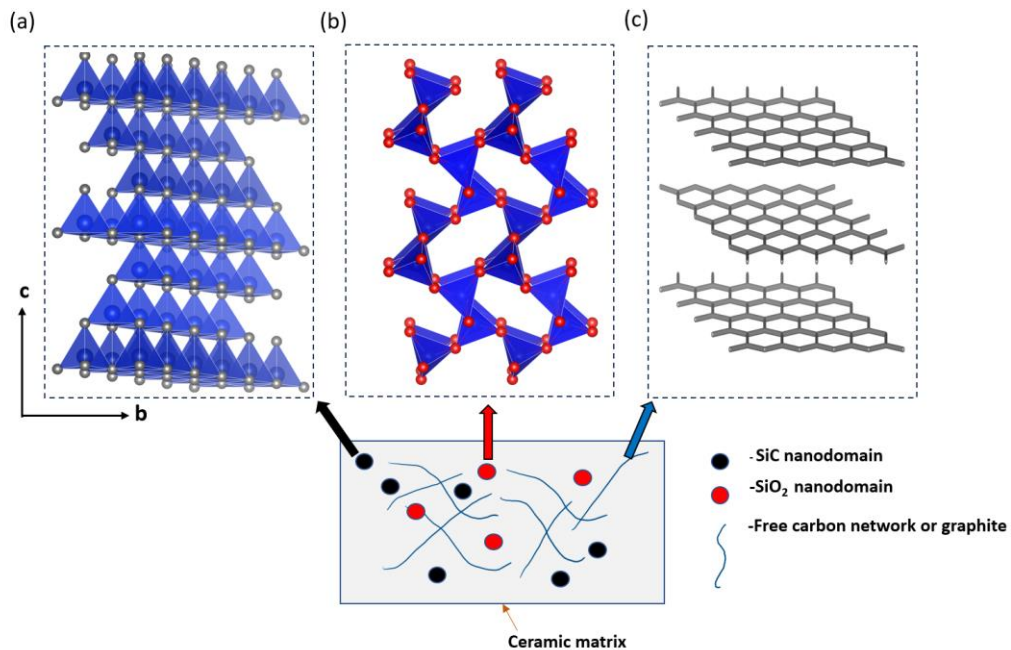
Figure 3: Illustration of a SiOC microstructure in high temperature semi-crystalline SiOC ceramics, synthesized from the pyrolysis of polysiloxane. (a) Packing

13

of tetrahedra in SiC domains; (b) Local dominant (other configurations may exist) six-membered ring structure in SiO_2 regions; (c) graphene layers in carbon rich regions in the PDC structure. In the crystal structures shown above: Si (tetrahedra) are blue, carbon is grey, oxygen is red. This figure is modified from reference 20

PDCs have complex microstructures (see Figure 3) and are attractive materials due to their high thermal stability, oxidation, and creep resistance,[11] resulting in their current and potential application in several industries, including aerospace, energy, and transportation.[10, 11] PDCs are attainable from the controlled thermolysis and ceramization of Si-containing preceramic polymers (PCPs) like polysiloxanes, polycarbodiimides, and polycarbosiloxanes.[11] Pyrolysis under an inert atmosphere results in the formation of SiO, SiC, SiCN, and SiOC ceramic systems.[10, 11]

Typically, high temperature pyrolysis of PCPs at temperatures below 1200 °C yields amorphous PDCs but by increasing pyrolysis temperature, their structure can evolve from amorphous to crystalline.[11, 51] In PDCs with excess carbon, phase transformations compete with carbothermal reduction (decomposition reactions). [10, 52] During carbothermal reduction in systems such as SiOCN, non-carbonaceous components like Si_3N_4 and SO_2 react with excess free carbons to yield evolved CO, N_2, and crystalline SiC.[10, 53, 54]

SiBCN systems have some of the highest decomposition temperature (~1950 °C).[10] The high thermal stability probably stems from the formation of CBN nanodomains in their microstructure, which reduces the reactivity of carbon within the

network at temperatures below ~2000 °C.[10] Similarly, adding elements such as Al, Ti, Zr, and Hf into the microstructure of SiOC and SiCN PDCs leads to the formation of PDCs persistent to ~2000 °C.[10, 55] It is not clear whether this enhanced apparent thermal stability is thermodynamically or kinetically driven.

We explored the thermochemistry of numerous PDC systems, including powders and fibers.[20, 56–58] Enthalpies of formation can be calculated from enthalpies of dissolution.[20, 53, 56, 59] Table 2 presents a summary of chemical formulas and enthalpies of formation. The work quantifies enthalpies of formation of the ceramic structures relative to crystalline components (β-SiC, SiO_2 (cristobalite), β-Si_3N_4 and C (graphite)).[60] This permits assessment of energetic stability arising from interdomain interactions within microstructures. More exothermic enthalpies relative to components indicate energetically more favorable interdomain interactions and/or more mixed bonding (Si bonded to C as well as O or N) in the PDCs.[20, 53] The investigations showed that most PDCs are energetically stable relative to binary components, which was initially not expected. [53, 61] Variations in the composition and bonding speciation result in significant thermodynamic variations.[62–65] Current findings suggest comparable stability in SiCN and SiOC PDC systems (see Table 2). The results from previous work indicate decreased thermodynamic drive for the formation of oxygen-free silicon carbonitride PDCs from binary components. However, SiC(O)(N) PDCs with moderate amounts of alloyed N and O show greater energetic stability.[65]

Recently, the effect of boron (B) on the thermodynamic stability of oxycarbide ceramics with various SiO(B)C compositions was studied.[66] There is superior resistance

to crystallization of structures with increasing B content, but this appears to be a kinetic effect at the cost of enthalpic destabilization.[66] Typically, B-containing oxycarbides ceramics (SiO(B)C), display great stabilization from microstructural modifications resulting from higher pyrolysis temperatures [64]. It should be noted that in simple SiOCs the temperature – stability trend is not so obvious, as some structures synthesized at 1200 °C are less thermodynamically stable than specimens pyrolyzed at higher (1450 °C) and lower (1000 °C) temperatures.[67] In addition to SiOCs, we investigated the microstructure and energetics of SiCNs derived through the polymeric route.[60] Structural characterization by NMR points to formation of H-terminated mixed bonds at the interfaces of stoichiometric domains in the SiCN specimens.[60, 68] Enthalpies of formation point to decreasing stabilization of the SiCN microstructures with increasing synthesis temperature.[60] Higher pyrolysis temperatures results in loss of residual hydrogen, and the calorimetric results may point to decreased stability of the mixed bonds with loss of terminal H.

The trends found so far vary significantly across PDC systems (SiOCs, SiCNs, SiCs), and are not simply dependent on synthesis temperature, but on compositional and microstructural variations in the ceramics as well.[53] This points to the need for further investigation of more compositions, for identification of descriptors in the chemistry and structure contributing to greater thermodynamic stabilization in PDCs.

Many aspects of the relationship between microstructure and thermodynamic stability of PDCs remain unexplored. Which features in PCPs (pendant groups, length of polymer chain) contribute to the formation of thermodynamically more stable PDCs, how

strongly and by what mechanism(s)? How does the thermodynamic stability of PDCs with dispersed mixed bonding units (not networks) compare to that of structures with mostly mixed bonding networks, in the form of nanodomains? What is the cost and benefit in terms of enthalpy, entropy, and free energy associated with structural modifications in PDCs?

Table 2. Enthalpies of formation of PDCs from binary crystalline components.

$(Si_aO_bC_cH_dN_eCa_fMg_gB_h)$ compositions where $a+b+c+d+e+f+g+h=1$										
a	b	c	d	e	f	g	h	Pyrolysis temperature (deg C)	$\Delta H^o_{f,\ comp}$ (kJ/mol)	Ref
0.112	0.227	0.47	0.191	0	0	0	0	800	-2.5 ± 3.4	56
0.283	0.588	0.078	0.052	0	0	0	0	1100	-3.2 ± 0.9	56
0.142	0.23	0.568	0.06	0	0	0	0	1100	-13.9 ± 3.9	56
0.313	0.473	0.213	0	0	0	0	0	1100	-15.2 ± 0.7	69
0.317	0.482	0.197	0	0	0	0.004	0	1100	-0.7 ± 0.7	69
0.2	0.4	0.2	0	0	0	0.0	0	1100	-6.9 ± 2.7	69

3 9	4 5	7 8				3 8				
0.262	0.454	0.252	0	0	0.013	0.018	0	1100	5.2 ± 2.2	69
0.364	0.513	0.123	0	0	0	0	0	1200	-19.8 ± 7.1	70
0.295	0.44	0.265	0	0	0	0	0	1200	-7.3 ± 7.0	70
0.271	0.374	0.355	0	0	0	0	0	1200	-34.2 ± 7.2	70
0.278	0.274	0.444	0	0	0	0	0	1200	-17.8 ± 7.0	70
0.259	0.238	0.503	0	0	0	0	0	1200	-128.2± 7.1	70
0.096	0.041	0.034	0.273	0.244	0	0	0	800	-42.4 ± 1.2	60
0.134	0.015	0.435	0.130	0.285	0	0	0	110	-25.8 ± 1.5	60
0.1	0.0	0.5	0.1	0.1	0	0	0	800	-32.0 ± 1.3	60

21	20	94	19	49						
0.126	0.019	0.671	0.034	0.151	0	0	0	1100	-25.9 ± 1.8	60
0.204	0	0.556	0	0.239	0	0	0	1100	-2.8 ± 6.4	62
0.368	0.496	0.226	0	0	0	0	0	1000	-70.7 ± 3.5	67
0.350	0.420	0.231	0	0	0	0	0	1200	-27.6 ± 3.7	67
0.349	0.424	0.227	0	0	0	0	0	1450	-61.2 ± 3.1	67
0.353	0.390	0.257	0	0	0	0	0	1000	-53.9 ± 3.6	67
0.364	0.378	0.258	0	0	0	0	0	1200	-40.4 ± 4.6	67
0.352	0.392	0.256	0	0	0	0	0	1450	-46.6 ± 4.5	67
0.3	0.2	0.3	0	0	0	0	0	1000	-53.3 ± 3.3	67

14	91	95								
0.299	0.311	0.386	0	0	0	0	0	1200	-33.4 ± 4.6	67
0.304	0.301	0.394	0	0	0	0	0	1450	-26.6 ± 3.6	67
0.262	0.189	0.549	0	0	0	0	0	1000	-51.9 ± 4.4	67
0.235	0.209	0.556	0	0	0	0	0	1200	-15.5 ± 5.9	67
0.246	0.190	0.564	0	0	0	0	0	1450	-46.2 ± 4.7[5]	67
0.275	0.008	0.376	0.246	0	0	0	0	1100	-26.6 ± 3.7	66
0.254	0.013	0.375	0.251	0	0	0	0.013	1100	-17.4 ± 3.2	66
0.252	0.006	0.381	0.231	0	0	0	0.037	1100	-15.1 ± 1.5	66
0.2	0.0	0.3	0.2	0	0	0	0.	1100	-10.5 ± 1.5	66

45	08	77	32				06			
0.230	0.009	0.371	0.230	0	0	0	0.083	1100	-1.4 ± 2.4	66
0.318	0.485	0.192	0.005	0	0	0	0	1100	-6.5 ± 2.4	63
0.345	0.523	0.088	0.044	0	0	0	0	1100	-13 ± 3.4	63
0.314	0.467	0.220	0	0	0	0	0	1200	-21.5 ± 2.4	64
0.274	0.487	0.207	0	0	0	0	0.031	1200	-12.8 ± 2.4	64
0.256	0.500	0.188	0	0	0	0	0.057	1200	-2.5 ± 2.6	64
0.307	0.461	0.232	0	0	0	0	0	1200	-4.9 ± 2.9	57
0.314	0.434	0.252	0	0	0	0	0	1600	-10.2 ± 3.2	57
0.0	0.1	0.7	0	0	0	0	0	1200	6.7 ± 2.2	57

8 5	4 4	7 1								
0.062	0.002	0.935	0	0	0	0	0	1450	-27.4 ± 1.7	[57]
0.05	0.003	0.947	0	0	0	0	0	1600	-2.2 ± 2.0	[57]
0.220	0.320	0.200	0.260	0	0	0	0	1200	-36.1 ± 3.2	[71]
0.371	0.003	0.363	0.263	0	0	0	0	600	-9.6 ± 9.1	[72]
0.254	0.196	0.226	0.325	0	0	0	0	600	-33.3 ± 7.5	[72]
0.185	0.256	0.177	0.383	0	0	0	0	600	-0.5 ± 7.1	[72]
0.164	0.261	0.150	0.425	0	0	0	0	600	-24.0 ± 7.1	[72]
0.36	0.452	0.100	0.086	0	0	0	0	600	-53.8 ± 7.0	[72]
0.4		0.5		0	0	0	0	1450	-12.0 ± 8.7	[20]

65	31									
0.4714	0.011	0.513	0	0	0	0	0		1450	-58.7 ± 6.9	[20]
0.518	0.002	0.475	0	0	0.003	0	0		1450	-71.1 ± 8.7	[20]

1.5 Concluding Remarks

Many aspects of the relationship between chemistry, structure, and thermodynamic stability of PDCs and MOFs remain unexplored. How does the thermodynamic stability of MOFs relate to different lattice vibrational modes?, in PDCs how does thermodynamic stability of the structures correlate with the size of individual nanodomains? Lastly, In what ways is the thermodynamics of PDCs similar to that of MOFs? Such understanding is necessary for the development of a framework for the predictive design of materials with high thermodynamic stability and desired functionality. Perhaps more answers may be attainable through combination of calorimetry and advanced characterization methods, including neutron and small angle x-ray scattering techniques. Thus, much research remains to be done.

REFERENCES

1. Roser, M., Ritchie, H. & Ortiz-Ospina, E. World Population Growth. *Our World Data* (2013).

2. World Population Clock: 7.9 Billion People (2022) - Worldometer.

3. *Economics of Natural Resource Scarcity: The State of the Debate*. (2005).

4. Holdren, J. P. & Ehrlich, P. R. Human Population and the Global Environment: Population growth, rising per capita material consumption, and disruptive technologies have made civilization a global ecological force. *Am. Sci.* **62**, 282–292 (1974).

5. Hallegatte, S., Fay, M. & Vogt-Schilb, A. Green Industrial Policies : When and How. *openknowledge.worldbank.org*. 16892 (2013)

6. Siegelman, R. L., Kim, E. J. & Long, J. R. Porous materials for carbon dioxide separations. *Nat. Mater.* **20**, 1060–1072 (2021).

7. Arakawa, H. *et al.* Catalysis Research of Relevance to Carbon Management: Progress, Challenges, and Opportunities. *Chem. Rev.* **101**, 953–996 (2001).

8. Tranchemontagne, D. J., Ni, Z., O'Keeffe, M. & Yaghi, O. M. Reticular Chemistry of Metal–Organic Polyhedra. *Angew. Chem. Int. Ed.* **47**, 5136–5147 (2008).

9. Yaghi, O. M. Reticular Chemistry in All Dimensions. *ACS Cent. Sci.* **5**, 1295–1300 (2019).

10. Colombo, P. *Polymer Derived Ceramics: From Nano-structure to Applications*. (DEStech Publications, Inc, 2010).

11. Colombo, P., Mera, G., Riedel, R. & Sorarù, G. D. Polymer-Derived Ceramics: 40 Years of Research and Innovation in Advanced Ceramics. *J. Am. Ceram. Soc.* **93**, 1805–1837 (2010).

12. Nagabhushana, G. P., Shivaramaiah, R. & Navrotsky, A. Thermochemistry of Multiferroic Organic–Inorganic Hybrid Perovskites [(CH3)2NH2][M(HCOO)3] (M = Mn, Co, Ni, and Zn). *J. Am. Chem. Soc.* **137**, 10351–10356 (2015).

13. Vasileiadou, E. S. *et al.* Insight on the Stability of Thick Layers in 2D Ruddlesden–Popper and Dion–Jacobson Lead Iodide Perovskites. *J. Am. Chem. Soc.* **143**, 2523–2536 (2021).

14. Wei, J. *et al.* Highly Stable Hybrid Perovskite Solar Cells Modified with Polyethylenimine via Ionic Bonding. *ChemNanoMat* **4**, 649–655 (2018).

15. Voskanyan, A. A., Goncharov, V. G., Novendra, N., Guo, X. & Navrotsky, A. Thermodynamics Drives the Stability of the MOF-74 Family in Water. *ACS Omega* **5**, 13158–13163 (2020).

16. Akimbekov, Z. *et al.* Experimental and Theoretical Evaluation of the Stability of True MOF Polymorphs Explains Their Mechanochemical Interconversions. *J. Am. Chem. Soc.* **139**, 7952–7957 (2017).

17. Hughes, J. T., Bennett, T. D., Cheetham, A. K. & Navrotsky, A. Thermochemistry of Zeolitic Imidazolate Frameworks of Varying Porosity. *J. Am. Chem. Soc.* **135**, 598–601 (2013).

18. Leonel, G. J., Mujib, S. B., Singh, G. & Navrotsky, A. Thermodynamic stabilization of crystalline silicon carbide polymer-derived ceramic fibers. *Int. J. Ceram. Eng. Sci.* 4, 315–326 (2022).

19. Ren, Z., Mujib, S. B. & Singh, G. High-Temperature Properties and Applications of Si-Based Polymer-Derived Ceramics: A Review. *Materials* **14**, 614 (2021).

20. Lin, Z.-J., Lü, J., Hong, M. & Cao, R. Metal–organic frameworks based on flexible ligands (FL-MOFs): structures and applications. *Chem. Soc. Rev.* **43**, 5867–5895 (2014).

21. Almáši, M., Király, N., Zeleňák, V., Vilková, M. & Bourrelly, S. Zinc(ii) and cadmium(ii) amorphous metal–organic frameworks (aMOFs): study of activation process and high-pressure adsorption of greenhouse gases. *RSC Adv.* **11**, 20137–20150 (2021).

22. Furukawa, H. *et al.* Ultrahigh Porosity in Metal-Organic Frameworks. *Science* **329**, 424–428 (2010).

23. Yeon, S.-H. *et al.* Carbide-derived-carbons with hierarchical porosity from a preceramic polymer. *Carbon* **48**, 201–210 (2010).

24. Xue, D.-X. *et al.* Topology meets MOF chemistry for pore-aperture fine tuning: ftw - MOF platform for energy-efficient separations via adsorption kinetics or molecular sieving. *Chem. Commun.* **54**, 6404–6407 (2018).

25. Lale, A. *et al.* Polymer-Derived Ceramics with engineered mesoporosity: From design to application in catalysis. *Surf. Coat. Technol.* **350**, 569–586 (2018).

26. Vakifahmetoglu, C., Presser, V., Yeon, S.-H., Colombo, P. & Gogotsi, Y. Enhanced hydrogen and methane gas storage of silicon oxycarbide derived carbon. *Microporous Mesoporous Mater.* **144**, 105–112 (2011).

27. Yang, K. *et al.* Preparation of high surface area activated carbon from coconut shells using microwave heating. *Bioresour. Technol.* **101**, 6163–6169 (2010).

28. Leonel, G. J., Lennox, C. B., Marrett, J. M., Friščić, T. & Navrotsky, A. Crystallographic and Compositional Dependence of Thermodynamic Stability of [Co(II), Cu(II), and Zn(II)] in 2-Methylimidazole-Containing Zeolitic Imidazolate Frameworks. *Chem. Mater.* (2023)

29. Mottillo, C. & Friščić, T. Carbon Dioxide Sensitivity of Zeolitic Imidazolate Frameworks. *Angew. Chem.* **126**, 7601–7604 (2014).

30. Navrotsky, A. & Leonel, G. J. Thermochemistry of hybrid materials. *Philos. Trans. R. Soc. Math. Phys. Eng. Sci.* **381**, 20220334 (2023).

31. Eddaoudi, M., F. Sava, D., F. Eubank, J., Adil, K. & Guillerm, V. Zeolite-like metal–organic frameworks (ZMOFs): design, synthesis, and properties. *Chem. Soc. Rev.* **44**, 228–249 (2015).

32. Mollick, S., Fajal, S., Mukherjee, S. & Ghosh, S. K. Stabilizing Metal–Organic Polyhedra (MOP): Issues and Strategies. *Chem. – Asian J.* **14**, 3096–3108 (2019).

33. Arhangelskis, M. *et al.* Theoretical Prediction and Experimental Evaluation of Topological Landscape and Thermodynamic Stability of a Fluorinated Zeolitic Imidazolate Framework. *Chem. Mater.* **31**, 3777–3783 (2019).

34. Novendra, N. *et al.* Linker Substituents Control the Thermodynamic Stability in Metal–Organic Frameworks. *J. Am. Chem. Soc.* **142**, 21720–21729 (2020).

35. Julien, P. A. & Friščić, T. Methods for Monitoring Milling Reactions and Mechanistic Studies of Mechanochemistry: A Primer. *Cryst. Growth Des.* **22**, 5726–5754 (2022).

36. Calvin, J. J. *et al.* Heat capacity and thermodynamic functions of crystalline and amorphous forms of the metal organic framework zinc 2-ethylimidazolate, Zn(EtIm)2. *J. Chem. Thermodyn.* **116**, 341–351 (2018).

37. Calvin, J. J., Rosen, P. F., Smith, S. J. & Woodfield, B. F. Heat capacities and thermodynamic functions of the ZIF organic linkers imidazole, 2-methylimidazole, and 2-ethylimidazole. *J. Chem. Thermodyn.* **132**, 129–141 (2019).

38. Bhunia, M. K., Hughes, J. T., Fettinger, J. C. & Navrotsky, A. Thermochemistry of Paddle Wheel MOFs: Cu-HKUST-1 and Zn-HKUST-1. *Langmuir* **29**, 8140–8145 (2013).

39. Hughes, J. T. & Navrotsky, A. MOF-5: Enthalpy of Formation and Energy Landscape of Porous Materials. *J. Am. Chem. Soc.* **133**, 9184–9187 (2011).

40. Wu, D. & Navrotsky, A. Thermodynamics of metal-organic frameworks. *J. Solid State Chem.* **223**, 53–58 (2015).

41. Akimbekov, Z., Wu, D., Brozek, C. K., Dincă, M. & Navrotsky, A. Thermodynamics of solvent interaction with the metal–organic framework MOF-5. *Phys. Chem. Chem. Phys.* **18**, 1158–1162 (2015).

42. Huskić, I., Pekov, I. V., Krivovichev, S. V. & Friščić, T. Minerals with metal-organic framework structures. *Sci. Adv.* **2**, e1600621 (2016).

43. Li, S. *et al.* Mechanochemical Synthesis, Accelerated Aging, and Thermodynamic Stability of the Organic Mineral Paceite and Its Cadmium Analogue. *ACS Omega* **4**, 5486–5495 (2019).

44. Petrovic, I., Navrotsky, A., Davis, M. E. & Zones, S. I. Thermochemical study of the stability of frameworks in high silica zeolites. *Chem. Mater.* **5**, 1805–1813 (1993).

45. Navrotsky, A. Energetics of nanoparticle oxides: interplay between surface energy and polymorphism†. *Geochem. Trans.* **4**, 34 (2003).

46. Piccione, P. M. *et al.* Thermochemistry of Pure-Silica Zeolites. *J. Phys. Chem. B* **104**, 10001–10011 (2000).

47. Valenzano, L. *et al.* Computational and Experimental Studies on the Adsorption of CO, N2, and CO2 on Mg-MOF-74. *J. Phys. Chem. C* **114**, 11185–11191 (2010).

48. Huskić, I. *et al.* Functionality in metal–organic framework minerals: proton conductivity, stability and potential for polymorphism. *Chem. Sci.* **10**, 4923–4929 (2019).

49. Rosen, P. F. *et al.* Thermodynamic Evidence of Structural Transformations in CO2-Loaded Metal–Organic Framework Zn(MeIm)2 from Heat Capacity Measurements. *J. Am. Chem. Soc.* **142**, 4833–4841 (2020).

50. Zhang, Y., Yin, X., Ye, F. & Kong, L. Effects of multi-walled carbon nanotubes on the crystallization behavior of PDCs-SiBCN and their improved dielectric and EM absorbing properties. *J. Eur. Ceram. Soc.* **34**, 1053–1061 (2014).

51. Saha, A. & Raj, R. Crystallization Maps for SiCO Amorphous Ceramics. *J. Am. Ceram. Soc.* **90**, 578–583 (2007).

52. Leonel, G. J., Guo, X., Singh, G., Gervais, C. & Navrotsky, A. Energetics and structure of SiC(N)(O) polymer-derived ceramics. *J. Am. Ceram. Soc.* **106**, 5086–5101 (2023).

53. Sasikumar, P. V. W. *et al.* Polymer derived silicon oxycarbide ceramic monoliths: Microstructure development and associated materials properties. *Ceram. Int.* **44**, 20961–20967 (2018).

54. Ionescu, E. *et al.* Polymer-Derived Ultra-High Temperature Ceramics (UHTCs) and Related Materials. in *Ceramics, Glass and Glass-Ceramics: From Early Manufacturing Steps Towards Modern Frontiers* (eds. Baino, F., Tomalino, M. & Tulyaganov, D.) 281–323 (Springer International Publishing, 2021).

55. Sugie, C., Navrotsky, A., Lauterbach, S., Kleebe, H.-J. & Mera, G. Structure and Thermodynamics of Silicon Oxycarbide Polymer-Derived Ceramics with and without Mixed-Bonding. *Materials* **14**, 4075 (2021).

56. Niu, M. *et al.* Structure and energetics of SiOC and SiOC-modified carbon-bonded carbon fiber composites. *J. Am. Ceram. Soc.* **100**, 3693–3702 (2017).

57. Tavakoli, A. H., Golczewski, J. A., Bill, J. & Navrotsky, A. Effect of boron on the thermodynamic stability of amorphous polymer-derived Si(B)CN ceramics. *Acta Mater.* **60**, 4514–4522 (2012).

58. Leonel, G. J., Guo, X., Singh, G. & Navrotsky, A. Compositional Analysis of SiOC(H) Powders: A Comparison of X-ray Photoelectron Spectroscopy (XPS) and Combustion Analysis. *Ceramics* **6**, 74–85 (2023).

59. Widgeon, S. *et al.* Nanostructure and Energetics of Carbon-Rich SiCN Ceramics Derived from Polysilylcarbodiimides: Role of the Nanodomain Interfaces. *Chem. Mater.* **24**, 1181–1191 (2012).

60. Mera, G., Navrotsky, A., Sen, S., Kleebe, H.-J. & Riedel, R. Polymer-derived SiCN and SiOC ceramics – structure and energetics at the nanoscale. *J. Mater. Chem. A* **1**, 3826–3836 (2013).

61. Michelle Morcos, R. et al. Enthalpy of Formation of Carbon-Rich Polymer-Derived Amorphous SiCN *Ceramics. J. Am. Ceram. Soc*. 91, 3349–3354 (2008).

62. Tavakoli, A. H., Armentrout, M. M., Narisawa, M., Sen, S. & Navrotsky, A. White Si–O–C Ceramic: Structure and Thermodynamic Stability. *J. Am. Ceram. Soc.* **98**, 242–246 (2015).

63. Tavakoli, A. H. *et al.* Energetics and Structure of Polymer-Derived Si–(B–)O–C Glasses: Effect of the Boron Content and Pyrolysis Temperature. *J. Am. Ceram. Soc.* **97**, 303–309 (2014).

64. Morcos, R. M. et al. Thermodynamically Stable SiwCxNyOz Polymer-Like, Amorphous Ceramics Made from Organic Precursors. J. Am. Ceram. Soc. 91, 2391–2393 (2008).

65. Tavakoli, A. H., Golczewski, J. A., Bill, J. & Navrotsky, A. Effect of boron on the thermodynamic stability of amorphous polymer-derived Si(B)CN ceramics. *Acta Mater.* **60**, 4514–4522 (2012).

66. Morcos, R. M. *et al.* Energetics of SixOyCz Polymer-Derived Ceramics Prepared Under Varying Conditions. *J. Am. Ceram. Soc.* **91**, 2969–2974 (2008).

67. Widgeon, S. *et al.* Effect of Precursor on Speciation and Nanostructure of SiBCN Polymer-Derived Ceramics. *J. Am. Ceram. Soc.* **96**, 1651–1659 (2013).

68. Ionescu, E., Sen, S., Mera, G. & Navrotsky, A. Structure, energetics and bioactivity of silicon oxycarbide-based amorphous ceramics with highly connected networks. *J. Eur. Ceram. Soc.* **38**, 1311–1319 (2018).

69. Varga, T. *et al.* Thermodynamically Stable SixOyCz Polymer-Like Amorphous Ceramics. *J. Am. Ceram. Soc.* **90**, 3213–3219 (2007).

70. Tavakoli, A. H., Armentrout, M. M., Sen, S. & Navrotsky, A. Hydrogenated Si–O–C nanoparticles: Synthesis, structure, and thermodynamic stability. *J. Mater. Res.* **30**, 295–303 (2015).

71. Chen, J. *et al.* Thermodynamic Stability of Low-k Amorphous SiOCH Dielectric Films. *J. Am. Ceram. Soc.* **99**, 2752–2759 (2016).

CHAPTER 2

THERMODYNAMIC STABILIZATION OF CRYSTALLINE SILICON CARBIDE

POLYMER DERIVED CERAMIC FIBERS

Abstract: Three crystalline SiC fibers were studied: Tyranno, Hi-Nicalon, and Sylramic™. Thermodynamic stability of the SiC fibers was determined by high temperature oxide melt solution calorimetry. Results shed light on the thermodynamic penalty or benefit associated with microstructural modification of the ceramic fibers and how energetics correlate to mechanical properties. Enthalpies of formation from components show greatest stabilization of the Sylramic^{TM} microstructure. In contrast, the microstructure in Tyranno is the least stable. The thermodynamic stability of the fibers increases with increasing mixed bonding (Si bonded to both C and O). From mechanical testing, Young's moduli of Tyranno, Hi-Nicalon, and Sylramic™ are 112, 205, and 215 GPa, respectively. Greater thermodynamic stability is correlated with a higher Young's modulus.

2.1 Introduction

Polymer derived ceramics (PDCs) refer to a class of ceramic materials obtained through pyrolysis of preceramic organometallic polymers .[1] Under appropriate synthesis

conditions, PDCs such as silicon oxycarbide (SiOC), silicon oxycarbonitride (SiCN), and silicon carbide (SiC) can be synthesized via controlled pyrolysis of preceramic polymers such as polycarbosiloxanes, polycarbodiamides, and polycarbosilanes (see Figure.1).[2] PDCs are notable due to their high thermal stability,[3] as well as corrosion and creep resistance. They have potential use in mechanical and aerospace technologies [2, 4] including manufacturing aircraft turbine engine components,[5–7] and are proposed as anode materials in lithium ion batteries.[8]
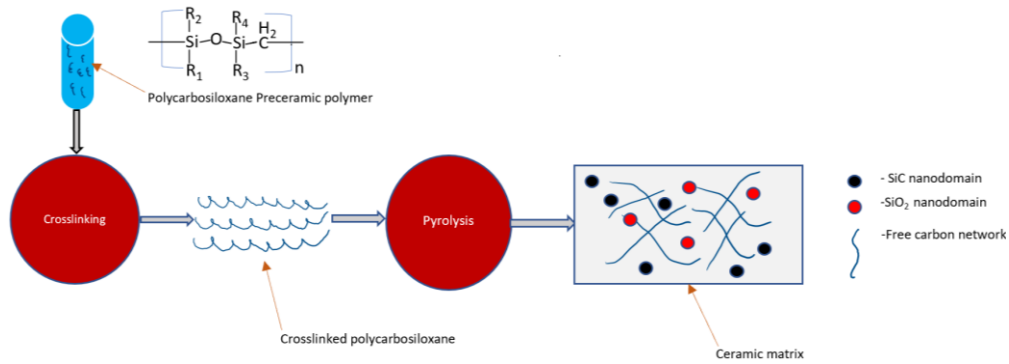
Figure 1. Schematic illustration of synthesis of SiOC PDCs through pyrolysis of polycarbosiloxane.

PDCs are distinct from other high temperature materials because of the ease in tunability of their microstructure[9] and the resulting mechanical properties.[10, 11] Previous studies have consistently shown that the microstructure of the final PDC depends on the structure of the initial preceramic polymer[12] and also on pyrolysis conditions.[13] The final composition of PDCs can be readily tuned by varying the organic groups in the backbone of the preceramic polymer[14] to ease manipulation of each species' content in the

pyrolyzed PDC.[15] This allows facile synthesis of compositionally similar materials with different microstructures such as those observed in SiOC systems.[16]

The resulting PDC microstructure is intrinsic to the nanodomains (1-3 nm)[17] present in the ceramic matrix.[18] Depending on the ratio of different domains present in the form of free carbons(C), silica (SiO_2), silicon carbide (SiC), and mixed bonding silicon oxycarbide (SiOC), the properties of the PDC vary significantly.[19] Pyrolysis temperature can determine which nanodomains are present and whether they are amorphous or crystalline.[20] This variability of PDCs allows tunability of their microstructure,[21] which influences macroscopic properties such as porosity[22]. Although previous studies have reported the synthesis,[23] potential applications,[4] and kinetics[24] of bulk PDCs and PDCs in fiber form, very few studies have investigated the thermodynamic stability of these materials. Due to the increasing potential applications of PDCs,[2, 25] now more than ever, it is important to understand the free-energy landscape of these systems. Thermodynamic studies permit distinction of metastability and real stability, which is important for understanding PDC reactivity and properties.

The engineering of PDC fibers is an area of interest within the ceramic community. A popular method for the synthesis of ceramic fibers involves the pyrolysis (under inert atmosphere) of electrospun preceramic polymers such as polymethyl-silsesquioxane.[26] Often, metal additives such as aluminum and titanium are grafted into the microstructure of PDCs as sintering aids during crosslinking.[27, 28] PDC fibers such as Hi-Nicalon, Tyranno, and Sylramic[TM] are commercially available.[7] The synthesis temperature for the manufacturing of these ceramic fibers can be as high as > 1700 °C,

which is higher than typical pyrolysis temperature for the synthesis of PDC powders.[7] Previous reports have focused on investigating the mechanical properties of these fibers and their composites.[29, 30] The energetic landscape of PDC fibers is still poorly understood. It is important to systematically investigate and identify factors that contribute to an increase in the thermodynamic stability of these materials. In PDC fibers, the microstructure changes depending on the species (Si, C, O, N) present in the bulk.[31] If different domains interact with one another, it is important to assess whether such interactions are energetically favorable or destabilizing. Depending on the ceramic fiber, the microstructure and interactions can be stabilized through the presence of mixed bonding (silicon bonded to both carbon and oxygen) in domains or in interdomain regions.[32] On the other hand, differences in the domains and their interactions could have a significant energetic cost, which could ultimately affect the free energy and stability of the fiber.[32, 33]

This study analyzes three different commercial SiC crystalline PDC fibers, Tyranno, Hi-Nicalon, and Sylramic™. All are nominally crystalline SiC fibers, with Hi-Nicalon and Sylramic™ containing small amounts of oxygen and/or nitrogen within the bulk. Structural characterization was performed by scanning electron microscopy (SEM), X-ray diffraction (XRD), Raman spectroscopy, X-ray photoemission spectroscopy (XPS), and combustion analysis. We describe the effect of mixed bonding and interdomain interactions on the thermodynamic stability of PDCs. We explore possible correlations between the microscopic and macroscopic properties of the three fibers.

2.2 Experimental Methods

The samples were obtained from commercial sources. The synthesis of commercial fibers has been described in previous studies.[7, 34, 35] The main steps in their synthesis involve curing (in air or by electron beam irradiation) of polycarbosilanes, polycarbosilazanes, or polysiloxanes preceramic polymers followed by their high temperature controlled pyrolysis.[36, 37] SEM of the fibers was carried out on a Carl Zeiss EVO MA10 system with incident voltage of 5 kV. Raman characterization was performed by use of a confocal Horiba Jobin Yvon LabRam ARAMIS system equipped with 633 nm HeNe laser at a laser power of 17 mW with a 50 X microscope objective. XRD was conducted at room temperature using a Bruker D2 Advance powder diffractometer with nickel-filtered CuKα radiation ($\lambda=1.5418$ Å) . The chemical composition of the surface was studied by XPS using a Thermo Scientific instrument with an Al Kα+ ion beam (beam energy = 1486.6 eV and spot size = 400 μm). To remove any surface contamination, the surface was sputtered with Ar+ at 3.0 keV for 2 min prior to measurement. The bulk elemental composition of the three fiber types was measured by a LECO Analyzer model CS844 or model ONH-836 following procedures described in the literature .[38] Tensile tests on fiber tows (untwisted multifilament bundles) were conducted using a Shimadzu AGS-X 5 KN Universal Testing Machine. Combustion analyses of bulk components were performed using LECO Analyzers (model No. ONH-836 and model No. CS844). Calorimetric measurements of enthalpy of dissolution were performed in a Setaram Alexsys calorimeter at 800 °C with molten sodium molybdate ($3Na_2O \cdot 4MoO_3$) as solvent under an oxygen atmosphere. Additional details are given in the discussion.

2.3 Results and Discussion

It is important to identify the existence/absence of crystalline phases in the microstructure of PDCs. In this study, XRD is used to confirm the presence of crystalline grains within the bulk of the PDC fibers. Well-defined peaks in the XRD patterns confirm the presence of SiC crystalline phases mainly of the 3C polytype; typical of the three fiber types.[39] Minor shifts in the main β-SiC peak are likely a result of differences in lattice strain.[40] Similarly, the breadth of the main β-SiC peak in Hi-Nicalon may be a result of slight differences in crystallite size compared to the other two fibers. All three fibers show unidentified peaks at around 29 ° (2θ) (see Figure 2), likely corresponding to substrate material.
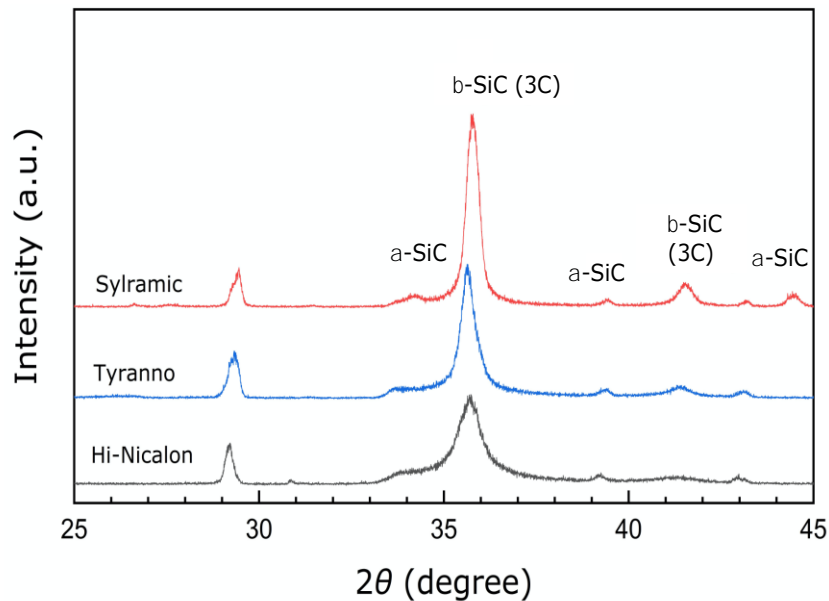
Figure 2. XRD patterns show presence of polycrystalline SiC grains in all three fibers. Graphite reflections are not observed; free carbon is present as amorphous carbon domains.

Darkfield SEM images at lower magnification allow identification of their geometry as shown in Figure 3. All three crystalline fiber types appear to be uniform in shape with smooth surfaces. The fibers show uniform diameters along the length of the fibers and no apparent cracks, cleavage, or pores were present in the fibers. A high magnification image (Figure 3) allows identification of differences in the diameter of individual fibers.
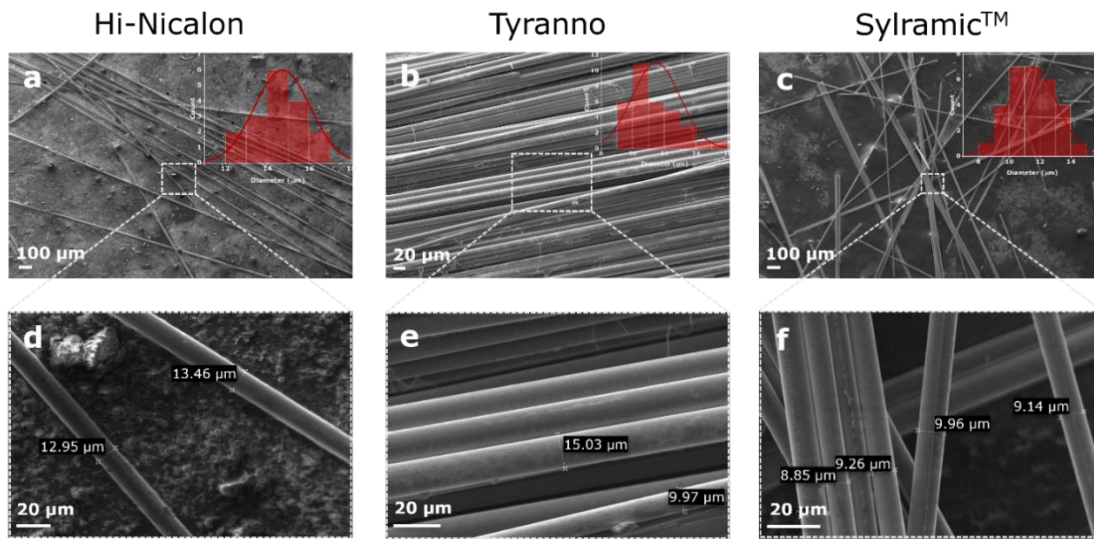
Figure 3. Scanning electron micrographs of (a) Hi-Nicalon, (b) Tyranno, and (c) Sylramic™ individual fiber. (d-f) High magnification images show uniform morphology but some variation in diameter of fibers.

Raman spectra are shown in Figure 4. The peak at ~790 cm^{-1} is assigned to the transverse optical (TO) mode and that at ~950 cm^{-1} is ascribed to the longitudinal optical (LO) mode vibration of β-SiC.[41] Raman surface analysis also allows identification of D (~1330 cm^{-1}), G (~1600 cm^{-1}), and G'(~2680 cm^{-1}) bands which correspond to disordered sp^2 carbon, graphitic sp^2 carbon, and resonant phonon scattering from

disordered sp^2 carbons, respectively. The integrated intensity of the full width at half maximum corresponding to the D (I_D) and G (I_G) bands allows identification of the ratio between disordered sp^2 and graphitic sp^2 carbons. Figure 4 suggests that I_D/I_G ratios increase from Sylramic^{TM} to Tyranno to Hi-Nicalon, thus indicating a decrease in the amount of sp^2 graphitic carbon relative to disordered sp^2 carbons in that order. The absence of D, G, and G' bands suggests the absence of free carbons in the Sylramic^{TM} fiber, this agrees with the results from bulk chemical composition by combustion analysis, see below. Lack of a turbostratic carbon phase in Sylramic^{TM} fiber has been reported by other groups as well [42, 43]
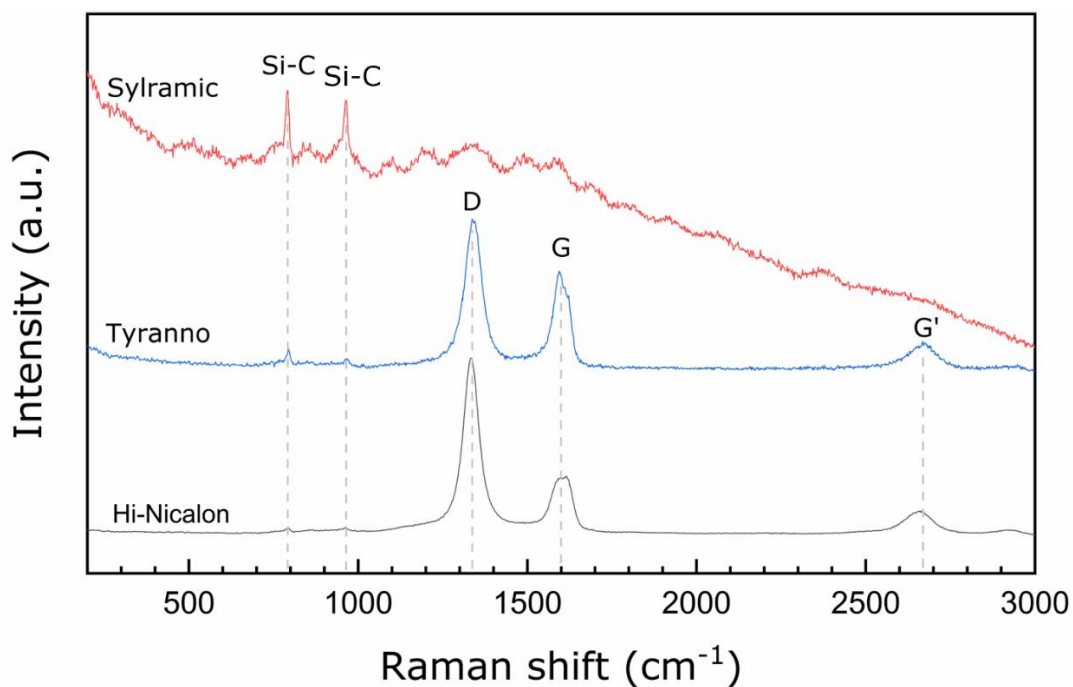
Figure 4. Raman spectra of fibers.

XPS is a surface sensitive technique which generally probes the structure to only about 5 nm in depth.[44, 45] Therefore, XPS results are mainly representative of the surface

38

compositions. Bulk chemical compositions and estimated phase percentages are provided in the combustion analysis section below. Therefore, in the discussion that follows, we make a distinction between surface and bulk compositions, especially since the XPS assignments of speciation are semiquantitative at best.

Spectra in Figure 5 show that all three fiber types contain a significant amount of C, Si, and O, with additional small amount of Ti observed in Sylramic[TM]. Ti was likely added as a sintering aid (in the form of TiB_2) or catalyst during crosslinking of the preceramic polymer. High resolution XPS spectra show the Si 2p, C 1s, and O 1s bonds.[46] For all three samples the spectra under Si 2p indicate the presence of Si-C (99.7 eV) and small amounts of Si-O (101.7 eV) character.[46] For the C 1s band, C-C (283.7±0.5 eV), C-Si (282.1 eV), and C-O (284.8 eV) peaks are observed.[26, 46]. Raman spectroscopy and bulk chemical analysis indicate that the amount of free carbon in the bulk of Sylramic[TM] fibers is negligible, therefore the high C 1s peak (see Figure 5) is likely indicative of surface contamination or reflects a gradient in the C concentration. Similarly, from XPS deconvolutions, high C-C peaks compared to C-Si peaks are also evident in Tyranno and Hi-Nicalon fibers. Bulk compositions suggest that all three fibers are mostly SiC. To form Si-C, C atoms must be bonded to Si. Therefore, because in these fibers, the surface carbon (from C 1s peak) and oxygen (from O 1s peak) content are significantly higher than those in the bulk, deviations of surface from bulk compositions may be attributed to high surface contamination arising from oxidation or other factors.

Because the size of the individual domains is likely variable and not well known, we refrain from referring to them as nanodomains (1-3 nm). The areas under the fitted

XPS curves provide semiquantitative estimation of the relative abundance of different

bonds on the surface. Figure 5 shows that in all three samples, Si-C bonds are present in

significantly larger amounts than Si-O, thus confirming that the microstructure of all

fibers contains significant amounts of SiC grains, which have been confirmed to be

crystalline from XRD analysis. Previous studies have reported the β-SiC grain size in

Tyranno, Hi-Nicalon, and Sylramic™ to be ~100 nm[7, 47, 48] Figure 5 also shows that both

on the surface of Tyranno and Hi-Nicalon the amount of O-C bonds is higher than that of

O-Si bonds. C in mixed bonds is only bonded to either Si or another C atom, hence the

formation of O-C bonds in SiC_xO_{4-x} mixed bonding units is yet to be reported in the

literature. Therefore, it is likely that most of the surface oxygen is present as C-O or C=O

bonds in the free carbon phase rather than in SiOC mixed bonding domains. Similarly,

the remaining oxygen in O-Si bonds may be present either as SiO_2 or in silicon

oxycarbide mixed bonding networks. However, in Sylramic™ , instead most of the

oxygen atoms are bonded to Si (O-Si bonds) and the remainder to C (O-C bonds). On the

surface of Tyranno, the content of Si-O bonds relative to Si-C bonds is greatest.

Figure 5 shows that relative to Si-C, the surface microstructure of both Hi-

Nicalon and Sylramic™ contains significantly lower amounts of Si-O bonds than

observed in Tyranno. XPS analysis (Figure 5) show that the surface of Hi-Nicalon fibers

have a higher content of C-C relative to C-Si bonds than Tyranno and Sylramic™. XPS

results suggest that the surface microstructure of Tyranno mainly consists of SiC grains

surrounded by some C-C and a significant amount of Si-O containing units or networks.

Similarly, it can be inferred that the surface of Hi-Nicalon and Sylramic™ consists of

crystalline SiC grains surrounded by some C-C and a small amount of Si-O bonds (as

amorphous SiO_2 or SiOC mixed bonding domains). In Hi-Nicalon and Tyranno, C-C bonds could be partly attributed to the presence of amorphous free carbon regions. However, the absence of free carbon in the bulk of Sylramic[TM] is confirmed by Raman analysis and estimated bulk phase assemblages, therefore, in Sylramic[TM] the C-C bonds resulting from surface contamination must not be attributed to the presence of free carbon phases. Similarly, the absence of oxygen in the bulk of Tyranno fibers, suggests that unlike in Hi-Nicalon and Sylramic[TM], the Si-O bonds on its surface cannot be partly attributed to the formation of amorphous SiO_2 or SiOC mixed bonding domains, instead Si-O bonds are likely a result of significant surface contamination.
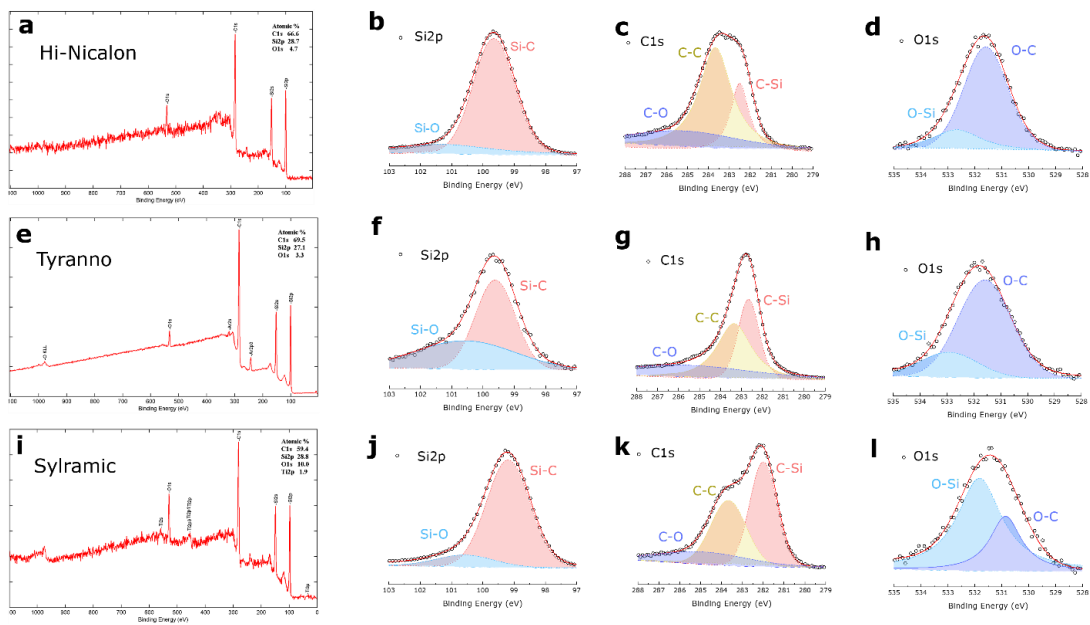
Figure 5. XPS analysis of fiber samples. Elemental survey and corresponding high resolution scan of the elements: (a-d) Hi-Nicalon; (e-h) Tyranno; (i-l) Sylramic[TM]. Trace amounts of Ti are observed in Sylramic[TM].

2.3.1 Mechanical Tensile Properties

Tensile strength of the SiC fiber bundles (multifilament tows) was determined at room temperature in ambient atmosphere using a Shimadzu AGS-X 5 KN Universal Testing Machine. The load was applied at a rate of 0.2 mm/min to provide a quasi-static tensile condition and epoxy was used to glue the fiber bundles onto carboard with approximately 30 mm slot as shown in Figure 6.[49] The cardboard coupons were cut on the sides after gripping in the test machine prior to application of the load as shown in Figure 6b. Figure 6c shows the samples mounted in the tensile tester. Previous works were conducted in a similar fashion where fiber bundles were mounted on cardboard or fiberglass tabs using epoxy.[50, 51] The cross-sectional area of the fiber bundle was calculated from the mass density and the mass of 30 mm fibers in individual tow similar to as reported by Callaway and Zok.[50] According to the manufacturers, the mass density of Hi-Nicalon type S, Tyranno, and Sylramic^{TM} are 3.1, 3.1, and 3.2 g cm^{-3}.[7]
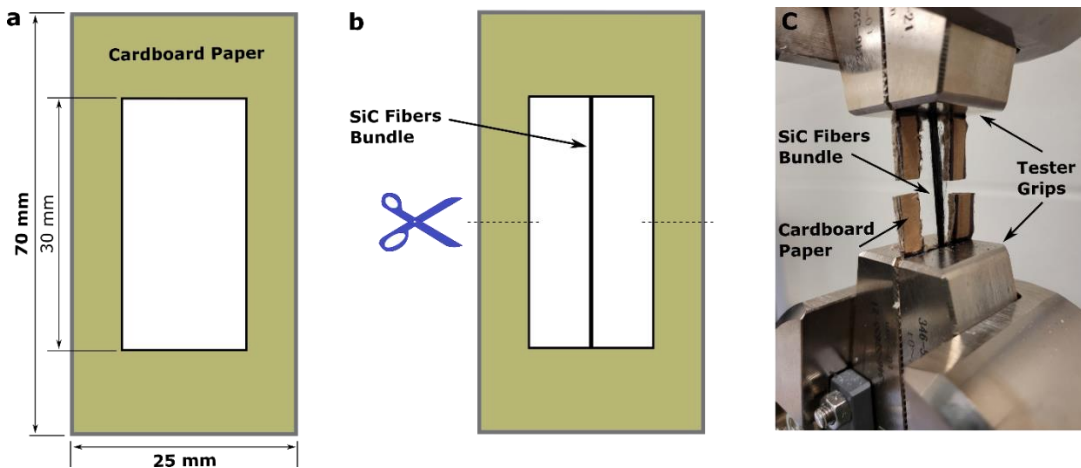
Figure 6. Tensile test set-up for the SiC fiber bundles or tows. (a) Cardboard paper dimensions with a 30 mm slot for the fiber bundle; (b) Fibers are glued onto the cardboard

using epoxy resin; (c) Fiber sample being pulled in the tensile tester. The sides of the cardboard are cut after mounting samples on the tester before application of load.

The tensile behavior (stress – strain response) of all three fiber bundles is shown in Figure 7 and the corresponding results (e.g. breaking strength and modulus) are presented in Table 1Table 1. Summary of the tensile properties of SiC fiber bundles.. Tyranno SiC fiber bundles provide the highest average ultimate tensile strength of 990 MPa, whereas the Hi-Nicalon and Sylramic^{TM} fiber bundles have tensile strengths of approximately 790 and 845 MPa, respectively. The Sylramic^{TM} fiber bundles have the highest Young's modulus of approximately 215 GPa, compared to Hi-Nicalon at 205 GPa and Tyranno at 112 MPa. However, Tyranno fibers have the highest strain-to-failure ratio (0.83 %) compared to that of Hi-Nicalon (0.45 %) and Sylramic^{TM} (0.47 %) fibers. The cross-sectional areas of the fiber bundles were also determined using average fiber diameter and number of fibers in individual tow. The tensile strength of the fibers calculated using this cross-sectional area were found to be approx. 10% lower compared to the strength calculated using cross-sectional area determined from mass density of the fiber bundle. However, the variation of diameter in an individual fiber tow makes it difficult to determine a mean diameter at a bundle cross-section,[52] therefore, may not be suitable for the calculation of bundle cross-sectional area. Notably all the fiber bundles showed a non-linear region, especially Tyranno and Sylramic^{TM} fibers, following the initial linear portion in the stress-strain curve. Similar trends in mechanical test data have been reported for individual fiber filaments, in which Sylramic^{TM} was shown to have highest breaking strength, followed by Tyranno and Hi-Nicalon. [53] Typically, the modulus of the SiC fibers provided by the manufacturer are in the range of (380-420) GPa, which is higher than the

values in Table 1.Table 1. Summary of the tensile properties of SiC fiber bundles.[7, 54] Tensile modulus of the fibers is usually reported as the pristine filament measured in air at room temperature.[55] The reported values here are lower than the values reported by the manufacturer for monofilaments. In general, the classical fiber bundle theory predicts that all fibers are loaded uniformly, and the fibers do not interact mechanically with one another.[56, 57] However, mechanical instabilities at or near the load maximum in a bundle test, as well as non-uniform strains on the bundle surface present challenges in determining the modulus and strength of fiber bundle. In addition, the diminished mechanical property response of fiber bundles could be attributed to the surface defects that generally get introduced during bundle-forming process,[55] and environmental effects over a period of time [58] (the SiC fiber bundles tested in this work were not pristine and they had a shelf-life of approx. 3 years after buying from the manufactures). The elastic moduli reported in the literature for SiC, SiOC, and SiCN ceramic fibers are usually in the range of 150 to 450 GPa depending on the pyrolysis temperature during synthesis.[19, 26, 59, 60]
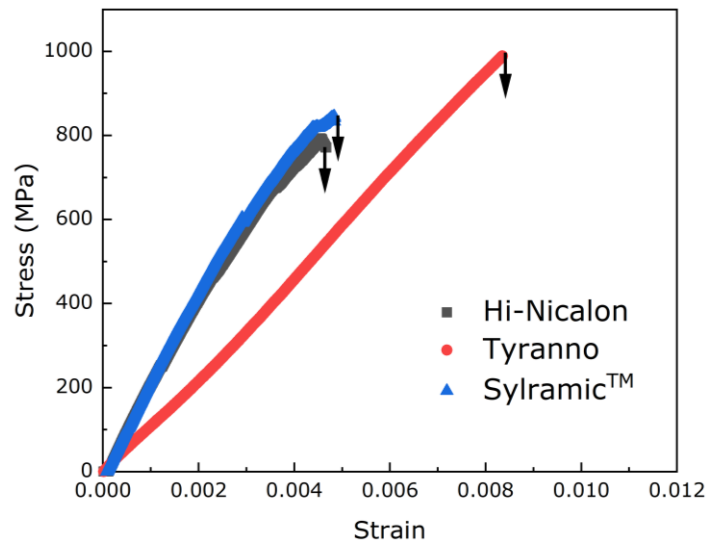
Figure 7: Tensile stress versus strain response of the fiber bundles.

We sought possible correlation (not causation) between mechanical behavior and bulk microstructural features of the samples. This would permit assessment of whether some structural modifications are consistent with differences in their mechanical properties. Hi-Nicalon and Sylramic^{TM} fibers appear to have very similar tensile properties. Estimated phase assemblage from bulk composition suggests that both fiber types consist of crystalline SiC grains surrounded by small amounts of XRD amorphous domains. Bulk compositions indicate that both in Hi-Nicalon and Sylramic^{TM}, the amorphous domains include minor amounts of SiO_2, with Sylramic^{TM} containing additional Si_3N_4. However, unlike Hi-Nicalon which includes free carbon phases in its microstructure, Sylramic^{TM} has excess Si, which may be incorporated in mixed bonding units and/or networks. Since in both fibers the amorphous domains are minor in amount (relative to SiC) compared to Tyranno, this might correlate with similarities in the mechanical properties of Hi-Nicalon and Sylramic^{TM} fibers.

Compared to Hi-Nicalon and Sylramic^{TM}, the microstructure of Tyranno consists of smaller amounts of crystalline SiC grains surrounded by significantly larger amounts of amorphous free carbon phases. Such bulk microstructural modifications are consistent with significant differences in the mechanical properties of Tyranno compared to Hi-Nicalon and Sylramic^{TM} fibers. The lower elastic modulus and higher strain to failure of Tyranno fiber bundles is consistent with the significantly smaller amount of crystalline SiC grains and larger amounts of amorphous free carbon phases. Under tension, amorphous domains are less resistant to elastic deformation (lower Young's modulus) compared to crystalline SiC, which makes up a larger portion of the microstructure in Hi-Nicalon and Sylramic^{TM} fibers. The lower strain to failure and higher modulus of

Sylramic[TM] fiber may be associated with the predominantly stoichiometric SiC phase, which is known to have higher elastic modulus than free or disordered carbon containing SiOC and SiCN microstructures.[19]

Table 1. Summary of the tensile properties of SiC fiber bundles.

SiC Fibers	Average Ultimate tensile strength (MPa)	Average Young's modulus (GPa)	Average strain to failure (%)
Hi-Nicalon	790	205	0.45
Tyranno	990	112	0.83
Sylramic[TM]	845	215	0.47

Morphology of the tested fibers was obtained using an SEM Zeiss MA 10. The cross-section of each fiber type was evaluated to delineate the fractures in the fibers during tensile tests. Figure 8 shows micrographs of the studied fibers. Although the fiber bundles demonstrated similar morphology, their fiber average diameter size and distribution differed. As shown in Figure 8 (d-e), the high-strength Hi-Nicalon fiber bundles have diameter varying in the range from 13-16 μm, whereas for Tyranno and Sylramic[TM] fibers have diameters between 10 and 13 μm. The strength of fibers usually reflects the diameter distribution and flaw size. However, no obvious mirror zone or

fracture behavior was identified for these ceramic fibers.[54] We conclude that the morphology variation in these samples does not strongly influence mechanical behavior, and other factors such as the presence of microcracks and sparsely distributed impurities (dust, lint, etc.) which get carbonized during processing, may be more important.
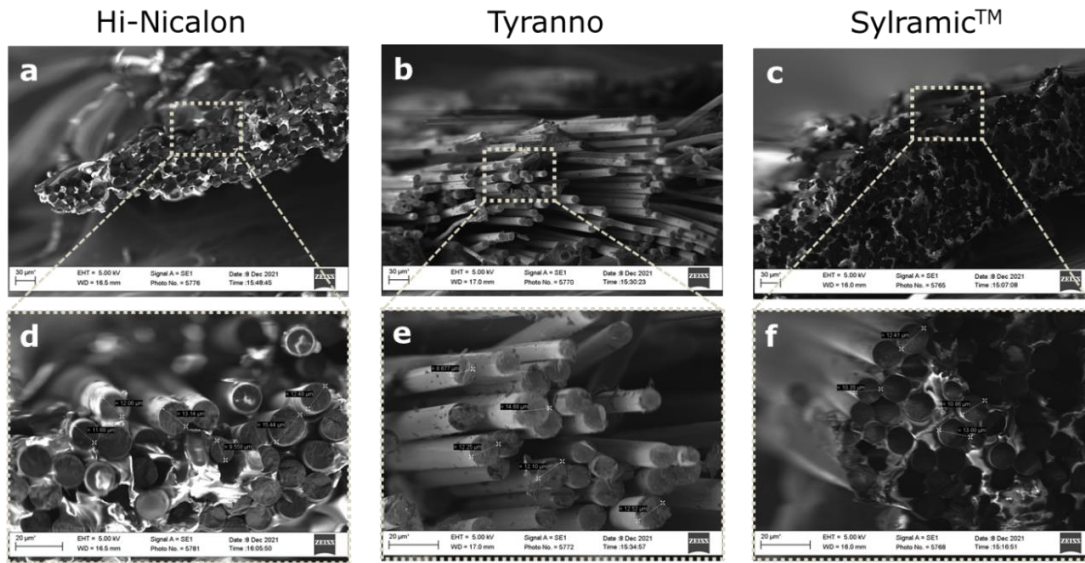
Figure 8. SEM micrographs of (a) Hi-Nicalon, (b) Tyranno, and (c) Sylramic™ SiC fibers obtained after tensile tests. (d through f) are the corresponding high-magnification images.

2.3.2 Combustion Analysis

Combustion analysis allows determination of bulk composition,[38] which is essential to the thermodynamic analysis. Analysis suggests that Tyranno mainly consists of C and Si species, while Sylramic™ and Hi-Nicalon both have relatively higher amounts of O and Si species present in the bulk. A summary of the analytical results is shown in Tables 2 and 3. XPS results suggest that Tyranno has small amounts of oxygen

(relative to Si and C). It is possible that in the bulk of Tyranno fibers, oxygen is present in amounts below the detection limit for combustion analysis, which is typically ~0.1 at%. Such small quantities of oxygen would have a negligible effect on the calculated enthalpy of formation discussed in the section that follows. XPS analysis also suggests the absence of N species near the surface of Sylramic™ fibers. This is possibly a result of N species being present in amounts below the detection limit of XPS (typically ~0.1 at %).[61]

Table 2. Summary of combustion analyses

Sample	Atomic %			
	C	O	N	Si
Tyranno	53.18	-	-	46.53
Hi-Nicalon	51.38	1.17	-	47.44
Sylramic™	47.56	0.2	0.3	51.82

Thermodynamically, in PDCs, clusters of C-N or C-O bonds are not favorable. Instead, clusters of Si-C, C-C, Si-O, and Si-N bonds are preferred.[62, 63] From their bulk compositions, it is suggested that Tyranno mainly consists of crystalline SiC and free carbons in the form of amorphous or sp^2 turbostratic domains. Bulk composition also suggests that Hi-Nicalon is mainly crystalline SiC with some amorphous SiO_2 – rich domains which may contain some carbon leading to mixed bonding ,and free carbon domains.[64] In addition to Si, O, and C, Sylramic™ also contains some nitrogen. The addition of nitrogen and/or oxygen to the bulk is considered in the thermodynamic cycle

for the respective fibers (see Table 4). The analyzed bulk composition is consistent with the presence of crystalline SiC, amorphous SiO_2, and Si_3N_4 domains.

Table 3. Bulk composition and estimated phase amounts obtained from combustion analysis. The reported quantity is mol%

Sample	Bulk composition based on $Si_aO_bC_cN_d$, (a+b+c+d=2) basis	SiC	SiO_2	Si_3N_4	C	Si
Tyranno	$Si_{0.93}C_{1.06}$	87.74	-	-	12.26	-
Hi-Nicalon	$Si_{0.95}O_{0.02}C_{1.03}$	90.38	0.96	-	8.66	-
Sylramic^{TM}	$Si_{1.040}O_{0.004}C_{0.95}N_{0.006}$	91.30	0.19	0.14	-	8.37

2.3.3 Thermochemistry

Enthalpies of formation were obtained using thermochemical cycles (Table 4) incorporating measured enthalpies of dissolution in a molten oxide solvent. Each of the three samples was dropped into 20 g of a sodium molybdate ($3Na_2O \cdot 4MoO_3$) melt at 800 °C in a commercial Setaram Alexsys calorimeter. To prepare the samples for dissolution, first, each of the three SiC fibers was individually ground into powders using a mortar and pestle. Using a Mettler Toledo microbalance with 10 μg accuracy, 3 mg of sample were weighed and pressed into a pellet using a 1.5 mm tungsten die. For each drop, pelletized samples were dropped into the isothermal calorimeter, where samples

underwent oxidative dissolution at 800 $^{\circ}$C. To help stir the sample into the oxide melt, and ensure a continuous oxidative environment, the melt was continuously bubbled with 30 mL/min of oxygen. During dissolution, to prevent baseline shifts resulting from the buildup of evolved gases such as CO_2, flushing at 100 mL/min was used. For each sample, during dissolution, a peak emerged from the initial baseline in the heat flow vs. time curve. Within 60 minutes of dropping the sample, the peak returned to the initial baseline. Integration of area under the curve, using the appropriate calibration factor, produced the heat of dissolution. This procedure is similar to that used in previous experiments on PDCs.[65] The final products of the oxidative dissolution experiment were cristobalite (SiO_2) precipitated from the sodium molybdate melt in which silica, evolved CO_2, and N_2 have very limited solubility.

Enthalpies of formation at 25 $^{\circ}$C are calculated relative to components and elements [63] namely Si, C (graphite), O_2 , and/or N_2, as shown in the reaction below:

aSi (s, 25 $^{\circ}$C) + cC (s, 25 $^{\circ}$C) + $\frac{b}{2}$ O_2 (g, 25°C) + $\frac{d}{2}$ N_2 (g, 25 $^{\circ}$C)$\rightarrow$ Si$_a$ O$_b$C$_c$N$_d$ (s, 25°C)
$\Delta H^{\circ}_{f, elem}$

(1)
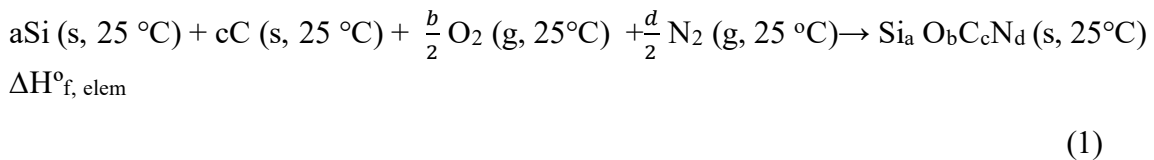
The oxidative dissolution reaction is described by

Si$_a$ O$_b$C$_c$N$_d$ (s, 25 $^{\circ}$C)+ $\frac{1}{2}$ (2a+ 2c -b) O_2 (g, 800 $^{\circ}$C)$\rightarrow$ aSiO$_2$ (s, 800°C) + cCO$_2$ (g, 800 $^{\circ}$C) + $\frac{d}{2}$N$_2$ (g, 800 $^{\circ}$C)

(2)
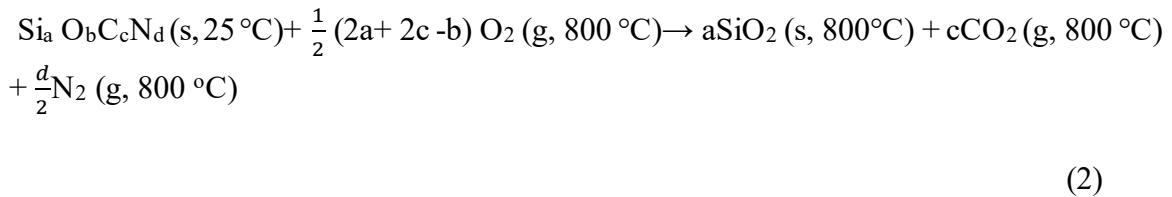
Enthalpies of dissolution ΔH_{dis} of Tyranno, Hi-Nicalon, and Sylramic[TM] have been determined to be -1,271.97± 8.71, -1194.11 ± 6.91, and -1031.82± 4.34 kJ/mol Si, respectively. As expected, enthalpies of dissolution become more exothermic as the amount of C present in the fiber, increases. This is due to the high exothermic effect resulting from oxidation of C to CO_2 (g, 800 °C) which is expelled from the melt.[66] With known initial and final state of our system, thermodynamic cycles (Table 4) allow calculation of enthalpies of formation from elements and binary components (Table 5).

Table 4. Thermochemical cycles and data used for calculating enthalpy of formation from elements $\Delta H^o_{f, elem}$ and from components $\Delta H^o_{f,comp}$

Enthalpies of formation from the elements ($\Delta H_{f,elem}$) a Si(s, 25 °C) + c C(s, 25 °C) + b/2 O_2 (g, 25 °C) + d/2 N_2 (g, 25 °C)→ $Si_aO_bC_cN_d$ (s, 25°C) (s, 25°C) $\Delta H^o_{f, elem}$ =?	ΔH (kJ/mol)
$Si_aO_bC_cN_d$ (s, 25 °C)+ ((2(a+c)-b)/2) O_2 (g, 800 °C) → a SiO_2 (s, 800 °C) + c CO_2 (g, 800 °C) + d/2 N_2 (g, 800 °C)	$\Delta H_{dis, SiC(N)(O)}$
Si (s, 25 °C) + O_2 (g, 800 °C) → SiO_2 (s, 800 °C)	ΔH_1= -883.13 ± 2.1
C (s, 25 °C) + O_2 (g, 800 °C) → CO_2 (g, 800 °C)	ΔH_2= -381.35 ± 0.13
O_2 (g, 25 °C) → O_2 (g, 800 °C)	ΔH_3= 25.34 ± 0.10
N_2 (g, 25 °C) → N_2 (g, 800 °C)	ΔH_4= 24.77 ± 0.10
$\Delta H^o_{f, elem}$ = - $\Delta H_{dis, SiC(N)(O)}$ + a ΔH_1 + c ΔH_2 + $\frac{b}{2}$ ΔH_3 + $\frac{d}{2}$ ΔH_4	$\Delta H^o_{f, elem}$

Enthalpies of formation from components ($\Delta H^o_{f,comp}$)	ΔH (kJ/mol)
(a-(b/2)-(3d/4)) SiC (s,25 oC) + (b/2) SiO_2 (s, 25 oC) + (d/4) Si_3N_4 (s, 25 oC) + (c-(a-(b/2)-(3d/4))) C (s, 25 oC) $\rightarrow$ $Si_aO_bC_cN_d$ (s, 25°C) (s, 25°C)	
$Si_aO_bC_cN_d$ (s, 25 °C)+ ((2(a+c)-b)/2) O_2 (g, 800 °C) $\rightarrow$ a SiO_2 (s, 800 °C) + c CO_2 (g, 800 °C) + d/2 N_2 (g, 800 °C)	$\Delta H_{dis,\ SiC\ (N)(O)}$
SiO_2 (S, 25 °C) $\rightarrow$ SiO_2 (s, 800 °C)	ΔH_1= 50.1 ± 0.10
SiC (S, 25 °C) + $2O_2$ (g, 800 °C)$\rightarrow$ SiO_2 (s, 800 °C) + CO_2 (g, 800 °C)	ΔH_2= -1192.28 ± 2.15
Si_3N_4 (s, 25 °C) + $3O_2$ (S, 25 °C)$\rightarrow$ $3SiO_2$ (s, 80 0 °C) + $2N_2$ (g, 800 °C)	ΔH_3= -1770.95 ± 4.0
C (s, 25 °C) + O_2 (g, 800 °C) $\rightarrow$ CO_2 (g, 800 °C)	ΔH_4 = -381.35 ± 0.13
ΔH^of, comp = $-\Delta H_{dis,\ SiC(N)(O)}$ + (b/2)ΔH_1 + (a-(b/2)-(3d/4))ΔH_2 + (d/4)ΔH_3 + (c-(a-(b/2)-(3d/4)))ΔH_4	$\Delta H^o_{f,comp}$

Table 5: Summary of enthalpies of dissolution, enthalpies of formation from elements and enthalpies of formation from components

Samples	Composition	$\Delta H_{dis,\ SiC}$ (kJ/mol Si)	$\Delta H^o_{f,\ elem}$ (kJ/mol Si)	$\Delta H^o_{f,comp}$ (kJ/mol Si)
Tyranno	$Si_{0.93}C_{1.06}$	-1,271.97± 8.7	-45.80 ± 8.9	+26.40 ± 8.9
Nicalon	$Si_{0.95}O_{0.02}C_{1.03}$	-1194.1 ± 6.91	-102.22 ± 7.2	-21.22 ± 7.2
Sylramic	$Si_{1.040}O_{0.004}C_{0.95}N_{0.006}$	-1031.82 ± 4.34	-199.42 ± 4.8	-124.84 ± 6.7

Uncertainty is two standard deviations of the mean.

2.3.4 Interdomain Interactions, Energetics, and Trends

From bulk compositions, for each of the three fibers, the expected domains present in the PDC are summarized in Table 3. The silica domains in Hi-Nicalon may

also contain some carbon, resulting in mixed bonding (silicon bonded to both oxygen and carbon) both within the domains and at their interfaces with carbon domains. The different domains may interact with one another.[63] To explore these interactions, enthalpies of formation are determined relative to crystalline components ($\Delta H^o_{f,comp}$ at 25 ^{o}C), namely: β-SiC, SiO_2 (cristobalite), C (graphite), and β-S_3N_4. Values for $\Delta H^o_{f,comp}$ close to zero indicate weak interdomain interaction and they could also point to the absence of mixed bonding domains. $\Delta H^o_{f,comp} < 0$ indicates energetically favorable interaction between the different domains, this could also point to the formation of a significant amount of mixed bonding domains. $\Delta H^o_{f,comp}$ for Tyranno, Hi-Nicalon, and Sylramic^{TM} have been determined to be $+26.40 \pm 8.9$, -21.22 ± 7.2, and -124.84 ± 6.7 kJ/mol Si, respectively. These exothermic values suggest favorable interactions in the samples with stronger interdomain interactions and/or formation of more mixed bonding domains in Sylramic^{TM} compared to Tyranno and Hi-Nicalon.

Tyranno, which contains mainly crystalline SiC with some free carbon (from combustion analysis), and possibly very low amounts of oxygen relative to Si and C (from XPS), has an enthalpy of formation ($\Delta H^o_{f, elem}$) closest to that reported for pure crystalline SiC. The thermodynamic stability of these structures appears to be related to their composition. The addition of O and N leads to increasing thermodynamic stability. Mixed bonding (silicon bonded to both carbon and oxygen) whether present in the domains or interdomain regions allows greater flexibility/less strain in bonds.[26] As shown in previous studies, less bond strain is consistent with greater thermodynamic stability.[31]

2.3.5 Link between Microscopic and Macroscopic Properties of Fibers

Results from thermodynamic measurements, structural characterization, and mechanical testing permit identification of some trends. From bulk compositions, thermodynamic stability of the fibers has been assessed. Although all three fibers contain crystalline SiC grains in their microstructure, their thermodynamic stability differs depending on the other domains present within the bulk. Addition of O and N to the bulk results in greater thermodynamic stability due to the formation of SiO_2, mixed bonding SiOC, and Si_3N_4 amorphous domains. The trend in the thermodynamic stability of the fibers is Sylramic^{TM} > H-Nicalon > Tyranno. In this study, greater thermodynamic stability of the fibers is associated with a higher Young's modulus. There appears to be a correlation between the mechanical properties of the PDC fibers and their bulk microstructure. The observed decreased resistance to elastic deformation of Tyranno fibers compared to both Hi-Nicalon and Sylramic^{TM} can be correlated to Tyranno fibers' smaller diameter and an increase in the amount of amorphous free carbon phases relative to crystalline SiC grains in the bulk of Tyranno fibers. Amorphous free carbon phases contain significantly less bond strain compared to crystalline SiC, thus resulting in greater flexibility.

2.4 Conclusions

This study stresses the relation of composition, microstructure, thermodynamics, and mechanical properties. From these results, it can be concluded that bulk microstructural modifications can have significant implications on the tensile strength

and thermodynamic stability of PDC fibers. Thermodynamic stability appears to systematically increase with the inclusion and increase in concentration of additional bulk species. Less resistance to elastic deformation of the fibers is consistent with increasing amounts (relative to SiC) of amorphous domains, which is also consistent with decreased thermodynamic stability. These results may serve as a bridge between microscopic and macroscopic properties of PDCs. Results from this study could serve as a useful tool for building a framework linking both microscopic and macroscopic properties of multicomponent ceramic fibers. To extend this work beyond the investigation of simple SiC systems, the next chapter is dedicated to the study of stabilization trends in complex SiOC materials.

REFERENCES

1. Colombo, P. Engineering porosity in polymer-derived ceramics. *J. Eur. Ceram. Soc.* **28**, 1389–1395 (2008).

2. Colombo, P., Mera, G., Riedel, R. & Sorarù, G. D. Polymer-Derived Ceramics: 40 Years of Research and Innovation in Advanced Ceramics. *J. Am. Ceram. Soc.* **93**, 1805–1837 (2010).

3. Ren, Z., Mujib, S. B. & Singh, G. High-Temperature Properties and Applications of Si-Based Polymer-Derived Ceramics: A Review. *Materials* **14**, 614 (2021).

4. Colombo, P. *Polymer Derived Ceramics: From Nano-structure to Applications.* (DEStech Publications, Inc, 2010).

5. Brinckmann, S. A. *et al.* Stereolithography of SiOC Polymer-Derived Ceramics Filled with SiC Micronwhiskers. *Adv. Eng. Mater.* **20**, 1800593 (2018).

6. Walsh, C., An, L., Kapat, J. S. & Chow, L. C. Feasibility of a High-Temperature Polymer-Derived-Ceramic Turbine Fabricated Through Micro-Stereolithography. in 1073–1080 (American Society of Mechanical Engineers Digital Collection, 2009).

7. Flores, O., Bordia, R. K., Nestler, D., Krenkel, W. & Motz, G. Ceramic Fibers Based on SiC and SiCN Systems: Current Research, Development, and Commercial Status. *Adv. Eng. Mater.* **16**, 621–636 (2014).

8. Idrees, M. *et al.* Polyborosilazane derived ceramics - Nitrogen sulfur dual doped graphene nanocomposite anode for enhanced lithium ion batteries. *Electrochimica Acta* **296**, 925–937 (2019).

9. Duan, W. *et al.* A review of absorption properties in silicon-based polymer derived ceramics. *J. Eur. Ceram. Soc.* **36**, 3681–3689 (2016).

10. Prasad, R. M. *et al.* Thermal decomposition of carbon-rich polymer-derived silicon carbonitrides leading to ceramics with high specific surface area and tunable micro- and mesoporosity. *J. Eur. Ceram. Soc.* **32**, 477–484 (2012).

11. Huang, K., Elsayed, H., Franchin, G. & Colombo, P. 3D printing of polymer-derived SiOC with hierarchical and tunable porosity. *Addit. Manuf.* **36**, 101549 (2020).

12. Ionescu, E., Kleebe, H.-J. & Riedel, R. Silicon-containing polymer-derived ceramic nanocomposites (PDC-NCs): preparative approaches and properties. *Chem. Soc. Rev.* **41**, 5032–5052 (2012).

13. Sasikumar, P. V. W. *et al.* Polymer derived silicon oxycarbide ceramic monoliths: Microstructure development and associated materials properties. *Ceram. Int.* **44**, 20961–20967 (2018).

14. Hotza, D. *et al.* Tape casting of preceramic polymers toward advanced ceramics: A review. *Int. J. Ceram. Eng. Sci.* **1**, 21–41 (2019).

15. Mera, G., Gallei, M., Bernard, S. & Ionescu, E. Ceramic Nanocomposites from Tailor-Made Preceramic Polymers. *Nanomaterials* **5**, 468–540 (2015).

16. Niu, M. *et al.* Structure and energetics of SiOC and SiOC-modified carbon-bonded carbon fiber composites. *J. Am. Ceram. Soc.* **100**, 3693–3702 (2017).

17. Saha, A., Raj, R., Williamson, D. L. & Kleebe, H.-J. Characterization of Nanodomains in Polymer-Derived SiCN Ceramics Employing Multiple Techniques. *J. Am. Ceram. Soc.* **88**, 232–234 (2005).

18. Papendorf, B. *et al.* High-Temperature Creep Behavior of Dense SiOC-Based Ceramic Nanocomposites: Microstructural and Phase Composition Effects. *J. Am. Ceram. Soc.* **96**, 272–280 (2013).

19. Sujith, R., Jothi, S., Zimmermann, A., Aldinger, F. & Kumar, R. Mechanical behaviour of polymer derived ceramics – a review. *Int. Mater. Rev.* **66**, 426–449 (2021).

20. Gu, J., Lee, S.-H., Lee, H.-S. & Kim, J.-S. Fast pyrolysis of a SiC-based polymer precursor using a spark plasma sintering apparatus – Effects of heating methods and pyrolysis atmosphere. *J. Eur. Ceram. Soc.* **41**, 2297–2305 (2021).

21. Yeon, S.-H. *et al.* Carbide-derived-carbons with hierarchical porosity from a preceramic polymer. *Carbon* **48**, 201–210 (2010).

22. Lale, A. *et al.* Polymer-Derived Ceramics with engineered mesoporosity: From design to application in catalysis. *Surf. Coat. Technol.* **350**, 569–586 (2018).

23. Chauhan, P. K., Sujith, R., Parameshwaran, R. & Prasad, A. V. S. S. Role of polysiloxanes in the synthesis of aligned porous silicon oxycarbide ceramics. *Ceram. Int.* **45**, 8150–8156 (2019).

24. Sorarù, G. D., Pederiva, L., Latournerie, J. & Raj, R. Pyrolysis Kinetics for the Conversion of a Polymer into an Amorphous Silicon Oxycarbide Ceramic. *J. Am. Ceram. Soc.* **85**, 2181–2187 (2002).

25. Kulkarni, A., Pearce, J., Yang, Y., Motta, A. & Sorarù, G. D. SiOC(N) Cellular Structures with Dense Struts by Integrating Fused Filament Fabrication 3D Printing with Polymer-Derived Ceramics. *Adv. Eng. Mater.* (2021), 2100535.

26. Vashisth, A. *et al.* Mechanical size effects of amorphous polymer-derived ceramics at the nanoscale: experiments and ReaxFF simulations. *Nanoscale* **11**, 7447–7456 (2019).

27. Ishikawa, T., Kajii, S., Hisayuki, T. & Kohtoku, Y. New Type of SIC-Sintered Fiber and its Composite Material. in *22nd Annual Conference on Composites, Advanced Ceramics, Materials, and Structures: A: Ceramic Engineering and Science Proceedings* 283–290 (John Wiley & Sons, Ltd, 1988).

28. Ishikawa, T., Kohtoku, Y., Kumagawa, K., Yamamura, T. & Nagasawa, T. High-strength alkali-resistant sintered SiC fibre stable to 2,200 °C. *Nature* **391**, 773–775 (1998).

29. Ichikawa, H. Recent advances in Nicalon ceramic fibres including Hi-Nicalon type S. *Ann. Chim. Sci. Matér.* **25**, 523–528 (2000).

30. Sauder, C., Brusson, A. & Lamon, J. Influence of Interface Characteristics on the Mechanical Properties of Hi-Nicalon type-S or Tyranno-SA3 Fiber-Reinforced SiC/SiC Minicomposites. *Int. J. Appl. Ceram. Technol.* **7**, 291–303 (2010).

31. Mera, G., Navrotsky, A., Sen, S., Kleebe, H.-J. & Riedel, R. Polymer-derived SiCN and SiOC ceramics – structure and energetics at the nanoscale. *J. Mater. Chem. A* **1**, 3826–3836 (2013).

32. Sugie, C., Navrotsky, A., Lauterbach, S., Kleebe, H.-J. & Mera, G. Structure and Thermodynamics of Silicon Oxycarbide Polymer-Derived Ceramics with and without Mixed-Bonding. *Materials* **14**, 4075 (2021).

33. Tavakoli, A. H., Golczewski, J. A., Bill, J. & Navrotsky, A. Effect of boron on the thermodynamic stability of amorphous polymer-derived Si(B)CN ceramics. *Acta Mater.* **60**, 4514–4522 (2012).

34. Yajima, S., Hasegawa, Y., Okamura, K. & Matsuzawa, T. Development of high tensile strength silicon carbide fibre using an organosilicon polymer precursor. *Nature* **273**, 525–527 (1978).

35. Yajima, S., Hayashi, J. & Omori, M. Continuous silicon carbide fiber of high tensile strength. *Chem. Lett.* **4**, 931–934 (1975).

36. Peng, C.-H. & Hwang, C.-C. Synthesis and characteristics of polycarbomethylsilane via a one-pot approach. *J. Mater. Res. Technol.* **9**, 15838–15848 (2020).

37. Sarkar, S. & Zhai, L. Polymer-Derived Non-Oxide Ceramic Fibers—Past, Present and Future. *Mater. Express* **1**, 18–29 (2011).

38. David, L., Bhandavat, R., Barrera, U. & Singh, G. Silicon oxycarbide glass-graphene composite paper electrode for long-cycle lithium-ion batteries. *Nat. Commun.* **7**, 10998 (2016).

39. Dong, S. M. *et al.* Characterization of nearly stoichiometric SiC ceramic fibres. *J. Mater. Sci.* **36**, 2371–2381 (2001).

40. Luo, Q. & Yang, S. Uncertainty of the X-ray Diffraction (XRD) sin2 ψ Technique in Measuring Residual Stresses of Physical Vapor Deposition (PVD) Hard Coatings. *Coatings* **7**, 128 (2017).

41. Mukaida, H. *et al.* Raman scattering of SiC: Estimation of the internal stress in 3C-SiC on Si. *J. Appl. Phys.* **62**, 254–257 (1987).

42. Rufino, B. *et al.* The effect of particle size on the formation and structure of carbide-derived carbon on β-SiC nanoparticles by reaction with chlorine. *Carbon* **49**, 3073–3083 (2011).

43. Patil, N. *et al.* Rapid Heating of Silicon Carbide Fibers under Radio Frequency Fields and Application in Curing Preceramic Polymer Composites. *ACS Appl. Mater. Interfaces* **11**, 46132–46139 (2019).

44. Ciftyürek, E., Šmíd, B., Li, Z., Matolín, V. & Schierbaum, K. Spectroscopic Understanding of SnO2 and WO3 Metal Oxide Surfaces with Advanced Synchrotron Based; XPS-UPS and Near Ambient Pressure (NAP) XPS Surface Sensitive Techniques for Gas Sensor Applications under Operational Conditions. *Sensors* **19**, 4737 (2019).

45. Seah, M. P. A review of the analysis of surfaces and thin films by AES and XPS. *Vacuum* **34**, 463–478 (1984).

46. NIST X-ray Photoelectron Spectroscopy Database. In NIST Standard Reference Database Number 20, National Institute of Standards and Technology: Gaithersburg MD, 20899, 2000.

47. DiCarlo, J. A. & Yun, H.-M. Non-oxide (Silicon Carbide) Fibers. in *Handbook of Ceramic Composites* (ed. Bansal, N. P.) 33–52 (Springer US, 2005).

48. Ustundag, E. & Fischman, G. S. *23nd Annual Conference on Composites, Advanced Ceramics, Materials, and Structures - A, Volume 20, Issue 3*. (John Wiley & Sons, 2009).

49. Youngblood, G. E., Lewinsohn, C., Jones, R. H. & Kohyama, A. Tensile strength and fracture surface characterization of Hi-Nicalon™ SiC fibers. *J. Nucl. Mater.* **289**, 1–9 (2001).

50. Callaway, E. B. & Zok, F. W. Strengths of ceramic fiber bundles: Theory and practice. *J. Am. Ceram. Soc.* **100**, 5306–5317 (2017).

51. Ikarashi, Y. *et al.* Direct comparison between monofilament and multifilament tow testing for evaluating the tensile strength distribution of SiC fibers. *J. Eur. Ceram. Soc.* **42**, 1928–1937 (2022).

52. Morimoto, T. & Ogasawara, T. Potential strength of Nicalon™, Hi Nicalon™, and Hi Nicalon Type S™ monofilaments of variable diameters. *Compos. Part Appl. Sci. Manuf.* **37**, 405–412 (2006).

53. Bunsell, A. R. & Piant, A. A review of the development of three generations of small diameter silicon carbide fibres. *J. Mater. Sci.* **41**, 823–839 (2006).

54. Sha, J. J., Nozawa, T., Park, J. S., Katoh, Y. & Kohyama, A. Effect of heat treatment on the tensile strength and creep resistance of advanced SiC fibers. *J. Nucl. Mater.* **329–333**, 592–596 (2004).

55. Hartman, D. R., Greenwood, M. E. & Miller, D. M. High strength glass fibers. *Mov. Forw. 50 Years Leadersh. Adv. Mater.* **39**, 521–533 (1994).

56. Chi, Z., Chou, T.-W. & Shen, G. Determination of single fibre strength distribution from fibre bundle testings. *J. Mater. Sci.* **19**, 3319–3324 (1984).

57. Coleman, B. D. On the strength of classical fibres and fibre bundles. *J. Mech. Phys. Solids* **7**, 60–70 (1958).

58. Martin, D. M., Akinc, M. & Oh, S. M. Effect of Forming and Aging Atmospheres on E-Glass Strength. *J. Am. Ceram. Soc.* **61**, 308–311 (1978).

59. Yajima, S., Hayashi, J., Omori, M. & Okamura, K. Development of a silicon carbide fibre with high tensile strength. *Nature* **261**, 683–685 (1976).

60. Bernard, S., Weinmann, M., Gerstel, P., Miele, P. & Aldinger, F. Boron-modified polysilazane as a novel single-source precursor for SiBCN ceramic fibers: synthesis, melt-spinning, curing and ceramic conversion. *J. Mater. Chem.* **15**, 289–299 (2005).

61. Shard, A. G. Chapter 4.3.1 - X-ray photoelectron spectroscopy. in *Characterization of Nanoparticles* (eds. Hodoroaba, V.-D., Unger, W. E. S. & Shard, A. G.) 349–371 (Elsevier, 2020).

62. Kroke, E. *et al.* Silazane derived ceramics and related materials. *Mater. Sci. Eng. R Rep.* **26**, 97–199 (2000).

63. Tavakoli, A. H., Golczewski, J. A., Bill, J. & Navrotsky, A. Effect of boron on the thermodynamic stability of amorphous polymer-derived Si(B)CN ceramics. *Acta Mater.* **60**, 4514–4522 (2012).

64. Tavakoli, A. H., Armentrout, M. M., Narisawa, M., Sen, S. & Navrotsky, A. White Si–O–C Ceramic: Structure and Thermodynamic Stability. *J. Am. Ceram. Soc.* **98**, 242–246 (2015).

65. Widgeon, S. *et al.* Nanostructure and Energetics of Carbon-Rich SiCN Ceramics Derived from Polysilylcarbodiimides: Role of the Nanodomain Interfaces. *Chem. Mater.* **24**, 1181–1191 (2012).

66. Navrotsky, A. Progress and new directions in high temperature calorimetry revisited. *Phys. Chem. Miner.* **24**, 222–241 (1997).

CHAPTER 3

CHEMISTRY, STRUCTURE, AND THERMODYNAMIC STABILIZATION OF SIOC POLYMER DERIVED CERAMICS MADE FROM COMMERCIAL PRECURSORS

Abstract: This study explores the energetics and structure of polymer derived ceramics (PDCs) derived from the pyrolysis of preceramic polymers: SPR-212 (SPR), polyhydromethylsiloxane (PHMS) blend, and 1,3,5,7-tetravinyl-1,3,5,7-tetramethylcyclotetrasiloxane (TTCS) at 1200 and 1500 °C. There are close similarities in the composition of PDCs derived from PHMS (blend) and SPR-212 at 1200 °C, but high-resolution X-ray photoelectron spectroscopy shows notable differences in their microstructure. Enthalpies of formation from components (SiC, SiO$_2$, and C, $\Delta H^o_{f, comp}$) show that PDCs derived from low-cost commercial precursors (PHMS blend) appear to be more thermodynamically stable than those derived from an industrial preceramic polymer (SPR-212). Thermodynamic stability of the SiOCs increases with pyrolysis temperature. The results suggest that differences in silicon mixed bonding environments and their relative amounts (SiO$_3$C, SiO$_2$C$_2$, or SiOC$_3$) lead to differences in thermodynamic stabilization.

3.1 Introduction

Recently, there has been significant increase in research for ultrahigh temperature materials, especially for application in the aerospace industry, [1, 2] where stable materials capable of withstanding high temperatures during re-entry are needed [3, 4]. SiOC ceramics are suitable candidates due to their robust chemical, structural, and thermal stability. [5–7] One method for the synthesis of such ceramics, relies on the high temperature sintering of silica and graphite ceramic powder mixtures.[8–10] This reaction requires high synthesis temperatures.[11–13] This approach does not provide efficient tunability of the shape, composition, microstructure, and properties. These factors make it less attractive for the industrial scale.

A significant advantage of the PDC route is the ease in tunability of composition, microstructure, and dimensionality of the ceramic material. [14–20] Tunability of microstructure can be achieved simply by varying the chemistry of the polymeric precursor. [21, 22] Tunability in the dimensions of the precursor permits efficient manufacturing of low dimensional structures such as thin films and ceramic fiber mats. This is possible by use of electrospinning, chemical vapor deposition, 3D printing, and other additive manufacturing techniques.[23, 24] Additionally, the PDC route permits efficient design and synthesis of various systems including SiCN and Si(B)CN, which cannot easily be synthesized by conventional ceramic powder processing methods.[25–27]

The thermal and chemical stabilities of PDCs are only some of the features contributing to their recent increase in popularity.[6, 28] As the application of these materials in different industries gains more significance, it is important to understand how different

preceramic polymers affect the composition and microstructure of pyrolyzed ceramic. These differences are likely to result in the formation of different nanoscale domains and interfacial interactions. [26, 29, 30] These modifications can be associated with changes in the free energy of systems.[31] Currently, it is understood that greater amounts of mixed bonding (Si bonded to both C and O) in the microstructure of precursor derived ceramics, like SiOC, SiCN, and SiOCN is consistent with greater thermodynamic stability.[32, 33] However, only few reports have investigated the stabilization promoted by different mixed bonding configurations.[21, 33]

Not many studies have investigated whether similar compositions and microstructure of SiOC PDCs derived from industrial precursors can be achieved from pyrolysis of low-cost commercial preceramic polymers. In this work we investigate the composition, structure, and thermodynamic stability of SiOCs derived from industrial precursor (SPR-212), as well as two low-cost preceramic polymers: polyhydromethylsiloxane (PHMS) polymer blend and tetramethylcyclotetrasiloxane (TTCS). Polymer derived SiOC ceramic is a general term that describes ceramics that contain free carbon in the SiO_xC_{4-x} mixed bonds (where, $0 \leq x \leq 4$) matrix. It should be noted that some SiOCs can have near stoichiometric compositions while others can have excess silicon. [34–37] This investigation permits assessment of how structure of polymeric precursors translates to compositional and microstructural differences in the SiOC ceramics. SPR-212 is a linear polymer and single source industrial precursor of SiOCs. The as obtained polymer can undergo low temperature curing at ~230 °C without the addition of a catalyst. The low viscosity of the precursor permits its use in applications including molding, coatings, and matrix composites. [38–40] TTCS is a cyclic single source

commercial precursor for development of PDCs with potential application as Li-ion battery anodes.[41, 42] Different PHMS polymer blends have been explored and are of interest for the synthesis of high temperature ceramics.[43–45]

In this study, six SiOC samples are investigated, SPR-1200, TTCS-1200, PHMS-1200, SPR-1500, TTCS-1500, and PHMS-1500. This work reports the synthesis, characterization, and thermodynamic analysis of the PDCs synthesized at 1200 and 1500 °C. All samples wereo btained from pyrolysis of polymeric precursors under inert atmosphere. There are systemic differences in the composition and microstructure of the samples, which lead to differences in thermodynamic stability. By systematically exploring these samples, it is possible to identify structural descriptors in preceramic polymers and PDCs contributing to the formation of SiOCs with thermodynamically more stable microstructures. This investigation identifies differences in the stabilization promoted by SiO_3C, $SiOC_3$, and SiO_2C_2 mixed bonding configurations. Structural characterization of the samples is done by Fourier transform infrared spectroscopy (FTIR), X-ray photoemission spectroscopy (XPS), high resolution XPS (HR-XPS), and Raman spectroscopy. High temperature oxide melt solution calorimetry is employed for assessment of thermodynamic stability of the materials.

3.2 Experimental Methods

3.2.1 Materials

Ceramics were derived from polymeric precursors: SPR-2012 (SPR) from Starfire Systems, 1,3,5-trivinyl-1,1,3,5,5-pentamethyltrisiloxane (TPTS), 1,3,5,7-tetravinyl-

1,3,5,7-tetramethylcyclotetrasiloxane (TTCS), and polyhydromethylsiloxane (PHMS), from Gelest, Inc. The Si : O ratio in SPR, TPTS, PHMS, and TTCS are 4 : 5, 3 : 2, 3 : 2, and 4 : 4, respectively. dicumyl peroxide (DCP) and platinum(0)-1,3- divinyl-1,1,3,3-tetramethyldisiloxane (DVD) were used as crosslinking catalysts. Structure of the oligomers is shown in Figure 1.
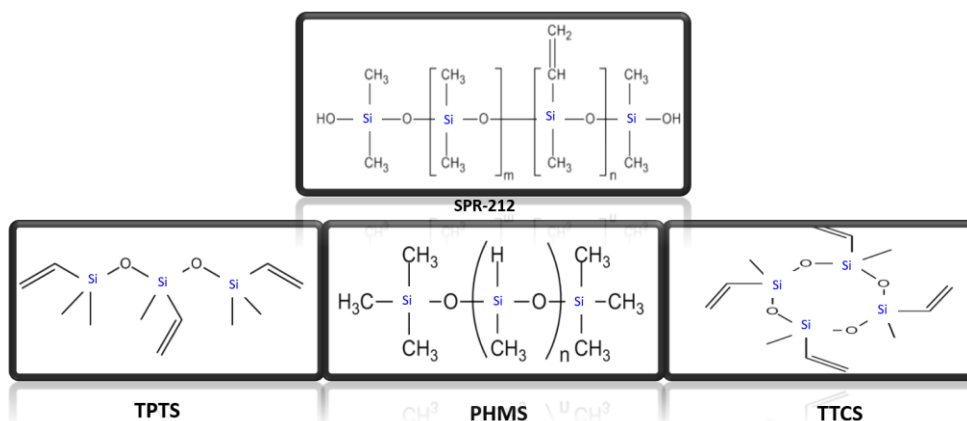
Figure 1. Structure of oligomers used for synthesis of the ceramic powders at 1200 and 1500 °C, under argon atmosphere.

3.2.2 Crosslinking

A blend of two oligomers: PHMS plus 40wt% TPTS and 1 wt% DVD, was employed as precursor for PHMS-derived SiOCs. SPR-212 was used as a single source industrial precursor (without the addition of catalyst) for synthesis of the SPR PDCs. TTCS-derived ceramics were obtained from mixture of TTCS plus 1 wt% DCP. All oligomers are crosslinked into infusible solid precursors at ~300 °C, under inert atmosphere.

67

3.2.3 Pyrolysis

Pyrolysis of the crosslinked precursors used a Netzsch STA 409 differential scanning calorimeter cell, using alumina crucibles. This allows accurate temperature control with low temperature gradients. The samples were heated from ambient to the final pyrolysis temperature at a ramp rate of 2 °C/min, under flowing argon (~50 mL/min). During temperature ramping, each sample was held at 400 °C for one hour, this ensures complete crosslinking of the precursor. Thermolysis of precursors was investigated at 1200 and 1500 °C, and resulted in the formation of SPR-1200, TTCS-1200, PHMS-1200, SPR-1500, TTCS-1500, and PHMS-1500 SiOCs. The PDCs were then ground into powders.

3.2.4 Characterization

FTIR experiments were performed by employing a bench-top Bruker TENSOR with platinum ATR accessory. Spectra were collected in the range of 4000-500 cm^{-1}. X-ray diffraction (XRD) experiments were conducted at ambient temperature using a bench-top Bruker D2 powder diffractometer employing a nickel-filtered CuKα radiation (wavelength= 1.5418 Å). Elemental analysis of the ceramic powders employed X-ray photoelectron spectroscopy (XPS). XPS experiments were performed by use of a Kratos AXIS Supra+ with a monochromatic Al Kα+ ion beam (beam energy = 1486.6 eV). Raman spectroscopy used a custom-built multi-wavelengths system with a 532 nm green laser at a power of 74 mW with a 50 X microscope objective. TG-DSC experiments employed a Setaram LABSYS Evo DTA/DSC.

3.2.5 Thermochemistry

In this study, the thermodynamic stability of the PDCs is assessed by thermochemical calculations of enthalpies of formation from elements ($\Delta H^o_{f,\ elem}$) and crystalline components ($\Delta H^o_{f,\ comp}$). Enthalpies of dissolution (ΔH_{dis}) were obtained from calorimetric experiments by employing a commercial twin Calvet type Seteram Alexsys calorimeter. Due to the high solubility of the PDCs in the oxide melt, 20 g of sodium molybdate ($3Na_2O \bullet MoO_3$) melt, at 800 °C were employed for oxidative dissolution. For each experiment, about 5 mg of sample were weighed using a Mettler Toledo microbalance with 10 µg accuracy. The weighed samples were pressed into a pellet using a 1.5 mm tungsten die. The pellets were then inserted into the melt for oxidative dissolution. The melt was continuously bubbled with 40 mL/min of oxygen, to maintain an oxidative environment. The gases evolved from dissolution of the sample were evacuated from the calorimeter by utilizing oxygen flushing at a flowrate of 100 mL/min. To ensure reproducibility, the experiments were repeated at least four times. This is a well-established technique that has been previously used to investigate similar systems.[46–49]

Reaction (1) describes the oxidative dissolution of SiOCs.

$$Si_a\ O_b\ C_c\ (s,\ 25\ °C) + (((2a) + ((2c)\text{-}b)/2)\ O_2\ (g,\ 800\ ^O C) \rightarrow a\ SiO_2\ (s,\ 800\ °C) + c\ CO_2\ (g,\ 800\ °C)\ \Delta H_{dis,\ SiOC}$$

(1)
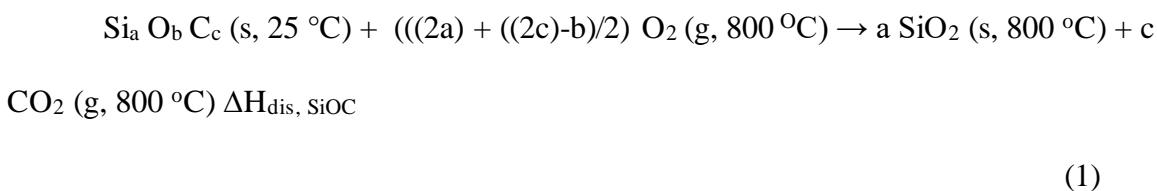
Enthalpy of formation of the SiOCs from the elements (Si, C, and O_2) is described by:

$$a\ Si(s,\ 25\ ^\circ C) + b/2\ O_2(g,\ 25\ ^\circ C) + c\ C\ (s,\ 25\ ^\circ C) \rightarrow Si_aO_bC_c\ (s,\ 25 ^\circ C)$$
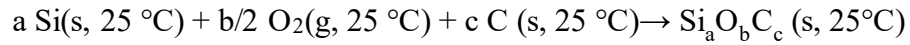
$$\Delta H^\circ_{f,\ elem}$$

(2)

Enthalpy of formation relative to crystalline components (β-SiC, SiO_2 (cristobalite), and C (graphite)) is described by:

$$(a-(b/2))\ SiC(s,\ 25\ ^\circ C) + (b/2)\ SiO_2(s,\ 25\ ^\circ C) + (c-(a-(b/2)))\ C\ (s,\ 25\ ^\circ C) \rightarrow$$

$$Si_aO_bC_c\ (s,\ 25 ^\circ C)\ \Delta H^\circ_{f,\ comp}$$

(3)
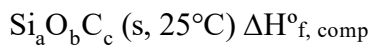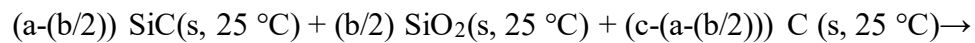
During dissolution, Si is oxidized and precipitates as cristobalite and C is oxidized into CO_2. Both CO_2 and O_2 evolve from the melt as gases.[33, 50, 51] The gaseous oxides have very low solubility in the melt.[33, 50, 51] By identifying the initial and final state of the system, enthalpies of dissolution ($\Delta H_{dis,\ SiOC}$) and thermodynamic cycles (see Tables 1-2) were employed to calculate enthalpies of formation.

Table 1. Thermochemical cycle for calculation of enthalpy of formation from elements $\Delta H^{\circ}_{f,\ elem.}$

Enthalpies of formation from the elements ($\Delta H_{f,\ elem}$) **a Si(s, 25 °C) + b/2 O$_2$(g, 25 °C) + c C (s, 25 °C)→** **Si$_a$O$_b$C$_c$ (s, 25°C) $\Delta H^{\circ}_{f,\ elem}$=?**	ΔH (kJ/mol)
Si$_a$ O$_b$ C$_c$ (s, 25 °C) + (((2a) + (2c)-b))/2) O$_2$ (g, 800 °C) → a SiO$_2$ (s, 800 °C) + c CO$_2$ (g, 800 °C)	$\Delta H_{dis,\ SiOC}$
Si (s, 25 °C) + O$_2$ (g, 800 °C) → SiO$_2$ (s, 800 °C)	ΔH_2 = -883.13 ± 2.1
C (s, 25 °C) + O$_2$ (g, 800 °C) → CO$_2$ (g, 800 °C)	ΔH_3 = -381.35 ± 0.13
O$_2$ (g, 25 °C) → O$_2$ (g, 800 °C)	ΔH_4= 25.34 ± 0.10
$\Delta H^{o}_{f,\ elem}$ = - $\Delta H_{dis,\ SiOC}$ + a ΔH_2 + c ΔH_3 + (b/2) ΔH_4	**$\Delta H^{o}_{f,\ elem}$**

Table 2. Thermochemical cycle for calculation of enthalpy of formation from components $\Delta H^{\circ}_{f,\ comp.}$

Enthalpies of formation from components ($\Delta H_{f,\ comp}$) **(a-(b/2)) SiC(s, 25 °C) + (b/2) SiO$_2$(s, 25 °C) + (c-(a-(b/2))) C (s, 25 °C)→ Si$_a$O$_b$C$_c$ (s, 25°C) $\Delta H^{o}_{f,\ comp}$= ?**	ΔH (kJ/mol)
Si$_a$ O$_b$ C$_c$ (s, 25 °C) + (((2a) + (2c)-b))/2) O$_2$ (g, 800 °C) → a SiO$_2$ (s, 800 °C) + c CO$_2$ (g, 800 °C)	$\Delta H_{dis,\ SiOC}$
SiO$_2$ (S, 25 °C) → SiO$_2$ (s, 800 °C)	ΔH_2 = 50.1± 0.10
SiC (S, 25 °C) + 2O$_2$ (g, 800 °C) → SiO$_2$ (s, 800 °C) + CO$_2$ (g, 800 °C)	ΔH_3 = -1192.28 ± 2.15

C (S, 25 °C) + O_2 (g, 800 °C) → CO_2 (g, 800 °C)	$\Delta H_4 = -381.35 \pm 0.13$
$\Delta H^o_{f, comp} = -\Delta H_{dis, SiOC} + (b/2) \Delta H_2 + (a-(b/2)) \Delta H_3 + (c-(a-(b/2))) \Delta H_4$	$\Delta H^o_{f, comp}$

3.3 Results and discussion

FTIR permits identification of functional groups in the structure of pre-ceramic polymers and corresponding PDCs.[52–54]. The high energy of the beam identifies vibrations corresponding to strong bonds with low polarizability like C-O and O-H, which are otherwise hard to observe by Raman spectroscopy. The spectra of crosslinked precursors (see Figure 2A) suggest presence of Si–O–Si (~1060 cm^{-1}) and Si–CH_3 (~1260 cm^{-1}) bond stretching, as well as other functional groups consistent with structure of the preceramic polymers.[52–54] The results point to evolution of organic groups during high temperature treatment of the polymeric precursors, as peaks corresponding to C-H and Si-H bonds are not detected in the spectra of samples pyrolyzed at 1200 and 1500 °C (see Figure 2b). Spectra of the ceramic powders (Figure 2b) suggest the presence of C=C (~1600 cm^{-1}), Si-O-Si (~1060 cm^{-1}), and Si-C (~800 cm^{-1}) bond stretch vibrational bands. These results are consistent with the structure of SiOCs.[55–60]
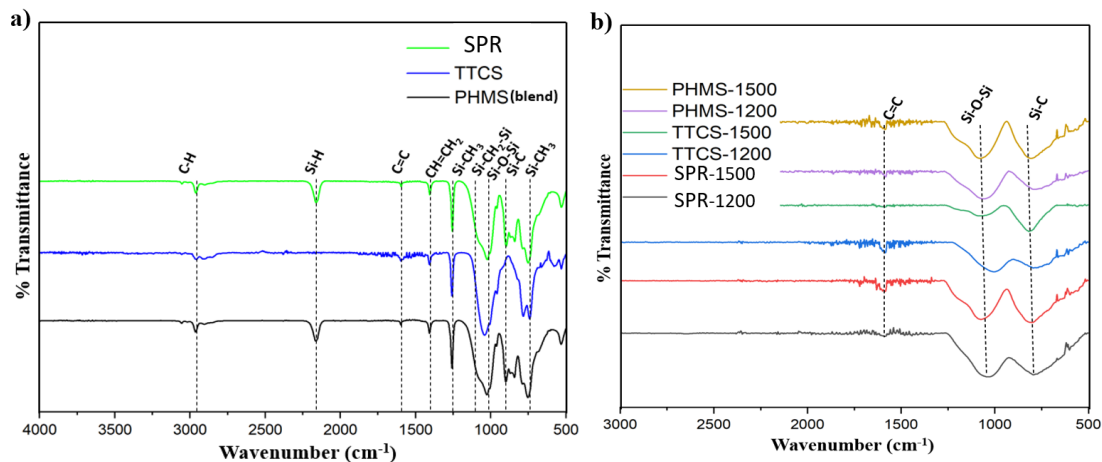
Figure 2. FTIR spectra of a) crosslinked polymeric precursors and b) SiOCs synthesized at 1200 and 1500 °C.

Thermal analysis of the precursors was conducted by use of TG-DSC (50 mL/min flowing argon atmosphere, 10 °C/min temperature ramping). The analyses were only conducted up to 1000 °C due to equipment limitations. The results in Figure 3 point to significant mass loss in all specimens up to ~800 °C, which results from evolution of volatile organics. SPR-212 and PHMS (blend) display comparable TG-DSC curves, with major mass loss occurring near ~ 500 °C. In contrast TTCS displays greatest mass loss at a lower temperature (~ 425 °C). The exothermic DSC peaks near ~300 °C likely correspond to crosslinking.[61] Other exothermic peaks beyond 400 °C may result from the ceramization step.[62] The results suggest that the trend in ceramization temperature is: PHMS (~550 °C) > SPR (~450 °C) > TTCS (~425 °C). This highlights the lower ceramization temperature in TTC precursors. The specimens do not display significant mass loss beyond ~800 °C, which is typical in PDCs.[63] The larger mass loss of TTCS may in part result from the release of greater amounts of hydrogen and/or water during

73

ceramization. We cannot determine other specific reasons for the greater mass loss in TTCS.
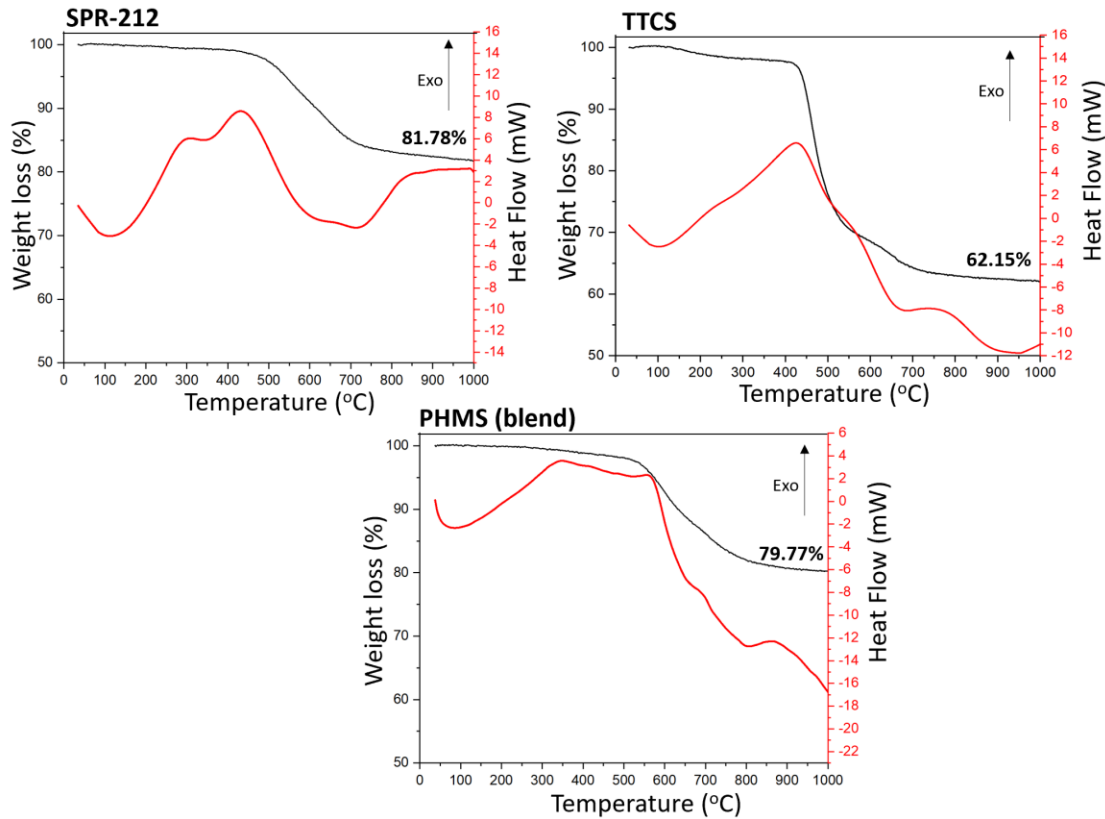
Figure 3. TG-DSC curves of crosslinked precursors

We employed XRD for detecting the presence or absence of crystalline (or poorly crystalline) phases in samples synthesized at high temperatures. The patterns (see Figure 4) confirm the formation of amorphous structures in samples synthesized at 1200 °C. The broad peaks in the spectra of PDCs synthesized at 1500 °C suggest nucleation and growth of poorly crystalline β-SiC grains upon increase in pyrolysis temperature.[30] The exposure of SiOC PDCs to high temperatures (>1400 °C) typically results in

carbothermal reduction, which occurs in parallel to growth of crystalline domains.[64–66] These results are in line with previous studies investigating similar materials.[33, 67, 68]
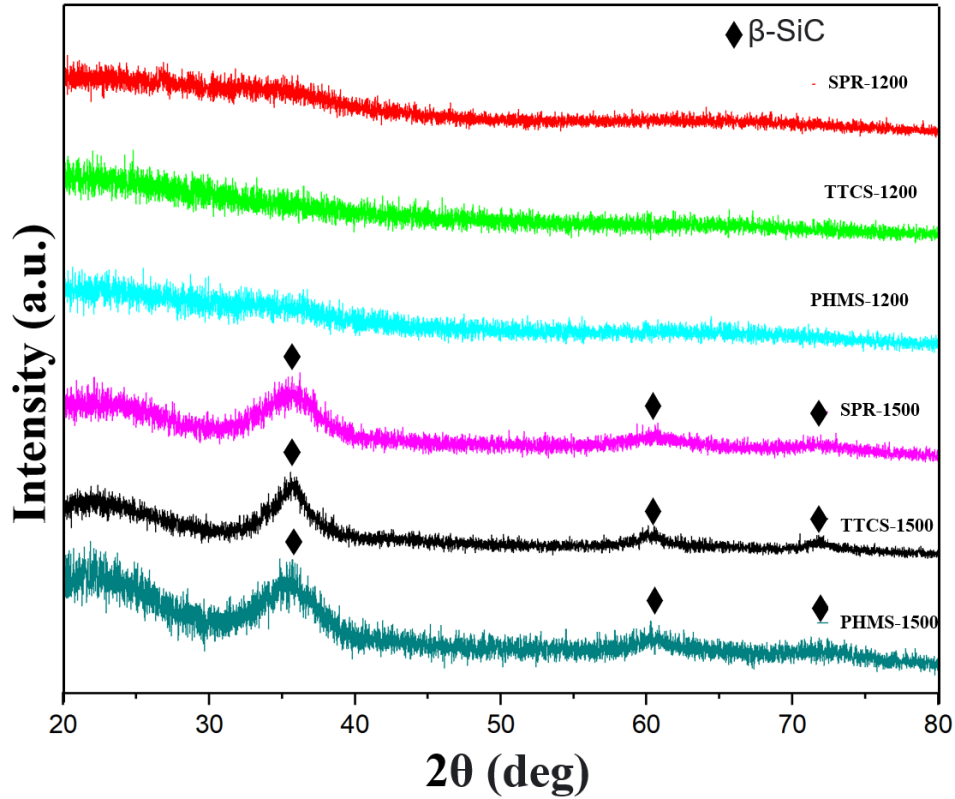
Figure 4. XRD patterns show growth of beta-SiC crystals in PDCs synthesized at 1500 ^oC. The spectra do not show peaks corresponding to graphite. This suggests that any free carbon may be present as amorphous domains.

Raman spectra (Figure 5) can identify the types of carbon present in the microstructure of PDCs. D ($\sim$1330 cm^{-1}) and G ($\sim$1600 cm^{-1}) bands correspond to sp^2-hybridized disordered and graphitic-like carbons, respectively. [23, 30] The integrated intensity of the full width at half maximum (FWHM) of the D(I_D) and G (I_G) bands permits identification of the ratio of disordered carbon D(I_D) to graphitic carbon G (I_G).

[30, 31] There is significant increase in the relative amount of graphitic (well-ordered) carbon with synthesis temperature (see Table 3). Curve fitting of the spectra permits identification of T (1204–1232 cm^{-1}) and D" (1490–1504 cm^{-1}) bands, which correspond to considerable amounts of sp^2-sp^3 bonds and amorphous carbon, respectively.[23] Figure 5 suggest significant decrease in the relative amount of sp^2-sp^3 bonds and amorphous carbons in the microstructure of samples synthesized at 1500 °C. Disorder induced D' bands (~1620 cm^{-1}) are only observed in the spectrum of SPR-1200.[69]

Table 3. Summary of D/G in the PDCs.

sample	D (I_D)/G (I_G) (FWHM)
SPR-1200	1.57
TTCS-1200	1.94
PHMS-1200	1.77
SPR-1500	1.00
TTCS-1500	1.33
PHMS-1500	1.11
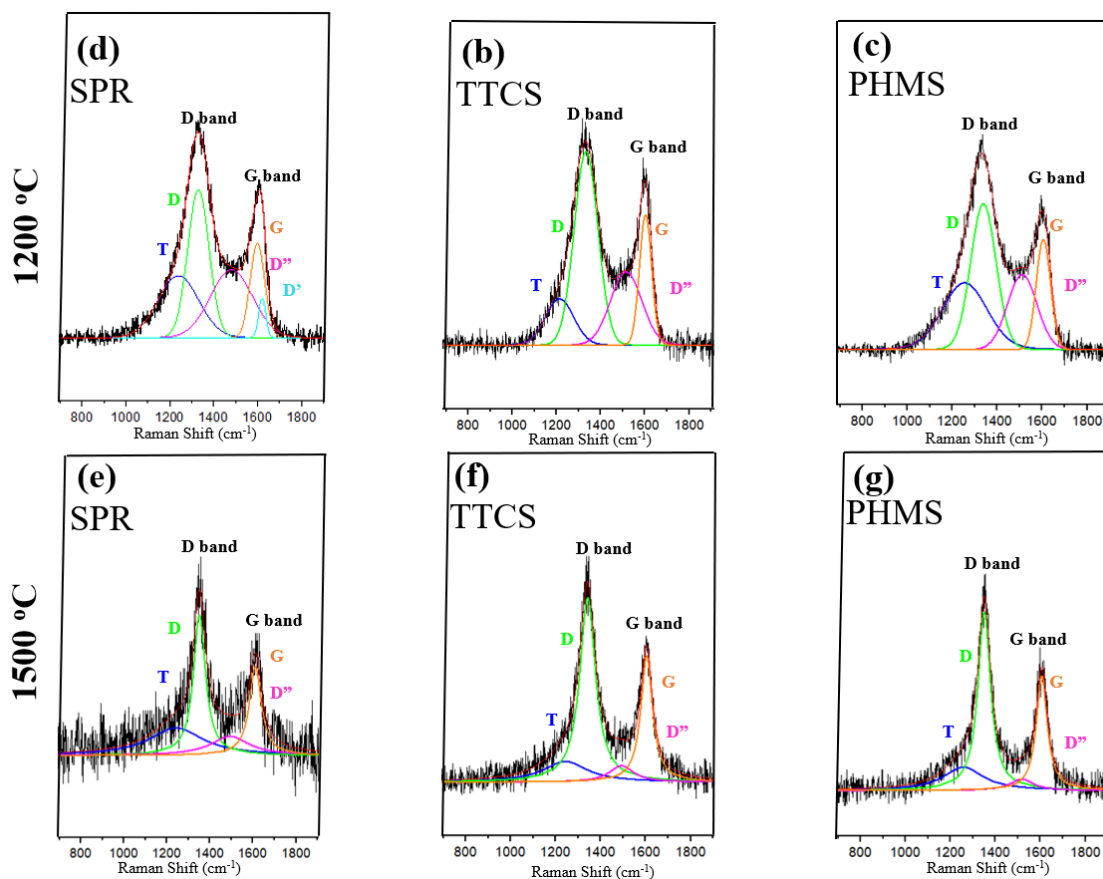
Figure 5. Raman spectra of a) SPR-1200, b) TTCS-1200, c) PHMS-1200, d) SPR-1500, e) TTCS-1500, f) PHMS-1500.

XPS permits elemental analysis as well as identification of bonding speciation in the structure of fine powders [30]. Identification of speciation and semi-quantitative assessment of their relative amounts was achieved by probing Si $2p$, O $1s$, and C $1s$ bonds.[70] Coupled with other characterization techniques such as Raman, XPS allows identification of differences in the microstructure of the PDCs synthesized at varying temperatures.[30] By employing appropriate curve fitting, the area under each convolution represents the relative amount of the types of bonds. HR-XPS spectra of the samples are shown in Figure 6.

C $1s$ convolutions show that all samples contain considerable amounts of C-O (~286.5 eV) and C-C (~285 eV) and C-Si (283.7 eV) bonds. [71, 72] In mixed bonding C is bonded to Si or to another C, and typically free carbon does not bond with significant amounts of oxygen. Therefore the C-O bonds may correspond to bond signatures from foreign carbon-containing impurities such as lint, pollen, or strongly bound CO_2, as previously reported.[73–75] This makes semiquantitative analysis of C 1s bonds by XPS alone challenging. [73] It is likely that C-Si convolutions also include bonds formed in SiC domains. Similarly, the presence of C-C bonds is consistent with Raman spectra (see Figure 1) and may correspond to free carbon or to C-C terminated mixed bonding. Si $2p$ convolutions of samples pyrolyzed at 1200 °C suggest the presence of significant amounts of SiO_4 (~104 eV), SiO_2C_2 (~102 eV), and SiO_3C (~102.9 eV), and $SiOC_3$ (~ 101 eV) bonds.[71, 76] SiO_4 correspond to amorphous SiO_2 (silica) domains and SiO_xC_{4-x} correspond to mixed bonding networks (Si bonded to both C and O).[77] From the samples synthesized at 1200 °C, SPR-1200 appears to have the greatest relative amount of SiO_4 bonds, while PHMS-1200 and TCCS-1200 display greatest relative amount of SiO_xC_{4-x} mixed bonding environments. The spectra further show that for samples synthesized at 1500 °C, the relative amount of SiO_4 (silica) bonds is greatest in PHMS-1500, although SPR-1500, and TTCS-1500 also display large relative amount of SiO_4 bonds compared to their analogues synthesized at lower temperature. This may indicate significant phase separation in the amorphous structures to form stoichiometric domains (SiO_2 and SiC) with increase in synthesis temperature. Additionally, the results in Figure 6 point to a decrease in the amount of SiO_3C relative to SiO_2C_2 and/or $SiOC_3$ mixed bonds, between

1200 and 1500 °C. This may suggest lower stability of SiO_3C compared to other mixed bonding networks.

SPR
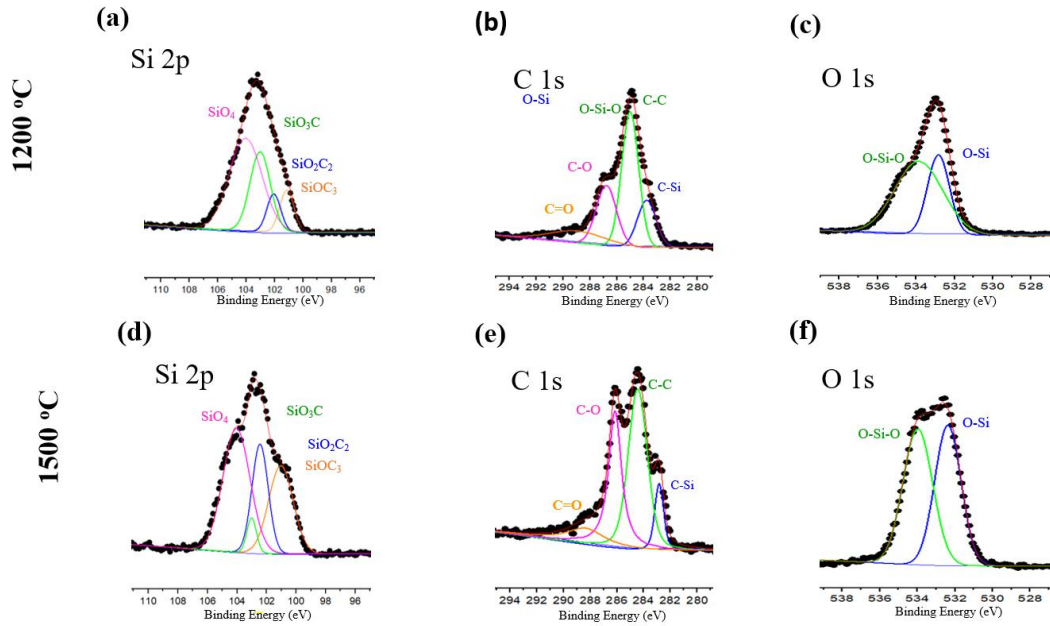
TTCS
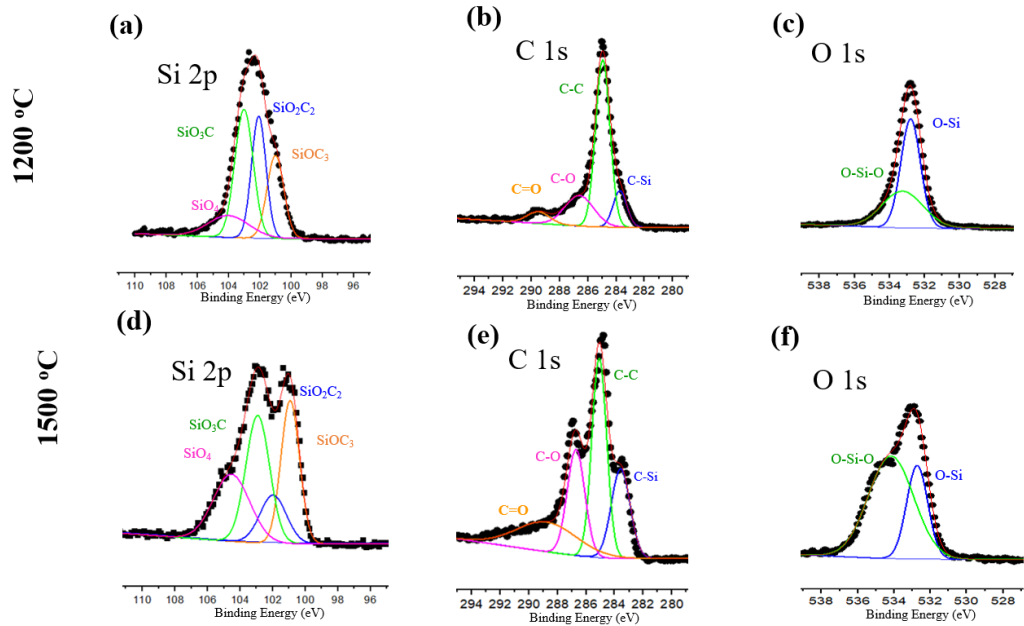
PHMS
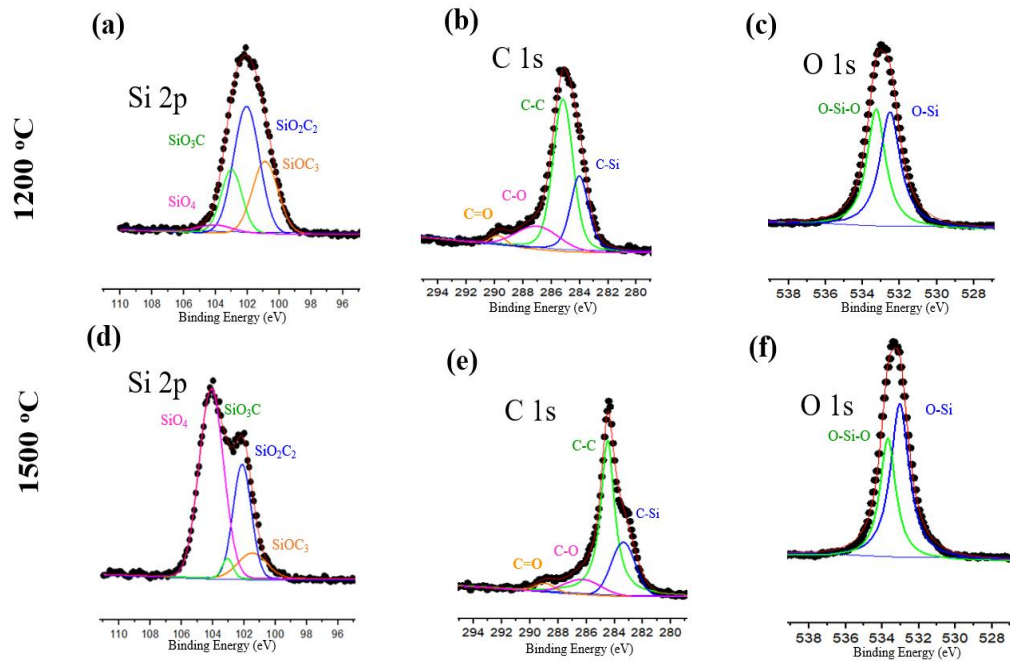
Figure 6. HR XPS of SPR, TTCS and PHMS derived ceramics.

3.3.1 Elemental Analysis

Thermodynamic analysis of PDCs requires accurate elemental compositions. XPS survey scans are useful in obtaining compositional information of fine ceramic powders synthesized at high temperatures, when residual hydrogen (if any) is scarce. The results from elemental analysis are summarized in Table 4. It is apparent that the Si : O ratio increases with pyrolysis temperature. In contrast, the Si : C ratio decreases with temperature. These results likely correspond to carbothermal reduction in the samples pyrolyzed at higher temperature (1500 °C). During carbothermal reduction SiO_2 domains react with excess free carbon phase to produce CO_2 (gas) and SiC. These results are consistent with the XRD pattern (see Figure 4) of samples pyrolyzed at 1500 °C, which

80

point to growth of β-SiC grains. XPS compositions are employed for thermodynamic analysis discussed in the section that follows.

Table 4. Elemental analysis of SiOC samples from XPS survey scan.

Elemental Composition by XPS			
	Elements (at.%)		
SiOC sample	C 1s	O 1s	Si 2p
SPR-1200	35.47 ± 1.11	30.56 ± 1.21	33.97 ± 0.1
SPR-1500	37.12 ± 0.04	27.32 ± 1.48	35.56 ± 1.46
TTCS-1200	50.28 ± 0.44	25.29 ± 1.24	24.43 ± 0.49
TTCS-1500	48.76 ± 1.04	19.37 ± 0.1	31.87 ± 0.94
PHMS-1200	38.16 ± 0.61	30.25 ± 2	31.62 ± 1.07
PHMS-1500	40.35 ± 2.55	28.57 ± 2.96	31.15 ± 0.11

Table 5. Composition and estimated phase assemblage of SiOCs derived from SPR-212, TTCS, and PHMS at 1200 and 1500 ^{o}C.

Sample	Composition $Si_xO_yC_z$ (x+y+z=1)	SiO_2 (mol%)	SiC (mol%)	C (mol%)
SPR-1200	$Si_{0.34}O_{0.31}C_{0.35}$	30.69	36.63	32.67
TTCS-1200	$Si_{0.25}O_{0.25}C_{0.50}$	20	20	60
PHMS-1200	$Si_{0.32}O_{0.30}C_{0.38}$	28.30	32.07	39.62

SPR-1500	$Si_{0.36}O_{0.27}C_{0.37}$	26.73	44.55	28.71
TTCS-1500	$Si_{0.32}O_{0.19}C_{0.49}$	16.24	38.46	45.30
PHMS-1500	$Si_{0.31}O_{0.29}C_{0.40}$	26.60	30.27	43.12

The results from elemental analysis suggest that pyrolysis of the PHMS (blend) at 1200 °C results in formation of SiOC with a composition and phase assemblage closest to that of the sample derived from SPR-212 industrial precursor (see Table 5). In contrast, there is significant difference of bonding speciation in their microstructure (from HR-XPS Si *2p* convolutions). No obvious similarities in composition and phase assemblage are observed in the samples synthesized at 1500 °C. Calorimetric experiments permit systematic assessment of the effect of composition and microstructure (including phase assemblage) on the thermodynamic stability of SiOCs. These results indicate that PDCs derived from the PHMS blend display the smallest change in composition, between 1200 and 1500 °C, even compared to samples derived from industrial precursor (SPR-212). This could point to higher stability of the PHMS-1200.

3.3.2 Energetics of Formation and Interdomain Interactions

The results from thermodynamic analysis of the SiOCs are summarized in Table 6. Overall, enthalpies of dissolution become more negative with increasing C and Si content, which results from highly exothermic oxidation of these elements. Enthalpies of formation permit identification of trends in the thermodynamic stability of the samples. More exothermic enthalpies of formation correspond to greater thermodynamic stability,

as entropic effects are relatively small in comparison to the highly exothermic enthalpies of formation from the elements.[30, 31]. For samples synthesized at 1200 and 1500 °C, enthalpies of formation from elements ($\Delta H^{\circ}_{f, elem}$) are most exothermic for samples derived from the PHMS (blend) precursor and least for PDCs derived from TTCS. This points to greatest enthalpic drive for the formation of the microstructure in PHMS-1500. The results further suggest that pyrolysis of the industrial SiOC precursor (SPR-212), results in formation of microstructures (SPR-1200 and SPR-1500) with intermediate stability relative to elements.

Table 6 also presents enthalpies of formation relative to components ($\Delta H^{\circ}_{f, comp}$), namely β-SiC, SiO_2 (cristobalite), and C (graphite). More exothermic enthalpy of formation from components corresponds to energetically more favorable interdomain interaction and/or greater amount of mixed bonding (supported by XPS convolutions).[30, 31]. Mixed bonding promotes greater stabilization of microstructures as a result of less bond strain compared to the interface between stoichiometric crystalline domains. The results show that for samples synthesized at 1200 °C, $\Delta H^{\circ}_{f, comp}$ is most exothermic for PHMS-1200 and least for TTCS-1200. Similarly, the results point to little energetically favorable interdomain interactions in SPR-1200. However, increasing synthesis temperature to 1500 °C, results in structural evolution suggesting highly favorable interdomain interaction and/or mixed bonding in the microstructure of SPR-1500, TTCS-1500, and PHMS-1500. At all temperatures PDCs derived from low-cost preceramic polymers PHMS (blend) result in structures with highest thermodynamic stability, even compared to samples derived from industrial precursor (SPR-212). Note that the positive enthalpy for the formation of TTCS-1200 could indicate unfavorable interdomain

interactions, however, it appears that the interactions become less unfavorable at 1500 °C, hence the more exothermic formation enthalpy in TTCS-1500. This complexity, perhaps related to both changes in domain structure and coarsening, may explain the superior stabilization of TTCS-derived SiOC in this temperature range. Structural characterization suggests that compositional changes are driven by carbothermal reduction. Compared to the other samples synthesized at 1200 °C, the higher C content and O/Si ratio in TTCS-1200 may provide greater drive for that reaction.

Table 6. Summary of enthalpies of dissolution (ΔH_{dis}), enthalpies of formation from elements ($\Delta H^o_{f, elem}$), and enthalpies of formation from components ($\Delta H^o_{f, comp}$).

Sample	Composition $Si_xO_yC_z(x+y+z=1)$	ΔH_{dis} (kJ/mol)	$\Delta H^o_{f, elem}$ (kJ/mol)	$\Delta H^o_{f, comp}$ (kJ/mol)
SPR-1200	$Si_{0.34}O_{0.31}C_{0.35}$	-275.41 ± 2.40	-154.40 ± 3.19	-0.31 ± 3.23
TTCS-1200	$Si_{0.25}O_{0.25}C_{0.50}$	-291.94 ± 2.77	-116.35 ± 3.48	$+6.16 \pm 3.51$
PHMS-1200	$Si_{0.32}O_{0.30}C_{0.38}$	-226.92 ± 2.21	-197.55 ± 3.05	-48.34 ± 3.09
SPR-1500	$Si_{0.36}O_{0.27}C_{0.37}$	-284.91 ± 2.78	-170.12 ± 3.50	-31.88 ± 3.52
TTCS-1500	$Si_{0.32}O_{0.19}C_{0.49}$	-299.76 ± 2.60	-167.29 ± 3.35	-64.80 ± 3.38

PHMS-1500	$Si_{0.31}O_{0.29}C_{0.40}$	-210.21 ± 1.70	-212.43 ± 2.71	-68.87 ± 2.74

3.3.3 Link between Microstructure and Thermodynamic Stability of PDCs

FTIR, XRD, Raman, and XPS all show that SiOCs derived from all three polymeric precursors undergo significant structural modifications between 1200 and 1500 ^{o}C Similarly, thermodynamic analysis (Table 6), shows increase in thermodynamic stability of the SiOCs with increasing pyrolysis temperature, independent of initial precursor. This shows that between 1200 and 1500 ^{o}C, the PDCs evolve towards thermodynamically more stable structures. For all synthesis temperatures, greater O content is consistent with greater thermodynamic stability (see $\Delta H^o_{f,\ elem}$). This may result from greater amounts of SiO_2 and/or SiO_xC_{4-x} mixed bonding domains (supported by HR-XPS convolutions). This highlights correlation between bonding speciation and thermodynamic stabilization.

It is important to stress the decrease in the O content of PDCs synthesized at 1500 ^{o}C (from elemental analysis), which occur in parallel with growth and nucleation of β-SiC grains (from XRD). The thermodynamic analysis suggests that growth/crystalization of β-SiC domains is thermodynamically favorable and occurs in parallel with increase in favorable interdomain interactions. This points to significant thermodynamic drive for carbothermal reduction in SiOCs to form more SiC.

Similarly, results from Raman spectroscopy (see Figure 5) indicate significant decrease in the relative amount of sp^2-sp^3 carbon bonds (T bands) as well as disordered carbons (from the ratio of D (I_D)/G (I_G) at FWHM) in samples synthesized at 1500 °C. This may point to consumption of amorphous free carbons during carbothermal reduction and/or formation of well-defined carbon networks at higher pyrolysis temperature. Additionally, HR-XPS convolutions and the phase assemblages suggest presence of significant amount of C-C bonds in all samples. This may imply that decrease in intensity of D" bands for high temperature (1500 °C) samples mainly result from formation of well-defined carbon networks. These observations could indicate significant stabilization of structures with decreasing amount of sp^2-sp^3 carbon bonds and with increase in ordering of the carbon network. HR-XPS convolutions (see Figure 6) permit identification of variation in bonding speciation with pyrolysis temperature. The results suggest an increase in the amount of SiO_2C_2 and/or $SiOC_3$ (relative to SiO_3C) mixed bonding with temperature. The increase in thermodynamic stability of the samples with pyrolysis temperature may point to higher stabilizing effect of SiO_2C_2 and/or $SiOC_3$ compared to SiO_3C mixed bonding environments. This is important as it permits the identification of an additional descriptor for increased thermodynamics stabilization in PDCs.

3.3.4 Link between Structure of Preceramic Polymers and Composition of PDCs

The compositions reported in Table 6 show that SiOCs derived from TTCS (cyclic structure) have the highest carbon content, in contrast, samples derived from SPR-212

(linear structure) display the lowest. TTCS and PHMS (linear polymer blend) precursors have large amounts of less hydrogenated (vinyl compared to methyl) carbonaceous pendant groups (see Figure 1). Such groups (vinyl, allyl) are expected to form more carbon rich SiOCs upon high temperature pyrolysis, as less carbon is expected to evolve as organics during thermal treatment.[78] Hence, the large amount of methyl instead of vinyl side-groups in the backbone of SPR-212 oligomers may explain the lower C content of SPR-1200 and SPR-1500 samples. Similarly, O content appears to be greatest in SiOCs derived from PHMS blend and SPR-212, and lowest in samples derived from TTCS. The results are consistent with significant loss of low molecular weight carbonaceous side groups (CH_3) in the PHMS blend and SPR-212, which ultimately results in increase in O concentration in the PDCs. We do not identify any obvious trends between thermodynamic stability ($\Delta H^{o}_{f,\ comp}$) and overall composition (Si, O, and C content) of the precursors. This is not surprising, as the amounts of different phases and strength of interdomain interactions, which determine the thermodynamic stabilization, are more strongly related to processing history than to bulk composition.

3.4 Conclusion

We report the structure and energetics of SiOCs derived from different preceramic polymers. PDCs derived from PHMS blend have a composition closest to SiOCs synthesized from SPR-212 industrial precursor. The results suggest greatest thermodynamic stability and more favorable interdomain interactions in the microstructure of samples derived from the PHMS blend. For each precursor the increase

in energetic stability of specimens synthesized at 1500 $^{\circ}$C is also consistent with a decrease in the relative amount of SiO_3C compared to SiO_2C_2 and/or $SiOC_3$ mixed bonds. The results highlight increased stabilization of SiOCs with formation of a well-ordered carbon network and decrease in relative amount of sp^2-sp^3 carbon bonds. This information could serve as a framework for the design of thermodynamically more stable SiOCs. Following investigation of the systematics for thermodynamic stabilization in SiC and SiOC materials, this dissertation work is expanded to the study of quaternary SiC(N)(O) PDC systems as well. This enables determination of stabilization trends in more complex systems, as well as assessment of the energetic effect resulting from addition of nitrogen to SiC(O) systems, as seen in the next chapter.

Acknowledgments

REFERENCES

1. Steyer, T. E. Shaping the Future of Ceramics for Aerospace Applications. *Int. J. Appl. Ceram. Technol.* **10**, 389–394 (2013).

2. Monteverde, F., Bellosi, A. & Scatteia, L. Processing and properties of ultra-high temperature ceramics for space applications. *Mater. Sci. Eng. A* **485**, 415–421 (2008).

3. Savino, R., Mungiguerra, S. & Di Martino, G. D. Testing ultra-high-temperature ceramics for thermal protection and rocket applications. *Adv. Appl. Ceram.* **117**, s9–s18 (2018).

4. Saccone, G., Gardi, R., Alfano, D., Ferrigno, A. & Del Vecchio, A. Laboratory, on-ground and in-flight investigation of ultra high temperature ceramic composite materials. *Aerosp. Sci. Technol.* **58**, 490–497 (2016).

5. Jia, Y. *et al.* Thermal properties of polymer-derived ceramic reinforced with boron nitride nanotubes. *J. Am. Ceram. Soc.* **102**, 7584–7593 (2019).

6. Ren, Z., Mujib, S. B. & Singh, G. High-Temperature Properties and Applications of Si-Based Polymer-Derived Ceramics: A Review. *Materials* **14**, 614 (2021).

7. Zhao, Z., Xiang, H., Dai, F.-Z., Peng, Z. & Zhou, Y. (TiZrHf)P2O7: An equimolar multicomponent or high entropy ceramic with good thermal stability and low thermal conductivity. *J. Mater. Sci. Technol.* **35**, 2227–2231 (2019).

8. Wei, G. C. Beta Sic Powders Produced by Carbothermic Reduction of Silica in a High-Temperature Rotary Furnace. *J. Am. Ceram. Soc.* **66**, c111–c113 (1983).

9. Moshtaghioun, B. M. *et al.* Rapid carbothermic synthesis of silicon carbide nano powders by using microwave heating. *J. Eur. Ceram. Soc.* **32**, 1787–1794 (2012).

10. Carassiti, L. *et al.* Ultra-rapid, sustainable and selective synthesis of silicon carbide powders and nanomaterials via microwave heating. *Energy Environ. Sci.* **4**, 1503–1510 (2011).

11. Taylor, A. & Laidler, D. S. The Formation and Crystal Structure of Silicon Carbide. *Br. J. Appl. Phys.* **1**, 174 (1950).

12. Ren, R., Yang, Z. & Shaw, L. L. Synthesis of Nanostructured Silicon Carbide through an Integrated Mechanical and Thermal Activation Process. *J. Am. Ceram. Soc.* **85**, 819–827 (2002).

13. Moshtaghioun, B. M., Monshi, A., Abbasi, M. H. & Karimzadeh, F. A study on the effects of silica particle size and milling time on synthesis of silicon carbide nanoparticles by carbothermic reduction. *Int. J. Refract. Met. Hard Mater.* **29**, 645–650 (2011).

14. Hagelüken, L. *et al.* Multiscale 2D/3D microshaping and property tuning of polymer-derived SiCN ceramics. *J. Eur. Ceram. Soc.* **42**, 1963–1970 (2022).

15. Duan, W. *et al.* A review of absorption properties in silicon-based polymer derived ceramics. *J. Eur. Ceram. Soc.* **36**, 3681–3689 (2016).

16. Ionescu, E., Kleebe, H.-J. & Riedel, R. Silicon-containing polymer-derived ceramic nanocomposites (PDC-NCs): preparative approaches and properties. *Chem. Soc. Rev.* **41**, 5032–5052 (2012).

17. Mera, G., Navrotsky, A., Sen, S., Kleebe, H.-J. & Riedel, R. Polymer-derived SiCN and SiOC ceramics – structure and energetics at the nanoscale. *J. Mater. Chem. A* **1**, 3826–3836 (2013).

18. Chaudhary, R. P. *et al.* Additive manufacturing of polymer-derived ceramics: Materials, technologies, properties and potential applications. *Prog. Mater. Sci.* **128**, 100969 (2022).

19. Ren, Z., Gervais, C. & Singh, G. Fabrication and characterization of silicon oxycarbide fibre-mats via electrospinning for high temperature applications. *RSC Adv.* **10**, 38446–38455 (2020).

20. Mujib, S. B. *et al.* Electrospun SiOC ceramic fiber mats as freestanding electrodes for electrochemical energy storage applications. *Ceram. Int.* **46**, 3565–3573 (2020).

21. Karakuscu, A., Guider, R., Pavesi, L. & Sorarù, G. D. Broad-band tunable visible emission of sol–gel derived SiBOC ceramic thin films. *Thin Solid Films* **519**, 3822–3826 (2011).

22. Mera, G., Tamayo, A., Nguyen, H., Sen, S. & Riedel, R. Nanodomain Structure of Carbon-Rich Silicon Carbonitride Polymer-Derived Ceramics. *J. Am. Ceram. Soc.* **93**, 1169–1175 (2010).

23. Yu, Y., Chen, Y., Xu, C., Fang, J. & An, L. Synthesis of Spherical Non-Oxide Silicon Carbonitride Ceramic Particles. *J. Am. Ceram. Soc.* **94**, 2779–2782 (2011).

24. Bhandavat, R., Pei, Z. & Singh, G. Polymer-derived ceramics as anode material for rechargeable Li-ion batteries: a review. *Nanomater. Energy* **1**, 324–337 (2012).

25. Tavakoli, A. H., Armentrout, M. M., Narisawa, M., Sen, S. & Navrotsky, A. White Si–O–C Ceramic: Structure and Thermodynamic Stability. *J. Am. Ceram. Soc.* **98**, 242–246 (2015).

26. Leonel, G. J., Mujib, S. B., Singh, G. & Navrotsky, A. Thermodynamic stabilization of crystalline silicon carbide polymer-derived ceramic fibers. *Int. J. Ceram. Eng. Sci.* **4**, 315–326 (2022).

27. Sugie, C., Navrotsky, A., Lauterbach, S., Kleebe, H.-J. & Mera, G. Structure and Thermodynamics of Silicon Oxycarbide Polymer-Derived Ceramics with and without Mixed-Bonding. *Materials* **14**, 4075 (2021).

28. Widgeon, S. *et al.* Nanostructure and Energetics of Carbon-Rich SiCN Ceramics Derived from Polysilylcarbodiimides: Role of the Nanodomain Interfaces. *Chem. Mater.* **24**, 1181–1191 (2012).

29. Niu, M. *et al.* Structure and energetics of SiOC and SiOC-modified carbon-bonded carbon fiber composites. *J. Am. Ceram. Soc.* **100**, 3693–3702 (2017).

30. Kleebe, H.-J. & Blum, Y. D. SiOC ceramic with high excess free carbon. *J. Eur. Ceram. Soc.* **28**, 1037–1042 (2008).

31. Zank, G. A. Preceramic Polymer — Derived Silicon Oxycarbides. in *Silicon-Containing Polymers: The Science and Technology of Their Synthesis and Applications* (eds. Jones, R. G., Ando, W. & Chojnowski, J.) 697–726 (Springer Netherlands, 2000).

32. Bujalski, D. R., Grigoras, S., Lee, W. (nancy), Wieber, G. M. & Zank, G. A. Stoichiometry control of SiOC ceramics by siloxane polymer functionality. *J. Mater. Chem.* **8**, 1427–1433 (1998).

33. Barrios, E. & Zhai, L. A review of the evolution of the nanostructure of SiCN and SiOC polymer derived ceramics and the impact on mechanical properties. *Mol. Syst. Des. Eng.* **5**, 1606–1641 (2020).

34. Ricohermoso, E. I., Klug, F., Schlaak, H., Riedel, R. & Ionescu, E. Electrically conductive silicon oxycarbide thin films prepared from preceramic polymers. *Int. J. Appl. Ceram. Technol.* **19**, 149–164 (2022).

35. Eterigho-Ikelegbe, O., Trammell, R. & Bada, S. Preparation and characterization of ceramic composites from South Africa coal discard. *Constr. Build. Mater.* **302**, 124164 (2021).

36. Development of High Performance Hierarchical Multi-Functional Ceramic Nanocomposites Employing Carbon-Nanotube Nanoforest and Pre-ceramic Polymers - ProQuest (2020).

37. David, L., Bhandavat, R., Barrera, U. & Singh, G. Silicon oxycarbide glass-graphene composite paper electrode for long-cycle lithium-ion batteries. *Nat. Commun.* **7**, 10998 (2016).

38. Bhandavat, R. & Singh, G. Stable and Efficient Li-Ion Battery Anodes Prepared from Polymer-Derived Silicon Oxycarbide–Carbon Nanotube Shell/Core Composites. *J. Phys. Chem. C* **117**, 11899–11905 (2013).

39. Varga, T. *et al.* Thermodynamically Stable SixOyCz Polymer-Like Amorphous Ceramics. *J. Am. Ceram. Soc.* **90**, 3213–3219 (2007).

40. Morcos, R. M. *et al.* Energetics of SixOyCz Polymer-Derived Ceramics Prepared Under Varying Conditions. *J. Am. Ceram. Soc.* **91**, 2969–2974 (2008).

41. Torrey, J. D. & Bordia, R. K. Processing of Polymer-Derived Ceramic Composite Coatings on Steel. *J. Am. Ceram. Soc.* **91**, 41–45 (2008).

42. Navrotsky, A. Progress and New Directions in Calorimetry: A 2014 Perspective. *J. Am. Ceram. Soc.* **97**, 3349–3359 (2014).

43. Michelle Morcos, R. *et al.* Enthalpy of Formation of Carbon-Rich Polymer-Derived Amorphous SiCN Ceramics. *J. Am. Ceram. Soc.* **91**, 3349–3354 (2008).

44. Chen, J. *et al.* Thermodynamic Stability of Low-k Amorphous SiOCH Dielectric Films. *J. Am. Ceram. Soc.* **99**, 2752–2759 (2016).

45. Ionescu, E. *et al.* Polymer-Derived Ultra-High Temperature Ceramics (UHTCs) and Related Materials. in *Ceramics, Glass and Glass-Ceramics: From Early Manufacturing Steps Towards Modern Frontiers* (eds. Baino, F., Tomalino, M. & Tulyaganov, D.) 281–323 (Springer International Publishing, 2021).

46. Guo, X. *et al.* Thermodynamics of formation of coffinite, USiO4. *Proc. Natl. Acad. Sci.* **112**, 6551–6555 (2015).

47. Navrotsky, A. Progress and new directions in high temperature calorimetry. *Phys. Chem. Miner.* **2**, 89–104 (1977).

48. Benning, L. G., Phoenix, V. R., Yee, N. & Tobin, M. J. Molecular characterization of cyanobacterial silicification using synchrotron infrared micro-spectroscopy1 1Associate editor: J. P. Amend. *Geochim. Cosmochim. Acta* **68**, 729–741 (2004).

49. Osswald, J. & Fehr, K. T. FTIR spectroscopic study on liquid silica solutions and nanoscale particle size determination. *J. Mater. Sci.* **41**, 1335–1339 (2006).

50. Lubguban, J. *et al.* Low-k organosilicate films prepared by tetravinyltetramethylcyclotetrasiloxane. *J. Appl. Phys.* **92**, 1033–1038 (2002).

51. Mastalerz, M. & Marc Bustin, R. Electron microprobe and micro-FTIR analyses applied to maceral chemistry. *Int. J. Coal Geol.* **24**, 333–345 (1993).

52. Thomas, P. S., Guerbois, J.-P., Russell, G. F. & Briscoe, B. J. FTIR Study of the Thermal Degradation of Poly(vinyl Alcohol). *J. Therm. Anal. Calorim.* **64**, 501–508 (2001).

53. Chen, Y., Caro, L. d., Mastalerz, M., Schimmelmann, A. & Blandón, A. Mapping the chemistry of resinite, funginite and associated vitrinite in coal with micro-FTIR. *J. Microsc.* **249**, 69–81 (2013).

54. Mendelovici, E., Frost, R. L. & Kloprogge, J. T. Modification of Chrysotile Surface by Organosilanes: An IR–Photoacoustic Spectroscopy Study. *J. Colloid Interface Sci.* **238**, 273–278 (2001).

55. Wu, X. C., Cai, R. Q., Yan, P. X., Liu, W. M. & Tian, J. SiCN thin film prepared at room temperature by r.f. reactive sputtering. *Appl. Surf. Sci.* **185**, 262–266 (2002).

56. Canaria, C. A., Lees, I. N., Wun, A. W., Miskelly, G. M. & Sailor, M. J. Characterization of the carbon–silicon stretch in methylated porous silicon—observation of an anomalous isotope shift in the FTIR spectrum. *Inorg. Chem. Commun.* **5**, 560–564 (2002).

57. Li, H. *et al.* Polymer–ceramic conversion of a highly branched liquid polycarbosilane for SiC-based ceramics. *J. Mater. Sci.* **43**, 2806–2811 (2008).

58. Mahmoudi, M. *et al.* Processing and 3D printing of SiCN polymer-derived ceramics. *Int. J. Appl. Ceram. Technol.* **19**, 939–948 (2022).

59. Colombo, P. *Polymer Derived Ceramics: From Nano-structure to Applications*. (DEStech Publications, Inc, 2010).

60. Sasikumar, P. V. W. *et al.* Polymer derived silicon oxycarbide ceramic monoliths: Microstructure development and associated materials properties. *Ceram. Int.* **44**, 20961–20967 (2018).

61. Li, M., Cheng, L., Ye, F., Wang, Y. & Zhang, C. Tailoring dielectric properties of PDCs-SiCN with bimodal pore-structure by annealing combined with oxidation. *J. Eur. Ceram. Soc.* **40**, 5247–5257 (2020).

62. Saha, A. & Raj, R. Crystallization Maps for SiCO Amorphous Ceramics. *J. Am. Ceram. Soc.* **90**, 578–583 (2007).

63. Sreeja, R., Jayalatha, T. & Devapal, D. Silicon oxycarbide (SiOC) foam from methylphenylpoly(silsesquioxane)(PS) by direct foaming technique. *J. Porous Mater.* (2022).

64. Sun, X., Yang, G., Tian, Z., Zhu, W. & Su, D. In-situ formation of titanium carbide in carbon-rich silicon oxycarbide ceramic for enhanced thermal stability. *J. Eur. Ceram. Soc.* **42**, 6935–6941 (2022).

65. Lee, A. Y. *et al.* Raman study of D* band in graphene oxide and its correlation with reduction. *Appl. Surf. Sci.* **536**, 147990 (2021).

66. Bin Mujib, S., Ribot, F., Gervais, C. & Singh, G. Self-supporting carbon-rich SiOC ceramic electrodes for lithium-ion batteries and aqueous supercapacitors. *RSC Adv.* **11**, 35440–35454 (2021).

67. Sang, Z. *et al.* SiOC nanolayer wrapped 3D interconnected graphene sponge as a high-performance anode for lithium ion batteries. *J. Mater. Chem. A* **6**, 9064–9073 (2018).

68. Greczynski, G. & Hultman, L. C 1s Peak of Adventitious Carbon Aligns to the Vacuum Level: Dire Consequences for Material's Bonding Assignment by Photoelectron Spectroscopy. *ChemPhysChem* **18**, 1507–1512 (2017).

69. Morgan, D. J. Comments on the XPS Analysis of Carbon Materials. *C* **7**, 51 (2021).

70. Zhao, H. *et al.* Synthesis, pyrolysis of a novel liquid SiBCN ceramic precursor and its application in ceramic matrix composites. *J. Eur. Ceram. Soc.* **37**, 1321–1329 (2017).

71. Wang, H., Zhu, W., Sun, X. & Su, D. Preparation of aerogel-like SiOC ceramic with honeycomb structure and its high-temperature performance. *J. Alloys Compd.* **937**, 168438 (2023).

72. Zhang, X. *et al.* Stable high-capacity and high-rate silicon-based lithium battery anodes upon two-dimensional covalent encapsulation. *Nat. Commun.* **11**, 3826 (2020).

73. Kollep, M. *et al.* Tomographic Volumetric Additive Manufacturing of Silicon Oxycarbide Ceramics. *Adv. Eng. Mater.* **24**, 2101345 (2022).

74. Key, T. S., Wilks, G. B. & Cinibulk, M. K. Effect of pendant groups on the mass yield and density of polycarbosilanes during pyrolysis. *J. Am. Ceram. Soc.* **105**, 2403–2410 (2022).

CHAPTER 4

ENERGETICS AND STRUCTURE OF SIC(N)(O) POLYMER DERIVED CERAMICS

Abstract: This study presents new experimental data on the thermodynamic stability of SiC(O) and SCN(O) ceramics derived from the pyrolysis of polymeric precursors: SMP-10 (polycarbosilane), PSZ-20 (polysilazane), and durazane-1800 (polysilazane) at 1200 $^{\circ}$C. There are close similarities in the structure of the polysilazanes, but they differ in crosslinking temperature. High-resolution X-ray photoelectron spectroscopy shows notable differences in the microstructure of all PDCs. The enthalpies of formation from components (SiC, SiO_2, Si_3N_4, and C, $\Delta H^{\circ}_{f, comp}$) show that PDC derived from durazane-1800 displays greatest thermodynamic stability. The results point to increased thermodynamic stabilization with addition of nitrogen to the microstructure of PDCs. Thermodynamic analysis suggests increased thermodynamic drive for forming SiCN(O) microstructures with an increase in the relative amount of SiN_xC_{4-x} mixed bonds and a decrease in silica. Overall, enthalpies of formation suggest superior stabilizing effect of SiN_xC_{4-x} compared to SiO_xC_{4-x} mixed bonds. The results indicate systematic stabilization of SiCN(O) structures with decrease in silicon and oxygen content. The destabilization of PDCs resulting from higher silicon content may reach a plateau at higher concentrations.

4.1 Introduction

Recent technological advances continue to fuel research and development of materials for application under extreme conditions.[1-3] Typically, materials like polymer-derived SiOCs, and SiCNs with high chemical, thermal, and mechanical stability are desired, as they may possess properties comparable to refractory ceramics such as ZrB_2 for which single-source precursors are not commercially available.[4-9] This has led to increase in the popularity of ceramics in various industries, including their application as sensors, mechanical seals, ceramic bearing.[10-12] By convention, ceramic systems are produced by high temperature sintering of powder mixtures. [13-15] Such techniques may not permit swift tunability of the microstructure and dimensions of the ceramics, thus deeming the synthesis process inefficient. [16-19] Other common approaches for synthesis of binary SiC and ternary SiOC systems include chemical vapor deposition and spark plasma sintering. The former is typically preferred for the production of thin films in the semiconductor industry.[20-24] Recently, polymer derived ceramics (PDCs) became a popular synthesis route to overcome conventional limitations.

The low viscosity of preceramic polymers permits their use as precursors for polymer infiltration and pyrolysis (PIP) in the development of ceramic matrix composites (CMCs).[25-28] Recent studies demonstrated tunability in the dimensions of PDCs through utilization of molding techniques.[29] This permits development of polymeric shapes that can be patterned by photolithography, plasma etching, and laser ablation techniques. These shapes can then be pyrolyzed into ceramics. [30, 31] The viscosity of the polymer can be adjusted for extrusion-based 3D printing, and this permits more controlled tunability

of the dimensions of PDCs during processing.[32–34] The ease in tunability of microstructure and dimensions of the ceramics makes the PDC route attractive for large scale application.

Typically, the microstructure of PDCs consists of regions containing X-ray amorphous free carbon and domains of the SiO_xC_{4-x} or SiN_xC_{4-x} mixed bonding network, where $0 \leq x \leq 4$.[35, 36] This complexity makes assessment of structure-property relation challenging.[37–39] Nonetheless, spectroscopic techniques like Fourier transform infrared spectroscopy (FTIR), X-ray photoemission spectroscopy (XPS) and Nuclear Magnetic Resonance (NMR) can be used to determine bonding speciation in the structure of PDCs.[40, 41]

Recently, PDCs fueled the development of commercial and industrial polymeric precursors for the synthesis of high temperature ceramics with tunable compositions.[42–45] Typically, SiC PDCs are less thermally stable than SiCN and SiOCs ceramics, which results in early crystallization of amorphous domains in binary SiC ceramics.[46] Most PDC studies emphasize the application of PDCs,[47, 48] only few investigate the free-energy landscape of ceramic materials derived through the polymeric route. As ceramics derived from industrial precursors increase in popularity, it is essential to understand their structure-property relation, especially the influence of chemistry and structure on the thermodynamic stability of PDCs. Such systematic studies help in the development of a framework for the predictive design and synthesis of PDCs with high thermodynamic stability and desired functionality.

This work investigates three ceramic samples derived from preceramic polymers: SMP-10, PSZ-20, and durazane-1800. We report the synthesis, characterization, and thermochemical analysis of the PDCs synthesized at 1200 °C, in flowing argon atmosphere. Systematic variations in the composition of the samples leads to differences in enthalpies of formation. This permits quantitative assessment of the interconnectivity between the chemistry, structure, bonding, and thermodynamic stability in PDCs. Chemical and structural characterization of the specimen are performed by XPS, high resolution XPS (HR-XPS), Raman spectroscopy, FTIR, and NMR. High temperature oxide melt solution calorimetry is employed to assess thermodynamic stability of the materials. The new compositions explored in this work fill-in gaps of composition-stability relations in PDCs.

4.2 Experimental Methods

4.2.1 Materials

The ceramics were derived from polymeric precursors: SMP-10 (SiC precursor, from Starfire Systems), PSZ-20 (SiCN precursor, from KiON CERASET®), and durazane-1800 (SiCN precursor, from Merck). SMP-10 only contains Si-C-H bonds, while durazane-1800 and PSZ-20 contain additional Si-N bonds. The SiCN precursors have comparable structures, the only difference could be in the ratio of Si-vinyl to Si-CH$_3$ groups. Structure of the oligomers is shown in Figure 1. We did not use crosslinking catalysts during synthesis of the PDCs.
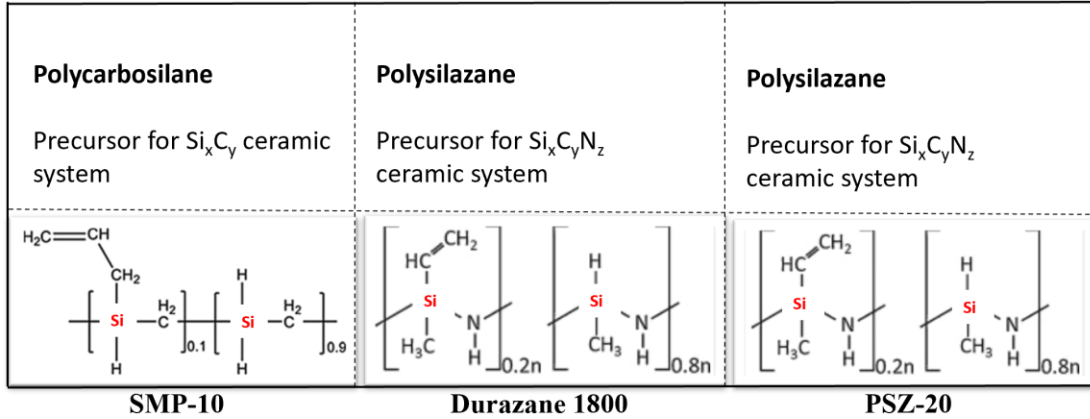
Figure 1. Structure of oligomers used for synthesis of the ceramic powders at 1200 °C, under flowing argon atmosphere.

4.2.2 Crosslinking

The single-source precursors (without the addition of catalyst) were employed for synthesis of the SiC and SiCNs. The as-received precursors were stored in a laboratory refrigerator, the specimens were left to equilibrate at room temperature before crosslinking. Crosslinking was performed in a beaker using a Benchmark hotplate (T_{max} ~300 °C) under magnetic stirring.SMP-10 (polycarbosilane) and PSZ-20 (polysilazane) oligomers were crosslinked into infusible solids at ~250 °C, using ~5 °C/min ramping rate, and 4 hr hold at the final crosslinking temperature, in a glovebox employing nitrogen atmosphere (~0.1 ppm oxygen). Durazane-1800 (polysilazane) has a higher curing temperature (~300 °C). The crosslinked polymers were then processed for pyrolysis. This procedure was decided based on curing requirements (time, atmosphere, raping rate) of the precursors, comparable to experimental parameters used in previous works.[45, 49, 50]

4.2.3 Pyrolysis

A Netzsch STA 409 differential scanning calorimeter cell, using alumina crucibles was employed for pyrolysis of the crosslinked precursors. The instrument permits precise temperature control and a low temperature gradient in samples. The specimens were pyrolyzed under flowing argon (~50 mL/min). The samples were heated from room temperature to 1200 °C at a ramping rate of 2 °C/min. During heating, the samples were held at 400 °C for one hour, this ensures complete crosslinking of the precursor, since the hotplate used for crosslinking can only achieve T_{max} ~300 °C. The ceramics formed during high temperature pyrolysis were then ground into fine powders.

4.2.4 Characterization

XPS experiments were performed by use of a Kratos AXIS Supra+ with a monochromatic Al Kα+ ion beam (beam energy = 1486.6 eV). Raman spectroscopy experiments employed a custom-built multi-wavelengths system with a 532 nm green laser at a power of 74 mW with a 50 X microscope objective. X-ray diffraction (XRD) experiments were performed at ambient conditions by use of a bench-top Bruker D2 powder diffractometer (nickel-filtered CuKα radiation, wavelength= 1.5418 Å). FTIR experiments were performed by employing a bench-top Bruker TENSOR with platinum ATR accessory. Thermal analyses were performed in a LABSYS evo DTA/DSC, under flowing argon atmosphere. Solid-state ^{29}Si MAS NMR spectra were recorded on a Bruker AVANCE 300 spectrometer (B_0 = 7.0 T, $\upsilon_0(^1H)$ = 300.29 MHz, $\upsilon_0(^{29}Si)$ = 59.66 MHz) using a 4 mm Bruker probe and spinning frequency of 12 kHz. Single-pulse ^{29}Si NMR

MAS spectra were recorded with recycle delays of 60 s. Chemical shift values were referenced to tetramethylsilane. The spectra were simulated with the DMFIT program.[51]

4.2.5 Calorimetry

Enthalpies of formation from elements ($\Delta H^{\circ}_{f, elem}$) and components ($\Delta H^{\circ}_{f, comp}$) were obtained by use of thermochemical cycles and enthalpies of dissolution (ΔH°_{dis}) obtained by high temperature oxide melt solution calorimetry at 800 °C. The calorimetric experiments were conducted by use of a commercial twin Calvet type Setaram Alexsys calorimeter, employing molten sodium molybdate ($3Na_2O \cdot 4MoO_3$) as solvent. ~5 mg of sample was weighed using a Mettler Toledo microbalance with 10 μg accuracy. The weighed sample was pressed into a pellet using a 1.5 mm tungsten die. The palletized sample was then dropped from room temperature into the melt in the hot calorimeter for oxidative dissolution. To maintain an oxidative environment, the melt was continuously under oxygen bubbling (40 mL/min). Oxygen flushing (100 mL/min) above the melt was used to expel any gases evolved during dissolution; ensuring a constant environment in the reaction chamber. This is a well-established technique, and more details are provided in previous studies.[52, 53] During dissolution of SiC(O) and SiCN(O) samples, N, and C evolve as N_2, and CO_2, respectively, and Si is oxidized and precipitates as high temperature cristobalite (SiO_2). [40]

The dissolution of SiCN(O) is described below:

$Si_aO_bC_cN_d$ (s, 25 °C) + ((2(a+c)-b)/2) O_2 (g, 800 °C) → a SiO_2 (s, 800 °C) + c CO_2 (g, 800 °C) + d/2 N_2 (g, 800 °C) $\Delta H_{dis, SiCN(O)}$
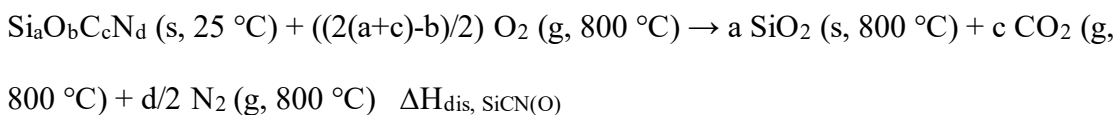
Reaction (2) describes dissolution of SiOC in the melt:

$Si_a O_b C_c$ (s, 25 °C) + ((2(a+c)-b)/2) O_2 (g, 800 °C) → a SiO_2 (s, 800 °C) + c CO_2

(g, 800 °C) $\Delta H_{dis, SiC(O)}$
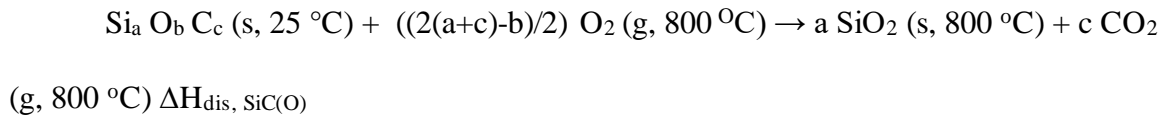
Enthalpy of formation of SiC(O) and SiCN(O) from elements is described by reactions

(3) and (4), respectively:

a Si(s, 25 °C) + b/2 O_2(g, 25 °C) + c C (s, 25 °C) → $Si_a O_b C_c$ (s, 25°C) $\Delta H^\circ_{f, elem}$=?

a Si(s, 25 °C) + c C(s, 25 °C) + b/2 O_2 (g, 25 °C) + d/2 N_2 (g, 25 °C) → $Si_a O_b C_c N_d$ (s,

25°C) (s, 25°C) $\Delta H^\circ_{f, elem}$ =?
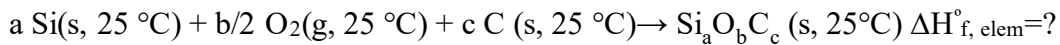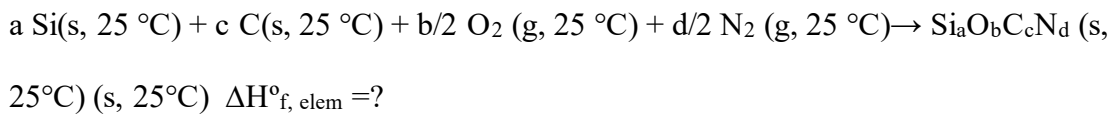
Reactions (5) and (6) describe formation of SiC(O) and SiCN(O) relative to crystalline

components (β-SiC, SiO_2 (cristobalite), β-Si_3N_4 and C (graphite)):

(a-(b/2)) SiC(s, 25 °C) + (b/2) SiO$_2$(s, 25 °C) + (c-(a-(b/2))) C (s, 25 °C)→ Si$_a$O$_b$C$_c$ (s, 25°C) $\Delta H^o_{f, comp}$= ?   `

(5)

(a-(b/2)-(3d/4)) SiC (s,25 °C) + (b/2) SiO$_2$ (s, 25 °C) + (d/4) Si$_3$N$_4$ (s, 25 °C) + (c-(a-(b/2)-(3d/4))) C (s, 25 °C) → Si$_a$O$_b$C$_c$N$_d$ (s, 25°C) (s, 25°C) $\Delta H^o_{f, comp}$ =?

(6)
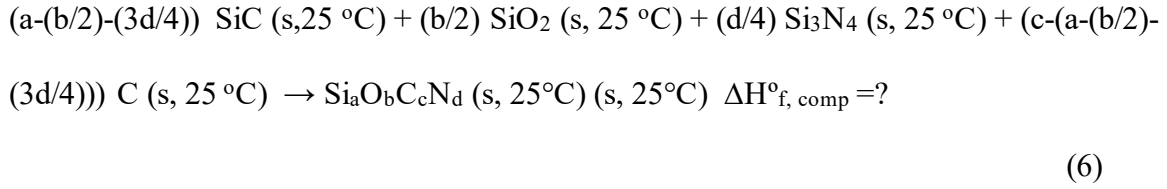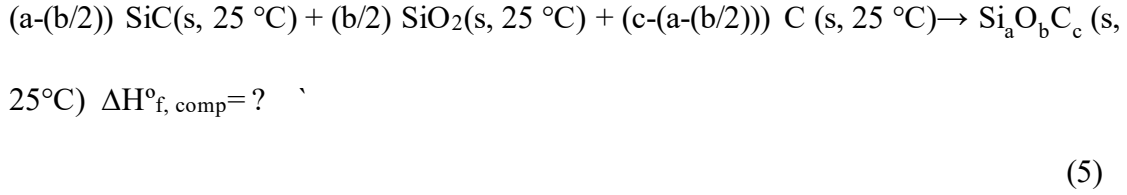
By identifying the initial and final state of the system during dissolution, we employed thermodynamic cycles (Tables 1-4) for thermochemical calculation of enthalpies of formation.

Table 1. Thermochemical cycle for calculation of enthalpy of formation of SiCN(O) from elements $\Delta H^\circ_{f, elem.}$

Enthalpies of formation from the elements ($\Delta H_{f, elem}$)	ΔH (kJ/mol)
a Si(s, 25 °C) + c C(s, 25 °C) + b/2 O$_2$ (g, 25 °C) + d/2 N$_2$ (g, 25 °C)→ Si$_a$O$_b$C$_c$N$_d$ (s, 25°C) (s, 25°C) $\Delta H^o_{f, elem}$ =?	
Si$_a$O$_b$C$_c$N$_d$ (s, 25 °C)+ ((2(a+c)-b)/2) O$_2$ (g, 800 °C) → a SiO$_2$ (s, 800 °C) + c CO$_2$ (g, 800 °C) + d/2 N$_2$ (g, 800 °C)	$\Delta H_{dis, SiCN(O)}$
Si (s, 25 °C) + O$_2$ (g, 800 °C) → SiO$_2$ (s, 800 °C)	ΔH_2 = -883.13 ± 2.1
C (s, 25 °C) + O$_2$ (g, 800 °C) → CO$_2$ (g, 800 °C)	ΔH_3 = -381.35 ± 0.13
O$_2$ (g, 25 °C) → O$_2$ (g, 800 °C)	ΔH_4= 25.34 ± 0.10
N$_2$ (g, 25 °C) → N$_2$ (g, 800 °C)	ΔH_5= 24.77 ± 0.10

$\Delta H^o_{f, elem} = - \Delta H_{dis, SiCN} + a\Delta H_2 + c\Delta H_3 + (b/2)\Delta H_4 +$ $(d/2)\Delta H_5$	$\Delta H^o_{f, elem}$

Table 2. Thermochemical cycle for calculation of enthalpy of formation of SiCN(O) from components $\Delta H^\circ_{f, comp}$.

Enthalpies of formation from components ($\Delta H_{f, comp}$)	ΔH (kJ/mol)
(a-(b/2)-(3d/4)) SiC (s,25 ºC) + (b/2) SiO$_2$ (s, 25 ºC) + (d/4) Si$_3$N$_4$ (s, 25 ºC) + (c-(a-(b/2)-(3d/4))) C (s, 25 ºC) $\rightarrow$ Si$_a$O$_b$C$_c$N$_d$ (s, 25°C) (s, 25°C) $\Delta H^o_{f, comp}$ =?	
Si$_a$O$_b$C$_c$N$_d$ (s, 25 °C)+ ((2(a+c)-b)/2) O$_2$ (g, 800 °C) $\rightarrow$ a SiO$_2$ (s, 800 °C) + c CO$_2$ (g, 800 °C) + d/2 N$_2$ (g, 800 °C)	$\Delta H_{dis, SiCN(O)}$
SiO$_2$ (s, 25 ºC) $\rightarrow$ SiO$_2$ (s, 800 ºC)	ΔH_2= 50.1± 0.10
SiC (s, 25 ºC) + 2O$_2$ (g, 800 ºC)$\rightarrow$ SiO$_2$ (s, 800 ºC) + CO$_2$ (g, 800 ºC)	ΔH_3 = -1192.28 ± 2.15
Si$_3$N$_4$ (s, 25 ºC) + 3O$_2$ (g, 800 ºC) $\rightarrow$ 3SiO$_2$ (s, 80 0 ºC) + 2N$_2$ (g, 800 ^{0}C)	ΔH_4= -1770.95 ± 4.0
C (s, 25 ºC) + O$_2$ (g, 800 ºC) $\rightarrow$ CO$_2$ (g, 800 ºC)	ΔH_5 = -381.35 ± 0.13
$\Delta H^o_{f, comp}$ = -$\Delta H_{dis, SiCN(O)}$ + (b/2)ΔH_2 + (a-(b/2)-(3d/4))ΔH_3 + (d/4)ΔH_4 + (c-(a-(b/2)-(3d/4)))ΔH_5	$\Delta H^o_{f, comp}$

Table 3. Thermochemical cycle for calculation of enthalpy of formation of SiC(O) from elements $\Delta H^{\circ}_{f, elem}$.

Enthalpies of formation from the elements ($\Delta H_{f, elem}$) a Si(s, 25 °C) + b/2 O$_2$(g, 25 °C) + c C (s, 25 °C)→ Si$_a$O$_b$C$_c$ (s, 25°C) $\Delta H^{\circ}_{f, elem}$=?	ΔH (kJ/mol)
Si$_a$ O$_b$ C$_c$ (s, 25 °C) + (((2a) + (2c)-b))/2) O$_2$ (g, 800 °C) → a SiO$_2$ (s, 800 °C) + c CO$_2$ (g, 800 °C)	$\Delta H_{dis, SiOC}$
Si (s, 25 °C) + O$_2$ (g, 800 °C) → SiO$_2$ (s, 800 °C)	ΔH_2 = -883.13 ± 2.1
C (s, 25 °C) + O$_2$ (g, 800 °C) → CO$_2$ (g, 800 °C)	ΔH_3 = -381.35 ± 0.13
O$_2$ (g, 25 °C) → O$_2$ (g, 800 °C)	ΔH_4= 25.34 ± 0.10
$\Delta H^{o}_{f, elem}$ = - $\Delta H_{dis, SiOC}$ + a ΔH_2 + c ΔH_3 + (b/2) ΔH_4	$\Delta H^{o}_{f, elem}$

Table 4. Thermochemical cycle for calculation of enthalpy of formation of SiC(O) from components $\Delta H^{\circ}_{f, comp}$.

Enthalpies of formation from components ($\Delta H_{f, comp}$) (a-(b/2)) SiC(s, 25 °C) + (b/2) SiO$_2$(s, 25 °C) + (c-(a- (b/2))) C (s, 25 °C)→ Si$_a$O$_b$C$_c$ (s, 25°C) $\Delta H^{o}_{f, comp}$= ?	ΔH (kJ/mol)
Si$_a$ O$_b$ C$_c$ (s, 25 °C) + (((2a) + (2c)-b)/2) O$_2$ (g, 800 °C) → a SiO$_2$ (s, 800 °C) + c CO$_2$ (g, 800 °C)	$\Delta H_{dis, SiOC}$
SiO$_2$ (S, 25 °C) → SiO$_2$ (s, 800 °C)	ΔH_2 = 50.1± 0.10
SiC (S, 25 °C) + 2O$_2$ (g, 800 °C) → SiO$_2$ (s, 800 °C) + CO$_2$ (g, 800 °C)	ΔH_3 = -1192.28 ± 2.15

C (S, 25 °C) + O$_2$ (g, 800 °C) → CO$_2$ (g, 800 °C)	ΔH_4 = -381.35 ± 0.13
$\mathbf{\Delta H^o_{f,\,comp}}$ = -$\mathbf{\Delta H_{dis,\,SiOC}}$ + (b/2) ΔH_2 + (a-(b/2)) ΔH_3 + (c-(a-(b/2))) ΔH_4	$\mathbf{\Delta H^o_{f,\,comp}}$

4.3 Results and discussion

FTIR experiments permit identification of functional groups in the structure of crosslinked polymeric precursors and corresponding ceramics. The results in Figure 2a confirm presence of organic groups in the structure of crosslinked precursors. The functional groups in the spectra are consistent with structure of the oligomers. The intensity of peaks in the spectra is proportional to the relative amounts of the corresponding bonds. The crosslinked polysilazanes (PSZ-20 and durazne-1800) have comparable structures, and the higher intensity of Si-CH$_2$-Si stretching vibrational peaks (1020 cm^{-1}) in durazane-1800 may indicate higher relative amounts of Si-CH$_2$ bonds per unit volume.[54, 55] Figure 2b summarizes results from FTIR of the PDCs pyrolyzed at 1200 °C. The spectra in Figure 2b suggest absence of C-H, N-H and Si-H bonds, which is consistent with evolution of H as organics during high temperature pyrolysis. The results in Figure 2b further point to the presence of C=C (~1600 cm^{-1}) and maybe some Si-O-Si (~1060 cm^{-1}) bonds in the samples.[56, 57] Additionally, Si-N bonds are identified in PDCs derived from durazane-1800 and PSZ-20. PDCs derived from SMP-10 yield SiC ceramics, while each PSZ-20 and durazane-1800 are precursors for SiCN. It is well known that it is difficult to obtain oxygen-free SiCNs and SiCs, especially since it is in part an impurity in the precursors.[58, 59] The peaks assigned to Si-O bonds in the structure

of the polymeric precursors and corresponding PDCs may indicate oxygen contamination during processing, therefore, to acknowledge presence of oxygen we refer to the pyrolyzed materials as SiC(O) and SiCN(O) ceramics.
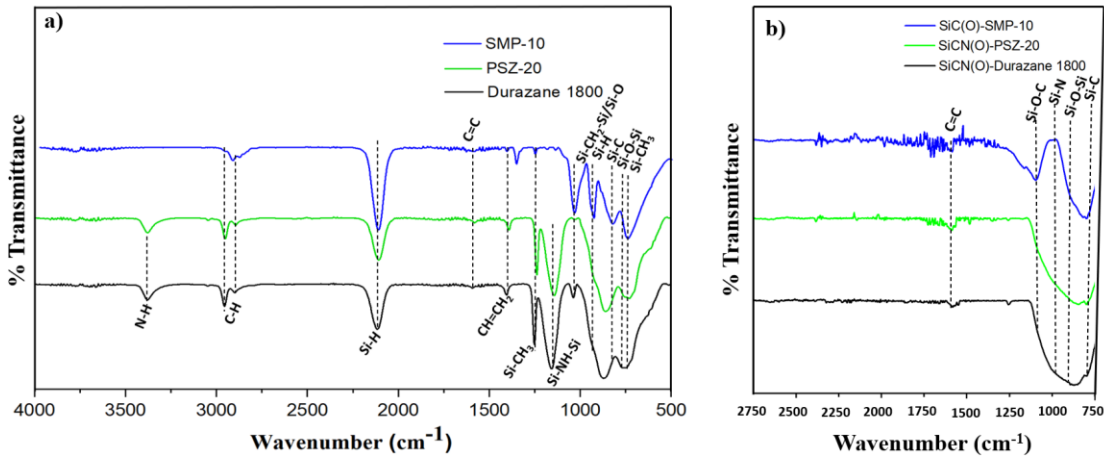
Figure 2. FTIR spectra of (a) crosslinked polymeric precursors, SMP-10, PSZ-20, and durazane-1800 (b) PDCs derived from preceramic polymers at 1200 $^{\circ}$C, in flowing argon.

Thermogravimetric (TG) and differential scanning calorimetric (DSC) curves during pyrolysis are shown in Figure 3. To account for buoyancy effect of the carrier gas, baseline TG-DSC signal (empty crucible) was subtracted from the sample run. All precursors undergo ~76 wt % loss between ambient temperature and 1200 $^{\circ}$C. Overall, the crosslinked precursors display acceptable ceramic yields of about 76 %, even without the use of crosslinking catalysts, and this is in good agreement with previous work.[50] The exothermic peaks near 200 $^{\circ}$C likely correspond to further crosslinking of precursors.[60] In these samples, the initiation of polymer to ceramic conversion may be indicated by the exothermic DSC peak near 400 $^{\circ}$C.[61] Durazane-1800 displays the highest crosslinking

temperature (~ 300 °C) and lowest ceramic yield relative to the crosslinked precursor

(~75.8 wt%). In contrast, PSZ-20 crosslinked polymers display lower thermal stability

with an onset decomposition temperature of ~250 °C. Figure 3 further shows that SMP-

10 (polycarbosilane) has the greatest ceramic yield and lowest crosslinking temperature

(~200 °C). The crosslinking temperature suggested from DSC curves (Figure 3) are

consistent with initial crosslinking temperatures of the oligomers, which point to PSZ-20

as a lower-temperature curing polysilazane. These results show significant differences in

the thermal behavior of crosslinked polymers, even in polysilazanes (PSZ-20 and

durazane-1800) with comparable chemical structures (see Figure 1 and Figure 2).

Overall, major changes in mass conclude near 900 °C, however, SMP-10 undergoes

minor secondary exothermic mass loss between 900 and 1150 °C, which may indicate

carbothermal reduction of silica networks (SiO_2) by free carbon and this results in the

crystallization of SiC domains.[62, 63]
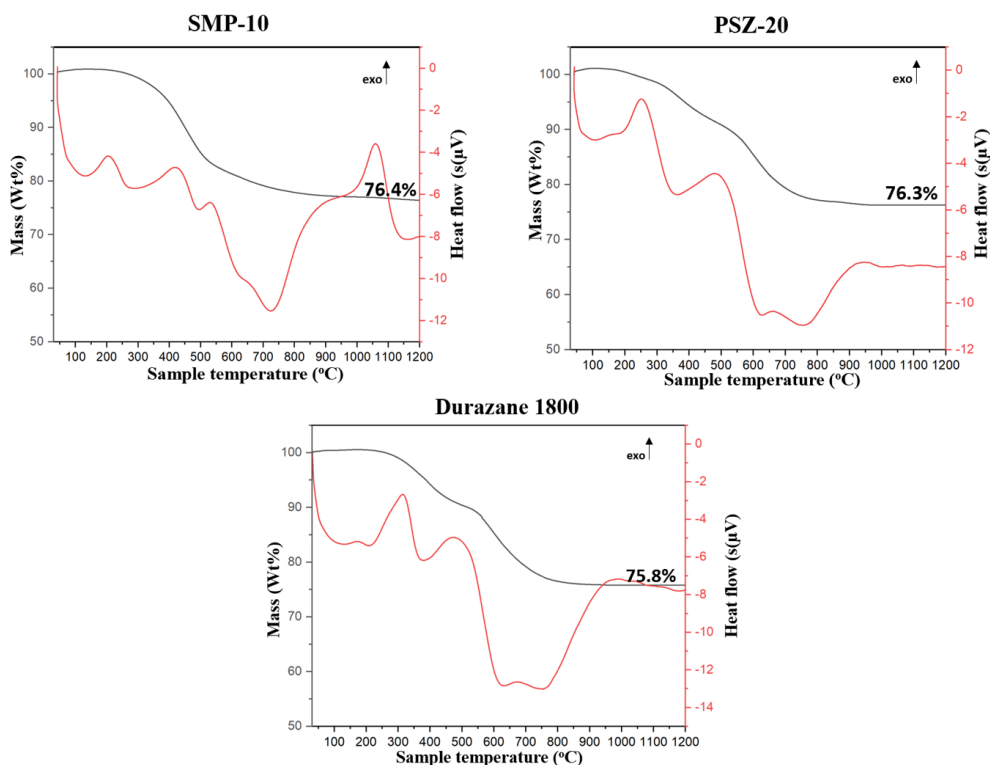
Figure 3. TG-DSC curves of crosslinked precursors during pyrolysis (from ambient conditions to 1200 °C), at ramp rate of 2 °C/min, in flowing argon.

XRD permits identification of crystallization and can help determine structural differences in crystalline materials including some SiC PDC fibers.[40] Typically, PDCs pyrolyzed at lower temperatures are amorphous.[64, 65] At high temperatures, crystallization in PDCs is promoted by carbothermal reduction.[66–68] The XRD patterns of the PDCs are summarized in Figure 4 and the results point to growth of poorly crystalline β-SiC grains in the SiC(O) derived from SMP-10. This may indicate carbothermal reduction, which results in phase separation and crystallization of amorphous domains.[66, 69, 70] The XRD patterns suggest amorphous microstructures in SiCN(O) samples derived from PSZ-20 and durazane-1800. The results summarized in Figure 4 suggest superior

110

resistance to crystallization in SiCN(O)s than in SiC(O)s PDCs, which is expected, as addition of N to SiC structures has been found to result in higher persistence to thermal degradation and crytalization.[46] Differences in the crystallization temperature/rates of these materials likely result from kinetic rather than thermodynamic factors, since in general PDCs evolve towards thermodynamically more stable structures with increasing pyrolysis temperature [52, 64, 71–73] Some kinetic factors for consideration may include difference in the activation energy for carbothermal reduction of distinct oxides and nitrides domains, as well as dissimilarities in the diffusion rate of different species.[64, 71]
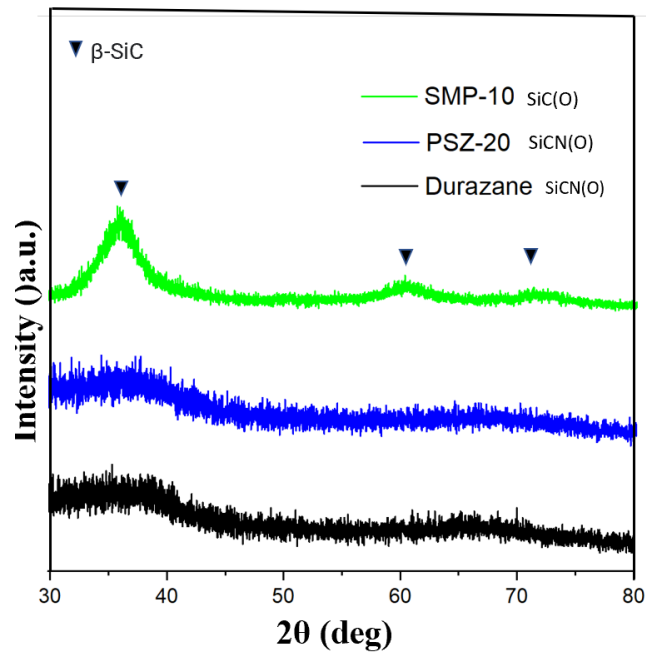
Figure 4. XRD patterns show growth of semicrytalline β -SiC in SiC(O) synthesized from SMP-10 at 1200 °C. The SiCN(O) samples derived from PSZ-20 and durazane-1800 are X-ray amorphous.

The types of carbon in the microstructure of the ceramic powders can be identified by Raman spectroscopy. The spectra are collected between 900 and 1900 Raman shift (cm^{-1}) and the results are summarized in Figure 5. D (~1330 cm^{-1}) and G (~1600 cm^{-1}) bands correspond to presence of sp^2-hybridized disordered and graphitic-like carbons, respectively. [30, 40] The integrated intensity of D (I_D) and G (I_G) bands at full width at half maximum (FWHM) permit assessment of the D (I_D)/G (I_G) ratio of bonding speciation.[52] It appears that all samples contain greater amounts of disordered (relative to graphitic) carbons. D" (1490–1504 cm^{-1}) and T (1204–1232 cm^{-1}) bands, which are obtained from curve fitting, indicate presence of significant amounts of amorphous carbon and sp^2-sp^3 bonds, respectively, in the microstructure of all specimens. For the SiCN(O)s, the sample derived from durazane-1800 displays largest integrated intensities of D" and T (relative to G and D) bands. [30, 74, 75] This points to lower relative amount of amorphous free carbon and sp^2-sp^3 bonds in SiCN(O) derived from PSZ-20.
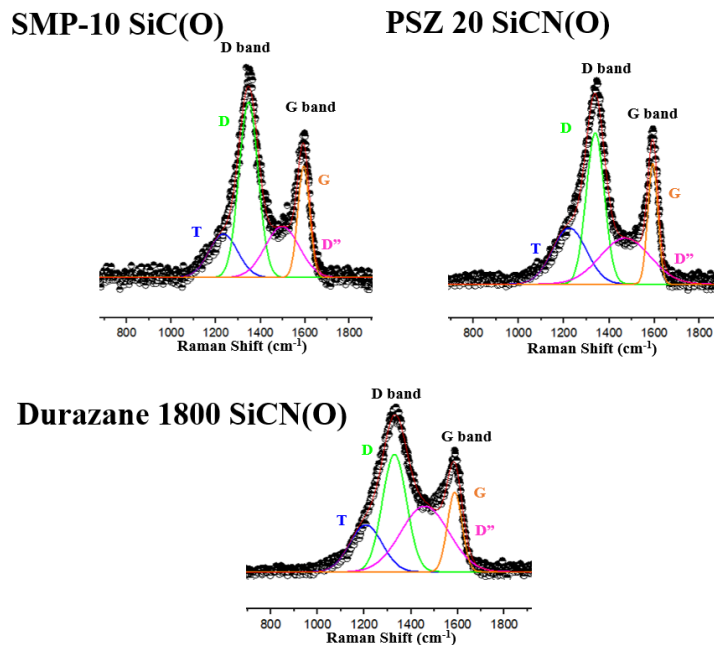
Figure 5. Raman spectra of PDC powders pyrolyzed at 1200 °C.

XPS is efficient for identification of different Si $2p$, C $1s$, O $1s$, and N $1s$ bonds, however, it is challenging to identify different SiN_xC_{4-x} bonds by XPS alone. NMR is powerful for characterization of short range order in ceramics, and analysis of the spectra permits differentiation of SiN_xC_{4-x} mixed bonding environments in PDCs.[52, 65, 74] Typically, ^{29}Si MAS NMR peak shifts are associated with different coordination environments (oxygen in SiO_xC_{4-x} or nitrogen in SiN_xC_{4-x} mixed bonds).[76] ^{29}Si MAS NMR experiments are performed on all samples and results are shown in Figure 6.

The spectrum of the SiC(O) specimen derived from SMP-10 shown in Figure 6, is characterized by a relatively broad peak centered around -18 ppm that confirms presence of SiC domains and is consistent with poor crystallinity (The breadth of NMR peaks increases with loss of crystallinity).[77, 78] The NMR spectrum of SMP-10 does not suggest presence of significant amount of SiO_4 bonds, which contrasts results from XPS (discussed in the next section) and could suggest greater sensitivity of XPS to SiO_4 sites (or may indicate surface effects). The ^{29}Si MAS NMR spectra of samples derived from PSZ-20 and durazane-1800 are characterized by a relatively broad signal centered around -30 ppm attributed to signature distribution of SiN_xC_{4-x} ($0 \leq x \leq 4$) units.[79] Appropriate peak fitting (with SiC_3N, SiC_2N_2, $SiCN_3$ and SiN_4 signals at $\square(^{29}Si) = -$1ppm, -16 ppm, -32 ppm and – 49 ppm respectively) permits identification of possible Si coordination number and bonding environments. The integrated area under each NMR peak is proportional to the amount of each environment it represents within the microstructure.[80] As expected, the results in Figure 6 suggest presence of significant amounts of Si_3N_4 domains (from SiN_4 bonds) in the SiCN(O) PDCs. It appears that the samples have significant amounts of tetrahedrally coordinated Si in SiN_2C_2, SiN_3C, and

SiN_4 environments, which are typical of localized mixed bonding domains in PDCs.[78, 81] Mixed bonds can exist as isolated units, connected two or three dimensional networks or at the interface between domains (C, Si_3N_4, SiC).[74, 78] The convolutions further suggest presence of only minor amounts of $SiNC_3$ mixed bonds in the samples. Overall, the relative amount of specific mixed bonds (from convolutions) appears to increase with greater N and less C per formula unit, as SiC_3N (~2%) < SiN_4 (~24%) < SiN_3C (~25%) < SiN_2C_2 (~40%) (see Figure 6). The minor peak near ~ -110 ppm is observed across all samples, which may indicate presence of SiO_4 species (~9% in SiCN(O) systems) in all the specimens,[81] and this is consistent with results from HR-XPS. The results do not suggest significant difference in the relative amounts of different SiN_xC_{4-x} bonds across the SiCN(O) specimens.

Typically, ^{29}Si CPMAS NMR can identify H termination in mixed bonding domains, especially in samples pyrolyzed at lower temperatures (H-rich samples).[81] However, samples pyrolyzed above 1200 °C typically have very low H content, which makes identification of H-terminated mixed bonds impractical.[78]
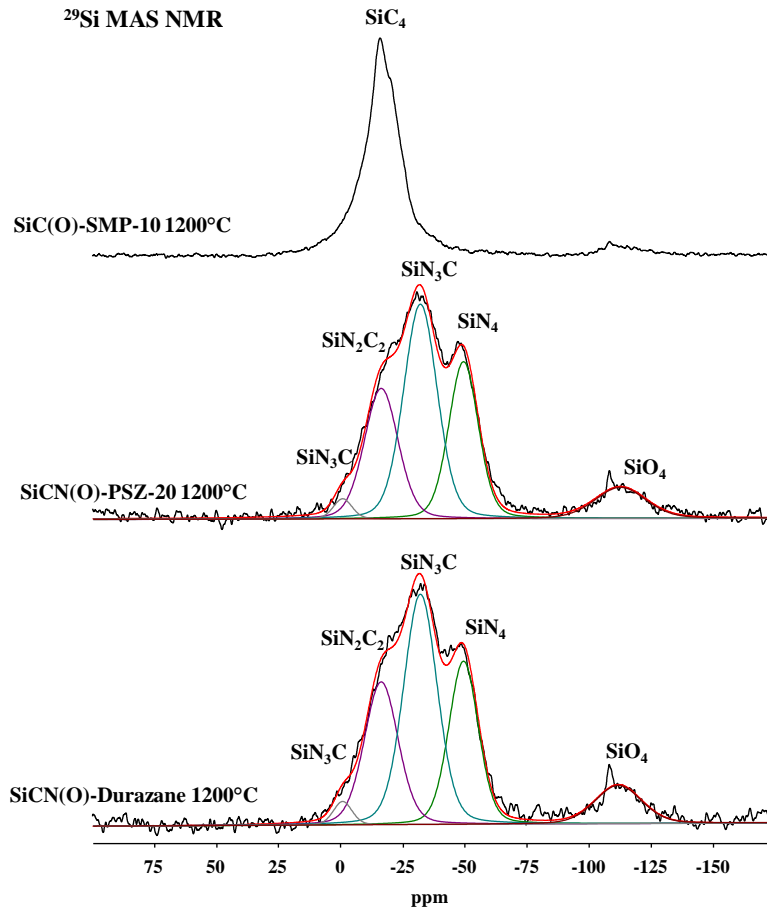
Figure 6. ^{29}Si MAS NMR of SiC(O) derived SMP-10 as well as SiCN(O)s derived from PSZ-20 and durazane-1800 at 1200°C, in flowing argon atmosphere.

The bonding speciation in the microstructure of the PDCs can be identified by HR-XPS. The deconvolutions are obtained by performing appropriate curve fitting, and the area under the curve is proportional to the relative amount of corresponding bonding character. HR-XPS curves of the specimens are summarized in Figure 7. C *1s* convolutions confirm presence of C-C (~285 eV), C-O (~289 eV), and C-N (~288.30 eV) bonds in the PDCs.[82–84] The presence of C-C bonds is consistent with results from Raman spectroscopy (see Figure 5) and may correspond to free carbon and/or C-C terminated

115

mixed bonding domains. It is probable that C=O, C-O, and C-N convolutions correspond to bonding character in the free carbon phase.

The Si *2p de*convolutions identify presence of Si-C (~101 eV), Si-O (~103 eV), and SiO_4 (~104 eV) bonds in all PDCs. [84, 85] The results further confirm presence of Si-N (~101.8 eV) bonds in the SiCN(O) specimens.[84] Typically, in mixed bonding, C is only bonded to Si or to another C. Therefore, SiO_4 bonds may correspond to formation of amorphous silica (SiO_2) domains. Only a small portion of Si-C and Si-O convolutions are expected to represent SiO_xC_{4-x} mixed bonding networks in the microstructure of the PDCs, as their respective NMR peaks are not observed (see Figure 6). It is likely that Si-C and Si-O bonds mostly include contributions from SiC (silicon carbide) and SiO_2 amorphous domains, respectively. Unfortunately, the Si-O and Si-C bonds from mixed bonds cannot be differentiated from those present in the corresponding stoichiometric domains. Additionally, Si-N bonds may represent formation of amorphous Si_3N_4 and/or SiN_xC_{4-x} mixed bonding domains. The results in Figure 7 may indicate that the SiC(O) sample contains larger relative amount of SiC domains (from Si-C convolutions) compared to SiCN(O)s. It is also apparent that SiCN(O) derived from durazane-1800 displays greatest amounts (relative to Si-O bonds) of Si_3N_4 and/or SiN_xC_{4-x} mixed bonding domains compared to the SiCN(O) specimen derived from PSZ-20. It should be noted that C 1*s* spectra suggest only minor amounts of N bonded to C in SiCN(O) samples, and this may imply that there are two chemical states in N 1*s*, specifically, N-Si and N-C. However, the sharp peak in the N 1*s* spectra of SiCN(O)s suggests negligible amounts of N-C relative to N-Si bonds. This would be consistent with scarce N-termination in the free carbon phase, relative to stoichiometric domains and mixed bonds.
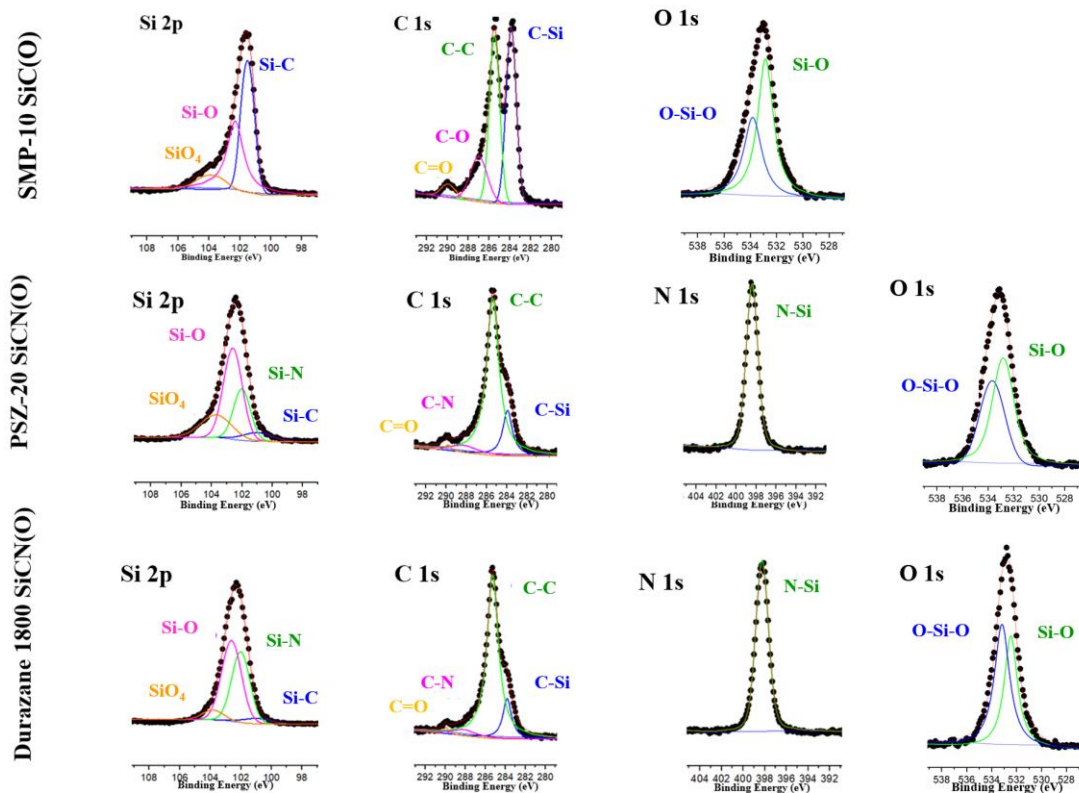
Figure 7. HR XPS of SiC(O) and SiCN(O) PDCs derived from SMP-10, PSZ-20, and durazane-1800.

4.3.1 Elemental analysis

Thermochemical calculations of enthalpies of formation require well characterized compositions. XPS is an efficient tool for characterization of PDCs pyrolyzed at high temperatures, when H from residual organics is scarce. In this work we employ XPS (Si *2p*, C *1s*, O *1s*, and N *1s*) survey scans for quantitation of Si, C, N, and O content in the samples. The results from survey scans confirm significant Si, C, and O content in all samples, and additional N is present in the microstructure of SiCN(O) PDCs. The calculated phase assemblages suggest greater relative amount of free carbon

in the SiC(O) compared to SiCN(O) ceramics. The results are summarized in Table 5. There are similarities in compositions derived from PSZ-20 and durazane-1800. The minor compositional differences may result from dissimilarities in curing temperature and the ratio of Si-vinyl to Si-methyl groups in the oligomers.

Table 5. Elemental analysis of SiOC samples from XPS survey scan. C_{free}/C is determined from C1s convolutions, by assuming that all C-C bonds are part of free carbon phase, and not mixed bonds.

Elements (at.%)							
SiC(N)(O) Precursor	Pyrolysis temperature (^oC)	Ideal PDC System	C	N	O	Si	C_{free}/C (%)
SMP-10	1200	SiC	48.24	-	17.90	33.85	40
PSZ-20	1200	SiC(N)	33.50	15.77	15.51	35.22	74.74
Durazane-1800	1200	SiC(N)	34.63	16.63	12.77	35.97	78.32

4.3.2 Systematics of Thermodynamic Stabilization in PDCs

The discussion that follows addresses thermodynamic stabilization in SiOC and SiOCN ceramic systems. Samples derived from the industrial precursors (PSZ-20, SMP-10, and durazane-1800) permit investigation of SiOCN compositions outside the range of structures previously explored by high temperature calorimetry. Thees data are valuable

additions to the thermodynamic database of PDCs previously investigated. The results

validate past knowledge on structure-stability trends in PDCs, and further suggest

possible systematic differences in the stabilizing effect of different mixed bonding

environments (oxygen or nitrogen). Additionally, this work identifies trends/correlations

between elemental content (composition) and thermodynamic stability of the ceramics.

Table 6. Summary of enthalpies of dissolution (ΔH_{dis}), enthalpies of formation from elements ($\Delta H^o_{f, elem}$), and enthalpies of formation from components ($\Delta H^o_{f, comp}$), of samples derived from industrial precursors.

Sample	Composition $Si_A O_B C_C N_D$ (A+B+C+D=1)	ΔH_{dis} (kJ/mol)	$\Delta H^o_{f, elem}$ (kJ/mol)	$\Delta H^o_{f, comp}$ (kJ/mol)
SMP-10	$Si_{0.34}O_{0.18}C_{0.48}$	-461.12 ± 4.12	-20 ± 4.63	80.12 ± 4.65
PSZ-20	$Si_{0.35}O_{0.16}C_{0.33}N_{0.16}$	-352.51 ± 0.98	-78.55 ± 2.32	33.89 ± 4.66
Durazane-1800	$Si_{0.36}O_{0.13}C_{0.35}N_{0.17}$	-362.31 ± 0.56	-85.09 ± 2.18	21.4 ± 4.58

The results from thermodynamic analysis are summarized in Table 6. The

enthalpies of dissolution (ΔH_{dis}) are most exothermic for the SiC(O) sample. This results

from highly exothermic enthalpies for the oxidation of greater amounts of C and Si, and

has been seen in previous studies.[52, 72, 81] Enthalpies of formation permit quantitation of

relative thermodynamic stabilities. The results in Table 6 show that enthalpies of

formation from elements ($\Delta H^{\circ}_{f, elem}$) are most exothermic for SiCN(O) PDCs compared to the SiC(O) specimen. The enthalpy of formation from elements includes the energetics for forming stoichiometric compounds (SiO_2, SiC, Si_3N_4) from the elements and are more exothermic than enthalpy of formation from those crystalline components. The entropy of formation from elements has a negative (destabilizing) contribution arising from confining N_2 and O_2 gas into stoichiometric solids. However, the highly exothermic enthalpies of formation from elements overcome the entropy effect and stabilize the structures. Considering the enthalpy of formation of the $Si_aO_bC_cN_d$ specimens from binary crystalline components SiO_2, SiC, Si_3N_4 ($\Delta H^{\circ}_{f, comp}$) allows one to focus on the interdomain interactions in the microstructure. Across all structures studied by calorimetry, each with a different composition, enthalpies from components range from -128 to +20 kJ/mol (see Table 7), note that results in Table 7 are in terms of per one mol of Si (kJ/mol Si).[40, 52, 86, 86–88] Since PDCs are amorphous, their entropies of formation from crystalline components are expected to be positive, arising from disorder. Such positive entropy effects add to the stabilization relative to binary crystalline components. Thus most PDCs have negative free energies of formation from the binary crystalline components and are thermodynamically stable with respect to an isocompositional mixture of these components and would not decompose to them. However, decomposition because of carbothermal reduction (under reducing conditions) or oxide formation (under oxidizing conditions) limit their stability at high temperature. Structural and chemical characterization in this study point to notable differences in the chemistry and structure of SiC(O) compared to the SCN(O), as expected. The microstructural modifications result in significant difference in the thermodynamic drive for the

formation of their corresponding structures (see Table 6). This permits identification of the influence of chemical species (Si, C, O, or N) on structure and stability. The results in Table 6 suggest that SiC(N)(O) structures, with alloyed amounts of both O and N (N/O < 2) can be more stable than SiC(O) specimens. Previous studies on PDC fibers and powders also point to greater stability of SiOCN samples with alloyed amounts of O and N species in the structure.[40, 87] The increased stabilization likely results from inclusion of both SiN_xC_{4-x} and SiO_xC_{4-x} mixed bonds in the PDCs.

Table 7. Summary of enthalpies of formation of amorphous SiOC and SiOCN PDCs, synthesized between 800 and 1200 °C. This data summarizes thermochemical analysis of some compositions previously investigated by high temperature calorimetry. The enthalpies are in terms of per one mol of Si.

$(Si_aO_bC_cH_dN_e)$ compositions where a+b+c+d+e=1							
Sample name (as referred in the cited literature)	a	b	c	d	e	Pyrolysis temperature (deg C)	$\Delta H^o_{f, comp}$ (kJ/mol of Si)
S1	0.364	0.513	0.123	0	0	1200	-54.4[89]
S2	0.295	0.44	0.265	0	0	1200	-24.7[89]

S3	0.271	0.374	0.355	0	0	1200	-126.2[89]
S4	0.278	0.278	0.444	0	0	1200	-64.0[89]
S5	0.259	0.238	0.503	0	0	1200	-495.0[89]
W1B	0.35	0.42	0.231	0	0	1200	-78.8[90]
W2B	0.364	0.378	0.258	0	0	1200	-111.0[90]
W3B	0.299	0.311	0.386	0	0	1200	-111.7[90]
W4B	0.235	0.209	0.556	0	0	1200	-65.9[90]
SiOC	0.314	0.467	0.22	0	0	1200	-68.5[91]
S1200	0.307	0.461	0.232	0	0	1200	-16.0[92]
CS1200	0.085	0.144	0.771	0	0	1200	84.1[92]
Si	0.345	0.523	0.088	0.044	0	1200	-60.9[91]
PhSiO$_{1.5}$_SG	0.112	0.227	0.47	0.191	0	800	-22.3[52]
HQ4_SG	0.283	0.588	0.078	0.052	0	1100	-11.3[52]
PhSiO$_{1.5}$_SG	0.142	0.23	0.568	0.06	0	1100	-97.9[52]
SiOC	0.313	0.473	0.213	0	0	1100	-48.5[93]
GM35	0.096	0.041	0.346	0.273	0.244	800	-441.7[81]
GM35	0.134	0.015	0.435	0.13	0.285	1100	-192.5[81]
HN1	0.121	0.02	0.594	0.119	0.149	800	-264.5[81]
HN1	0.126	0.019	0.671	0.034	0.151	1100	-205.5[81]
S3	0.204	0	0.556	0	0.239	1100	-13.7[94]

| Black | 0.318 | 0.485 | 0.192 | 0.005 | 0 | 1100 | -13[95] |

An important factor in the thermodynamic stabilization of PDC structures includes mixed bonding which can occur at the interface of stoichiometric domains (Si_3N_4, SiO_2, C, and SiC). [74, 78] Previous investigations show that more mixed bonding can stabilize structures by as much as 20 kJ/mol. Nonetheless, there is still a lingering question whether SiN_xC_{4-x} and SiO_xC_{4-x} mixed bonds differ significantly in their stabilizing effect. In this work, the Si $2p$ convolutions and NMR spectra confirm presence of significant amounts of SiN_xC_{4-x} mixed bonds in SiCN(O) specimens, but not in the SiC(O) derived from SMP-10. There is systematic thermodynamic stabilization of the PDCs with addition of SiN_xC_{4-x} bonds, as Table 6 highlights the lower thermodynamic stability of the SiC(O) specimen. This indicates significant (~60 kJ/mol) enthalpic stabilization from addition of SiN_xC_{4-x} mixed bonds to SiC(O) systems, which is ~10 kJ/mol higher than stabilization from addition of SiO_xC_{4-x} mixed bonds to SiC PDC fibers.[40] Furthermore, Si $2p$ XPS convolutions of the SiCN(O) samples (see Figure 6) also suggest the greatest relative amount of SiO_2 and/or SiO_xC_{4-x} (from Si-O bonds) as well as the lowest amount of Si_3N_4 and/or SiN_xC_{4-x} mixed bonds (from Si-N bonds) in the SiCN(O) derived from PSZ-20 (compared to durazane-1800). The enthalpies of formation in Table 6 highlight the lower stability of the SiCN(O) structure derived from PSZ-20 (compared to durazane-1800). Overall, the results may indicate a greater stabilizing effect from SiN_xC_{4-x} compared to SiO_xC_{4-x} mixed bonds. This could imply significant stabilization of quaternary SiOCN structures by tuning the ratio of SiO_xC_{4-x} to SiN_xC_{4-x} mixed bonds. It is likely that there exists an optimum ratio that promotes greatest stability.

The SiCN(O) specimens in Table 6 are outside the compositional range of structures previously studied. This permits assessment of systematics in the correlation between elemental content and thermodynamic stability in PDCs. This is important since only few studies explored enthalpic stabilization in quaternary SiCN(O) structures (see Figure 8(a-b)). Overall, the results in Figure 8(a-b) point to increased stabilization relative to binary crystalline components of quaternary SiOCN systems with decrease in Si and O content. In contrast, greater O content appears to destabilize ternary SiOC systems (see Figure 8(c-d)). In both systems (SiOC and SiOCN), destabilization at higher Si content may reach a plateau, which could imply only minor/negligible further destabilization of the structures with much higher Si content (see Figure 8(a and c)). The effect of O content on thermodynamic stability (see Figure 8(b and d)) may reach a plateau as well. No obvious correlation is observed between enthalpy of formation and C content. The results show that the addition of significant amounts of N species to SiOC structures can significantly impact the systematic trend for increased stabilization in the ceramics. This implies that the correlations are system dependent (SiOC or SiCNO). The semicrystaline structure of the SiC(O) specimen (confimed from XRD) may contribute to its more positive enthalpy of formation, compared to the other amorphous samples synthesized at 1200 °C (Figurues 8(c and d)).
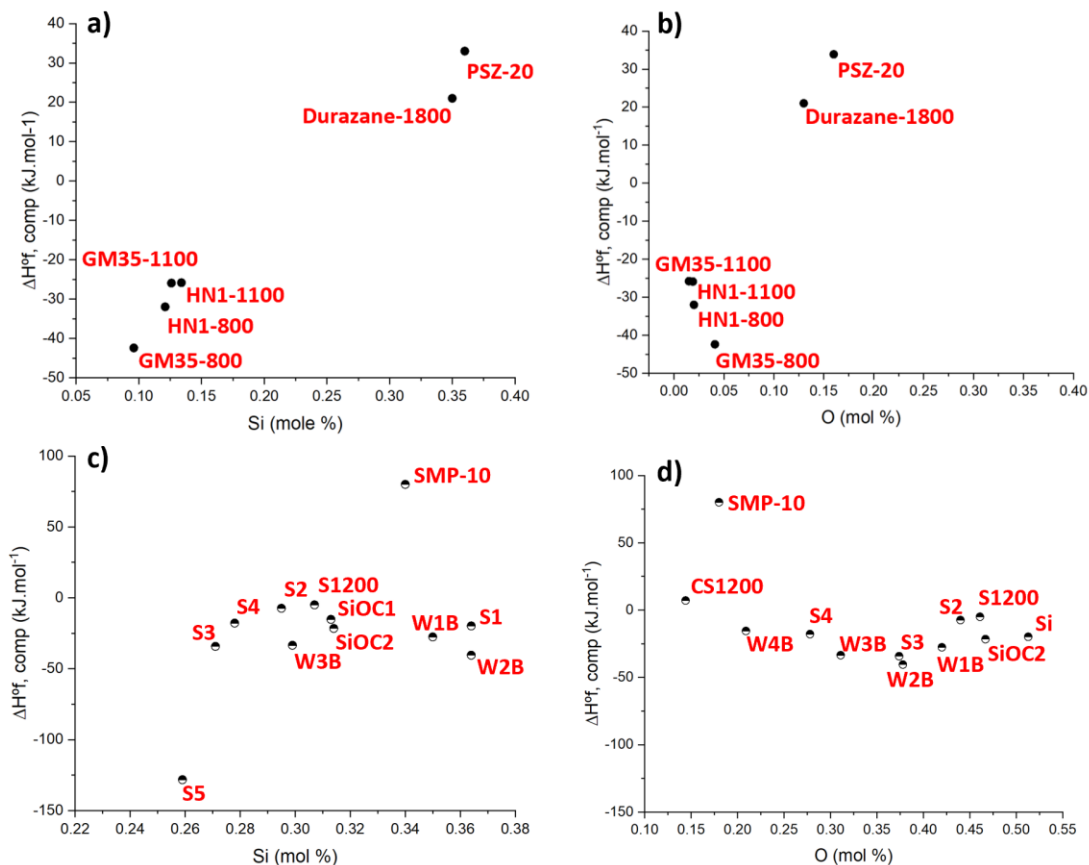
Figure 8. Correlation between enthalpy of formation of SiOCN structures as function of a) Si and b) O content. Enthalpy of formation of SiOC PDCs synthesized at 1200 °C as function of c) Si and d) O content. This includes data from references 81, 89,90, 92 in Table 7.

The effect of synthesis temperature is an important factor to be considered in the thermodynamic stabilization of PDCs, however, in this current work we constrain the synthesis temperature to 1200 °C due to equipment limitations. Typically, there are microstructural modifications associated with pyrolysis time and temperature.[52, 71, 88, 91] The accumulated thermochemical data indicate overall increase in the thermodynamic stability of PDCs with increasing pyrolysis temperature (800-1450 °C).[90, 91] Some

samples synthesized at intermediate temperature (1200 °C) are energetically less stable than specimens synthesized at lower (800-1000 °C) and higher (1400 °C) temperatures. [90, 91]. Such lower stability may reflect decrease of H-terminated mixed bonds, due to evolution of residual (H) up to ~1200 °C, as previously reported.[74] This highlights the significant stabilizing effect of H termination in low-temperature samples, especially those containing nitrogen. It is expected that the SiCN(O) quaternary systems would display a temperature-stability trend similar to that of SiOC and SiCN parent structures, as previous works indicate.[81] However, several fundamental questions still remain. Does the stability of PDCs depend on porosity, and if so, how? How does the stabilizing effect of different metal fillers depend on ionic radius and/or electronegativity of the metal, and is it temperature dependent? How do ionic radius, electronegativity and other metal descriptors influence, temperature-stability relation, including thermodynamic resistance to carbothermal reduction and crystallization in PDCs. To what extent do such trends differ for SiOC, SiCN, and SiOCN systems? What factors, thermodynamic and/or kinetic limit the compositions at which PDCs can be made? Thus, much systematic work still remains to be done. Future investigations require more thermodynamic measurements and perhaps the use of softwares like CALPHAD to compare with experimental data and predict thermodynamic properties of multicomponent PDC systems.[96, 97]

4.4 Conclusions

In this study, we measured the energetics of SiC(O) and SiCN(O) PDC compositions derived from industrial preceramic polymers. The structure-stability trends are consistent

126

with the current understanding of thermodynamic stabilization in PDCs observed across other structures derived from both commercial and other tailor-made precursors. Overall, the thermodynamic stability of the quaternary SiCN(O) PDCs increases with increase in N content and decrease in the relative amount of O. New observations suggest greater stabilizing effect of SiN_xC_{4-x} compared to SiO_xC_{4-x} mixed bonds. This study poses new questions for the rigorous understanding of thermodynamic stabilization in PDCs. This is important in understanding the effect of composition and microstructure (independent of synthesis method) on the thermodynamic drive for phase separation and decomposition (into binary carbides, oxides, nitrides) in amorphous ceramics structures, including CMCs developed by PIP technique. Considering filler incorporation as an important consideration in the development of PDCs, often providing tunability of porosity, thermal stability, and mechanical properties, it should be acknowledged that not much is known about how different fillers influence the structural evolution and thus the thermodynamic stability of PDCs. To this end the next chapter investigates the energetics of metal filler addition in SiOC precursors (polysiloxanes) and predicts the most stable filler incorporation, based on thermodynamic analyses.

Acknowledgements

REFERENCES

1. Luo, X., Wang, J., Dooner, M. & Clarke, J. Overview of current development in electrical energy storage technologies and the application potential in power system operation. *Appl. Energy* **137**, 511–536 (2015).

2. Eswarappa Prameela, S. *et al.* Materials for extreme environments. *Nat. Rev. Mater.* 1–8 (2022).

3. Davidovits, J. Geopolymers: Inorganic polymeric new materials. *J. Therm. Anal. Calorim.* **37**, 1633–1656 (2005).

4. Chauhan, S. S., Abraham, M. & Choudhary, V. Superior EMI shielding performance of thermally stable carbon nanofiber/poly(ether-ketone) composites in 26.5–40 GHz frequency range. *J. Mater. Sci.* **51**, 9705–9715 (2016).

5. Hamerton, I. & Mooring, L. 7 - The use of thermosets in aerospace applications. in *Thermosets* (ed. Guo, Q.) 189–227 (Woodhead Publishing, 2012).

6. Iqbal, A., Saeed, A. & Ul-Hamid, A. A review featuring the fundamentals and advancements of polymer/CNT nanocomposite application in aerospace industry. *Polym. Bull.* **78**, 539–557 (2021).

7. Keller, T. M. & Price, T. R. Amine-Cured Bisphenol-Linked Phthalonitrile Resins. *J. Macromol. Sci. Part - Chem.* **18**, 931–937 (1982).

8. Liu, C. *et al.* Synthesis, characterization, and ceramization of a carbon-rich SiCw-ZrC-ZrB2 preceramic polymer precursor. *Ceram. Int.* **45**, 16097–16104 (2019).

9. Xie, Z., Deng, X., Suo, X., Zhou, T. & Gou, Y. Synthesis and characterization of zirconium diboride precursor based on polycentric bridge bonds. *Mater. Chem. Phys.* **159**, 178–184 (2015).

10. Mansfield, B., Torres, S., Yu, T. & Wu, D. A Review on Additive Manufacturing of Ceramics. in (American Society of Mechanical Engineers Digital Collection, 2019).

11. Parikh, P. B. Alumina Ceramics: Engineering Applications and Domestic Market Potential. *Trans. Indian Ceram. Soc.* **54**, 179–184 (1995).

12. Chaudhary, R. P. *et al.* Additive manufacturing of polymer-derived ceramics: Materials, technologies, properties and potential applications. *Prog. Mater. Sci.* **128**, 100969 (2022).

13. Wei, G. C. Beta Sic Powders Produced by Carbothermic Reduction of Silica in a High-Temperature Rotary Furnace. *J. Am. Ceram. Soc.* **66**, c111–c113 (1983).

14. Moshtaghioun, B. M. *et al.* Rapid carbothermic synthesis of silicon carbide nano powders by using microwave heating. *J. Eur. Ceram. Soc.* **32**, 1787–1794 (2012).

15. Carassiti, L. *et al.* Ultra-rapid, sustainable and selective synthesis of silicon carbide powders and nanomaterials via microwave heating. *Energy Environ. Sci.* **4**, 1503–1510 (2011).

16. Zhao, W. *et al.* Ultralight polymer-derived ceramic aerogels with wide bandwidth and effective electromagnetic absorption properties. *J. Eur. Ceram. Soc.* **37**, 3973–3980 (2017).

17. Salles, V., Bernard, S., Brioude, A., Cornu, D. & Miele, P. A new class of boron nitride fibers with tunable properties by combining an electrospinning process and the polymer-derived ceramics route. *Nanoscale* **2**, 215–217 (2010).

18. Prasad, R. M. *et al.* Thermal decomposition of carbon-rich polymer-derived silicon carbonitrides leading to ceramics with high specific surface area and tunable micro- and mesoporosity. *J. Eur. Ceram. Soc.* **32**, 477–484 (2012).

19. Wang, B. *et al.* Polymer derived SiBCN(O) ceramics with tunable element content. *Ceram. Int.* **48**, 10280–10287 (2022).

20. Mazo, M. A., Tamayo, A., Caballero, A. C. & Rubio, J. Electrical and thermal response of silicon oxycarbide materials obtained by spark plasma sintering. *J. Eur. Ceram. Soc.* **37**, 2011–2020 (2017).

21. Yu, S., Tu, R. & Goto, T. Preparation of SiOC nanocomposite films by laser chemical vapor deposition. *J. Eur. Ceram. Soc.* **36**, 403–409 (2016).

22. Vasudev, M. C., Anderson, K. D., Bunning, T. J., Tsukruk, V. V. & Naik, R. R. Exploration of Plasma-Enhanced Chemical Vapor Deposition as a Method for Thin-

Film Fabrication with Biological Applications. *ACS Appl. Mater. Interfaces* **5**, 3983–3994 (2013).

23. Rajagopalan, T. *et al.* Low temperature deposition of nanocrystalline silicon carbide films by plasma enhanced chemical vapor deposition and their structural and optical characterization. *J. Appl. Phys.* **94**, 5252–5260 (2003).

24. Jonas, S., Ptak, W. S., Sadowski, W., Walasek, E. & Paluszkiewicz, C. FTIR In Situ Studies of the Gas Phase Reactions in Chemical Vapor Deposition of SiC. *J. Electrochem. Soc.* **142**, 2357 (1995).

25. Goerke, O., Feike, E., Heine, T., Trampert, A. & Schubert, H. Ceramic coatings processed by spraying of siloxane precursors (polymer-spraying). *J. Eur. Ceram. Soc.* **24**, 2141–2147 (2004).

26. Greil, P. Polymer Derived Engineering Ceramics. *Adv. Eng. Mater.* **2**, 339–348 (2000).

27. Lücke, J., Hacker, J., Suttor, D. & Ziegler, G. Synthesis and Characterization of Silazane-Based Polymers as Precursors for Ceramic Matrix Composites. *Appl. Organomet. Chem.* **11**, 181–194 (1997).

28. Hurwitz, F. I. Filler/Polycarbosilane Systems as CMC Matrix Precursors. in *22nd Annual Conference on Composites, Advanced Ceramics, Materials, and Structures: A: Ceramic Engineering and Science Proceedings* 267–274 (John Wiley & Sons, Ltd, 1988).

29. Grossenbacher, J., Gullo, M. R., Grandjean, R., Kiefer, T. & Brugger, J. Sub micrometer ceramic structures fabricated by molding a polymer-derived ceramic. *Microelectron. Eng.* **97**, 272–275 (2012).

30. Ren, Z., Gervais, C. & Singh, G. Fabrication and characterization of silicon oxycarbide fibre-mats via electrospinning for high temperature applications. *RSC Adv.* **10**, 38446–38455 (2020).

31. Mujib, S. B. *et al.* Electrospun SiOC ceramic fiber mats as freestanding electrodes for electrochemical energy storage applications. *Ceram. Int.* **46**, 3565–3573 (2020).

32. Chen, Z. *et al.* 3D printing of ceramics: A review. *J. Eur. Ceram. Soc.* **39**, 661–687 (2019).

33. Zhao, L., Wang, X., Xiong, H., Zhou, K. & Zhang, D. Optimized preceramic polymer for 3D structured ceramics via fused deposition modeling. *J. Eur. Ceram. Soc.* **41**, 5066–5074 (2021).

34. Chen, H. *et al.* 3D printing of SiC ceramic: Direct ink writing with a solution of preceramic polymers. *J. Eur. Ceram. Soc.* **38**, 5294–5300 (2018).

35. Schiavon, M. A., Gervais, C., Babonneau, F. & Soraru, G. D. Crystallization Behavior of Novel Silicon Boron Oxycarbide Glasses. *J. Am. Ceram. Soc.* **87**, 203–208 (2004).

36. Ionescu, E., Kleebe, H.-J. & Riedel, R. Silicon-containing polymer-derived ceramic nanocomposites (PDC-NCs): preparative approaches and properties. *Chem. Soc. Rev.* **41**, 5032–5052 (2012).

37. Tavakoli, A. H., Gerstel, P., Golczewski, J. A. & Bill, J. Effect of boron on the crystallization of amorphous Si–(B–)C–N polymer-derived ceramics. *J. Non-Cryst. Solids* **355**, 2381–2389 (2009).

38. Terauds, K. & Raj, R. Limits to the Stability of the Amorphous Nature of Polymer-Derived HfSiCNO Compounds. *J. Am. Ceram. Soc.* **96**, 2117–2123 (2013).

39. Kleebe, H.-J., Suttor, D., Müller, H. & Ziegler, G. Decomposition-Crystallization of Polymer-Derived Si-C-N Ceramics. *J. Am. Ceram. Soc.* **81**, 2971–2977 (1998).

40. Leonel, G. J., Mujib, S. B., Singh, G. & Navrotsky, A. Thermodynamic stabilization of crystalline silicon carbide polymer-derived ceramic fibers. *Int. J. Ceram. Eng. Sci.* **4**, 315–326 (2022).

41. Soraru, G. D., Babonneau, F. & Mackenzie, J. D. Structural evolutions from polycarbosilane to SiC ceramic. *J. Mater. Sci.* **25**, 3886–3893 (1990).

42. Nazari, K. A. *et al.* Preceramic polymer composite: Fabrication process and mechanical performance. *Mater. Lett.* **318**, 132218 (2022).

43. Nabat Al-Ajrash, S. M., Browning, C., Eckerle, R. & Cao, L. Initial development of preceramic polymer formulations for additive manufacturing. *Mater. Adv.* **2**, 1083–1089 (2021).

44. Jana, P., Santoliquido, O., Ortona, A., Colombo, P. & Sorarù, G. D. Polymer-derived SiCN cellular structures from replica of 3D printed lattices. *J. Am. Ceram. Soc.* **101**, 2732–2738 (2018).

45. Apostolov, Z. D., Heckman, E. P., Key, T. S. & Cinibulk, M. K. Effects of low-temperature treatment on the properties of commercial preceramic polymers. *J. Eur. Ceram. Soc.* **40**, 2887–2895 (2020).

46. Colombo, P. *Polymer Derived Ceramics: From Nano-structure to Applications*. (DEStech Publications, Inc, 2010).

47. Lale, A. *et al.* Polymer-Derived Ceramics with engineered mesoporosity: From design to application in catalysis. *Surf. Coat. Technol.* **350**, 569–586 (2018).

48. Bernard, S., Fiaty, K., Cornu, D., Miele, P. & Laurent, P. Kinetic Modeling of the Polymer-Derived Ceramics Route: Investigation of the Thermal Decomposition Kinetics of Poly[B-(methylamino)borazine] Precursors into Boron Nitride. *J. Phys. Chem. B* **110**, 9048–9060 (2006).

49. Key, T. S., Patel, D. K., Wilks, G. B. & Cinibulk, M. K. Modeling the pyrolysis of preceramic polymers: A kinetic study of the polycarbosilane SMP-10. *J. Eur. Ceram. Soc.* **41**, 6356–6365 (2021).

50. Key, T. S. *et al.* Process modeling of the low-temperature evolution and yield of polycarbosilanes for ceramic matrix composites. *J. Am. Ceram. Soc.* **101**, 2809–2818 (2018).

51. Massiot, D. *et al.* Modelling one- and two-dimensional solid-state NMR spectra. *Magn. Reson. Chem.* **40**, 70–76 (2002).

52. Sugie, C., Navrotsky, A., Lauterbach, S., Kleebe, H.-J. & Mera, G. Structure and Thermodynamics of Silicon Oxycarbide Polymer-Derived Ceramics with and without Mixed-Bonding. *Materials* **14**, 4075 (2021).

53. Navrotsky, A. Progress and New Directions in Calorimetry: A 2014 Perspective. *J. Am. Ceram. Soc.* **97**, 3349–3359 (2014).

54. Deepa, M., Sharma, N., Agnihotry, S. A. & Chandra, R. FTIR investigations on ion–ion interactions in liquid and gel polymeric electrolytes: LiCF3SO3-PC-PMMA. *J. Mater. Sci.* **37**, 1759–1765 (2002).

55. Zhang, G. Y. & Peak, D. Studies of Cd(II)–sulfate interactions at the goethite–water interface by ATR-FTIR spectroscopy. *Geochim. Cosmochim. Acta* **71**, 2158–2169 (2007).

56. Bruzzoniti, M. C. *et al.* Polymer-derived ceramic aerogels as sorbent materials for the removal of organic dyes from aqueous solutions. *J. Am. Ceram. Soc.* **101**, 821–830 (2018).

57. Bin Mujib, S., Ribot, F., Gervais, C. & Singh, G. Self-supporting carbon-rich SiOC ceramic electrodes for lithium-ion batteries and aqueous supercapacitors. *RSC Adv.* **11**, 35440–35454 (2021).

58. Santhosh, B. *et al.* Processing and thermal characterization of polymer derived SiCN(O) and SiOC reticulated foams. *Ceram. Int.* **46**, 5594–5601 (2020).

59. Zhao, W. *et al.* Facile preparation of ultralight polymer-derived SiOCN ceramic aerogels with hierarchical pore structure. *J. Am. Ceram. Soc.* **102**, 2316–2324 (2019).

60. Li, H. *et al.* Polymer–ceramic conversion of a highly branched liquid polycarbosilane for SiC-based ceramics. *J. Mater. Sci.* **43**, 2806–2811 (2008).

61. Mahmoudi, M. *et al.* Processing and 3D printing of SiCN polymer-derived ceramics. *Int. J. Appl. Ceram. Technol.* **19**, 939–948 (2022).

62. Li, M., Cheng, L., Ye, F., Wang, Y. & Zhang, C. Tailoring dielectric properties of PDCs-SiCN with bimodal pore-structure by annealing combined with oxidation. *J. Eur. Ceram. Soc.* **40**, 5247–5257 (2020).

63. Liu, X. *et al.* Enhanced microwave-absorption properties of polymer-derived SiC/SiOC composite ceramics modified by carbon nanowires. *Ceram. Int.* **46**, 20742–20750 (2020).

64. Colombo, P., Mera, G., Riedel, R. & Sorarù, G. D. Polymer-Derived Ceramics: 40 Years of Research and Innovation in Advanced Ceramics. *J. Am. Ceram. Soc.* **93**, 1805–1837 (2010).

65. Hung, I., Ionescu, E., Sen, J., Gan, Z. & Sen, S. Structure and Connectivity in an Amorphous Silicon Oxycarbide Polymer-Derived Ceramic: Results from 2D 29Si NMR Spectroscopy. *J. Phys. Chem. C* **125**, 4777–4784 (2021).

66. Saha, A. & Raj, R. Crystallization Maps for SiCO Amorphous Ceramics. *J. Am. Ceram. Soc.* **90**, 578–583 (2007).

67. Bae, S.-G. *et al.* Effect of carbon and oxygen on the high-temperature properties of silicon carbide–hafnium carbide nanocomposite fiber. *J. Eur. Ceram. Soc.* (2022)

68. Sasikumar, P. V. W. *et al.* Polymer derived silicon oxycarbide ceramic monoliths: Microstructure development and associated materials properties. *Ceram. Int.* **44**, 20961–20967 (2018).

69. Rau, A. V., Knott, K. & Lu, K. Porous SiOC/SiC ceramics via an active-filler-catalyzed polymer-derived method. *Mater. Chem. Front.* **5**, 6530–6545 (2021).

70. Wang, K., Wang, H. & Cheng, Y.-B. Synthesis of nanostructured silicon carbide spheres from mesoporous C–SiO2 nanocomposites. *Chem. Commun.* **46**, 303–305 (2009).

71. Poerschke, D. L., Braithwaite, A., Park, D. & Lauten, F. Crystallization behavior of polymer-derived Si-O-C for ceramic matrix composite processing. *Acta Mater.* **147**, 329–341 (2018).

72. Leonel, G. J., Guo, X., Singh, G. & Navrotsky, A. Compositional Analysis of SiOC(H) Powders: A Comparison of X-ray Photoelectron Spectroscopy (XPS) and Combustion Analysis. *Ceramics* **6**, 74–85 (2023).

73. Michelle Morcos, R. *et al.* Enthalpy of Formation of Carbon-Rich Polymer-Derived Amorphous SiCN Ceramics. *J. Am. Ceram. Soc.* **91**, 3349–3354 (2008).

74. Mera, G., Navrotsky, A., Sen, S., Kleebe, H.-J. & Riedel, R. Polymer-derived SiCN and SiOC ceramics – structure and energetics at the nanoscale. *J. Mater. Chem. A* **1**, 3826–3836 (2013).

75. David, L., Bhandavat, R., Barrera, U. & Singh, G. Silicon oxycarbide glass-graphene composite paper electrode for long-cycle lithium-ion batteries. *Nat. Commun.* **7**, 10998 (2016).

76. Zybill, C., Handwerker, H. & Friedrich, H. Silaorganometallic Chemistry on the Basis of Multiple Bonding. in *Advances in Organometallic Chemistry* (eds. Stone, F. G. A. & West, R.) vol. 36 229–281 (Academic Press, 1994).

77. Farnan, I., Cho, H. & Weber, W. J. Quantification of actinide α-radiation damage in minerals and ceramics. *Nature* **445**, 190–193 (2007).

78. Widgeon, S. *et al.* Effect of Precursor on Speciation and Nanostructure of SiBCN Polymer-Derived Ceramics. *J. Am. Ceram. Soc.* **96**, 1651–1659 (2013).

79. Berger, F., Müller, A., Aldinger, F. & Müller, K. Solid-state NMR Investigations on Si-B-C-N Ceramics derived from Boron-Modified Poly(allylmethylsilazane). *Z. Für Anorg. Allg. Chem.* **631**, 355–363 (2005).

80. Widgeon, S. J. *et al.* 29Si and 13C Solid-State NMR Spectroscopic Study of Nanometer-Scale Structure and Mass Fractal Characteristics of Amorphous Polymer Derived Silicon Oxycarbide Ceramics. *Chem. Mater.* **22**, 6221–6228 (2010).

81. Widgeon, S. *et al.* Nanostructure and Energetics of Carbon-Rich SiCN Ceramics Derived from Polysilylcarbodiimides: Role of the Nanodomain Interfaces. *Chem. Mater.* **24**, 1181–1191 (2012).

82. Xue, J. *et al.* Enhanced microwave absorbing properties of Y2O3 modified PDC SiCN ceramics with heterogeneous amorphous interface. *J. Alloys Compd.* **931**, 167499 (2023).

83. Jia, Y., Chowdhury, M. A. R. & Xu, C. Complex impedance spectra of polymer-derived SiC annealed at ultrahigh temperature. *J. Am. Ceram. Soc.* **103**, 6860–6868 (2020).

84. Feng, Y., Feng, N., Wei, Y. & Bai, Y. Preparation and improved electrochemical performance of SiCN–graphene composite derived from poly(silylcarbondiimide) as Li-ion battery anode. *J. Mater. Chem. A* **2**, 4168–4177 (2014).

85. Sang, Z. *et al.* SiOC nanolayer wrapped 3D interconnected graphene sponge as a high-performance anode for lithium ion batteries. *J. Mater. Chem. A* **6**, 9064–9073 (2018).

86. Chen, J. *et al.* Thermodynamic Stability of Low-k Amorphous SiOCH Dielectric Films. *J. Am. Ceram. Soc.* **99**, 2752–2759 (2016).

87. Morcos, R. M. *et al.* Thermodynamically Stable SiwCxNyOz Polymer-Like, Amorphous Ceramics Made from Organic Precursors. *J. Am. Ceram. Soc.* **91**, 2391–2393 (2008).

88. Tavakoli, A. H., Golczewski, J. A., Bill, J. & Navrotsky, A. Effect of boron on the thermodynamic stability of amorphous polymer-derived Si(B)CN ceramics. *Acta Mater.* **60**, 4514–4522 (2012).

89. Varga, T. *et al.* Thermodynamically Stable SixOyCz Polymer-Like Amorphous Ceramics. *J. Am. Ceram. Soc.* **90**, 3213–3219 (2007).

90. Morcos, R. M. *et al.* Energetics of SixOyCz Polymer-Derived Ceramics Prepared Under Varying Conditions. *J. Am. Ceram. Soc.* **91**, 2969–2974 (2008).

91. Tavakoli, A. H. *et al.* Energetics and Structure of Polymer-Derived Si–(B–)O–C Glasses: Effect of the Boron Content and Pyrolysis Temperature. *J. Am. Ceram. Soc.* **97**, 303–309 (2014).

92. Niu, M. *et al.* Structure and energetics of SiOC and SiOC-modified carbon-bonded carbon fiber composites. *J. Am. Ceram. Soc.* **100**, 3693–3702 (2017).

93. Ionescu, E., Sen, S., Mera, G. & Navrotsky, A. Structure, energetics and bioactivity of silicon oxycarbide-based amorphous ceramics with highly connected networks. *J. Eur. Ceram. Soc.* **38**, 1311–1319 (2018).

94. Michelle Morcos, R. *et al.* Enthalpy of Formation of Carbon-Rich Polymer-Derived Amorphous SiCN Ceramics. *J. Am. Ceram. Soc.* **91**, 3349–3354 (2008.

95. Tavakoli, A. H., Armentrout, M. M., Narisawa, M., Sen, S. & Navrotsky, A. White Si–O–C Ceramic: Structure and Thermodynamic Stability. *J. Am. Ceram. Soc.* **98**, 242–246 (2015).

96. Petry, N.-C. *et al.* Oxidation resistance of ZrB2-based monoliths using polymer-derived Si(Zr,B)CN as sintering aid. *J. Am. Ceram. Soc.* **105**, 5380–5394 (2022).

97. Barrios, E. & Zhai, L. A review of the evolution of the nanostructure of SiCN and SiOC polymer derived ceramics and the impact on mechanical properties. *Mol. Syst. Des. Eng.* **5**, 1606–1641 (2020).

CHAPTER 5

STRUCTURAL AND THERMODYNAMIC ANALYSIS OF METAL FILLER

INCORPORATION IN $SI_aO_b(M)_cC_d$ POLYMER DERIVED CERAMICS

Abstract: This work systematically investigates the thermodynamic stability of $Si_aO_b(M)_cC_d$ structures derived from polymeric precursors incorporating metal fillers: Ta, Nb, and Hf, at 1200 and 1500 °C. Structural characterization of the polymer derived ceramics (PDCs) employs X-ray diffraction (XRD), Fourier transform infrared spectroscopy (FTIR), and X-ray photoelectron spectroscopy (XPS). Enthalpies of formation relative to crystalline components (metal oxide, silica, silicon carbide, and graphite) are obtained from thermodynamic measurements by high temperature oxide melt solution calorimetry. The enthalpies of formation from components (SiC, SiO_2, Si_3N_4, and C, $\Delta H^o_{f, comp}$) show that incorporation of Hf results in most thermodynamically stable structures at all synthesis temperatures. $Si_aO_b(M)_cC_d$ specimens employing Nb fillers undergo the most stable structural evolution in this temperature range. The results indicate strong thermodynamic drive for carbothermal reduction of metal oxide domains. Incorporation of Ta provides the greatest stabilization of SiO_3C mixed bonding environments. Ultimately, the choice of metal filler influences composition, structural evolution, and thermodynamic stability in PDCs.

5.1 Introduction

The processing of organometallic precursors such as polysilazanes, polycarbosilanes, and polysiloxanes at elevated temperatures permits attainability of $Si_xC_yN_z$, Si_xC_y, and $Si_xO_yC_z$ refractory materials with high chemical, thermal, and mechanical stability.[1, 2] Over the past five decades the synthesis of carbide, nitride, and oxide ceramic materials through the polymeric route has increased in popularity.[1] Polymer derived ceramics (PDCs) are especially attractive due to spinnability of the precursors, which permits attainability of ceramic fibers.[3–5] Additionally, appropriate processing of preceramic polymers permits development of high temperature ceramic films.[6, 7] This is especially important in response to current interest for the development of protective coatings for application in aerospace systems.[8–11]

Recent PDC works highlight incorporation of fillers (sacrificial, active, passive) in ceramic structures.[12, 13] The use of sacrificial fillers like polymethylmethacrylate (PMMA) typically results in increased porosity of the final ceramics.[14] Similarly, active metallic or intermetallic fillers can reduce volume shrinkage of preceramic polymers during thermal treatment.[1] Other studies have also demonstrated greater resistance to crystallization in PDCs incorporating boron.[15] As the use of PDC fillers increases, it is essential to understand how choice of filler influences composition as well as microstructure. [16–20] It is especially important to identify the effect of filler and corresponding structural modification on the thermodynamic stability of the respective ceramics, since stability determines propensity for phase separation and decomposition in PDCs.[5, 21–25]

In the past, thermodynamic works investigated structure-stability relations in various PDC systems, including the effect of composition, mixed bonding, and pyrolysis temperature on the thermodynamic stability.[5, 22, 25] To this end, the present work is the first work to systematically investigate the structural evolution and thermodynamic stabilization in PDCs incorporating Hf, Nb, and Ta. We report the synthesis, characterization, and thermodynamic analysis of the structures synthesized at 1200 and 1500 °C. Structural and chemical characterization are done by X-ray diffraction (XRD), Fourier transform infrared spectroscopy (FTIR), and X-ray photoelectron spectroscopy (XPS). Thermodynamic measurements employ high temperature oxide melt solution calorimetry. This work permits assessment of the influence of choice of metal filler as well as of synthesis temperature on the composition, structure, and thermodynamic stability of SiO(M)Cs (where M = metal), thus permitting identification of the energy landscape for metal filler incorporation in PDCs.

5.2 Experimental Methods

5.2.1 Materials and Crosslinking

The liquid siloxane SPR-2012 (stored in a laboratory freezer) from Starfire Systems was used as polymeric precursor for the PDCs. Structure of the precursor is shown in Figure 1. The preceramic polymer (equilibrated to ambient temperature for ~12 hrs) was mixed with 30 wt % of either Hf, Nb, or Ta metal powders (from Fisher Scientific), under magnetic stirring for one hour in a glovebox employing a nitrogen

atmosphere (~0.1 ppm oxygen content). This results in Hf, Nb, and Ta modified SPR-212 precursors. Crosslinking of the precursor mixtures was done in a beaker on a hotplate, under inert atmosphere (in glovebox). The hotplate employed a temperature ramping of ~5 °C/min. Before pyrolysis, the precursor mixtures were each crosslinked into rigid solids at 300 °C (T_{max} of hotplate) for 3 hrs. It should be noted that during crosslinking (under stirring) significant metal content settled on the bottom and sticks to the walls of the beaker. Localized aggregation of metal powders could be observed throughout the precursors and this results in metal distribution inhomogeneity across the final crosslinked specimens. We did not employ the use of any crosslinking catalysts in the synthesis of the specimens.
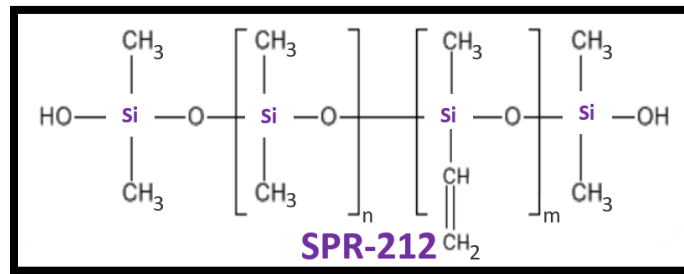
Figure 1. Structure of single source industrial precursor (SPR-212) for SiOCs.

5.2.2 Pyrolysis

High temperature pyrolysis of the crosslinked precursors was done in a Netzsch STA 409 differential scanning calorimeter cell, using alumina crucibles, under flowing argon atmosphere (50 mL/min). Pyrolysis of precursors was investigated at 1200 and 1500 °C. The pyrolysis employed a temperature ramping of 2 °C/min to final pyrolysis temperature. This resulted in the formation of Hf-1200, Nb-1200, Ta-1200, Hf-1500, Nb-

1500, and Ta-1500 specimens. The resulting ceramics were then ground into fine powders by the use of an agate mortar and pestle, in the glovebox operating at ambient temperature. During milling each specimen was manually ground for at least 10 minutes to ensure homogenous mixing in each powdered sample.

5.2.3 Characterization

XRD experiments employed a table-top Bruker D2 powder diffractometer (nickel-filtered CuKα radiation, wavelength= 1.5418 Å). FTIR employed a Bruker TENSOR instrument with platinum ATR accessory. XPS experiments were done using a Kratos AXIS Supra+, employing monochromatic Al Kα+ ion beam, with beam energy = 1486.6 eV. For each fine powder, three different locations were selected for XPS experiments.

5.2.4 Thermochemistry

Calorimetric measurements were done by oxide melt solution calorimetry in a commercial Seteram Alexsys calorimeter. Dissolution of the PDCs occurs in 20 g of sodium molybdate ($3Na_2O \bullet MoO_3$) melt, at 800 °C. This technique measures enthalpies of dissolution (ΔH_{dis}) and permits quantitation of enthalpies of formation relative to elements ($\Delta H^o_{f, elem}$) and components ($\Delta H^o_{f, comp}$). In the first step ~ 5 mg of the sample was weighed using a Mettler Toledo microbalance (~10 μg accuracy) and then pressed into a pellet using a 1.5 mm tungsten die. In the second step the pellet was inserted into the calorimeter, where it undergoes oxidative dissolution in the melt. The melt was

continuously bubbled with 40 mL/min of oxygen, this ensures continuous oxidative environment. The samples employed oxygen flushing (~ 100 mL/min) to evacuate any evolved gases resulting from dissolution of the specimen. During dissolution Si is oxidized to cristobalite (SiO_2), which precipitates from the melt, C is oxidized to CO_2 (evolves from melt), and the metal is oxidized to metal oxide (Ta_2O_5, HfO_2, Nb_2O_5) which dissolve in the melt.[5, 25–27] For each sample the experiments were repeated at least six times. More experimental details are provided in previous work.[27]

Reaction (1) describes the oxidative dissolution of $Si_aO_b(M)_cC_d$ specimens, where M = Hf, Nb, or Ta

$Si_aO_bM_cC_d$ (s, 25 °C) + ((2a + 2d +(c/e)f)-b)/2 O_2 (g, 800 °C) → a SiO_2 (s, 800 °C) + d CO_2 (g, 800 °C) + (c/e) M_eO_f (sol, 800 °C) ΔH^o_{dis}

$$(1)$$
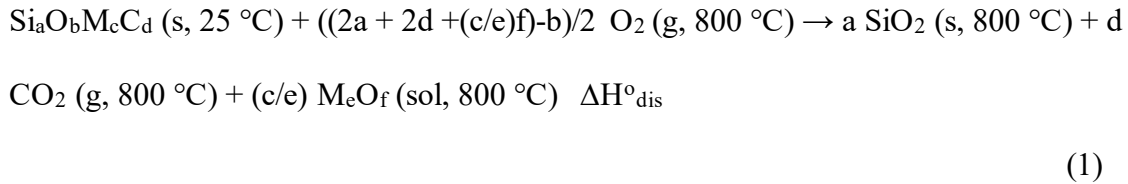
Enthalpy of formation of $Si_aO_b(M)_cC_d$ from the elements (Si, C, M and O_2) is described below:

aSi (solid, 25 °C) + b/2 O_2 (gas, 25 °C) + d C (solid, 25 °C) + c M (gas, 25 °C)→ $Si_aO_bM_cC_d$ (s, 25 °C) $\Delta H^o_{f, elem}$

$$(2)$$
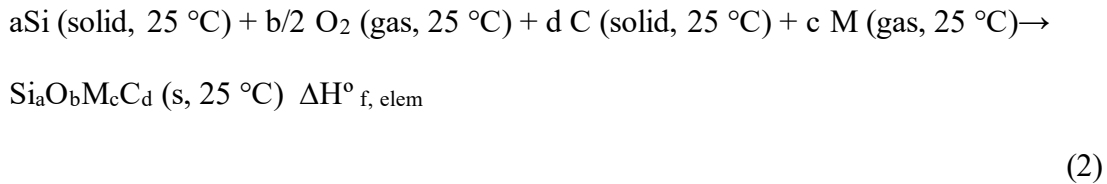
Reactions (3-4) describe enthalpy of formation relative to crystalline components (β-SiC, SiO_2 (cristobalite), C (graphite), and most stable metal oxide M_xO_y or carbide M_xC_y :

(a-((b-(c/e)f)/2)) SiC (s, 25 °C)+ ((b-(c/e)f)/2) SiO$_2$ (s, 25 °C)+ (c/e) M$_e$O$_f$ (s, 25 °C)+ (d-

(a-((b-(c/e)f)/2))) C (s, 25 °C) → Si$_a$O$_b$M$_c$C$_d$ (s, 25 °C) ΔH°$_{f,comp}$, where M$_e$O$_f$ = Ta$_2$O$_5$,

HfO$_2$, or Nb$_2$O$_5$.

$$(3)$$

(a-(b/2)) SiC (s, 25 °C)+ (b/2) SiO$_2$ (s, 25 °C) + c MC (s, 25 °C)+ (d-(a-(b/2))- c) C (s,

25 °C) → Si$_a$O$_b$M$_c$C$_d$ (s, 25 °C) ΔH°$_{f,comp}$, where MC= TaC, HfC, or NbC.

$$(4)$$
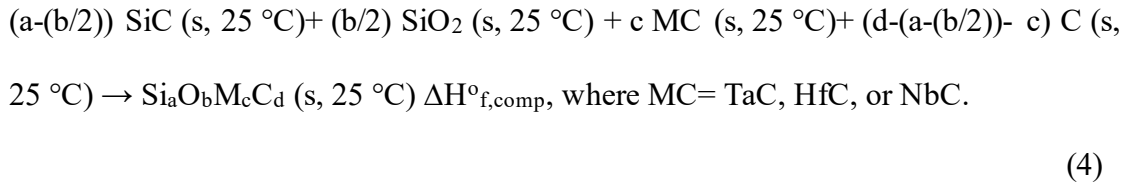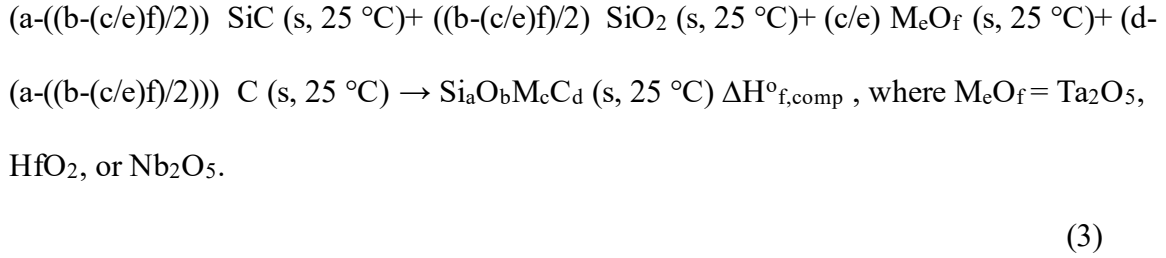
Given that the initial and final states of the system are known, enthalpies of formation

were determined by employing enthalpies of dissolution and thermodynamic cycles

(Tables 1-4).

Table 1. Thermochemical cycle for calculation of enthalpy of oxidation ΔH°$_{OX}$, at 25 °C

Si$_a$O$_b$M$_c$C$_d$ (s, 25 °C) + ((2a + 2d +(c/e)f)-b)/2 O$_2$ (g, 25 °C) → a SiO$_2$ (s, 25 °C) + d CO$_2$ (g, 25 °C) + (c/e) M$_e$O$_f$ (s, 25 °C) ΔH°$_{dis}$) ΔH° $_{Ox}$ =?	ΔH (kJ/mol)
Si$_a$O$_b$M$_c$C$_d$ (s, 25 °C) + ((2a + 2d +(c/e)f)-b)/2 O$_2$ (g, 800 °C) → aSiO$_2$ (s, 800 °C) + dCO$_2$ (g, 800 °C) + (c/e)M$_e$O$_f$ (sol, 800 °C)	ΔH$_{dis}$
O$_2$ (g, 25 °C) → O$_2$ (g, 800 °C)	ΔH$_2$= 25.3

SiO₂ (s, 25 °C) → SiO₂ (s, 800 °C)	ΔH_3= 50.1
CO₂ (s, 25 °C) → CO₂ (g, 800 °C)	ΔH_4= 37.5
M$_e$O$_f$ (s, 25 °C) → M$_e$O$_f$ (sol, 800 °C)	ΔH_5= 108.72 ± 2 (Ta₂O₅) = 85.01 ± 2 (HfO₂) = 111.50 ± 0.16 (Nb₂O₅)
$\Delta H°_{OX} = \Delta H_{dis}$ + ((2a + 2d +(c/e)f)-b)/2 ΔH_2 – a ΔH_3 - dΔH_4 - (c/e) ΔH_5	$\Delta H°_{OX}$

Table 2. Thermochemical cycle for calculation of enthalpy of formation from elements $\Delta H°_{f, elem}$, at 25 °C

	ΔH (kJ/mol)
a Si (s, 25 °C) + b/2 O₂ (g, 25 °C + d C (s, 25 °C) + c M (g, 25 °C)→ Si$_a$O$_b$M$_c$C$_d$ (s, 25 °C) $\Delta H°_{f, elem}$ =?	
Si$_a$O$_b$M$_c$C$_d$ (s, 25 °C) + ((a*2+d*2+(c*f/e)-(b))/2) O₂ (g, 25 °C) → aSiO₂ (s, 25 °C) + dCO₂ (g, 25 °C) + (c/e)M$_e$O$_f$ (s, 25 °C)	$\Delta H°_{OX}$
Si (s, 25 °C) + O₂ (g, 25 °C)→SiO₂ (s, 25 °C)	ΔH_2= −908.4 ± 2.1 [28]
C (s, 25 °C) + O₂ (g, 25 °C)→CO₂ (g, 25 °C)	ΔH_3= −393.5 ± 0.1 [28]

eM (s, 25 °C) + (f/2) O₂ (g, 25 °C)→ M_eO_f (s, 25 °C)	ΔH_4= -2045.976 (Ta$_2$O$_5$) [28] = -1899.536 (Nb$_2$O$_5$)[28] = -1117.63 ± 0.39 (HfO$_2$) [29]
$\Delta H^o_{f, elem}$ = -ΔH_{Ox} + a ΔH_2 + d ΔH_3 + (c/e) ΔH_4	$\Delta H^o_{f, elem}$

Table 3. Thermochemical cycle for calculation of enthalpy of formation from crystalline components (β-SiC, SiO₂ (cristobalite), C (graphite), and metal oxide M_xO_y (metal oxide) $\Delta H^{\circ}_{f, comp}$, at 25 °C

(a-((b-(c/e)f)/2)) SiC (s, 25 °C)+ ((b-(c/e)f)/2) SiO₂ (s, 25 °C)+ (c/e) M_eO_f (s, 25 °C)+ (d-(a-((b-(c/e)f)/2))) C (s, 25 °C) → Si_aO_bM_cC_d (s, 25 °C) $\Delta H^o_{f,comp}$=?	ΔH (kJ/mol)
aSi (solid, 25 °C) + b/2O₂ (gas, 25 °C) + dC (s, 25 °C) + cM (gas, 25 °C)→ Si_aO_bM_cC_d (s, 25 °C)	$\Delta H^o_{f, elem}$
Si (solid, 25 °C) + C (solid, 25 °C)→SiC (s, 25 °C)	ΔH_2= −73.2 ± 6.3 [28]
Si (solid, 25 °C) + O₂ (gas, 25 °C)→SiO₂ (s, 25 °C)	ΔH_3= −908.4 ± 2.1 [28]
eM (s, 25 °C) + (f/2) O₂ (g, 25 °C)→ M_eO_f (s, 25 °C)	ΔH_4= -2045.97 ± 2.1 (Ta$_2$O$_5$)[28] = -1899.536 (Nb$_2$O$_5$) [28]

	$= -1117.63 \pm 0.39$ (HfO$_2$) [29]
$\Delta H^o_{f, comp} = \Delta H^o_{f, elem}$ - (a-((b-(c/e)f)/2)) ΔH_2 - ((b-(c/e)f)/2) ΔH_3 – (c/e) ΔH_4	$\Delta H^o_{f, comp}$

Table 4. Thermochemical cycle for calculation of enthalpy of formation from crystalline components (β-SiC, SiO$_2$ (cristobalite), C (graphite), and M$_x$C$_y$ (metal carbide)) $\Delta H^{\circ}_{f, comp}$, at 25 °C

(a-(b/2)) SiC (s, 25 °C)+ (b/2) SiO$_2$ (s, 25 °C) + c MC (s, 25 °C)+ (d-(a-(b/2))- c) C (s, 25 °C) → Si$_a$O$_b$M$_c$C$_d$ (s, 25 °C) $\Delta H^o_{f,comp}$=?	ΔH (kJ/mol)
aSi (solid, 25 °C) + b/2O$_2$ (g, 25 °C) + dC (s, 25 °C) + cM (gas, 25 °C)→ Si$_a$O$_b$M$_c$C$_d$ (s, 25 °C)	$\Delta H^o_{f, elem}$
Si (solid, 25 °C) + C (s, 25 °C)→SiC (s, 25 °C)	ΔH_2= -73.2 ± 6.3 [28]
Si (solid, 25 °C) + O$_2$ (g, 25 °C)→SiO$_2$ (s, 25 °C)	ΔH_3=-908.4 ± 2.1[28]
M (s, 25 °C) + C (s, 25 °C)→ MC (s, 25 °C)	ΔH_4=-144.097 (TaC)[28] = -138.91 (NbC)[28] = -218.82 (HfC)[30]
$\Delta H^o_{f, comp} = \Delta H^o_{f, elem}$ - (a-(b/2)) ΔH_2 - (b/2) ΔH_3 – c ΔH_4	$\Delta H^o_{f, comp}$

- s=solid, sol=solution, g=gas

5.3 Results and discussion

FTIR permits identification of functional groups in structures. Spectra of the crosslinked precursors and corresponding PDCs are summarized in Figure 2 (a-b). The intensity of FTIR peaks is proportional to the amount of corresponding bonds.[31, 32] The results in Figure 2 indicate presence of Si–O–Si ($\sim$1060 cm^{-1}), Si–CH$_3$ ($\sim$1260 cm^{-1}), C=C ($\sim$1600 cm^{-1}), Si-O-Si ($\sim$1060 cm^{-1}), Si-C/M-O ($\sim$800 cm^{-1}), and M-C ($\sim$600 cm^{-1}) bond stretch vibrational bands in the specimens. [33–45] The results further point to the evolution of organic groups during high temperature pyrolysis, which is typical during ceramization; thus C-H and Si-H bonds are not observed in the PDCs synthesized at 1200 and 1500 °C (see Figure 2). The Si-O-Si and Si-C bonds are consistent with SiOC structures. [36–41]
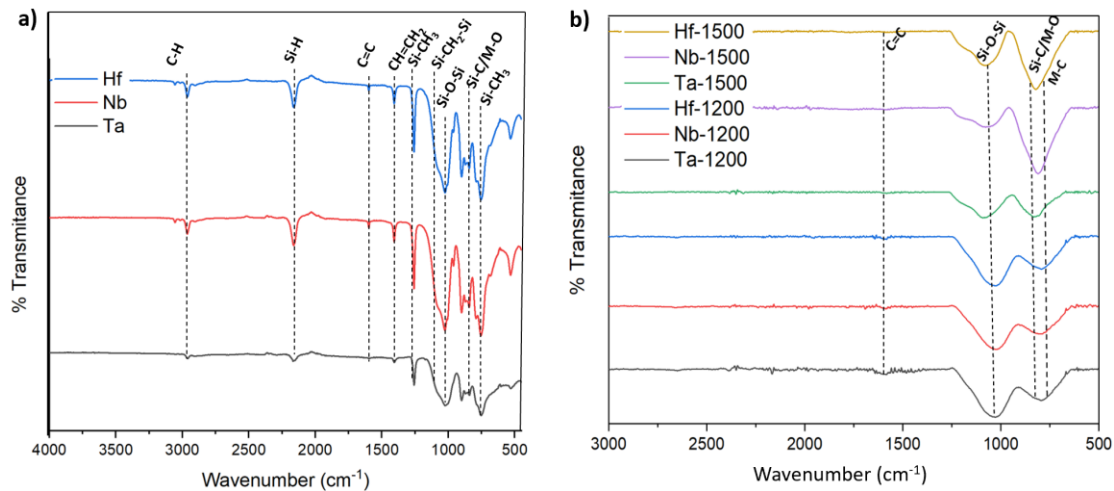
Figure 2. FTIR spectra of (a) crosslinked precursors and (b) corresponding $Si_aO_b(M)_cC_d$ PDCs synthesized at 1200 and 1500 °C.

XRD permits assessment of crystallinity. This allows determination of crystallization behavior in the PDC depending on choice of metal as well as pyrolysis temperature. Typically, SiOCs pyrolyzed below 1250 °C are X-ray amorphous, increasing synthesis temperature above 1450 °C promotes crystallization of β-SiC domains. [46–48] All $Si_aO_b(M)_cC_d$ samples display peaks corresponding to some identifiable metal carbide and oxide phases. The results in Figure 3 further indicate crystallization of β-SiC domains (main peaks at 2θ= 35.60°, 60°, and 72°) in PDCs pyrolyzed at 1500 °C. [49, 50] The unidentified XRD peaks may correspond to other crystalline metal oxide, carbide or oxycarbide phases. Overall, all samples display increase in the relative intensity of peaks corresponding to metal carbide with increasing synthesis temperature. This could imply carbothermal reduction of metal oxide phases at higher synthesis temperature (1500 °C).[51–53]
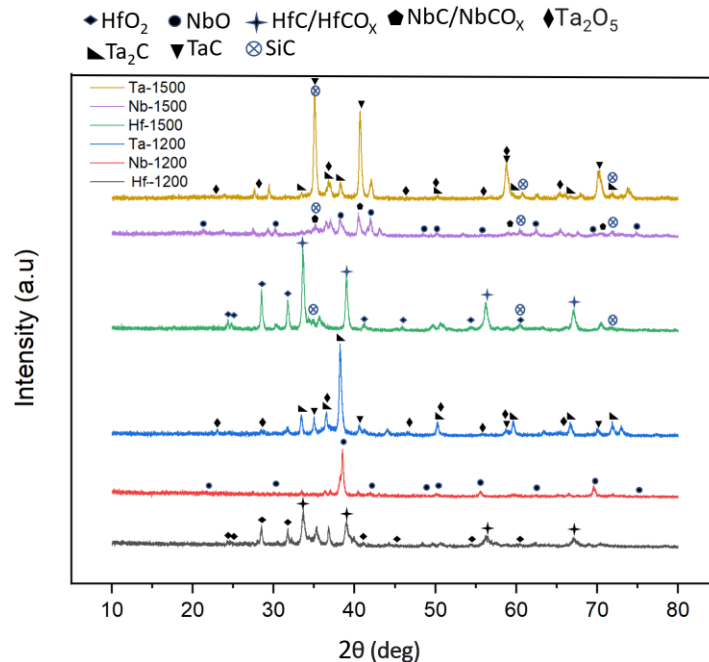
Figure 3. XRD patterns of $Si_aO_b(M)_cC_d$ ceramics. The results show significant crystallization of metal oxide and/or carbide phases in all PDCs.

148

HR-XPS identification of bonding environments in PDC microstructures was done by surveying Si 2p, C 1s, O 1s, Ta 4f, Nb 3d, and Hf 4f bonds.[5, 21] The results are summarized in Figure 4. By employing suitable curve fitting, the area under the convolution curves is proportional to the relative amount of corresponding bonds in the microstructures.[54] This permits semiquantitative assessment of microstructural differences in samples, resulting from choice of metal filler and pyrolysis temperature.

Si 2p convolutions suggest presence of SiO_4 (~104 eV), $SiOC_3$ (~101.5 eV), SiO_2C_2 (~102 eV) and SiO_3C (~102.9 eV) bonds in all samples.[55, 56] Generally, SiO_4 bonds correspond to amorphous silica (SiO_2) domains. Overall, the relative amount of SiO_4 bonds appears to increase with synthesis temperature, which is consistent with phase separation of the amorphous $Si_aO_bC_c$ microstructure at higher temperatures. The results further indicate presence of SiO_2C_2, $SiOC_3$ and SiO_3C bonds and this correspond to SiO_xC_{4-x} mixed bonding environments (Si bonded to O and C) in the samples, which is typical in PDCs.[57] The results in Figure 4 show general increase of $SiOC_3$ compared to SiO_3C mixed bonds with increasing synthesis temperature, and this may indicate greater resistance to thermal degradation of $SiOC_3$ mixed bonding networks. However, it should be highlighted that addition of Ta may promote thermal stabilization of SiO_3C bonds in PDC structures, as suggested by the relative increase in SiO_3C bonds with temperature in samples incorporating Ta fillers (see Figure 4).

C 1s convolutions permit identification of C-O (~286.5 eV) and C-C (~285 eV) and C-Si (~283 eV) bonds (see Figure 4). [55, 58] In mixed bonding C is bonded to Si or to another C, hence, C-O bonds may correspond to oxygen termination in free carbon phases or adventitious carbons (e.g. absorbed CO_2). C-C and C-Si bonds may correspond

to presence of free carbon and silicon carbide (SiC) domains, respectively. It should be noted that C-C and C-Si convolutions can be representative of mixed bonding domains as well.[5, 57] C1s convolutions in Figure 4 indicate general increase in the amount of C-O (relative to C-C and C-Si) bonds with pyrolysis temperature, with exception of samples employing Ta fillers. This may indicate decrease in the relative amount of C-Si and C-C bonds in samples employing Nb, and Hf. Such a change may result from formation of more metal-Si bonds (e.g. metal silicates), loss of SiO_xC_{4-x} mixed bonds (from phase separation), and/or carbothermal reduction of metal oxides by free carbon to form metal carbide at higher synthesis temperature, as suggested by Ta 4f, Nb 3d, and Hf 4f convolutions. The weak signal corresponding to metal bonds results from the low amount of the metal fillers in the compositions, as demonstrated below. Overall, the peak positions in metal convolutions are consistent with previous works and the current NIST database.[59–67] It is likely that C 1s convolutions do not show C-metal bonds due to their much lower relative amounts compared to C-C, C-Si, and C-O bonds.

Ta

(a1) Si 2p — 1200 °C: SiO₂C₂, SiOC₃, SiO₃, SiO₄
(a2) C 1s: C-C, C-O, C=O, C-Si
(a3) O 1s: O-Si, Ta-O/SiO
(a4) Ta 4f: TaC, Ta₂O₅, Ta-C, Ta₂O₅

(a5) Si 2p — 1500 °C: SiO₂C₂, SiO₃C, SiOC₃, SiO₄
(a6) C 1s: C-C, C-O, C=O, C-Si
(a7) O 1s: Ta-O/SiO, O-Si
(a8) Ta 4f: TaC, Ta₂O₅, Ta-C, Ta₂O₅

Nb

(b1) Si 2p — 1200 °C: SiO₃C, SiO₂C₂, SiO₄, SiOC₃
(b2) C 1s: C-C, C-O, C=O, C-Si
(b3) O 1s: Nb-O/SiO, O-Si
(b4) Nb 3d: Nb₂O₅, NbOₓ/Nb, Nb₂O₅, NbC

(b5) Si 2p — 1500 °C: SiO₂C₂, SiO₃C, SiOC₃, SiO₄
(b6) C 1s: C-C, C-O, C=O, C-Si
(b7) O 1s: O-Si, Nb-O/SiO
(b8) Nb 3d: Nb₂O₅, NbOₓ/Nb, Nb₂O₅, NbC

151

Figure 4. HR XPS of the PDCs synthesized from metal modified SiOC precursors, under flowing argon atmosphere, at 1200 and 1500 °C.

Compositional analysis of the PDCs was done by survey-XPS experiments. This technique permits efficient elemental analysis of PDCs fine powders synthesized at high temperature (>1000 °C), when residual hydrogen content is negligible.[21] The results from compositional analysis are summarized in Tables 5. The compositions confirm presence of Si,C, O, and corresponding metals in all samples, it should be noted that the results further indicate that metals are present in minor amounts. This may in part be attributed to possible selection of metal-deficient portions of the crosslinked precursor for pyrolysis (*due to severe inhomogeneity of metal distribution*), as described in the crosslinking section. Typically, metal additives are introduced to preceramic polymers as compound

precursors including metal oxides, metal tetrachlorides, and even organometallic acids (e.g. boric acid). [68–70] The Incorporation of metal powders, which are more reactive, may result in further loss of metal content from the formation of volatile metal complexes (e.g. ethoxides) at processing conditions. [71–73] Unreacted volatiles may continue to evolve during pyrolysis. As expected, the results suggest significant decrease in the O : Si (and O : M) as well as C : Si (and C: M) ratio with increasing pyrolysis temperature. This is consistent with carbothermal reduction of metal oxide and/or silica domains to form evolved CO and carbides of metal and/or silicon.[51–53]

Overall, incorporation of Ta metal appears to permit retention of greatest amount of O and Ct with increasing synthesis temperature. The C content is greatest in samples employing Hf metal fillers, in contrast O content is highest in specimens employing Ta. These differences are likely associated with dissimilarities in the relative amount of mixed bonds, metal carbide and oxide phases in the microstructures, as suggested by HR-XPS spectra of the metal, including Ta 4f, Nb 3d, and Hf 4f convolutions.

Table 5. Summary of $Si_aO_b(M)_cC_d$ compositions.

Elemental Composition by XPS							
		Elements (at.%)					
Sample	Composition $Si_1O_a(M)_bC_c$ (normalized per Si)	C 1s	O 1s	Si 2p	Ta 4f	Nb 3d	Hf 4f
Ta-1200	$Si_1O_{1.028}Ta_{0.012}C_{1.375}$	40.31	30.08	29.26	0.34	-	-

Ta-1500	$Si_1O_{1.009}Ta_{0.015}C_{1.342}$	39.87	29.97	29.7	0.45	-	-
Nb-1200	$Si_1O_{1.014}Nb_{0.006}C_{1.437}$	41.56	29.33	28.92	-	0.18	-
Nb-1500	$Si_1O_{0.725}Nb_{0.009}C_{1.136}$	39.58	25.25	34.83	-	0.32	-
Hf-1200	$Si_1O_{1.006}Hf_{0.018}C_{1.611}$	44.32	27.68	27.51	-	-	0.48
Hf-1500	$Si_1O_{0.855}Hf_{0.014.}C_{1.363}$	42.16	26.46	30.94	-	-	0.44

5.3.1 Thermodynamic Stability and Interdomain Interactions

This investigation surveys the energy landscape for metal (Ta, Hf, Nb) incorporation in $Si_aO_b(M)_cC_d$. This permits identification of any differences in the stability trend resulting from choice of metal. Such fundamental understanding is essential for the development of a framework for stable incorporation of metal additives in PDC structures.

Thermodynamic analysis was done using thermochemical data obtained from calorimetry. Enthalpies of formation from elements ($\Delta H^o_{f, elem}$) and components ($\Delta H^o_{f, comp}$) was determined using enthalpies of dissolution (ΔH^o_{dis}) and thermodynamic cycles. The free energy of formation depends on the change in enthalpy and entropy. Typically, the entropy term for formation from elements is negative, which results from confinement of gaseous O_2 in the structures, however, this is compensated by a highly exothermic enthalpy term. In contrast, the free energy of formation from crystalline

154

components is dominated by enthalpy; the entropy term is of lower magnitude and may be positive because of possible disorder, which would further stabilize the structures. The results are summarized in Tables 6. Overall, the formation of all structures both from elements and from binary components is thermodynamically favorable.

Table 6. Summary of standard enthalpies of dissolution (ΔH_{dis}), enthalpies of oxidation (ΔH^o_{Ox}), enthalpies of formation from elements ($\Delta H^o_{f, elem}$), and enthalpies of formation from components ($\Delta H^o_{f, comp}$).

Sample	Composition $Si_aO_bM_cC_d$	ΔH_{dis} (kJ/mol)	ΔH^o_{Ox} (kJ/mol)	$\Delta H^o_{f, elem}$ (kJ/mol)	$\Delta H^o_{f, comp}$ (kJ/mol)
Nb-1200	$Si_1O_{1.014}Nb_{0.006}C_{1.437}$	-845.36 ± 6.62	-900.67 ± 6.62	-578.88 ± 6.94	-82.80 ± 9.82 (**metal oxide**) -81.40 ± 9.82 (**metal carbide**)
Ta-1200	$Si_1O_{1.028}Ta_{0.012}C_{1.375}$	-770.26 ± 6.48	-825.01 ± 6.78	-636.72 ± 7.10	-137.82 ± 9.72 (**metal oxide**) - 135.72 ± 9.72 (**metal carbide**)
Hf-1200	$Si_1O_{1.006}Hf_{0.018}C_{1.611}$	-749.49 ± 5.27	-807.74 ± 5.64	-754.70 ± 6.03	-256.31 ± 8.97 (**metal oxide**) -257.94 ± 8.97 (**metal carbide**)
Nb-1500	$Si_1O_{0.725}Nb_{0.009}C_{1.136}$	-715.87 ± 6.62	-763.91 ± 6.62	-600.05 ± 6.94	-224.98 ± 9.60 (**metal oxide**)

					-222.84 ± 9.60 (**metal carbide**)
Ta-1500	$Si_1O_{1.009}Ta_{0.015}C_{1.342}$	-721.20 ±2.23	- 775.48 ± 2.99	-676.34 ± 3.65	-182.80 ± 7.85 (**metal oxide**) -179.92 ± 7.85 (**metal carbide**)
Hf-1500	$Si_1O_{0.855}Hf_{0.014}C_{1.363}$	-680.56 ± 5.57	-733.64 ± 5.92	-726.74 ± 6.29	-292.54 ± 9.38 (**metal oxide**) -293.43 ± 9.38 (**metal carbide**)

An important consideration in the application of PDC structures is their propensity for oxidation. The oxidation enthalpies (ΔH°_{Ox}) correspond to change in enthalpy for oxidative decomposition of the PDCs into SiO_2, CO_2, and metal oxide at ambient conditions (see Tables 6). Overall, the enthalpic drive for oxidation increases in the following order: Hf-1500 < Nb-1500 < Ta-1500 < Hf-1200 < Ta-1200 < Nb-1200. This may indicate lower propensity for oxidation in specimens employing Hf fillers. In contrast, for samples synthesized at 1500 °C Ta appears to be most energetically favorable for the oxidation reaction. Nb shows greatest enthalpic drive for oxidative decomposition in samples synthesized at 1200 °C. Overall, choice of metal fillers appears to influence composition, microstructure, and enthalpic drive for oxidation in PDCs.

Since HR-XPS and XRD suggest presence of both metal carbide and metal oxide domains, enthalpies of formation from components are calculated relative to individual phase assemblages comprised of either metal oxide or metal carbide (see Tables 6). This permits identification of the most stable phase assemblage. Generally, the results in Tables 6 ($\Delta H^o_{f, \text{comp}}$) do not indicate significant difference from choice of either metal carbide or oxide as reference. The thermodynamic analysis further permits determination of effect of synthesis temperature on the stability of samples synthesized at 1200 and 1500 ^{o}C. The more exothermic enthalpies of formation of samples pyrolyzed at 1500 ^{o}C indicate more favorable enthalpic drive for microstructural modifications at higher synthesis temperature. The addition of Hf forms the most stable structures at all temperatures. Samples incorporating Nb (Nb-1200 and Nb-1500) display greatest thermodynamic stabilization with increasing pyrolysis temperatures (see $\Delta H^o_{f, \text{comp}}$ in Tables 6). In contrast specimens with Hf (Hf-1200 and Hf-1500) display the least stabilization difference between 1200 and 1500 ^{o}C. Greater stability relative to crystalline components suggests more favorable interdomain interactions and/or more mixed bonding in the microstructures. The general trend of increase in stability with increasing synthesis temperature appears to be independent of choice of metal. It should be noted that overall, results from HR-XPS and XRD highlight consumption of metal-oxygen and formation of metal-carbon bonds between 1200-1500 ^{o}C, perhaps implying a more stable incorporation of metal carbide fillers.

5.4 Conclusions

This work investigates thermodynamic stabilization in $Si_aO_b(M)_cC_d$ structures incorporating Ta, Hf, or Nb. Generally, higher synthesis temperature promotes increase in the ratio of $SiOC_3 : SiO_3C$ mixed bonds. Ta metal fillers stabilize the formation of SiO_3C bonds. Between 1200 and 1500 °C higher synthesis temperature is consistent with greater thermodynamic stabilization of the structures. These results indicate most stable incorporation of Hf into SiOC microstructures, independent of synthesis temperature. Choice of metal filler impacts the microstructure and thermodynamic stability of the PDCs. metal carbide fillers may form more stable $Si_aO_b(M)_cC_d$ structures. This work provides initial framework for stable incorporation of metal fillers in PDCs.

Acknowledgement

REFERENCES

1. Colombo, P., Mera, G., Riedel, R. & Sorarù, G. D. Polymer-Derived Ceramics: 40 Years of Research and Innovation in Advanced Ceramics. *J. Am. Ceram. Soc.* **93**, 1805–1837 (2010).

2. Colombo, P. *Polymer Derived Ceramics: From Nano-structure to Applications*. (DEStech Publications, Inc, 2010).

3. Miele†, P., Bernard, S., Cornu, D. & Toury, B. Recent Developments in Polymer-Derived Ceramic Fibers (PDCFs): Preparation, Properties and Applications – A Review. *Soft Mater.* **4**, 249–286 (2007).

4. Duperrier, S. *et al.* Design of a Series of Preceramic B-Tri(methylamino)borazine-Based Polymers as Fiber Precursors: Architecture, Thermal Behavior, and Melt-Spinnability. *Macromolecules* **40**, 1018–1027 (2007).

5. Leonel, G. J., Mujib, S. B., Singh, G. & Navrotsky, A. Thermodynamic stabilization of crystalline silicon carbide polymer-derived ceramic fibers. *Int. J. Ceram. Eng. Sci.* **4**, 315–326 (2022).

6. Luan, X., Gu, S., Zhang, Q., Cheng, L. & Riedel, R. An electrically conductive SiBCN film prepared via polymer-derived ceramic and chemical vapor deposition methods. *Sens. Actuators Phys.* **330**, 112824 (2021).

7. Goerke, O., Feike, E., Heine, T., Trampert, A. & Schubert, H. Ceramic coatings processed by spraying of siloxane precursors (polymer-spraying). *J. Eur. Ceram. Soc.* **24**, 2141–2147 (2004).

8. Steyer, T. E. Shaping the Future of Ceramics for Aerospace Applications. *Int. J. Appl. Ceram. Technol.* **10**, 389–394 (2013).

9. Saccone, G., Gardi, R., Alfano, D., Ferrigno, A. & Del Vecchio, A. Laboratory, on-ground and in-flight investigation of ultra high temperature ceramic composite materials. *Aerosp. Sci. Technol.* **58**, 490–497 (2016).

10. Torrey, J. D. & Bordia, R. K. Processing of Polymer-Derived Ceramic Composite Coatings on Steel. *J. Am. Ceram. Soc.* **91**, 41–45 (2008).

11. Soboyejo, W. O. *et al.* Review of High Temperature Ceramics for Aerospace Applications. *Adv. Mater. Res.* **1132**, 385–407 (2016).

12. Barroso, G. S., Krenkel, W. & Motz, G. Low thermal conductivity coating system for application up to 1000°C by simple PDC processing with active and passive fillers. *J. Eur. Ceram. Soc.* **35**, 3339–3348 (2015).

13. Parcianello, G., Bernardo, E. & Colombo, P. Cordierite ceramics from silicone resins containing nano-sized oxide particle fillers. *Ceram. Int.* **39**, 8893–8899 (2013).

14. Vakifahmetoglu, C., Presser, V., Yeon, S.-H., Colombo, P. & Gogotsi, Y. Enhanced hydrogen and methane gas storage of silicon oxycarbide derived carbon. *Microporous Mesoporous Mater.* **144**, 105–112 (2011).

15. Sarkar, S., Gan, Z., An, L. & Zhai, L. Structural Evolution of Polymer-Derived Amorphous SiBCN Ceramics at High Temperature. *J. Phys. Chem. C* **115**, 24993–25000 (2011).

16. Zhou, S., Mei, H., Chang, P., Lu, M. & Cheng, L. Molecule editable 3D printed polymer-derived ceramics. *Coord. Chem. Rev.* **422**, 213486 (2020).

17. Scheffler, M., Greil, P., Berger, A., Pippel, E. & Woltersdorf, J. Nickel-catalyzed in situ formation of carbon nanotubes and turbostratic carbon in polymer-derived ceramics. *Mater. Chem. Phys.* **84**, 131–139 (2004).

18. Greil, P. Polymer Derived Engineering Ceramics. *Adv. Eng. Mater.* **2**, 339–348 (2000).

19. Wang, X., Wang, J. & Wang, H. Performance and structural evolution of high-temperature organic adhesive for joining Al2O3 ceramics. *Int. J. Adhes. Adhes.* **45**, 1–6 (2013).

20. Hernández-Rodríguez, P. & López-Honorato, E. Polymer derived SiC environmental barrier coatings with superwetting properties. *Ceram. Int.* **43**, 11289–11295 (2017).

21. Leonel, G. J., Guo, X., Singh, G. & Navrotsky, A. Compositional Analysis of SiOC(H) Powders: A Comparison of X-ray Photoelectron Spectroscopy (XPS) and Combustion Analysis. *Ceramics* **6**, 74–85 (2023).

22. Morcos, R. M. *et al.* Energetics of SixOyCz Polymer-Derived Ceramics Prepared Under Varying Conditions. *J. Am. Ceram. Soc.* **91**, 2969–2974 (2008).

23. Varga, T. *et al.* Thermodynamically Stable SixOyCz Polymer-Like Amorphous Ceramics. *J. Am. Ceram. Soc.* **90**, 3213–3219 (2007).

24. Niu, M. *et al.* Radiation Effects in the Crystalline–Amorphous SiOC Polymer-Derived Ceramics: Insights from Experiments and Molecular Dynamics Simulation. *ACS Appl. Mater. Interfaces* **13**, 40106–40117 (2021).

25. Sugie, C., Navrotsky, A., Lauterbach, S., Kleebe, H.-J. & Mera, G. Structure and Thermodynamics of Silicon Oxycarbide Polymer-Derived Ceramics with and without Mixed-Bonding. *Materials* **14**, 4075 (2021).

26. Zlotnik, S., Sahu, S. K., Navrotsky, A. & Vilarinho, P. M. Pyrochlore and Perovskite Potassium Tantalate: Enthalpies of Formation and Phase Transformation. *Chem. – Eur. J.* **21**, 5231–5237 (2015).

27. Navrotsky, A. Progress and New Directions in Calorimetry: A 2014 Perspective. *J. Am. Ceram. Soc.* **97**, 3349–3359 (2014).

28. Thomas C. Allison. NIST-JANAF Thermochemical Tables - SRD 13. (2013).

29. Kornilov, A. N., Ushakova, I. M., Huber, E. J. & Holley, C. E. The enthalpy of formation of hafnium dioxide. *J. Chem. Thermodyn.* **7**, 21–26 (1975).

30. Mah, A. D. *Heats of Formation of Zirconium Carbide and Hafnium Carbide*. (U.S. Department of the Interior, Bureau of Mines, 1964).

31. Ikezawa, Y., Sawatari, T. & Terashima, H. In situ FTIR study of pyridine adsorbed on Au(111), Au(100) and Au(110) electrodes. *Electrochimica Acta* **46**, 1333–1337 (2001).

32. Yelil Arasi, A., Juliet Latha Jeyakumari, J., Sundaresan, B., Dhanalakshmi, V. & Anbarasan, R. The structural properties of Poly(aniline)—Analysis via FTIR spectroscopy. *Spectrochim. Acta. A. Mol. Biomol. Spectrosc.* **74**, 1229–1234 (2009).

33. Benning, L. G., Phoenix, V. R., Yee, N. & Tobin, M. J. Molecular characterization of cyanobacterial silicification using synchrotron infrared micro-spectroscopy1 1Associate editor: J. P. Amend. *Geochim. Cosmochim. Acta* **68**, 729–741 (2004).

34. Osswald, J. & Fehr, K. T. FTIR spectroscopic study on liquid silica solutions and nanoscale particle size determination. *J. Mater. Sci.* **41**, 1335–1339 (2006).

35. Low-k organosilicate films prepared by tetravinyltetramethylcyclotetrasiloxane: Journal of Applied Physics: Vol 92, No 2.

36. Mastalerz, M. & Marc Bustin, R. Electron microprobe and micro-FTIR analyses applied to maceral chemistry. *Int. J. Coal Geol.* **24**, 333–345 (1993).

37. Thomas, P. S., Guerbois, J.-P., Russell, G. F. & Briscoe, B. J. FTIR Study of the Thermal Degradation of Poly(vinyl Alcohol). *J. Therm. Anal. Calorim.* **64**, 501–508 (2001).

38. Chen, Y., Caro, L. d., Mastalerz, M., Schimmelmann, A. & Blandón, A. Mapping the chemistry of resinite, funginite and associated vitrinite in coal with micro-FTIR. *J. Microsc.* **249**, 69–81 (2013).

39. Mendelovici, E., Frost, R. L. & Kloprogge, J. T. Modification of Chrysotile Surface by Organosilanes: An IR–Photoacoustic Spectroscopy Study. *J. Colloid Interface Sci.* **238**, 273–278 (2001).

40. Canaria, C. A., Lees, I. N., Wun, A. W., Miskelly, G. M. & Sailor, M. J. Characterization of the carbon–silicon stretch in methylated porous silicon— observation of an anomalous isotope shift in the FTIR spectrum. *Inorg. Chem. Commun.* **5**, 560–564 (2002).

41. Wu, X. C., Cai, R. Q., Yan, P. X., Liu, W. M. & Tian, J. SiCN thin film prepared at room temperature by r.f. reactive sputtering. *Appl. Surf. Sci.* **185**, 262–266 (2002).

42. Castro, D. C. *et al.* Synthesis and Characterization of Mesoporous Nb $_2$ O $_5$ and Its Application for Photocatalytic Degradation of the Herbicide Methylviologen. *J. Braz. Chem. Soc.* (2015)

43. Ramadoss, A., Krishnamoorthy, K. & Kim, S. J. Novel synthesis of hafnium oxide nanoparticles by precipitation method and its characterization. *Mater. Res. Bull.* **47**, 2680–2684 (2012).

44. Zhang, N., Li, L. & Li, G. Nanosized amorphous tantalum oxide: a highly efficient photocatalyst for hydrogen evolution. *Res. Chem. Intermed.* **43**, 5011–5024 (2017).

45. Babar, Z. U. D. *et al.* Magnetic phase transition from paramagnetic in Nb 2 AlC-MAX to superconductivity-like diamagnetic in Nb 2 C-MXene: an experimental and computational analysis. *RSC Adv.* **10**, 25669–25678 (2020).

46. Tressler, R. E. Recent developments in fibers and interphases for high temperature ceramic matrix composites. *Compos. Part Appl. Sci. Manuf.* **30**, 429–437 (1999).

47. Duan, W. *et al.* Synthesis and microwave absorption properties of SiC nanowires reinforced SiOC ceramic. *J. Eur. Ceram. Soc.* **34**, 257–266 (2014).

48. Blum, Y. D., MacQueen, D. B. & Kleebe, H.-J. Synthesis and characterization of carbon-enriched silicon oxycarbides. *J. Eur. Ceram. Soc.* **25**, 143–149 (2005).

49. Jafari, B. *et al.* Development of a new composite ceramic membrane from mullite, silicon carbide and activated carbon for treating greywater. *Ceram. Int.* **47**, 34667–34675 (2021).

50. Alper, J. P. *et al.* Silicon carbide nanowires as highly robust electrodes for micro-supercapacitors. *J. Power Sources* **230**, 298–302 (2013).

51. Kwon, H., Kim, W. & Kim, J. Stability Domains of NbC and Nb(CN) During Carbothermal Reduction of Niobium Oxide. *J. Am. Ceram. Soc.* **98**, 315–319 (2015).

52. Sacks, M. D., Wang, C.-A., Yang, Z. & Jain, A. Carbothermal reduction synthesis of nanocrystalline zirconium carbide and hafnium carbide powders using solution-derived precursors. *J. Mater. Sci.* **39**, 6057–6066 (2004).

53. Réjasse, F., Trolliard, G., Rapaud, O., Maître, A. & David, J. TEM study of the reaction mechanisms involved in the carbothermal reduction of hafnia. *RSC Adv.* **5**, 45341–45350 (2015).

54. Paprocki, K. *et al.* The comparative studies of HF CVD diamond films by Raman and XPS spectroscopies. *Opt. Mater.* **95**, 109251 (2019).

55. Sang, Z. *et al.* SiOC nanolayer wrapped 3D interconnected graphene sponge as a high-performance anode for lithium ion batteries. *J. Mater. Chem. A* **6**, 9064–9073 (2018).

56. Zhang, X. *et al.* Stable high-capacity and high-rate silicon-based lithium battery anodes upon two-dimensional covalent encapsulation. *Nat. Commun.* **11**, 3826 (2020).

57. Mera, G., Navrotsky, A., Sen, S., Kleebe, H.-J. & Riedel, R. Polymer -derived SiCN and SiOC ceramics – structure and energetics at the nanoscale. *J. Mater. Chem. A* **1**, 3826–3836 (2013).

58. Greczynski, G. & Hultman, L. C 1s Peak of Adventitious Carbon Aligns to the Vacuum Level: Dire Consequences for Material's Bonding Assignment by Photoelectron Spectroscopy. *ChemPhysChem* **18**, 1507–1512 (2017).

59. Lahoz, R., Espinós, J. P., Yubero, F., González-Elipe, A. R. & Fuente, G. F. de la. "In situ" XPS studies of laser-induced surface nitridation and oxidation of tantalum. *J. Mater. Res.* **30**, 2967–2976 (2015).

60. Powell, C. NIST X-ray Photoelectron Spectroscopy Database. In NIST Standard Reference Database Number 20, National Institute of Standards and Technology: Gaithersburg MD, 20899, 2000. (1989).

61. Lee, S., Yun, D.-J., Rhee, S.-W. & Yong, K. Atomic layer deposition of hafnium silicate film for high mobility pentacene thin film transistor applications. *J. Mater. Chem*. **19**, 6857–6864 (2009).

62. Hans, K., Latha, S., Bera, P. & Barshilia, H. C. Hafnium carbide based solar absorber coatings with high spectral selectivity. *Sol. Energy Mater. Sol. Cells* **185**, 1–7 (2018).

63. Gupta, A., Mittal, M., Singh, M. K., Suib, S. L. & Pandey, O. P. Low temperature synthesis of NbC/C nano-composites as visible light photoactive catalyst. *Sci. Rep.* **8**, 13597 (2018).

64. Chang, Y.-Y. *et al.* Biological Characteristics of the MG-63 Human Osteosarcoma Cells on Composite Tantalum Carbide/Amorphous Carbon Films. *PLOS ONE* **9**, e95590 (2014).

65. Hellwig, M. *et al.* Stabilization of Amide-Based Complexes of Niobium and Tantalum Using Malonates as Chelating Ligands: Precursor Chemistry and Thin Film Deposition. *Chem. Mater.* **19**, 6077–6087 (2007).

66. Mullapudi, G. S. R. *et al.* Low-Temperature Deposition of Inorganic–Organic HfO2–PMMA Hybrid Gate Dielectric Layers for High-Mobility ZnO Thin-Film Transistors. *ACS Appl. Electron. Mater.* **1**, 1003–1011 (2019).

67. Aubry, D. *et al.* Molecular functionalization of tantalum oxide surface towards development of apatite growth. *Appl. Surf. Sci.* **255**, 4765–4772 (2009).

68. Lyu, Y., Tang, H. & Zhao, G. Effect of Hf and B incorporation on the SiOC precursor architecture and high-temperature oxidation behavior of SiHfBOC ceramics. *J. Eur. Ceram. Soc.* **40**, 324–332 (2020).

69. A. Abass, M., A. Syed, A., Gervais, C. & Singh, G. Synthesis and electrochemical performance of a polymer-derived silicon oxycarbide/boron nitride nanotube composite. *RSC Adv.* **7**, 21576–21584 (2017).

70. Ionescu, E. *et al.* Polymer-Derived SiOC/ZrO2 Ceramic Nanocomposites with Excellent High-Temperature Stability. *J. Am. Ceram. Soc.* **93**, 241–250 (2010).

71. Okamura, H. & Bowen, H. K. Preparation of alkoxides for the synthesis of ceramics. *Ceram. Int.* **12**, 161–171 (1986).

72. Yang, S. *et al.* Preparation of high-purity tantalum ethoxide by vacuum distillation. *Trans. Nonferrous Met. Soc. China* **18**, 196–201 (2008).

73. Bickmore, C. R., Waldner, K. F., Treadwell, D. R. & Laine, R. M. Ultrafine Spinel Powders by Flame Spray Pyrolysis of a Magnesium Aluminum Double Alkoxide. *J. Am. Ceram. Soc.* **79**, 1419–1423 (1996).

CHAPTER 6

CRYSTALLOGRAPHIC AND COMPOSITIONAL DEPENDENCE OF THERMODYNAMIC STABILITY OF [CO(II), CU(II), AND ZN(II)] IN 2-METHYLIMIDAZOLE-CONTAINING ZEOLITIC IMIDAZOLATE FRAMEWORKS (ZIFS)

Abstract: We report the first systematic study experimentally investigating the effect of changes to the divalent metal node on the thermodynamic stability of 3-dimensional (3D) and 2-dimensional (2D) zeolitic imidazolate frameworks (ZIFs) based on 2-methylimidazolate linkers. In particular, the comparison of enthalpies of formation for materials based on cobalt, copper, and zinc suggests that the use of nodes with larger ionic radii metals leads to a stabilization of the porous sodalite topology with respect to the corresponding higher density diamondoid-topology polymorphs. The stabilizing effect of metals is dependent on the framework topology and dimensionality. With previous works pointing to solvent-mediated transformation of 2D ZIF-L structures to their 3D analogs in the sodalite topology, thermodynamic measurements show that contrary to popular belief, the 2D frameworks are energetically stable, thus, shedding light on the energetic landscape in these materials. Additionally, the calorimetric data confirm that a change in dimensionality (3D → 2D) and the presence of structural water

within the framework can stabilize structures by as much as 40 kJ/mol, making the formation of zinc-based ZIF-L material under such conditions thermodynamically preferred to the formation of both ZIF-8 and its dense, diamondoid-topology polymorph.

6 .1 Introduction

Metal organic frameworks (MOFs) have emerged over the last two decades as a promising class of advanced materials based on metal-containing nodes bridged through organic linkers, capable of forming two- (2D) and three-dimensional (3D) frameworks.[1] The linker-node assembly offers a high-degree of tunability,[2–5] providing access to potentially porous materials with a wide range of applications, from catalysis, gas sorption, to rocket propellants.[6–10] A subclass of these materials are zeolitic imidazolate frameworks (ZIFs),[6, 7, 11–15] based on tetrahedrally coordinated metal nodes bridged through azolate linkers,[11, 16, 17] resulting in materials with analogous topologies as those found in natural zeolites.[15]

By employing different metal-ligand combinations,[17, 18] a wide range of frameworks have been prepared with tunable material properties,[19–21] from sorption selectivity to material porosity.[8, 10, 22] Moreover, ZIFs and related composites also offer exceptional thermal and hydrothermal stability, including under acidic or basic conditions,[23, 24] which is considered a prerequisite for any wide-spread application.[25, 26] Furthermore, various ZIF polymorphs are accessible through variations of the synthesis conditions.[18, 27, 28] For example, real-time studies of the mechanochemical ball-milling preparation of ZIF-8, a popular ZIF material based on divalent zinc nodes and 2-

methylimidazolate linkers (MeIm⁻), have revealed the sequential formation of the highly porous SOD-topology material ZIF-8, followed by the appearance of katsenite (*kat*) and finally diamondoid (*dia*) topology polymorphs.[17, 28, 29]

A considerable amount of effort has gone into investigating the synthesis of MOFs,[18, 29, 30] as well as the thermal stability[31] and resistance to structural degradation in water[5] of such materials, often with an emphasis on their kinetic stability.[32] Despite a focus on the kinetics of reactivity,[32] thermodynamic investigations are required to assess whether reactions can take place at all. To the best of our knowledge, the current explorations of the driving forces underlying MOF formation remain limited to a small number of systematic studies on the thermodynamic stability of MOFs, despite such understanding being critical to distinguish between metastability and real stability, an important parameter for the adoption and development of MOFs in long-term applications. Recently, the thermodynamic stability of the MOF-74 family has been demonstrated to be directly related to their resistance to hydrolysis.[33] Our team has previously investigated the relationship between linker substituent and thermodynamic stability of isostructural ZIFs, suggesting that thermodynamic stability correlates with electrostatic surface potential and Hammett σ-constants of the substituent.[17] The same study shows that variations in linker substituents of isostructural MOFs can cause enthalpy of formation to change by as much as 30 kJ/mol.[17]

In this work, we present a complementary approach to assess ZIF stability, by investigating the stabilizing effect of metal substitution across a series of topologically similar frameworks. Rather than investigating the effect of linker substituents in

isostructural ZIFs,[17] we investigate the enthalpic contribution of metal substitution on topologically similar ZIFs, namely; SOD-Co(MeIm)$_2$,[34] SOD-Zn(MeIm)$_2$,[15] *dia*-Co(MeIm)$_2$,[35] *dia*-Cu(MeIm)$_2$,[36] and *dia*-Zn(MeIm)$_2$ [35] (Figure 1). This allows the direct assessment of the thermodynamic stability of these ZIFs. This systematic study enables better understanding of the stabilizing effects arising from the choice of metal nodes, and what role framework topology has on metal effects. Furthermore, we expand on our work investigating 3D materials to include 2D layered systems Zn-ZIF-L[37] and Co-ZIF-L,[38] allowing us to capture the effect of framework dimension on thermodynamic stability.
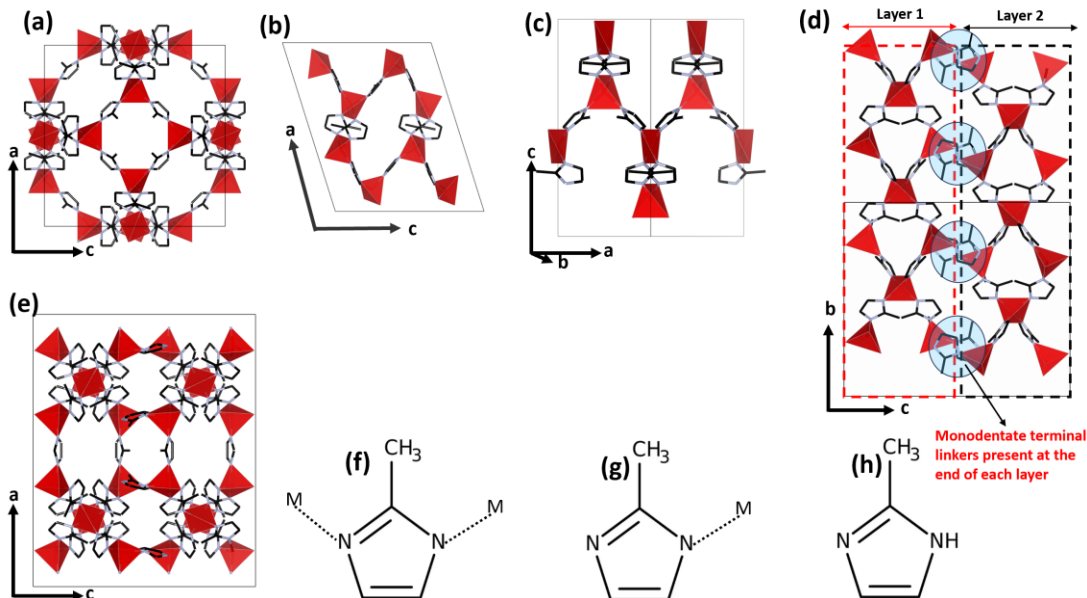
Figure 1. Structure of ZIFs in (a) 3-dimensional (3D) SOD topology, (b) 3-dimensional Zn and Co *dia* topology, (c) 3-dimensional (3D) Cu *dia* topology with distorted polyhedra, and (d-e) 2-dimensional (2D) ZIF-L configuration. All ZIFs contain (f) bidentate bridging linkers, however, ZIF-L has additional (g) terminal HMeIm, and (h) free linkers between adjacent layers. Red tetrahedra represent metal (M(II)) centers. C-H

bonds, water, and free linkers (in ZIF-L) are omitted for simplicity. Carbon and nitrogen are depicted by black and blue, respectively.

6.2 Experimental Method

6.2.1 Materials and Methods

All reagents and solvents were obtained from commercial sources and were used without further purification. The materials investigated in this work have been reported in previous studies.[15, 34, 39, 40]

6.2.2 Thermogravimetric Analysis (TGA)

A Mettler-Toledo TGA/DSC 1 system was used to conduct thermogravimetric analysis (TGA) on a sample weighing between 5 and 10 mg loaded in a 70 µL alumina pan. The sample was heated from 25 to 700 °C at a rate of 10 °C/min, with a continuous flow of air at 40 mL/min. Exceptionally, TGA data of Co-ZIF-L, Zn-ZIF-L and *dia*-Co(MeIm)$_2$ were recorded on a TAS Lab TGA 5500, with samples between 5 and 10 mg, loaded in a 100 µL platinum pan. The samples were heated from 25 to 700 °C at a rate of 10 °C/min, with a continuous flow of air at 25 mL/min.

6.2.3 Powder X-ray Diffraction (PXRD)

A Bruker D2 Phaser powder diffractometer, equipped with a Ni-filtered Cu-$K\alpha$ (λ = 1.5418 Å) source and Lynxeye 1D detector (Bruker AXS, Madison, WI, USA) was used to obtain powder X-ray diffractograms.

6.2.4 Fourier-Transform Infrared Attenuated Total Reflectance (FTIR-ATR) Spectroscopy

Infrared spectra were obtained using a Bruker Alpha II FTIR spectrometer and are reported in wavenumber (cm^{-1}) units.

6.2.5 Synthetic Procedures

Synthesis of SOD-Zn(MeIm)$_2$:

The material SOD-Zn(MeIm)$_2$ was synthesized using the liquid-assisted grinding (LAG) methodology. To a 15 mL stainless steel milling jar were added ZnO (1 mmol, 81.38 mg), 2.1 mmol HMeIm (2.1 mmol, 172.41 mg), NH$_4$OAc (0.13 mmol, 10 mg), and 100 μL of ethanol with two 1.3 g stainless steel milling balls. The mixture was ball milled at 30 Hz for 30 minutes, when PXRD analysis revealed the absence of reflections corresponding to ZnO. The product was washed by stirring overnight in 20 mL of methanol, was isolated by filtration, and evacuated by exposure to a high vacuum at 80 °C overnight.

Synthesis of SOD-Co(MeIm)$_2$:

SOD-Co(Meim)$_2$ was synthesized according to a previous report.[41]

Synthesis of *dia*-Zn(MeIm)$_2$:

The material *dia*-Zn(MeIm)$_2$ was synthesized by adding ZnO (0.81 mmol, 66 mg), HmeIm (1.63 mmol, 134 mg), and 35 µL of 10% aqueous acetic acid to a 15 mL poly(methylmethacrylate) milling jar with two 1.3 g stainless steel milling balls. The mixture was ball milled at 30 Hz for 90 minutes, when PXRD analysis revealed the absence of reflections corresponding to ZnO. The product was then washed by stirring for 30 minutes in water, isolated by filtration, then washed overnight by stirring in 20 mL of benzene. The material was collected again by filtration and exposed to high vacuum at 80 °C overnight.

Synthesis of *dia*-Co(MeIm)$_2$:

The material *dia*-Co(MeIm)$_2$ was synthesized according to a recent report.[39]

Synthesis of *dia*-Cu(MeIm)$_2$:

The material *dia*-Cu(MeIm)$_2$ was synthesized according to a recent report.[36]

Synthesis of Zn-ZIF-L:

For synthesis of the materials Zn-ZIF-L, a mixture consisting of Zn(NO$_3$)$_2$·6 H$_2$O (1 mmol, 298 mg), HMeIm (8 mmol, 656 mg) and 25 µL water was mixed by resonant acoustic mixing (RAM) for 30 minutes at 60 *g* to yield ZIF-L, confirmed by PXRD analysis. The ZIF was stirred in 15 mL of water for 60 minutes, followed by centrifugation at 4,500 rpm for 15 mins and microcrystalline product recovered by decanting, repeated three times.[40]

Synthesis of Co-ZIF-L:

For the synthesis of Co-ZIF-L, a mixture of $Co(NO_3)_2 \cdot 6\ H_2O$ (1 mmol, 291 mg), HMeIm (8 mmol, 656 mg) and 25 µL water was agitated by resonant acoustic mixing (RAM) for 30 minutes at 60 g to yield Co-ZIF-L, confirmed by PXRD analysis. The ZIF was stirred in 15 mL of water for 60 minutes, followed by centrifugation at 4,500 rpm for 15 mins and microcrystalline product recovered by decanting, repeated three times.[40]

6.2.6 Thermodynamic Measurements

A CSC 4400 isothermal microcalorimeter used for solution calorimetry was calibrated through the dissolution of KCl at 298.15 K. For calorimetric measurements and calculations, thermodynamic cycles (see Tables 1-3) were prepared for each of the ZIFs. For dissolution of the samples, 25 g of 5 N aqueous HCl solution was placed in a 50 mL Teflon cell under mechanical stirring at 0.5 Hz. The Teflon cell was inserted and contained inside the calorimeter maintained at 298.15 K. More details on the experimental procedure are provided in previous work.[13] The results we report show calculated statistical uncertainties within a 95 % confidence interval.

6.3 Results and Discussion

The prepared ZIFs were analyzed by (XRD, FTIR, and TG-DSC). The measured Fourier-transform infrared attenuated total reflectance (FTIR-ATR) spectra (see Figure 2) indicate the presence of expected framework bonds. Powder X-ray diffraction (PXRD), and the results confirm formation of the desired frameworks (see Figures 3-5).

Thermogravimetric analysis (TGA) performed in air (see Figure 6) enabled the experimental evaluation of the metal content in the materials, with the final metal oxide residue formed during oxidative decomposition of the MOFs consistent with the expected chemical compositions.
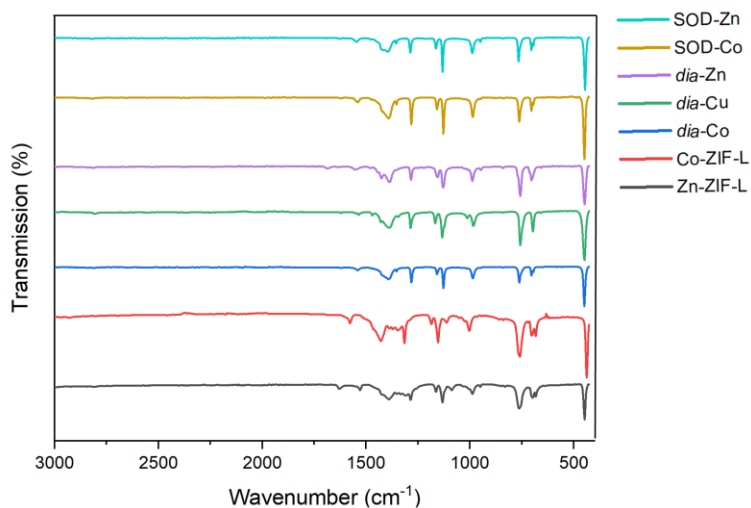
Figure 2. FTIR spectra of the prepared ZIFs.
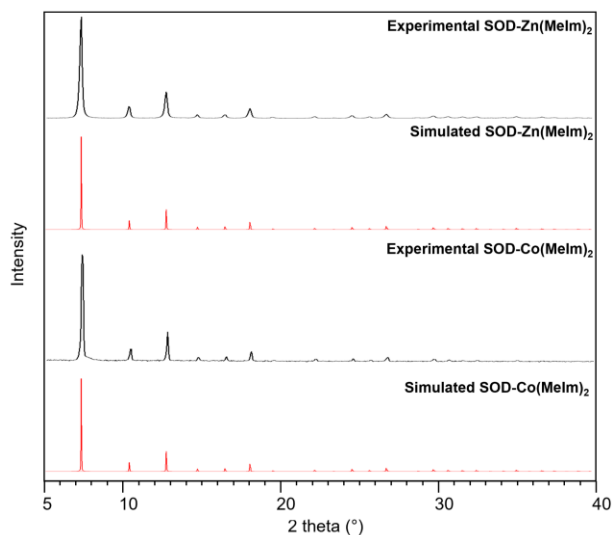
Figure 3. PXRD patterns of synthesized SOD-ZIFs compared to PXRD patterns simulated from crystal structure data for SOD-Zn(MeIm)$_2$ (CSD code: VELVOY), and SOD-Co(MeIm)$_2$ (CSD code: GITTOT).
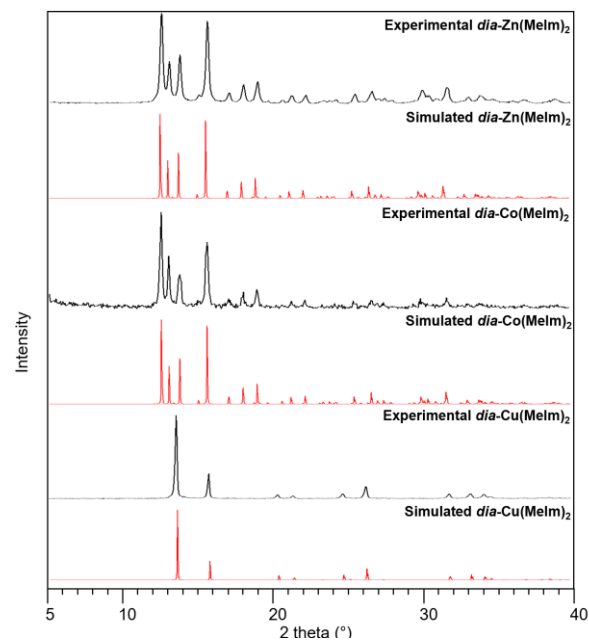
Figure 4. PXRD patterns of synthesized *dia*-ZIFs compared to PXRD patterns simulated from crystal structure data for *dia*-Zn(MeIm)$_2$, *dia*-Co(MeIm)$_2$ (CSD code: OFERUN01), and *dia*-Cu(MeIm)$_2$ (CSD code: TEYZAC).
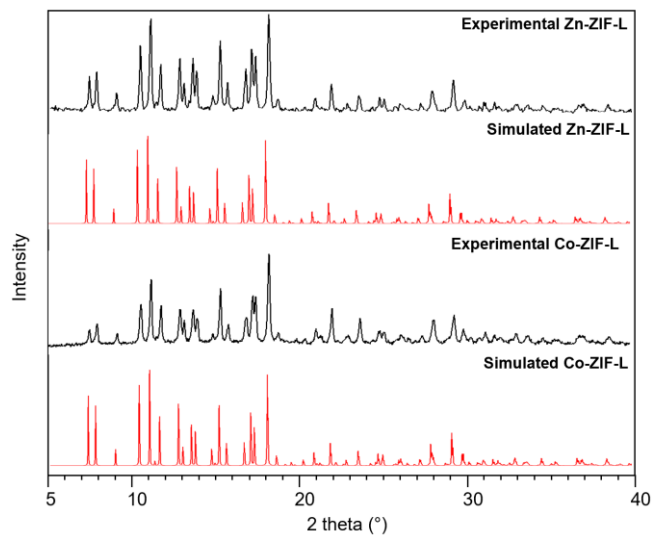
Figure 5. PXRD patterns of synthesized ZIF-L materials compared to PXRD patterns simulated from crystal structure data for Zn-ZIF-L (CSD code: IWOZOL).
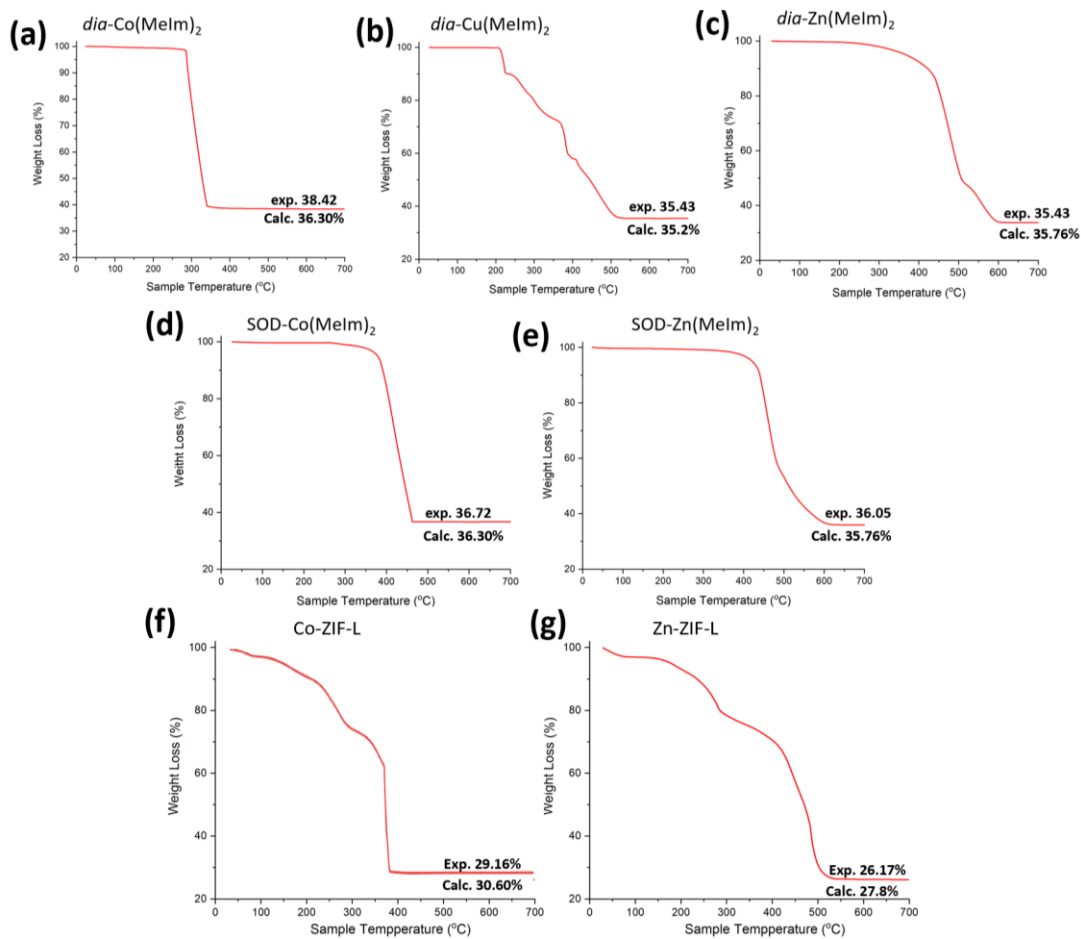
Figure 6. Thermograms for prepared ZIFs, with experimental (Exp.) and calculated (Calc.) residue indicated, based on oxidative decomposition to (a, d) Co_3O_4, (b) Cu_2O, and (c, e, g) ZnO.

6.3.1 Thermodynamic Analysis

Acid solution calorimetry permits quantitation of enthalpies of dissolution of each of the frameworks as well as corresponding metal oxides and ligands. The use of enthalpies of dissolution and appropriate thermodynamic cycles (see Tables 1-3) enables determination of the enthalpic drive for the formation of each framework. To ensure that

176

the heats of dissolution used for calculating heats of formation of the MOFs did not include enthalpic contributions resulting from the formation of cation coordination complexes from the interaction between dissolved linker and cation, separate experiments are conducted. The enthalpies associated with the individual dissolution of ~5 mg of CuO and 2-methylimidazole (HMeIm) in fresh HCl solution are -53.34 ± 0.95, and -43.56 ± 0.26 kJ/mol, respectively, based on four individual calorimetric runs for each material. The average enthalpy of dissolution for 5 mg of CuO in HCl solution containing ~5 mg of already dissolved MeIm is -53.03 ± 0.81 kJ/mol. The average enthalpy of dissolution for 5 mg of HMeIm in HCl solution containing ~5 mg of already dissolved CuO is -43.75 ± 0.59 kJ/mol. It is concluded that no significant interaction occurs between the cations and linkers in the dissolved MOFs. The enthalpies of dissolution of the frameworks, linker, and corresponding metal oxide are summarized in Table 4.

6.3.2 Thermochemical Cycles

Table 1: Thermochemical cycle used to calculate enthalpy of formation (ΔH°_f) of *dia* and SOD frameworks relative to metal (M) oxides and organic linker 2-methylimidazole (HmeIm) in kJ/mol.

MO (s, 298 K) + 2HmeIm (s, 298 K)→M(MeIm)$_2$ (s, 298 K) + H$_2$O (l, 298)
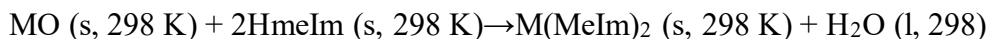
Reaction	ΔH (kJ/mol)
M(MeIm)$_2$ (s, 298 K) → M^{+2} (aq, 298 K) + 2 MeIm^{-1} (aq, 298 K)	ΔH_1

MO (s, 298 K) +2H$^+$ (aq, 298 K) $\rightarrow$ M^{+2} (aq, 298 K)+ H$_2$O (aq, 298 K)	ΔH_2
HmeIm (s, 298 K) $\rightarrow$ H$^+$ (aq, 298 K) + MeIm^{-1} (aq, 298 K)	ΔH_3
H$_2$O (l, 298 K) $\rightarrow$ H$_2$O (aq, 298 K)	ΔH_4
$\Delta H^o_f = -\Delta H_1 + \Delta H_2 + 2\Delta H_3 - \Delta H_4$	ΔH^o_f

Table 2. Thermochemical cycle used to calculate enthalpy of formation (ΔH^o_f) of ZIF-L relative to endmembers, Metal(M) oxide and organic linker (HMeIm) in kJ/mol.

MO (s, 298 K) $+ \frac{5}{2}$ HMeIm (s, 298 K) $+ \frac{1}{2}$ H$_2$O (l, 298 K) $\rightarrow$

M(MeIm)$_2$(HMeIm)$_{1/2}$(H$_2$O)$_{3/2}$ (s, 298 K)

Reaction	ΔH (kJ/mol)
M(MeIm)$_2$(HMeIm)$_{1/2}$(H$_2$O)$_{3/2}$ (s, 298 K) $\rightarrow$ M^{+2} (aq, 298 K) $+ \frac{5}{2}$ MeIm^{-1} (aq, 298 K) $+ \frac{3}{2}$ H$_2$O (aq, 298K) $+ \frac{1}{2}$H$^+$ (aq, 298 K)	ΔH_1
H$_2$O (l, 298 K) $\rightarrow$ H$_2$O (aq, 298 K)	ΔH_2
HMeIm (s, 298 K) $\rightarrow$ H$^+$ (aq, 298 K) + MeIm^{-1} (aq, 298 K)	ΔH_3
MO (s, 298 K) +2H$^+$ (aq, 298 K) $\rightarrow$ M^{+2} (aq, 298 K) + H$_2$O (aq, 298 K)	ΔH_4
$\Delta H^o_f = -\Delta H_1 + \frac{1}{2}\Delta H_2 + \frac{5}{2}\Delta H_3 + \Delta H_4$	ΔH^o_f

Table 3. Thermochemical cycle used to calculate enthalpy of formation ($\Delta H^o{}_f$) of ZIF-L from SOD or dia-Co or $Zn(Meim)_2$ and linker and water in kJ/mol.

SOD-M(MeIm)$_2$ (s, 298 K) $+\frac{1}{2}$HMeIm (s, 298 K) $+\frac{3}{2}$ H$_2$O (l, 298 K) $\rightarrow$

M(MeIm)$_2$(HMeIm)$_{1/2}$(H$_2$O)$_{3/2}$ (s, 298 K)

Reaction	ΔH (kJ/mol)
M(MeIm)$_2$(HMeIm)$_{1/2}$(H$_2$O)$_{3/2}$ (s, 298 K) $\rightarrow$ M $^{+2}$ (aq, 298 K) $+\frac{5}{2}$MeIm $^{-1}$ (aq, 298 K) $+ +\frac{3}{2}$H$_2$O (aq, 298K) $+\frac{1}{2}$H$^+$ (aq, 298 K)	ΔH_1
H$_2$O (l, 298 K) $\rightarrow$ H$_2$O (aq, 298 K)	ΔH_2
HMeIm (s, 298 K) $\rightarrow$ H $^+$ (aq, 298 K) $+$ MeIm $^{-1}$ (aq, 298 K)	ΔH_3
SOD-M(MeIm)$_2$ (s, 298 K) $\rightarrow$ M $^{+2}$ (aq, 298 K) $+$ 2MeIm $^{-1}$ (aq, 298 K)	ΔH_4
$\Delta H^o{}_f = -\Delta H_1 + \frac{3}{2} \Delta H_2 + \frac{1}{2} \Delta H_3 + \Delta H_4$	$\Delta H^o{}_f$

- Aq=aqueous; s=solid, l=liquid

Table 4. Enthalpies of dissolution in 5N HCl at 298.15 K and formation from endmembers (metal oxide, linker, and balance water).

Sample	ΔH_{dis} (kJ/mol)	$\Delta H^o{}_f$ (kJ/mol)
HMeIm	-43.75 $\pm$ 0.59	-

H_2O[28]	-0.5	-
CuO	-53.03 ± 0.81	-
CoO[42]	-105.82 ± 0.36	-
ZnO[42]	-72.29 ± 0.17	-
dia-Co(Meim)$_2$	-146.81 ± 0.30	-46.01 ± 0.75
dia-Cu(MeIm)$_2$	-126 ± 0.99	-14.03 ± 1.40
dia-Zn(MeIm)$_2$	-127.86 ± 1.26	-31.43 ± 1.26
SOD-Co(MeIm)$_2$	-177.5 ± 0.51	-15.32 ± 0.86
SOD-Zn(MeIm)$_2$	-137.50 ± 0.94	- 21.79 ± 0.94
Co-ZIF-L	-178.52 ± 0.32	-36.92 ± 0.76
Zn-ZIF-L	-120.29 ± 0.52	-61.62 ± 0.94

Table 5. Summary of reactions utilized for the assessment of enthalpic changes associated with the formation of ZIF-L. All enthalpies are reported as kJ/mol.

reaction	ΔH^o_f (from end members)	ΔH^o_f (from *dia*)	ΔH^o_f (from SOD)

1.ZnO (s, 298.15 K) + $\frac{5}{2}$ HMeIm (s, 298.15 K) + $\frac{1}{2}$ H$_2$O (l, 298.15 K) $\rightarrow$ Zn(MeIm)$_2$(HMeIm)$_{1/2}$(H$_2$O)$_{3/2}$ (S, 298.15 K))	-61.62 ± 0.94		
2. Zn(MeIm)$_2$ (s, 298.15 K) + $\frac{1}{2}$HMeIm (s, 298.15 K) + $\frac{3}{2}$H$_2$O (l, 298.15 K) $\rightarrow$ Zn(MeIm)$_2$(HMeIm)$_{1/2}$(H$_2$O)$_{3/2}$ (s, 298.15 K)		-30.19 ± 1.33	-39.83 ± 1.14
3. CoO (s, 298.15 K) + $\frac{5}{2}$HMeIm (s, 298.15 K) + $\frac{1}{2}$H$_2$O (l, 298.15 K) $\rightarrow$ Co(MIm)$_2$(HMeIm)$_{1/2}$(H$_2$O)$_{3/2}$ (s, 298.15 K)	-36.92 ± 0.76		
4. Co(MeIm)$_2$ (s, 298.15 K) + $\frac{1}{2}$HMeIm (s, 298.15 K) + $\frac{3}{2}$H$_2$O (l, 298.15 K) $\rightarrow$ Co(MeIm)$_2$(HMeIm)$_{1/2}$(H$_2$O)$_{3/2}$ (s, 298.15 K)		+9.08 ± 0.73	-21.60 ± 0.84

The heats of dissolution of all the metal oxides and linkers are exothermic (Table 4). Relative to endmembers (metal oxide and linker), the heat of formation of the 3D ZIFs are summarized in Table 4. Examining the heat of formation in different dense-phase *dia*-topology ZIFs shows that the Co(II)-material is much more exothermic compared to both Zn- and Cu(II)-based analogues. Interestingly, the same trend is not observed for the corresponding porous SOD-topology polymorphs, wherein the heat of formation is more exothermic for the Zn-based ZIF-8 than the Co(II)-based ZIF-67.[43] In these systems, a more exothermic enthalpy of formation translates to overall greater thermodynamic stability with respect to hydrolysis, with the understanding that entropic effects are small. Consequently, the enthalpies of formation can be assumed to reflect the overall energetic landscape of these polymorphic systems. These results indicate that the stabilizing effect of different metals is highly dependent on the framework density, which is dictated by its topology (see Table 4).

Additionally, we use the enthalpies of reactions (1-4) (Table 5) to assess the thermodynamic stability of the 2D ZIF-L structures. The enthalpy of formation for the Co-ZIF-L and Zn-ZIF-L frameworks with respect to endmembers (metal oxide, linker, and water), is strongly exothermic by 37 kJ/mol and 62 kJ/mol, respectively. Similarly, both reactions (2) and (4) show that by starting from a 3D material with the open SOD topology as a reactant, the enthalpies for forming Zn-ZIF-L and Co-ZIF-L are exothermic by 40 kJ/mol and 22 kJ/mol, respectively. These results suggest that if one considers the formation of the ZIF-L materials starting from the corresponding less dense SOD-topology frameworks in combination with additional linker and water, the stabilizing effect arising from a change in dimensionality from the 3D SOD-topology structure to the

2D ZIF-L material is comparable to and can be greater than that resulting from the formation of dense and more stable *dia*-polymorphs from the more porous, metastable SOD-topology ZIFs (see Figure 7).
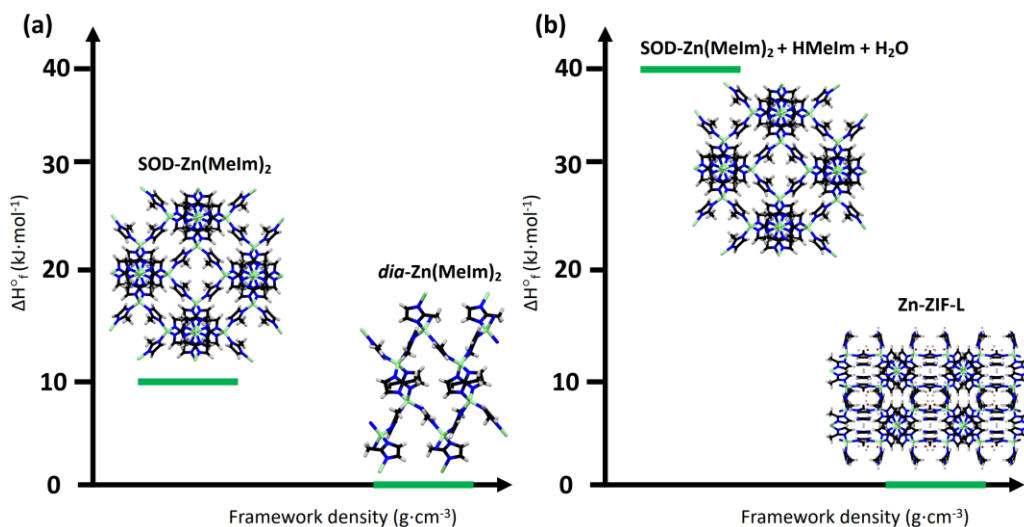
Figure 7. Enthalpy diagrams for structures employing Zn(II) metal atoms as nodes, showing: (a) higher metastability in SOD structures compared to *dia* polymorphs, (b) higher enthalpy of SOD topology, water, and linker compared to Zn-ZIF-L analogues.

Subsequently, we investigate different references for assessment of stability in ZIF-L structures (see Table 5). The results in Table 5 highlight three main aspects of the thermodynamic stability of ZIF-L frameworks. First, the endothermic heat for reaction (4) (ΔH°_f (from *dia*)) shows that the replacement of SOD-Co(MeIm)$_2$ by *dia*-Co(MeIm)$_2$ as reactant significantly disfavors the formation of Co-ZIF-L, thus indicating metastability of the 2D framework with increasing density of the 3D analogue in the Co(II) system. Surprisingly, a much smaller destabilization of Zn-ZIF-L frameworks is observed upon replacement of SOD-Zn(MeIm)$_2$ by the denser and more stable

polymorph (dia-Zn(MeIm)$_2$) as reactant, hence, the formation reaction (2) remains thermodynamically favorable (exothermic). This points not only to the discussed superior stability of Zn- and Co-ZIF-L structures compared to the respective SOD-topology ZIFs specimens, but also indicates that in the presence of additional linker and water, formation of Zn-ZIF-L structure should even be preferred to the formation of the dense 3D dia-topology one. Although stabilization of a 2D structure over a denser 3D one can be seen as counterintuitive, we note that a recent report has established that the 2D layered polymorph of mercury(II) imidazolate should be more exothermic than its 3D quartz (qtz) topology analogue.[44] Second, for reactions 2 and 4, the difference between $\Delta H^o{}_f$ from dia and from SOD is directly related to the difference in the thermodynamic stability (enthalpy of formation) of the 3D polymorphs. Third, the highly exothermic formation of Co-ZIF-L and Zn-ZIF-L from anhydrous 3D ZIFs and water suggests that the water in the structure is present as an actively participating stabilizing agent, and not simply as a space-filling component. The addition of water and hydrogen bonding in the interlayer space may serve as a major source for the thermodynamic stability of 2D ZIF-L frameworks.

Previous reports have demonstrated that Zn-ZIF-L and Co-ZIF-L can undergo a solvent-mediated transformation into corresponding SOD-topology materials ZIF-8 and ZIF-67, respectively. [37, 38, 45] This may result from stabilization of Sodalite structures by inclusion of other solvents. Typically, the stability of a material is referred to as kinetic persistence to phase degradation, under a given set of conditions, even if allowed by thermodynamics, often without knowledge of the energetic drive for the reaction (i.e., true stability). Hence, the results in this work confirm the high thermodynamic stability

of the 2D frameworks.[46, 47] This expands current knowledge of the energetic landscape in MOFs.

This study further permits the identification of various stabilization trends. For example, for materials with a SOD topology, Zn(II) containing materials are more stable than Co(II), and a similar observation is made for the 2D materials. However, for the close-packed *dia* topology materials, the opposite trend is observed, with stability decreasing from Co(II), to Zn(II), to Cu(II). In the SOD topology materials, there is an increase in thermodynamic stability of the framework with increasing ionic radius of the metal, with Zn(II) having the greatest stabilizing effect. However, in the *dia* topology materials, smaller ionic radii nodes such as Co(II) seem to promote greater thermodynamic stability. These results suggest that the strength of organic and inorganic interactions is significantly dependent on the framework topology and dimensionality. The calculated enthalpies of formation further reveal that nodes consisting of larger ionic radii metals stabilize the porous SOD topology relative to the denser polymorphs in the *dia* configuration.

It should be noted that the relative thermodynamic stability of materials with different substituents is determined by the respective bond strengths. In turn, these bond strengths are influenced by both the electronegativity, and the ionic radius. Differences in electronegativity of the metal atom can lead to dissimilarities in metal-ligand bond length and/or strength,[48, 49] resulting in different thermodynamic stabilization effects. For the metal substituents in this study, the electronegativity decreases from Cu, to Co and Zn, with specific values being 1.90, 1.88 and 1.65 on the Pauling scale.[50–52] Although the

metal-ligand bond lengths in ZIF-8 and ZIF-67 are similar (~2 Å),[53, 54] it is possible that Co(II) forms stronger bonds, which would be consistent with destabilization from lattice strain. Additionally, it is likely that an optimum bond distance exists that permits the favorable formation of shorter and/or stronger bonds while minimizing lattice strain, in turn establishing a constraint on the electronegativity of metal atoms likely to stabilize frameworks dependent on topology.

Thermodynamic analysis of the *dia*-topology ZIFs reveals an increase in the stability of the structure with increasing electronegativity of the metal node upon substitution of Zn by Co(II). Further increase in electronegativity of the metal atom, upon substitution of Co(II) by Cu(II) results, however, in decreased stabilization relative to endmembers. The electronegativity of the atoms suggests that in the close-packed topology, there is only a minor decrease in bond strength resulting from substitution of Co(II) by Cu(II). These results could indicate an energetic penalty for lattice strain. Ultimately, in the *dia* topology, metal atoms with electronegativity higher than ~1.88 show less enthalpic stabilization relative to endmembers. Furthermore, Cu(II) atoms preferentially adopt a square planar coordination, reflecting Jahn–Teller effect.[55–57] The highly distorted tetrahedral coordination of Cu(II) in the herein explored *dia*-Cu(MeIm)$_2$ may contribute to the lower stabilizing effect of Cu(II) metal atoms, as seen in spinels.[55–57] In contrast, Zn(II) promotes the greatest stabilization in the SOD-topology as well as in the ZIF-L systems. This is apparent, as the substitution of Zn(II) by Co(II) atoms decreases the thermodynamic drive for forming the more porous frameworks. In this work, the stabilizing effect of metal nodes in SOD and ZIF-L frameworks decreases for metal atoms with electronegativity higher than ~1.65. This may suggest that compared to

their denser analogues in the *dia* topology, SOD and ZIF-L structures are more prone to destabilization resulting from lattice strain.

These observations point to a tradeoff between bond strength and lattice dynamics in framework materials such as ZIFs. Thermodynamically favorable configurations are expected to include strong bonds and reduced lattice strain. Such optimization of bonding can enable MOFs to be structurally flexible, allowing dynamic processes such as gate-opening.[58–60] It should be stressed that the electronegativity-stability relations we report, specifically the electronegativity values corresponding to thermodynamic penalty in the SOD- and *dia*-topology structures may be specific to the ZIFs and metals herein investigated. It is likely that electronegativity alone may not completely describe energetic interplay in these materials, as the same topology-dependent electronegativity cut-off values may not apply to other MOF systems. Nevertheless, the trends seen here can serve as a starting point for identification and comparison of metal descriptors for increased stabilization across different reticular structures.

6.4 Conclusions

This study provides a thermodynamic assessment of how different choices of the divalent metal node, from Co to Cu and Zn affect the thermodynamic stability of zeolitic imidazolate framework materials across both the more open SOD-, as well as denser *dia*-topologies. Moreover, we also provide an experimental evaluation of the thermodynamic stability of two-dimensional ZIF-L structures based on Co(II) and Zn nodes, compared to

corresponding three-dimensional *dia-* and SOD-topology framework materials. The results point to a possible optimum combination of bond strength and lattice strain to maximize stability of the frameworks relative to endmembers. In the *dia*-topology, incorporation of metals with electronegativity higher than ~1.88 decreases the thermodynamic drive for forming the framework. In the SOD-topology, the thermodynamic drive for forming the zeolitic imidazolate framework decreases upon the inclusion of metals with electronegativity higher than ~1.65. The presented thermodynamic analysis also reveals that the two-dimensional ZIF-L structures possess high thermodynamic stability, which is likely to be enhanced by presence of included water. As a result, the formation of Zn-ZIF-L and Co-ZIF-L structures is found to be thermodynamically driven with respect to popular 3-dimensional frameworks ZIF-8 and ZIF-67, respectively. Moreover, thermodynamic data also shows that the formation of Zn-ZIF-L should also be thermodynamically preferred, if additional linker and water are accessible, to the formation of the dense *dia*-topology polymorph of ZIF-8. These results point to the importance of the effect of the metal, topology, and dimensionality (2D or 3D) on the design of thermodynamically more stable MOFs. The systematics observed in the energetics of formation in these materials provide an initial framework for the prediction and development of MOFs with greater thermodynamic stability and desired functionality. To investigate if the stabilization trends observed in ZIFs are system-dependent, the MOFs work in the next chapter is expanded to the investigation of metal substitution in topologically similar boron imidazolate frameworks (BIFs).

REFERENCES

1. Yaghi, O. M. Reticular Chemistry: Molecular Precision in Infinite 2D and 3D. *Mol. Front. J.* **03**, 66–83 (2019).

2. Kim, H. & Seop Hong, C. MOF-74-type frameworks: tunable pore environment and functionality through metal and ligand modification. *CrystEngComm* **23**, 1377–1387 (2021).

3. Liu, J. *et al.* A Tunable Bimetallic MOF-74 for Adsorption Chiller Applications. *Eur. J. Inorg. Chem.* **2018**, 885–889 (2018).

4. Wei, R. *et al.* Tuning the Properties of Zr6O8 Nodes in the Metal Organic Framework UiO-66 by Selection of Node-Bound Ligands and Linkers. *Chem. Mater.* **31**, 1655–1663 (2019).

5. Wade, C. R., Corrales-Sanchez, T., Narayan, T. C. & Dincă, M. Postsynthetic tuning of hydrophilicity in pyrazolate MOFs to modulate water adsorption properties. *Energy Environ. Sci.* **6**, 2172–2177 (2013).

6. Titi, H. M. *et al.* Hypergolic zeolitic imidazolate frameworks (ZIFs) as next-generation solid fuels: Unlocking the latent energetic behavior of ZIFs. *Sci. Adv.* **5**, eaav9044 (2019).

7. Titi, H. M. *et al.* Metal–Organic Frameworks as Fuels for Advanced Applications: Evaluating and Modifying the Combustion Energy of Popular MOFs. *Chem. Mater.* **31**, 4882–4888 (2019).

8. Metzger, E. D. *et al.* Highly Selective Heterogeneous Ethylene Dimerization with a Scalable and Chemically Robust MOF Catalyst. *ACS Sustain. Chem. Eng.* **7**, 6654–6661 (2019).

9. Liu, J. *et al.* MOF-enabled confinement and related effects for chemical catalyst presentation and utilization. *Chem. Soc. Rev.* **51**, 1045–1097 (2022).

10. Smoljan, C. S. *et al.* Engineering Metal–Organic Frameworks for Selective Separation of Hexane Isomers Using 3-Dimensional Linkers. *J. Am. Chem. Soc.* **145**, 6434–6441 (2023).

11. Wang, H., Pei, X., Kalmutzki, M. J., Yang, J. & Yaghi, O. M. Large Cages of Zeolitic Imidazolate Frameworks. *Acc. Chem. Res.* **55**, 707–721 (2022).

12. Huang, X.-C., Lin, Y.-Y., Zhang, J.-P. & Chen, X.-M. Ligand-Directed Strategy for Zeolite-Type Metal–Organic Frameworks: Zinc(II) Imidazolates with Unusual Zeolitic Topologies. *Angew. Chem. Int. Ed.* **45**, 1557–1559 (2006).

13. Huang, X., Zhang, J. & Chen, X. [Zn(bim)2] · (H2O)1.67: A metal-organic open-framework with sodalite topology. *Chin. Sci. Bull.* **48**, 1531–1534 (2003).

14. Zhang, J.-P., Zhang, Y.-B., Lin, J.-B. & Chen, X.-M. Metal Azolate Frameworks: From Crystal Engineering to Functional Materials. *Chem. Rev.* **112**, 1001–1033 (2012).

15. Park, K. S. *et al.* Exceptional chemical and thermal stability of zeolitic imidazolate frameworks. *Proc. Natl. Acad. Sci.* **103**, 10186–10191 (2006).

16. R. Redfern, L. & K. Farha, O. Mechanical properties of metal–organic frameworks. *Chem. Sci.* **10**, 10666–10679 (2019).

17. Novendra, N. *et al.* Linker Substituents Control the Thermodynamic Stability in Metal–Organic Frameworks. *J. Am. Chem. Soc.* **142**, 21720–21729 (2020).

18. B. Lennox, C. *et al.* Simplifying and expanding the scope of boron imidazolate framework (BIF) synthesis using mechanochemistry. *Chem. Sci.* **12**, 14499–14506 (2021).

19. Wang, J. *et al.* Metal organic framework-based nanostructure materials: applications for non-lithium ion battery electrodes. *CrystEngComm* **24**, 2925–2947 (2022).

20. A. Pearson, M., Bhagchandani, S., Dincă, M. & A. Johnson, J. Mixing ligands to enhance gas uptake in polyMOFs. *Mol. Syst. Des. Eng.* **8**, 591–597 (2023).

21. Zheng, Z., Hanikel, N., Lyu, H. & Yaghi, O. M. Broadly Tunable Atmospheric Water Harvesting in Multivariate Metal–Organic Frameworks. *J. Am. Chem. Soc.* **144**, 22669–22675 (2022).

22. Luo, J. *et al.* Hydrogen Adsorption in a Highly Stable Porous Rare-Earth Metal-Organic Framework: Sorption Properties and Neutron Diffraction Studies. *J. Am. Chem. Soc.* **130**, 9626–9627 (2008).

23. Gao, S. *et al.* Improving the Acidic Stability of Zeolitic Imidazolate Frameworks by Biofunctional Molecules. *Chem* **5**, 1597–1608 (2019).

24. Yuan, S. *et al.* Stable Metal–Organic Frameworks: Design, Synthesis, and Applications. *Adv. Mater.* **30**, 1704303 (2018).

25. Kouser, S., Hezam, A., Khadri, M. J. N. & Khanum, S. A. A review on zeolite imidazole frameworks: synthesis, properties, and applications. *J. Porous Mater.* **29**, 663–681 (2022).

26. Mo, Z., Tai, D., Zhang, H. & Shahab, A. A comprehensive review on the adsorption of heavy metals by zeolite imidazole framework (ZIF-8) based nanocomposite in water. *Chem. Eng. J.* **443**, 136320 (2022).

27. W. Lewis, D. *et al.* Zeolitic imidazole frameworks: structural and energetics trends compared with their zeolite analogues. *CrystEngComm* **11**, 2272–2276 (2009).

28. Akimbekov, Z. *et al.* Experimental and Theoretical Evaluation of the Stability of True MOF Polymorphs Explains Their Mechanochemical Interconversions. *J. Am. Chem. Soc.* **139**, 7952–7957 (2017).

29. Katsenis, A. D. *et al.* In situ X-ray diffraction monitoring of a mechanochemical reaction reveals a unique topology metal-organic framework. *Nat. Commun.* **6**, 6662 (2015).

30. Al Obeidli, A., Ben Salah, H., Al Murisi, M. & Sabouni, R. Recent advancements in MOFs synthesis and their green applications. *Int. J. Hydrog. Energy* **47**, 2561–2593 (2022).

31. Howarth, A. J. *et al.* Chemical, thermal and mechanical stabilities of metal–organic frameworks. *Nat. Rev. Mater.* **1**, 1–15 (2016).

32. Rieth, A. J., Wright, A. M. & Dincă, M. Kinetic stability of metal–organic frameworks for corrosive and coordinating gas capture. *Nat. Rev. Mater.* **4**, 708–725 (2019).

33. Voskanyan, A. A., Goncharov, V. G., Novendra, N., Guo, X. & Navrotsky, A. Thermodynamics Drives the Stability of the MOF-74 Family in Water. *ACS Omega* **5**, 13158–13163 (2020).

34. Saliba, D., Ammar, M., Rammal, M., Al-Ghoul, M. & Hmadeh, M. Crystal Growth of ZIF-8, ZIF-67, and Their Mixed-Metal Derivatives. *J. Am. Chem. Soc.* **140**, 1812–1823 (2018).

35. Shi, Q., Chen, Z., Song, Z., Li, J. & Dong, J. Synthesis of ZIF-8 and ZIF-67 by Steam-Assisted Conversion and an Investigation of Their Tribological Behaviors. *Angew. Chem. Int. Ed.* **50**, 672–675 (2011).

36. Xu, Y. *et al.* Experimentally Validated Ab Initio Crystal Structure Prediction of Novel Metal–Organic Framework Materials. *J. Am. Chem. Soc.* **145**, 3515–3525 (2023).

37. Deacon, A. *et al.* Understanding the ZIF-L to ZIF-8 transformation from fundamentals to fully costed kilogram-scale production. *Commun. Chem.* **5**, 1–10 (2022).

38. Zhang, J., Zhang, T., Yu, D., Xiao, K. & Hong, Y. Transition from ZIF-L-Co to ZIF-67: a new insight into the structural evolution of zeolitic imidazolate frameworks (ZIFs) in aqueous systems. *CrystEngComm* **17**, 8212–8215 (2015).

39. Shi, Q., Chen, Z., Song, Z., Li, J. & Dong, J. Synthesis of ZIF-8 and ZIF-67 by Steam-Assisted Conversion and an Investigation of Their Tribological Behaviors. *Angew. Chem. Int. Ed.* **50**, 672–675 (2011).

40. M. Titi, H., Do, J.-L., J. Howarth, A., Nagapudi, K. & Friščić, T. Simple, scalable mechanosynthesis of metal–organic frameworks using liquid-assisted resonant acoustic mixing (LA-RAM). *Chem. Sci.* **11**, 7578–7584 (2020).

41. Qian, J., Sun, F. & Qin, L. Hydrothermal synthesis of zeolitic imidazolate framework-67 (ZIF-67) nanocrystals. *Mater. Lett.* **82**, 220–223 (2012).

42. Hughes, J. T., Bennett, T. D., Cheetham, A. K. & Navrotsky, A. Thermochemistry of Zeolitic Imidazolate Frameworks of Varying Porosity. *J. Am. Chem. Soc.* **135**, 598–601 (2013).

43. Xu, W. *et al.* Entropy-Driven Mechanochemical Synthesis of Polymetallic Zeolitic Imidazolate Frameworks for CO2 Fixation. *Angew. Chem. Int. Ed.* **58**, 5018–5022 (2019)
.

44. Speight, I. R. *et al.* Disappearing Polymorphs in Metal–Organic Framework Chemistry: Unexpected Stabilization of a Layered Polymorph over an Interpenetrated Three-Dimensional Structure in Mercury Imidazolate. *Chem. – Eur. J.* **26**, 1811–1818 (2020).

45. Fu, H., Wang, Z., Wang, X., Wang, P. & Wang, C.-C. Formation mechanism of rod-like ZIF-L and fast phase transformation from ZIF-L to ZIF-8 with morphology changes controlled by polyvinylpyrrolidone and ethanol. *CrystEngComm* **20**, 1473–1477 (2018).

46. Lee, S., Oh, S. & Oh, M. Atypical Hybrid Metal–Organic Frameworks (MOFs): A Combinative Process for MOF-on-MOF Growth, Etching, and Structure Transformation. *Angew. Chem.* **132**, 1343–1349 (2020).

47. Low, Z.-X. *et al.* Crystal Transformation in Zeolitic-Imidazolate Framework. *Cryst. Growth Des.* **14**, 6589–6598 (2014).

48. Cheng, C.-C. *et al.* Gold nanocrystal decorated trimetallic metal organic frameworks as high performance electrocatalysts for oxygen evolution reaction. *Appl. Catal. B Environ.* **286**, 119916 (2021).

49. Gao, K., Guo, X., Zheng, B., Wang, J. & Wang, L. Investigation of interface compatibility in stiff polymer/metal–organic frameworks. *Mater. Today Chem.* **20**, 100458 (2021).

50. Hartmann, M. J., Häkkinen, H., Millstone, J. E. & Lambrecht, D. S. Impacts of Copper Position on the Electronic Structure of [Au25-xCux(SH)18]− Nanoclusters. *J. Phys. Chem. C* **119**, 8290–8298 (2015).

51. Hao, J. *et al.* Unraveling the electronegativity-dominated intermediate adsorption on high-entropy alloy electrocatalysts. *Nat. Commun.* **13**, 2662 (2022).

52. Kamdar, M. H. The occurrence of liquid-metal embrittlement. *Phys. Status Solidi A* **4**, 225–233 (1971).

53. Timofeeva, M. N. *et al.* Tuning the catalytic properties for cycloaddition of CO2 to propylene oxide on zeolitic-imidazolate frameworks through variation of structure and chemical composition. *Mol. Catal.* **529**, 112530 (2022).

54. Zaręba, J. K., Nyk, M. & Samoć, M. Co/ZIF-8 Heterometallic Nanoparticles: Control of Nanocrystal Size and Properties by a Mixed-Metal Approach. *Cryst. Growth Des.* **16**, 6419–6425 (2016).

55. Sahu, S. K. & Navrotsky, A. Thermodynamics of copper-manganese and copper-iron spinel solid solutions. *J. Am. Ceram. Soc.* **100**, 3684–3692 (2017).

56. Fu, L., Yang, H., Hu, Y., Wu, D. & Navrotsky, A. Tailoring Mesoporous γ-Al2O3 Properties by Transition Metal Doping: A Combined Experimental and Computational Study. *Chem. Mater.* **29**, 1338–1349 (2017).

57. Shivaramaiah, R., Tallapragada, S., Nagabhushana, G. P. & Navrotsky, A. Synthesis and thermodynamics of transition metal oxide based sodium ion cathode materials. *J. Solid State Chem.* **280**, 121011 (2019).

58. E. Casco, M. *et al.* Gate-opening effect in ZIF-8: the first experimental proof using inelastic neutron scattering. *Chem. Commun.* **52**, 3639–3642 (2016).

59. Krokidas, P. *et al.* ZIF-67 Framework: A Promising New Candidate for Propylene/Propane Separation. Experimental Data and Molecular Simulations. *J. Phys. Chem. C* **120**, 8116–8124 (2016).

60. Nijem, N. *et al.* Tuning the Gate Opening Pressure of Metal–Organic Frameworks (MOFs) for the Selective Separation of Hydrocarbons. *J. Am. Chem. Soc.* **134**, 15201–15204 (2012).

CHAPTER 7

EXPERIMENTAL INVESTIGATION OF THERMODYNAMIC STABILIZATION IN
BORON IMIDAZOLATE FRAMEWORKS (BIFS) SYNTHESIZED BY
MECHANOCHEMISTRY

Reference: Leonel GJ, Lennox CB, Scharrer M, Jayanthi K, Friščic T, Navrotsky A.
Experimental Investigation of Thermodynamic Stabilization in Boron Imidazolate
Frameworks (BIFs) Synthesized by Mechanochemistry. J Phys Chem C. 2023.

Abstract: This study experimentally explores the energetics for the formation of boron-
imidazolate frameworks (BIFs), which are synthesized by mechanochemistry. The
topologically similar frameworks employ the same tetratopic linker based on
tetrakis(imidazolyl)boric acid, but differ in the monovalent cation metal nodes. This
permits assessment of stabilizing effect of metal nodes in frameworks with sodalite
(SOD) and diamondoid (*dia*) topologies. The enthalpy of formation from endmembers
(metal oxide and linker), which define thermodynamic stability of the structures, has been
determined by use of acid-solution calorimetry. The results show that heavier metal atoms
in the node promote greater energetic stabilization of denser structures. Overall, in BIFs
the relation between cation descriptors (ionic radius, electronegativity) and
thermodynamic stability depends on framework topology. Thermodynamic stability
increases with metallic character of the cation employed as metal node, independent of
framework topology. The results suggest unifying aspects for thermodynamic
stabilization across MOF systems.

7.1 Introduction

Metal organic frameworks (MOFs) are self-assembled, highly porous structures comprised of metal-containing secondary building units linked by organic ligands.[1, 2] This field of reticular chemistry has led to development of subclasses of MOFs, including zeolitic imidazolate frameworks (ZIFs) and boron imidazolate frameworks (BIFs).[3, 4] These materials continue to increase in popularity due to the facile manipulation of their electronic and transport properties, through the use of appropriate metal-ligand combinations.[5, 6] This permits fine-tuning of material properties to meet current and future technological demands.[7, 8] To date, MOFs have promising application in quantum dot semiconductors, biomedical imaging, and molecular sieving.[9–11] Additionally, recent work in actinide science has explored developing MOFs based on f-block elements (uranium, thorium, and plutonium), which have potential use in nuclear energy and waste management applications.[12–14]

Common routes for the synthesis of frameworks include solvothermal syntheses and mechanochemistry.[4, 15–17] To reduce possible negative environmental impact from use of large amounts of solvents, recent work continues to explore alternative synthesis approaches.[18] Solvent-free synthesis can be achieved by use of mechanochemical synthesis methods like ball-milling, including liquid-assisted grinding, hence, the synthesis of MOFs is no longer limited to reactants that must be completely dissolved in liquid media.[19] Fundamentally, the reaction conditions in the solvothermal and mechanochemical approaches are different, which has in some cases enabled the observation of materials and topologies so far only accessible by mechanochemistry.[3, 4, 20]

The sodalite (SOD) and diamondoid (*dia*) topologies are often observed across both ZIFs and BIFs.[4, 20] Structures in the SOD topology are typically much more porous compared to denser frameworks in the *dia* topology.[20, 21] Past work shows that difference in the thermodynamic stability of may be associated with differences in density of the frameworks with longer grinding leading to denser and more stable phases. [3, 20, 22]

Previous works investigated stability trends in MOFs. The results indicate that in MOFs, thermal as well as thermodynamic stability is determined by both the coordination number and local environment around the metal.[2, 3, 23–25] Most studies explore the synthesis and potential application of novel structures,[26, 27] , nonetheless, current knowledge of structure-property relation in MOFs is scarce, and this is an important consideration for the long-term application of these materials. Various studies have explored computational routes to address this problem, however, experimental data validating the results from machine learning and/or atomistic models is lacking.[28–31] Additionally, since thermodynamic stability is an important factor in the modular design of MOFs, it is essential to identify structural descriptors in the linkers and metal centers contributing to greater thermodynamic stability in MOFs. This is possible through development of a unifying framework for systematic stabilization of MOFs across different topologies and dimensions (2-dimensional (2D) and 3-dimensional (3D)).

Previous works employed calorimetric methods to investigate the thermodynamic stability of MOFs, including ZIFs employing ditopic 2-methylimidazolate (MeIm$^-$) ligands.[2, 3, 25] In this work we investigate the stability of four BIFs based on tetrakis(imidazolyl)boric acid (H[B(MeIm)$_4$]) ligand (see Figure 1a): *dia*-LiB(MeIm)$_4$,

dia-AgB(MeIm)₄, SOD-CuB(MeIm)₄, and SOD-AgB(MeIm)₄. The structures employ the same organic linker but different metal nodes. This systematic investigation permits identification of structural descriptors in metal atoms as well as quantitation of their stabilizing effect across different framework topologies. The chemical and structural characterization of the samples is done by Fourier-transform infrared spectroscopy (FTIR), thermal analysis (TGA-DSC), and powder X-ray diffraction (XRD). The thermochemical analyses employ enthalpies of formation. This is the first work employing calorimetry to explore the thermodynamic stability of BIFs based on tetratopic linkers (see Figure 1a). This is a valuable addition to the current MOF thermodynamic database, which permits expansion of current knowledge on structure-stability relations in BIFs and other MOFs, as well as validation of general trends suggested from previous DFT calculations.[4]
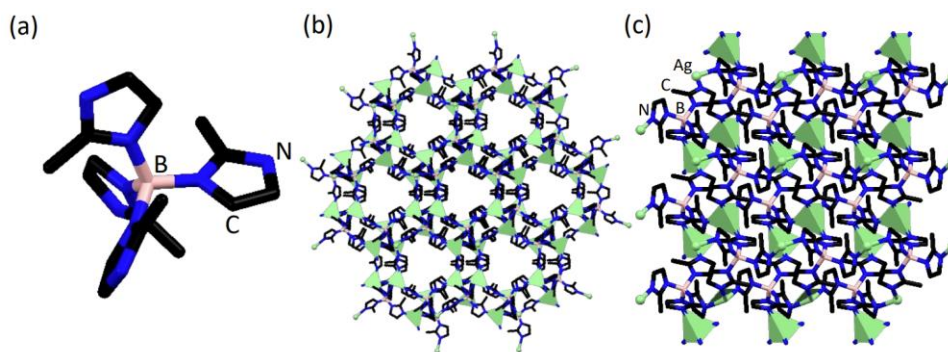

Figure 1. Illustration of: (a) the BIF ligand [B(Meim)₄⁻], (b) structure of a BIF in the sodalite (SOD) topology, (c) structure of a BIFs in the diamondoid (*dia*) topology. (pink=boron, blue=nitrogen, black=carbon, and green=metal centers).

7.2 Experimental Methods

7.2.1 Synthesis of BIFs

All BIFs were synthesized through the mechanochemical route that was previously reported,[4] and detailed description of the synthesis procedure and characterization is provided below and in appendix A.

Synthesis of *dia*-LiB(Meim)$_4$:

LiOH (0.5 mmol, 12 mg) was added to a 15 mL stainless-steel jar along with two stainless steel balls (7mm, 1.37g), H[B(Meim)4] (0.5mmol, 170mg) and 182 µL of a 3:1 mixture of MeCN : amb ($\eta = 0.5$ µL mg-1). The reaction was milled for 60 minutes at 25 Hz and the product was activated by stirring in 15 mL of MeCN for 18 hours, before dried at 80 °C and reduced pressure overnight.

Synthesis of *dia*-AgB(Meim)$_4$:

AgNO$_3$ (0.25 mmol, 42.5 mg) and K$_2$CO$_3$ (0.125 mmol, 17.25 mg) were added to a 15 mL stainless steel jar with two stainless-steel balls (7 mm, 1.37 g), H[B(Meim)$_4$] (0.25 mmol, 85 mg) and 36 µL of MeCN ($\eta = 0.25$ µL mg^{-1}). The reaction mixture was milled for 60 minutes at 25 Hz and then washed with 15 mL of cold MeOH for 30 minutes and acetone for 18 hours, then dried at 80°C and reduced pressure overnight.

7.2.2 Thermodynamic Measurements

Enthalpies of formation were calculated using dissolution enthalpies obtained by room temperature acid solution calorimetry in a CSC4400 isothermal microcalorimeter. Dissolution of KCl was employed for calibration of the calorimeter. This is a well-established technique, and the procedure has been employed for investigation of other MOFs and similar materials.[3, 32] Previous works describe the calorimetric experiments in more detail.[3, 33]

7.3 Results and Discussion

XRD patterns are shown in Figure 2. The experimental patterns are consistent with those calculated using CCDC Mercury software based on published crystallographic data for dia-LiB(MeIm)$_4$, dia- AgB(MeIm)$_4$, SOD- CuB(MeIm)$_4$, and SOD-AgB(MeIm)$_4$ structures.[4] The measured Fourier-transform infrared attenuated total reflectance (FTIR-ATR) spectra (see Figure 3) are consistent with boron-imidazolate as well as imidazolate-metal bonds, which are expected in BIFs. Thermogravimetric analysis (TGA) enables quantitation of metal content in the frameworks, the results are consistent with the expected stoichiometry (see Figure 4).
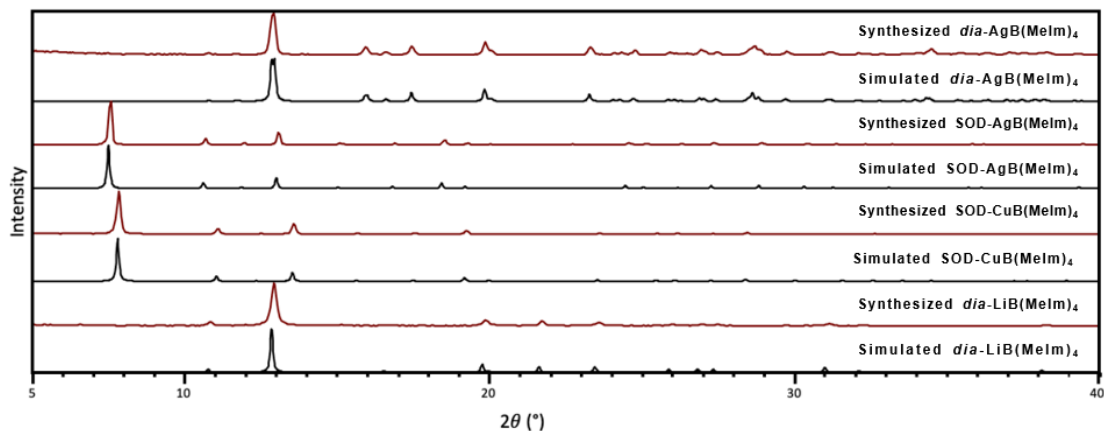
Figure 2. Experimental and simulated powder X-ray diffraction patterns of herein investigated BIFs, from top-to-bottom: (a) measured for dia-AgB(MeIm)$_4$, (b) simulated for dia-AgB(MeIm)$_4$ (CSD: CAHWAN), (c) measured for SOD-AgB(MeIm)$_4$, (d) simulated for SOD-AgB(MeIm)$_4$ (CSD: CAHWAN01), (e) measured for SOD-CuB(MeIm)$_4$, (f) simulated for SOD-CuB(MeIm)$_4$ (CSD: MOXJOZ), (g) measured for dia-LiB(MeIm)$_4$, and (h) simulated for dia-LiB(MeIm)$_4$ (CSD: MOXKUG).
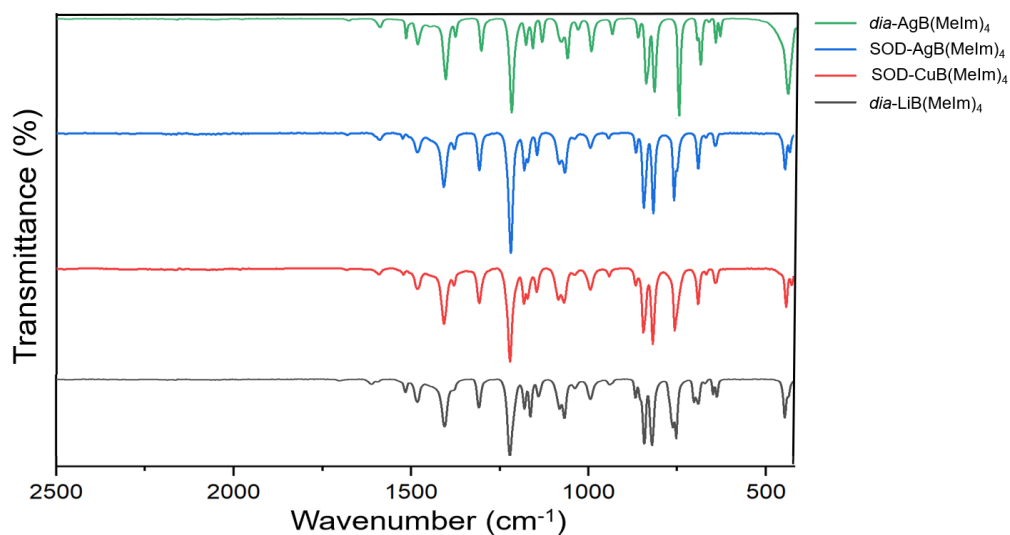
Figure 3. FTIR Spectra of as-prepared BIFs
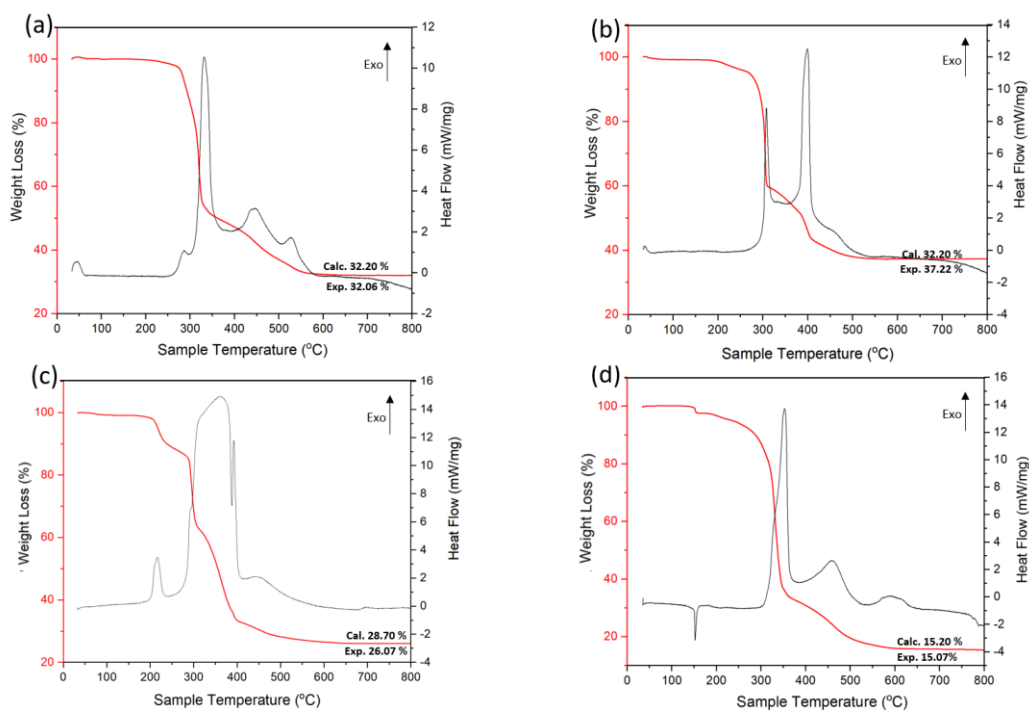
Figure 4. Thermograms for prepared BIFs, with experimental (Exp.) and calculated (Calc.) residue indicated for (a) SOD-AgB(Meim)$_2$, (b) *dia*-AgB(Meim)$_2$, (c) SOD-CuB(Meim)$_2$ and (d) *dia*-LiB(Meim)$_2$. Theoretical residue is calculated based on oxidative decomposition to (a, b) Ag and B$_2$O$_3$, (c) CuO and B$_2$O$_3$, and (d) Li$_2$O and B$_2$O$_3$.

7.3.1 Thermodynamics of BIFs and other MOFs

Current knowledge of the thermodynamics of MOFs is based on previous studies on frameworks comprised of oxygen-based linkers, including paddlewheel-type MOFs, as well as structures employing ditopic nitrogen-based linkers, such as ZIFs.[2, 3] The present work aims to expand upon these studies, investigating thermodynamic stability of BIFs. In the present study, thermodynamic analysis employs enthalpies of dissolution (ΔH_{dis}) of the frameworks and endmembers (monovalent metal oxide as well as linker).

Li$_2$O and Cu$_2$O are soluble in 5N HCl, and the thermochemical cycle shown in Table 1 permits calculation of enthalpies of formation of the respective frameworks (LiB(MeIm)$_4$ and CuB(MeIm)$_4$). In contrast, Ag$_2$O precipitates as AgCl in 5N HCl (-185.32 $\pm$ 0.60 kJ/mol), therefore the thermodynamic cycle describing the formation of SOD and *dia* AgB(MeIm)$_4$ BIFs is modified accordingly (see Table 2).

The results are summarized in Table 3. Enthalpies of formation (ΔH^o_f) permit determination of relative thermodynamic stability of different MOFs. In reactions involving only crystalline solids, enthalpy is the dominant term in the free energy as the entropy term is usually small. Since the energetics of forming these materials is dominated by the enthalpic term, a more exothermic enthalpy of formation typically corresponds to lower free energy, and thus, greater thermodynamic stability.

Table 1. Thermodynamic cycles for enthalpy of formation of MB(MeIm)$_4$ structures, where M = Cu$^+$ or Li$^+$.

½ M$_2$O (s, 298 K) + HB(MeIm)$_4$ (s, 298 K) → MB(MeIm)$_4$ (s, 298 K) + ½ H$_2$O (l, 298K) ΔH_f=?
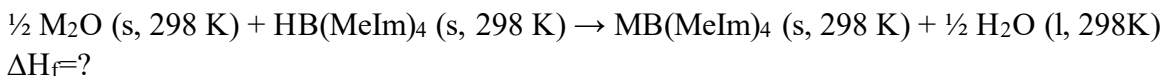
Reaction	ΔH (kJ/mol)
MB(MeIm)$_4$ (s, 298 K) → M$^+$ (aq, 298 K) + B(MeIm)$_4$ $^-$ (aq, 298 K)	ΔH_1
M$_2$O (s, 298 K) + 2H $^+$ (aq, 298 K) → 2M $^+$ (aq, 298 K) + H$_2$O (aq, 298 K)	ΔH_2
HB(MeIm)$_4$ (s, 298 K) → H $^+$ (aq, 298 K) + B(MeIm)$_4$ $^-$ (aq, 298 K)	ΔH_3

H$_2$O (l, 298 K) $\rightarrow$ H$_2$O (aq, 298 K)	ΔH_4
$\Delta H_f= -\Delta H_1 + \frac{1}{2} \Delta H_2 + \Delta H_3 - \frac{1}{2} \Delta H_4$	ΔH_f

l: liquid phase, s: solid phase, aq: aqueous

Table 2. Thermochemical cycle for enthalpies of formation of Ag-BIFs relative to endmembers (monovalent metal oxide and linker)

$\frac{1}{2}$ Ag$_2$O (s, 298 K) + HB(MeIm)$_4$ (s, 298 K) $\rightarrow$ AgB(MeIm)$_4$ (s, 298 K) + $\frac{1}{2}$ H$_2$O (l, 298K)

ΔH_f=?
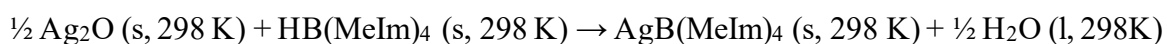
Reaction	ΔH (kJ/mol)
AgB(MeIm)$_4$ (s, 298 K) + HCl (aq, 298 K)$\rightarrow$ AgCl (s, 298 K) + B(MeIm)$_4$ $^-$ (aq, 298 K) + H$^+$ (aq, 298 K)	ΔH_1
Ag$_2$O (s, 298 K) + 2HCl (aq, 298 K) $\rightarrow$ 2AgCl (s, 298 K) + H$_2$O (aq, 298 K)	ΔH_2
HB(MeIm)$_4$ (s, 298 K) $\rightarrow$ H$^+$ (aq, 298 K) + B(MeIm)$_4$ $^-$ (aq, 298 K)	ΔH_3
H$_2$O (l, 298 K) $\rightarrow$ H$_2$O (aq, 298 K)	ΔH_4
$\Delta H_f= -\Delta H_1 + \frac{1}{2} \Delta H_2 + \Delta H_3 - \frac{1}{2} \Delta H_4$	ΔH_f

- Aq=aqueous; s=solid, l=liquid

Table 3. Enthalpies of dissolution in 5N HCl at 25 °C and enthalpies of formation of BIFs from metal oxide and linker.

Sample	BET Surface area (m²/g)	ΔH_{dis} (kJ/mol)	ΔH^o_f (kJ/mol)
HB(MeIm)$_4$	-	-144.42 ± 0.43 (4)	-
H$_2$O[20]	-	-0.5	-
Li$_2$O[a]	-	-254.036 ± 0.27 (5)	-
Ag$_2$O	-	-185.32 ± 0.60 (6)	-
Cu$_2$O	-	-246.80 ± 0.59 (5)	-
dia-LiB(MeIm)$_4$	-	-176.82 ± 0.66 (5)	-94.35 ± 0.97
dia-AgB(MeIm)$_4$	-	-137.54 ± 0.62 (5)	-99.28 ± 0.96
SOD-AgB(MeIm)$_4$	1020[4]	-186.93 ± 0.28 (5)	-49.89 ± 0.79
SOD-CuB(MeIm)$_4$	935[4]	-206.48 ± 0.72 (5)	-61.07 ± 1.02

a: enthalpy of dissolution of Li$_2$O is calculated from dissolution of Li$_2$CO$_3$; error is reported as two standard deviations from the mean; value in parenthesis () represents number of experiments.

Table 3 shows that BIFs have enthalpies of formation between -61 and -99 kJ/mol (relative to monovalent metal oxide and linker). These are much more exothermic than values for ZIFs, which typically range between -30 and -4 kJ/mol, as seen in ZIFs employing MeIm⁻ linkers.[3] This can result both from difference in chemistry and in structure of BIFs compared to ZIFs. In terms of chemistry, the formation reaction can be

viewed as an acid-base neutralization where the acidic linker reacts with the basic oxide to form a metal oxygen linkage and release water. The monovalent oxides in BIFs are stronger bases than ZnO. The boron-containing linker may also be a stronger acid than its boron-free counterpart. The larger difference in acid-base character will make the neutralization reaction more exothermic/favorable (see Figure 5). It is possible that introduction of boron linker centers stabilizes the frameworks. This may result from several factors, including less steric hindrance in bonds between metal centers and organic linkers, different size and charge of cations, differences in chemical bonding, or differences in electron distribution and bond angles in the linker. Our previous study has reported first-principles calculations of relative stabilities of herein studied SOD- and dia-frameworks.[4]
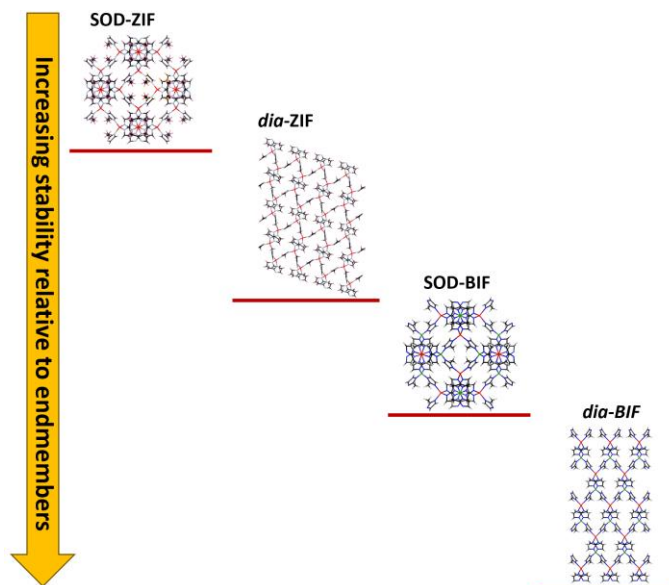

Figure 5. Comparison of energetic landscape in BIFs and ZIFs, based on energetics of formation from endmembers (metal oxide and ligand). The figure highlights greater stability of BIFs relative to endmembers. Overall, for both ZIFs and BIFs, the more dense *dia*-topology structures present greater stability than their SOD-topology counterparts.

Despite differences in the magnitude of enthalpies of formation relative to endmembers, increase in framework density appears to be a unifying framework descriptor for thermodynamic stabilization across both BIF and ZIF systems (see Figure 5).[20, 22] The thermodynamic analysis of Ag-based frameworks (see Table 3) points to greater thermodynamic drive for the formation of dia-AgB(MeIm)$_4$ compared to SOD-AgB(MeIm)$_4$. This is consistent with results from previous ZIF studies, which indicate that the porous SOD-topology polymorphs are metastable relative to the denser dia-topology counterpart frameworks.[3, 20] It is also qualitatively consistent with the conclusions of our previous computational study based on periodic density-functional theory (DFT) calculations,[4] although the enthalpy difference between dia- and SOD-topology polymorphs of AgB(MeIm)$_4$ is herein measured to be ca. 50 kJ/mol, which is significantly different from the previously calculated ca. 9 kJ/mol difference. The reason for this difference remains unclear. Overall, it is likely that increase in framework density is a unifying descriptor for enhanced stabilization across all MOFs (not just BIFs and ZIFs), which would imply that any metal-ligand combination could be stabilized by accessing denser polymorphs.

To further explore the possible systematics in the stabilizing effect of metal nodes in BIFs, we investigate correlations between metal descriptors (electronegativity, ionic radius, metallic character) and their corresponding thermodynamic trends across different framework topologies. The results in Table 3 highlight three main points: (1) In BIFs: heavier metal atoms promote further stabilization of denser polymorphs, (2) denser polymorphs show less destabilization from choice of metal, (3) the stabilizing effect of metal nodes increases with metallic character of the cation. Additionally, for the porous

BIF structure in the SOD topology, monovalent Cu nodes promote the greatest energetic stability.

The Pauling electronegativity of Li (0.98),[34] Cu (1.9),[35] and Ag (1.93)[36] influences the ability of metal nodes to pull electrons from the linker, and this affects metal-ligand bond strength and length. An optimal combination of strong (short) bonds with reduced lattice strain is desirable for favorable interaction at the interfaces between the metal nodes and the organic linkers. In the SOD topology, employing Ag^+ instead of Cu^+ results in a thermodynamic penalty of ~12 kJ/mol. This indicates significant destabilization of the porous framework with only minor increase in the electronegativity of metal atoms, perhaps due to lattice strain, which is destabilizing.[37–39] In contrast, in the *dia*-topology, the effect of electronegativity appears to be opposite and more subtle, as significant dissimilarities in the electronegativity of Ag^+ and Li^+ only result in ~5 kJ/mol enthalpy difference in *dia*-BIFs (see Table 3). This suggests only minor differences in the thermodynamic stability of denser BIF polymorphs arising from choice of metal.

Ionic radius may also impact the interaction between metal atoms and organic ligands Li =73 pm,[40] Cu =77 pm, [41, 42] and Ag =115 pm.[41, 43] We define metallic character as the ratio of electronegativity to ionic radius, with Li = 0.013, Cu = 0.025, and Ag = 0.016. The measured enthalpies show positive correlation between metallic character and stabilizing effect of metal nodes for all framework topologies. Other works investigating the thermodynamic stability of MOF-74 frameworks, using oxygen-based linkers suggest similar correlations.[25] These regularities may point to metallic character as another

unifying descriptor for increased thermodynamic stabilization across MOFs, independent of linker environment (oxygen or nitrogen) or coordination number.

It is known that other metals can be employed as nodes in BIF structures,[44–46] and the results in this work shed light on possible constraints for increased thermodynamic stabilization. In BIFs, metal (M)—nitrogen (N) as well as boron (B)—nitrogen (N) (in tetratopic ligand) bonds (Figure 1a) should be strong enough to prevent collapse of the framework to other more thermodynamically favorable structures. There may exist an ideal electronegativity and ionic radius of metal atoms to make the most stable BIFs. Deviations from ideal metal (M)—nitrogen (N) bond length and/or (strength) are expected to result in thermodynamic penalty. This places restrictions on the favorable electronegativity of metal nodes (depending on topology). If electronegativity of the metal is lower than optimum, M—N bond strength will be suboptimal (weaker), and likely less stable. In contrast, metal atoms with electronegativity greater than the optimum (depending on topology), may form shorter and/or stronger M—N bonds, but this may be at the cost of decreased electron density around the B—N bonds (weakening of bonds between boron linker center and nitrogen). This is important, since electron density in the linker influences framework stability.[3] It should also be highlighted that suboptimally shorter M—N bonds can result in increased lattice strain, especially in SOD-topology BIFs, as suggested in this work. The strength of both B—N and M—N bonds must be considered in the rational design of stable frameworks. The present results indicate most favorable incorporation of metal atoms with electronegativity greater than ~0.98 for BIFs in the *dia* topology, and lower than 1.93 in the porous polymorph (SOD). It should be stressed that other electronic and magnetic factors may affect the trends

identified thus far. Additionally, it is likely that some of the trends herein observed (e.g. electronegativity limit for increased stabilization) may be system-dependent and may not translate to other systems employing different metal-ligand combinations.

7.3.2 Practical Implications

The surface area of MOFs can be well beyond that of activated carbon, which makes them desirable candidates for molecular sieving and storage, however, hydrolysis of the frameworks is a challenge.[47, 48] The term "stability" is often used in two different senses, one indicating thermodynamic stability against some decomposition reaction and the other indicating kinetic persistence of the phase when exposed to aqueous media for a period of time under a given set of conditions, often without knowledge of the thermodynamics. The first case implies true stability controlled by thermodynamics, the second implies kinetically slow decomposition, even if allowed by thermodynamics. It should be highlighted that the reverse of the formation reaction in Tables 1-2 does not describe hydrolysis in BIFs; hydrolytic decomposition should form thermodynamically more stable products than the oxide and linker molecule. These hydrolysis products are likely dominated by metal hydroxides and hydrolyzed or decomposed linker molecules. Differences in the free energy of hydrolysis reactions determine the thermodynamic propensity for framework degradation. The complexity of possible hydrolysis reactions makes it difficult to unambiguously compute their energetics. Nevertheless, the added stability of hydroxides compared to oxides will make hydrolysis thermodynamically favorable, especially under basic conditions.

The BET surface area (m^2/g) of mechanochemically-synthesized SOD-AgB(MeIm)$_4$ and SOD-CuB(MeIm)$_4$ were previously reported to be 1020 and 935, respectively.[4] The porous MOFs can be employed for gas adsorption applications.[49, 50] This and previous works indicate a tradeoff between thermodynamic stability and surface area/porosity (adsorption capacity) of the structures.[3, 20] This is an important consideration as recent efforts continue to investigate gas storage in MOFs, especially the capture of CO_2.[51] Additionally, denser MOFs can display ferroelectric properties that are desirable for application in computer RAMs.[52, 53] The high thermodynamic stability of denser MOFs, including *dia*-BIFs may favor their long-term applications.

7.4 Conclusions

This study investigates the stabilizing effect of metal nodes across isostructural BIFs in the SOD and *dia* topology. The results confirm greater stability of all compositions with increasing density of the framework. In the denser *dia* topology, BIFs employing metal atoms with larger ionic radius and higher electronegativity are thermodynamically more stable. Overall, across the SOD and *dia* topology, the thermodynamic stability of the BIFs increases with metallic character of the nodes. The results suggest unifying systematics in the thermodynamic stabilization of BIFs and other MOF systems, leading to the ability to tailor, using thermodynamic constraints, stable structures with desirable properties. Lastly, MOFs are of great interest due to their potential use in CO_2 capture, however not much is known about the energetics of guest-host interactions during sorption processes, and that is the focus of the next chapter.

REFERENCES

1. Du, L. *et al.* Hierarchically Self-Assembled MOF Network Enables Continuous Ion Transport and High Mechanical Strength. *Adv. Energy Mater.* **12**, 2200501 (2022).

2. Bhunia, M. K., Hughes, J. T., Fettinger, J. C. & Navrotsky, A. Thermochemistry of Paddle Wheel MOFs: Cu-HKUST-1 and Zn-HKUST-1. *Langmuir* **29**, 8140–8145 (2013).

3. Novendra, N. *et al.* Linker Substituents Control the Thermodynamic Stability in Metal–Organic Frameworks. *J. Am. Chem. Soc.* **142**, 21720–21729 (2020).

4. B. Lennox, C. *et al.* Simplifying and expanding the scope of boron imidazolate framework (BIF) synthesis using mechanochemistry. *Chem. Sci.* **12**, 14499–14506 (2021).

5. Liu, J. *et al.* Electric Transport Properties of Surface-Anchored Metal–Organic Frameworks and the Effect of Ferrocene Loading. *ACS Appl. Mater. Interfaces* **7**, 9824–9830 (2015).

6. Zhao, Z., Ma, X., Li, Z. & Lin, Y. S. Synthesis, characterization and gas transport properties of MOF-5 membranes. *J. Membr. Sci.* **382**, 82–90 (2011).

7. Feng, X. *et al.* Series d–f Heteronuclear Metal–Organic Frameworks: Color Tunability and Luminescent Probe with Switchable Properties. *Inorg. Chem.* **56**, 1713–1721 (2017).

8. Liu, W., Erol, O. & Gracias, D. H. 3D Printing of an In Situ Grown MOF Hydrogel with Tunable Mechanical Properties. *ACS Appl. Mater. Interfaces* **12**, 33267–33275 (2020).

9. Aguilera-Sigalat, J. & Bradshaw, D. Synthesis and applications of metal-organic framework–quantum dot (QD@MOF) composites. *Coord. Chem. Rev.* **307**, 267–291 (2016).

10. Chen, W. & Wu, C. Synthesis, functionalization, and applications of metal–organic frameworks in biomedicine. *Dalton Trans.* **47**, 2114–2133 (2018).

11. Llabrés i Xamena, F. X., Corma, A. & Garcia, H. Applications for Metal−Organic Frameworks (MOFs) as Quantum Dot Semiconductors. *J. Phys. Chem. C* **111**, 80–85 (2007).

12. Su, J. & Chen, J. MOFs of Uranium and the Actinides. in *Lanthanide Metal-Organic Frameworks* (ed. Cheng, P.) 265–295 (Springer, 2015)..

13. Lv, K., Fichter, S., Gu, M., März, J. & Schmidt, M. An updated status and trends in actinide metal-organic frameworks (An-MOFs): From synthesis to application. *Coord. Chem. Rev.* **446**, 214011 (2021).

14. A. Dolgopolova, E., M. Rice, A. & B. Shustova, N. Actinide-based MOFs: a middle ground in solution and solid-state structural motifs. *Chem. Commun.* **54**, 6472–6483 (2018).

15. Ni, Z. & Masel, R. I. Rapid Production of Metal−Organic Frameworks via Microwave-Assisted Solvothermal Synthesis. *J. Am. Chem. Soc.* **128**, 12394–12395 (2006).

16. DeSantis, D. *et al.* Techno-economic Analysis of Metal–Organic Frameworks for Hydrogen and Natural Gas Storage. *Energy Fuels* **31**, 2024–2032 (2017).

17. Stolar, T. & Užarević, K. Mechanochemistry: an efficient and versatile toolbox for synthesis, transformation, and functionalization of porous metal–organic frameworks. *CrystEngComm* **22**, 4511–4525 (2020).

18. Głowniak, S., Szczęśniak, B., Choma, J. & Jaroniec, M. Mechanochemistry: Toward green synthesis of metal–organic frameworks. *Mater. Today* **46**, 109–124 (2021).

19. Friščić, T. New opportunities for materials synthesis using mechanochemistry. *J. Mater. Chem.* **20**, 7599–7605 (2010).

20. Akimbekov, Z. *et al.* Experimental and Theoretical Evaluation of the Stability of True MOF Polymorphs Explains Their Mechanochemical Interconversions. *J. Am. Chem. Soc.* **139**, 7952–7957 (2017).

21. López-Cabrelles, J. *et al.* Multivariate sodalite zeolitic imidazolate frameworks: a direct solvent-free synthesis. *Chem. Sci.* **13**, 842–847 (2022).

22. Arhangelskis, M. *et al.* Theoretical Prediction and Experimental Evaluation of Topological Landscape and Thermodynamic Stability of a Fluorinated Zeolitic Imidazolate Framework. *Chem. Mater.* **31**, 3777–3783 (2019).

23. Mu, B. & Walton, K. S. Thermal Analysis and Heat Capacity Study of Metal–Organic Frameworks. *J. Phys. Chem. C* **115**, 22748–22754 (2011).

24. Lu, P. *et al.* What can pKa and NBO charges of the ligands tell us about the water and thermal stability of metal organic frameworks? *J. Mater. Chem. A* **2**, 16250–16267 (2014).

25. Voskanyan, A. A., Goncharov, V. G., Novendra, N., Guo, X. & Navrotsky, A. Thermodynamics Drives the Stability of the MOF-74 Family in Water. *ACS Omega* **5**, 13158–13163 (2020).

26. Zou, J.-P. *et al.* Two Novel Metal−Organic Frameworks (MOFs) with (3,6)-Connected Net Topologies: Syntheses, Crystal Structures, Third-Order Nonlinear Optical and Luminescent Properties. *Cryst. Growth Des.* **10**, 2613–2619 (2010).

27. Wang, C. *et al.* New Strategies for Novel MOF-Derived Carbon Materials Based on Nanoarchitectures. *Chem* **6**, 19–40 (2020).

28. Nandy, A., Duan, C. & Kulik, H. J. Audacity of huge: overcoming challenges of data scarcity and data quality for machine learning in computational materials discovery. *Curr. Opin. Chem. Eng.* **36**, 100778 (2022).

29. Leong, C. F., Usov, P. M. & D'Alessandro, D. M. Intrinsically conducting metal–organic frameworks. *MRS Bull.* **41**, 858–864 (2016).

30. Taddei, M. *et al.* Mixed-linker UiO-66: structure–property relationships revealed by a combination of high-resolution powder X-ray diffraction and density functional theory calculations. *Phys. Chem. Chem. Phys.* **19**, 1551–1559 (2017).

31. Tong, M., Yang, Q., Xiao, Y. & Zhong, C. Revealing the structure–property relationship of covalent organic frameworks for CO 2 capture from postcombustion gas: a multi-scale computational study. *Phys. Chem. Chem. Phys.* **16**, 15189–15198 (2014).

32. Nagabhushana, G. P., Shivaramaiah, R. & Navrotsky, A. Direct calorimetric verification of thermodynamic instability of lead halide hybrid perovskites. *Proc. Natl. Acad. Sci.* **113**, 7717–7721 (2016).

33. Akimbekov, Z., Wu, D., Brozek, C. K., Dincă, M. & Navrotsky, A. Thermodynamics of solvent interaction with the metal–organic framework MOF-5. *Phys. Chem. Chem. Phys.* **18**, 1158–1162 (2015).

34. Matsunaga, T. *et al.* Magnesium borohydride: A new hydrogen storage material. *Renew. Energy* **33**, 193–196 (2008).

35. Hartmann, M. J., Häkkinen, H., Millstone, J. E. & Lambrecht, D. S. Impacts of Copper Position on the Electronic Structure of [Au25-xCux(SH)18]− Nanoclusters. *J. Phys. Chem. C* **119**, 8290–8298 (2015).

36. Teo, B. K. & Zhang, H. Molecular Machines: Molecular Structure of [(p-Tol3P)10Au13Ag12Cl8](PF7)—a Cluster with a Biicosahedral Rotorlike Metal Core and an Unusual Arrangement of Bridging Ligands. *Angew. Chem. Int. Ed. Engl.* **31**, 445–447 (1992).

37. Majzlan, J., Navrotsky, A. & Evans, B. J. Thermodynamics and crystal chemistry of the hematite–corundum solid solution and the FeAlO3 phase. *Phys. Chem. Miner.* **29**, 515–526 (2002).

38. Ngene, P., Longo, A., Mooij, L., Bras, W. & Dam, B. Metal-hydrogen systems with an exceptionally large and tunable thermodynamic destabilization. *Nat. Commun.* **8**, 1846 (2017).

39. Lilova, K. *et al.* A Synergistic Approach to Unraveling the Thermodynamic Stability of Binary and Ternary Chevrel Phase Sulfides. *Chem. Mater.* **32**, 7044–7051 (2020).

40. Aspinall, H. C. *et al.* Pinwheel-Shaped Heterobimetallic Lanthanide Alkali Metal Binaptholates: Ionic Size Matters! *Organometallics* **19**, 5416–5423 (2000).

41. Rakhsha, A. H. *et al.* Ag and Cu doped ZnO nanowires: A pH-Controlled synthesis via chemical bath deposition. *Materialia* **5**, 100212 (2019).

42. Liu, A. *et al.* High-performance p-channel transistors with transparent Zn doped-CuI. *Nat. Commun.* **11**, 4309 (2020).

43. Peng, H. *et al.* Simultaneous realization of broad temperature stability range and outstanding dielectric performance in (Ag+, Ta5+) co–doped TiO2 ceramics. *J. Alloys Compd.* **783**, 423–427 (2019).

44. Wen, T. *et al.* A boron imidazolate framework with mechanochromic and electrocatalytic properties. *Mater. Horiz.* **5**, 1151–1155 (2018).

45. Zheng, S. *et al.* Porous Metal Carboxylate Boron Imidazolate Frameworks. *Angew. Chem. Int. Ed.* **49**, 5362–5366 (2010).

46. Zhang, H.-X., Liu, M., Wen, T. & Zhang, J. Synthetic design of functional boron imidazolate frameworks. *Coord. Chem. Rev.* **307**, 255–266 (2016).

47. Wang, T. C. *et al.* Ultrahigh Surface Area Zirconium MOFs and Insights into the Applicability of the BET Theory. *J. Am. Chem. Soc.* **137**, 3585–3591 (2015).

48. Hu, Z. & Srinivasan, M. P. Mesoporous high-surface-area activated carbon. *Microporous Mesoporous Mater.* **43**, 267–275 (2001).

49. Liu, G. *et al.* Mixed matrix formulations with MOF molecular sieving for key energy-intensive separations. *Nat. Mater.* **17**, 283–289 (2018).

50. Hu, Z. *et al.* Combination of Optimization and Metalated-Ligand Exchange: An Effective Approach to Functionalize UiO-66(Zr) MOFs for CO2 Separation. *Chem. – Eur. J.* **21**, 17246–17255 (2015).

51. Yu, J. *et al.* CO2 Capture and Separations Using MOFs: Computational and Experimental Studies. *Chem. Rev.* **117**, 9674–9754 (2017).

52. Park, C., Lee, K., Koo, M. & Park, C. Soft Ferroelectrics Enabling High-Performance Intelligent Photo Electronics. *Adv. Mater.* **33**, 2004999 (2021).

53. Fu, D.-W., Zhang, W. & Xiong, R.-G. The first metal–organic framework (MOF) of Imazethapyr and its SHG, piezoelectric and ferroelectric properties. *Dalton Trans.* 3946–3948 (2008)

CHAPTER 8

SYSTEMATIC INVESTIGATION OF CO$_2$ ADSORPTION ENERGETICS IN METAL

ORGANIC FRAMEWORKS BASED ON IMIDAZOLYL LINKERS

Reference: This work has been submitted for publication in the Journal of *Physical*

Chemistry C.

Abstract: This study explores systematics in the energetics of CO$_2$ adsorption in 3-dimentional (3D) metal organic frameworks employing imidazolyl ligands, namely ditopic 2-methylimidazole (HMeIm) in Zn(MeIm)$_2$ (ZIF-8), Co(MeIm)$_2$ (ZIF-67), and tetratopic tetrakis(imidazolyl) boric acid (HB(MeIm)$_4$) in CuB(MeIm)$_4$ (Cu-BIF-3). All frameworks have the sodalite (SOD) topology. Direct gas adsorption calorimetric experiments enable quantitation of energetic drive for CO$_2$ confinement in the frameworks. The general trend in the integral adsorption enthalpy ΔH_{int} (kJ/mol) is Cu-BIF-3 > ZIF-8 > ZIF-67. In ZIFs greater porosity is consistent with more favorable CO$_2$ incorporation. Overall, the use of larger linkers in BIFs provides greatest enhancement of the energetics of CO$_2$ adsorption in MOFs. The strength of guest-host interactions depends strongly on choice of linker and metal.

8.1 Introduction

The current increase in demand for energy, transportation, and food supply stresses the need for up-scaling production processes.[1–5] However, in the past few decades there has been increasing concerns over the negative effects of large-scale

greenhouse gas emissions from industrial activity.[6–8] To overcome this challenge, current efforts include the development of materials suitable for molecular sieving and gas storage.[9] This necessitates the use of structures with sufficient porosity and persistence to thermal decomposition.[10–12] Currently, materials with the desired properties include zeolites, activated carbon, and metal organic frameworks (MOFs).[13, 14]

Metal organic frameworks are reticular structures comprised of metal nodes linked by organic ligands.[15] Zeolitic imidazolate frameworks (ZIFs) and boron imidazolate frameworks (BIFs) are special subclasses of MOFs.[16, 17] Mechanochemically synthesized BIFs and ZIFs can form polymorphs with different porosities.[16, 18, 19] The polymorphs differ in physicochemical properties, and this makes MOFs a versatile class of materials with potential application in various industries.[20, 21] MOFs can possess porosity (storage capacity) far greater than activated carbon and zeolite structures,[22–24] this makes MOFs great candidates for capture of greenhouse gases, including carbon dioxide (CO_2).[22–24] Additionally, porous BIFs and ZIFs can form isostructural frameworks employing same linker but different metals and vice-versa.[16, 17, 25] The choice of metal-ligand combination permits modulation of their thermal persistence to decomposition, porosity, as well as strength of guest-host interaction with confined guest molecules (e.g. CO_2).[26–28] With increasing popularity in the use of MOFs for molecular storage applications, it is essential to investigate the thermochemistry and identify the energetic landscape of guest-host interactions in these materials.

To date, multiple studies investigate the synthesis and application of MOFs for molecular sieving and storage applications, however, knowledge of systematics in the

thermochemistry of guest-host interactions in MOFs is lacking.[29] With increasing

popularity in the use of MOFs for molecular storage applications, it is essential to

identify effect of choice of metal and ligand on the energetic drive for confinement of

guest molecules.[30–32] Such understanding could permit identification of structural

descriptors for energetic stabilization of framework interaction with confined molecules.

This could further enable modulation of frameworks for the efficient separation of noble

gases, which is currently challenging.[33]

Previous works calculated isosteric heats of CO_2 adsorption in MOFs by

employing a polynomial fit to two or more adsorption isotherms at different

temperatures.[34, 35]In addition to the propagation of large uncertainty from this multistep

process, with this method alone it is especially challenging to obtain isosteric heats of

adsorption at zero coverage, since further fitting is necessary.[34, 36] This problem stresses

the need for direct calorimetric measurements of heats of adsorption in materials,

including MOFs. To this end, previous thermodynamic works investigated the

calorimetry of low-pressure CO_2 adsorption in CD-MOFs.[34] In this work we explore

direct calorimetry of CO_2 adsorption in three frameworks: $Zn(MeIm)_2$, $Co(MeIm)_2$, and

$CuB(MeIm)_4$, which are commonly known as ZIF-8, ZIF-67, and Cu-BIF-3, respectively.

This is the first work to employ direct calorimetric experiments to systematically

investigate energetics of CO_2 adsorption in porous Co and Zn ZIFs based on ditopic 2-

methylimidazolate linkers, and a Cu-BIF employing tetratopic boron-imidazolate linker

(see Figure 1).[16, 17] This is a valuable addition to our understanding of the energetic

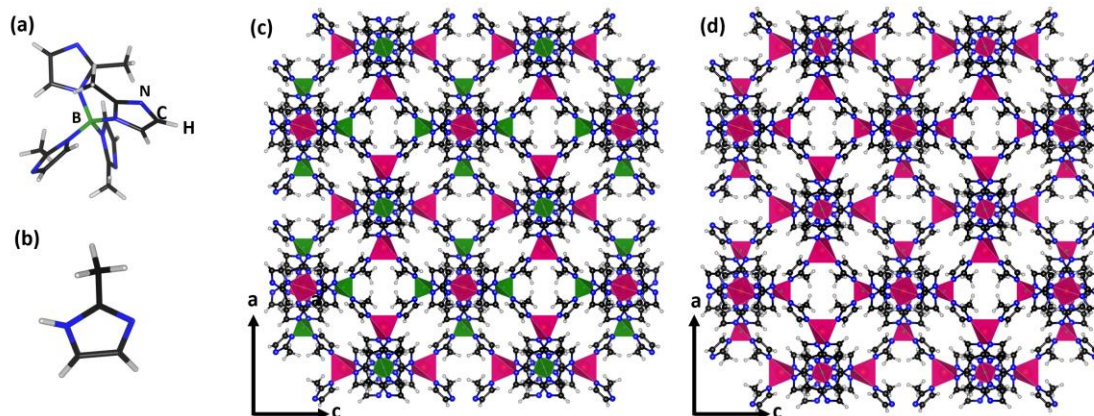landscape for CO_2 adsorption in MOFs.

221

Figure 1. Structure of (a) tetratopic tetrakis(imidazolyl) boric acid ligand, (b) 2-methylimidazole ligand, and framework configuration of (c) BIFs, and (d) ZIFs in the SOD topology, white= hydrogen, black=carbon, blue=nitrogen, green=boron, red= Cu (in figure c) and Zn or Co (in figure d).

8.2 Experimental Methods

8.2.1 Materials

The synthesis and characterization of the materials was performed at ASU following procedures similar to those reported in chapters 6 and 7 of this dissertation document, and the results agree with previous reports.[16, 37–39] Phase identification was performed by X-ray diffraction. Fourier-transform infrared spectroscopy (FTIR) spectra confirmed presence of bonds consistent with ZIFs and BIFs, respectively. TG-DSC confirmed metal content in the frameworks from thermal decomposition in air.

8.2.2 Gas Adsorption Calorimetry

Direct adsorption calorimetric experiments employed a commercial gas adsorption analyzer Micromeritics ASAP2020, coupled to a benchtop Calvet-type Seteram Sensys microcalorimeter. For analysis ~50 mg of the sample was loaded into a custom-made silica glass forked tube. In the first step, the top (gas inlet/outlet) of the tube was loaded into the degassing port of the gas adsorption analyzer, and degassed for 12 hr, at 25°C, under vacuum ($<10^{-3}$ Pa). The second step was determination of surface area of degassed specimens as well as quantitation of the free space in the tube, this uses five-point nitrogen adsorption at -195.8 °C. In the third step, the tube was loaded on the analysis port of the volumetric dosing system (ASAP2020), simultaneously, the bottom portion of the forked tube was inserted into the twin chambers of the microcalorimeter see Figure 2. Before gas adsorption calorimetry the sample was evacuated for another 12hr, at 25°C this ensures complete removal of any confined species. For gas adsorption calorimetric experiments, the ASAP 2020 analyzer used incremental dosing mode (~0.020 mmol CO_2/dose, up to 700 mmHg) and a minimum equilibration time of ~1.5 hrs. The amount of CO_2 adsorbed was determined from the pressure drop. This enabled simultaneous acquisition of gas adsorption isotherms and the heat effect corresponding to each dose. Two trials were conducted per fresh MOF sample. This is a well-established technique, more experimental details are provided in previous works.[34, 40–43]
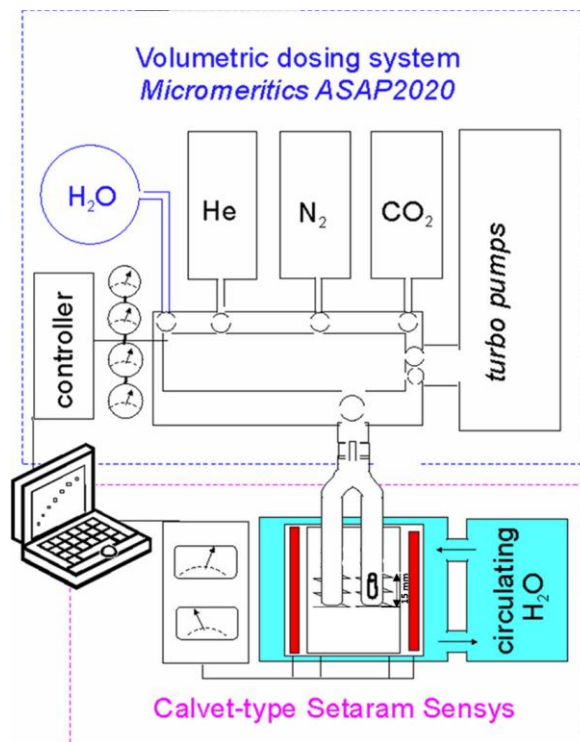
Figure 2. Setup of instrumentation used for gas adsorption calorimetry. Reprinted with permission from [34]. Copyright 2013 American Chemical Society

8.3 Results and Discussion

8.3.1 BET Surface Area

Surface area measurements allowed identification of differences in porosity of the samples. The results from BET (m^2/g) measurement are summarized in Table 1. The results show that ZIF-8 presents the highest porosity and Cu-BIF-3 the lowest. Overall, the results point to comparable porosity in BIFs and ZIFs. Differences in surface area can be expected to result in significant dissimilarities in the CO_2 storage capacity of these materials.

Table 1. Summary of framework topology, dimension, and surface area.

Samples	Common name	Framework dimension	BET area (m^2/g)
SOD-Zn(MeIm)$_2$	ZIF-8	3D	1570
SOD-Co(MeIm)$_2$	ZIF-67	3D	1510
SOD-CuB(MeIm)$_4$	Cu-BIF-3	3D	933

8.3.2 CO_2 Adsorption Isotherms

The adsorption isotherms determine quantity (normalized per surface area) of CO_2 adsorbed by the frameworks between 0 and ~1 relative pressure (P_o/P), where P_o= 760 mmHg. The results are summarized in Figure 3. The curves point to only minor CO_2 coverage in all frameworks up to P_o/P ~0.2. Between 0 and 0.6, ZIF-67 presents higher CO_2 coverage compared to ZIF-8. At higher pressure (P_o/P >0.6) the difference is within experimental error. Overall, beyond P_o/P ~0.2 Cu-BIF-3 displays the highest coverage. The results may be associated with dissimilarities in the energetics of interaction between the frameworks and confined CO_2 molecules, as discussed in the next section.
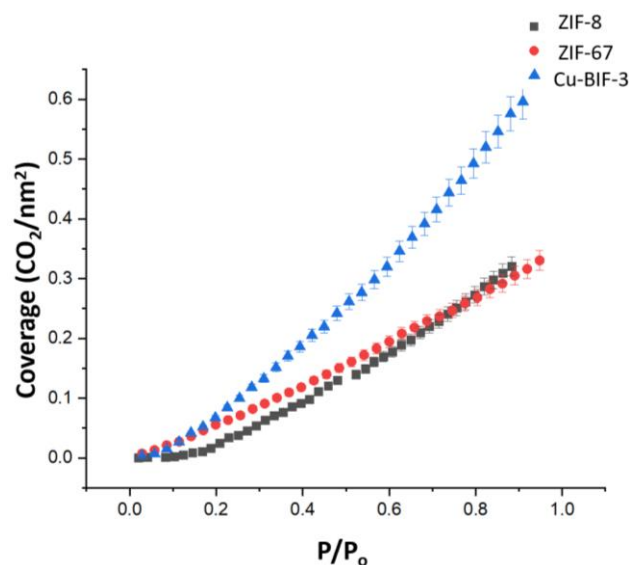
Figure 3. Summary of isotherms corresponding to CO_2 adsorption in frameworks (25°C, up to ~700 mmHg). X-axis represents relative pressure; Y-axis corresponds to CO_2 coverage in the frameworks (CO_2 /nm^2)

8.3.3 Thermochemistry of CO_2 Adsorption

Direct calorimetric measurements permit quantitation of differential and integral enthalpy of adsorption in these materials. Differential enthalpy of adsorption (ΔH_{diff}) refers to the change in total enthalpy of the system as a single small CO_2 dose)s is transferred from the gas phase and adsorbed at constant temperature (normalized per mole of gas) .[44–46] Integral adsorption enthalpy (ΔH_{int}) refers to total integrated heat effect normalized per mole up to a given amount of CO_2 adsorbed by the framework. Generally, the free energy change for adsorption is dominated by the enthalpy term,[47, 48] therefore more exothermic adsorption enthalpy corresponds to greater thermodynamic drive for interactions (binding) between CO_2 (guest) and the framework (host). This

permits direct comparison of the strength of guest-host interactions in these MOF systems.

In porous materials like MOFs the adsorption sites may differ in energy, and generally more energetic sites interact more strongly with confined guest molecules.[34, 43, 49] Integral enthalpy curves permit determination of systematic differences in the total enthalpy of CO_2 confinement in frameworks across the pressure range. Comparison of ZIF-8 and ZIF-67 shows how choice of metal affects binding energetics. Additionally, studying Cu-BIF-3 enables initial assessment of differences in the energetics of adsorption in ZIFs and BIFs. The differential and integral enthalpy curves corresponding to adsorption isotherms are summarized in Figure 4 (a-b).
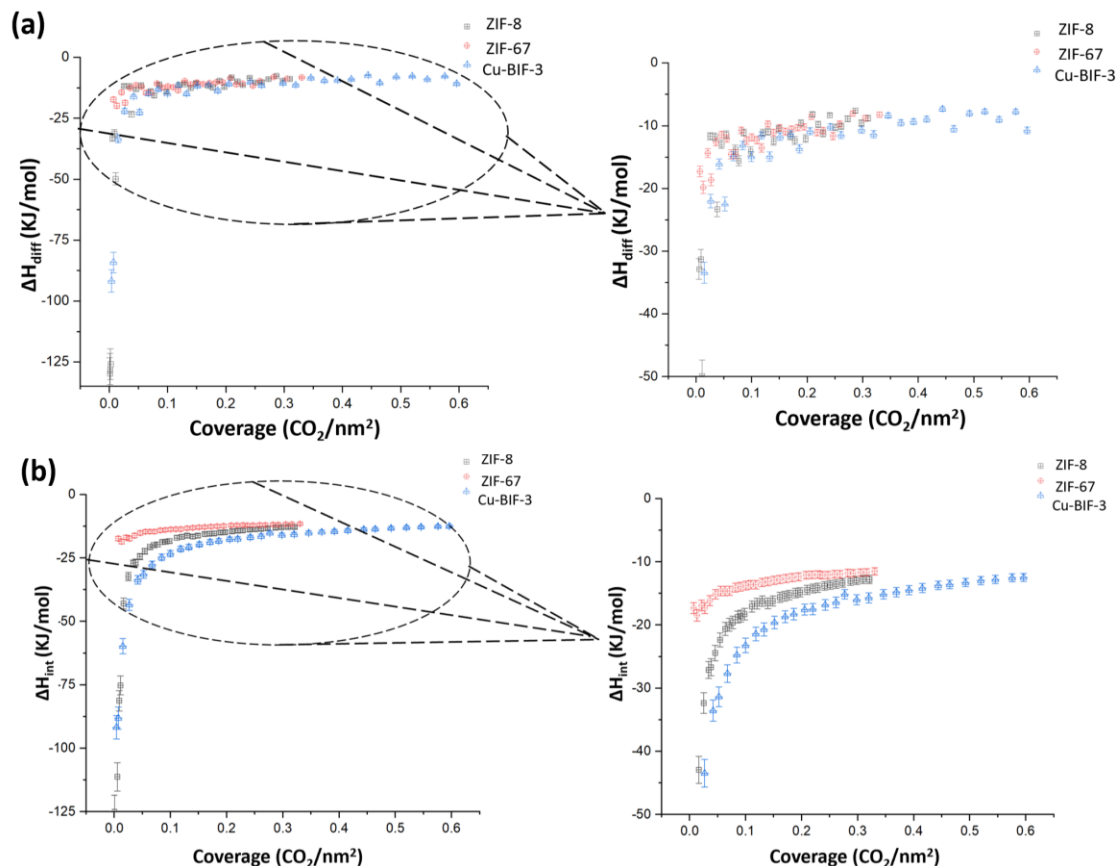
Figure 4. Enthalpy curves corresponding to (a) differential enthalpy and (b) integral enthalpy of adsorption. The figures on the right are zoomed in versions of figures on the left.

Figure 4a shows that the most energetically favorable confinement of guest molecules occurs at zero coverage, as generally expected and seen in many other systems.[34, 43] The results further indicate that initial binding enthalpy is exothermic by ~120, 90, and 17 kJ/mol in ZIF-8, Cu-BIF-3, and ZIF-67, respectively. These values are in the chemisorption range, implying strong adsorption in the bare structures. The results highlight the energetically favorable adsorption sites in fresh ZIF-8 and Cu-BIF-3 near zero coverage. The enthalpy curves rapidly become less exothermic with increasing CO_2

dosage, which reflects repulsion between confined CO_2 molecules in the framework at higher coverage. Eventually, all curves approach a plateau (near ~ -10 kJ/mol) with increasing CO_2 loading (see Figure 4). Most exothermic binding probably occurs in the cages of the framework, while subsequent less exothermic adsorption can result from surface binding.[42] Overall, at high coverage the enthalpies of adsorption (ΔH_{diff}) are within the physisorption range, which is expected for short-range Van der Waals interaction between the adsorption sites and confined guest-molecules.[34, 43]

Systematic differences can be observed from integral adsorption enthalpies (Figure 4b). Overall, across the pressure range, energetic drive for CO_2 confinement decreases in the following order: Cu-BIF-3 > ZIF-8 > Co-ZIF-67. This trend is consistent across the entire pressure range. These results highlight increasing thermodynamic drive for CO_2 incorporation in isostructural ZIFs from substitution of Co(II) by larger Zn(II) metal atoms as nodes. This may be explained by the higher porosity of ZIF-8, perhaps implying that in 3D SOD ZIFs employing the same linker, greater porosity is consistent with more favorable CO_2 adsorption, resulting from less repulsion between confined CO_2 molecules.

Figure 4b shows that in this pressure range, Cu-BIF-3 presents the most exothermic (favorable) integral enthalpy of adsorption, which may explain its greatest CO_2 coverage compared to the other specimens (Figure 3), despite its lower porosity. We do not observe any trends between electronegativity of the metal atoms and corresponding adsorption energetics, which may rule-out metal atoms as main CO_2 binding sites in these MOFs. Considering the lower porosity, such dissimilarities in the

adsorption energetics of BIFs compared to ZIFs likely result from choice of linker, especially since differences in the ionic radii of the metals is minor. The results in Figure 4b suggest enhancement of CO_2 incorporation energetics in MOFs by use of tetratopic tetrakis (imidazolyl) boric acid (in BIFs) instead of ditopic 2-methylimidazole (in ZIFs) ligands. This shows that although greater porosity is generally consistent with more favorable energetics CO_2 incorporation, less porous structures like BIFs can display enhanced adsorption energetics from choice of a larger linker. This enhancement is an important positive consideration in the design of MOFs for CO_2 storage. The high enthalpic drive for adsorption in Cu-BIF-3 could enable superior selectivity for CO_2 separation from multicomponent systems. The overall energetic landscape in these materials is shown in Figure 5 and the results are summarized in Table 2.
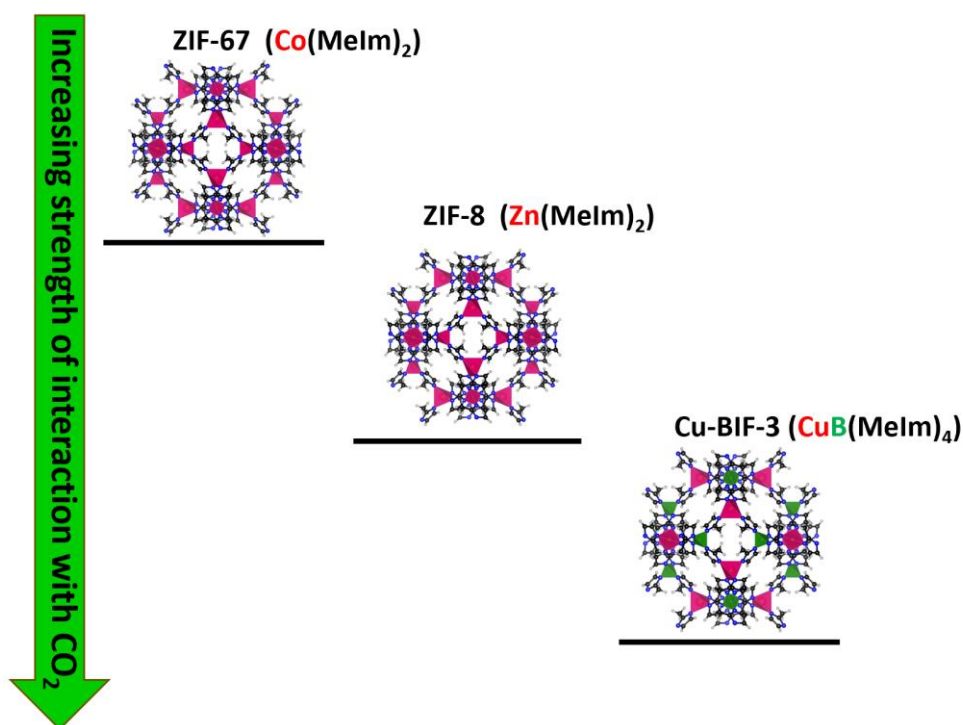

Figure 5. Energetic landscape of CO_2 adsorption in the frameworks.

Table 2. Summary of differential and integral enthalpy for CO_2 adsorption, between ~0-0.3 CO_2 coverage (CO_2/nm^2)

Sample	CO_2 loading (CO_2/nm^2)	ΔH_{diff} (kJ/mol)	ΔH_{int} (kJ/mol)
ZIF-8	~0	-126.00	-126.00
	0.1	-14.10	-15.3
	0.3	-9.85	-13.6
ZIF-67	~0	-17.30	-17.30
	0.1	-11.87	-13.72
	0.3	-8.83	-11.67
Cu-BIF-3	~0	-91.73	-91.73
	0.1	-14.90	-23.26
	0.3	-11.40	-15.68

8.4 Conclusions

This study investigates CO_2 adsorption in 3D ZIF and BIF frameworks in the SOD topology. In ZIFs, greater porosity corresponds to more favorable CO_2 confinement, which can be highly exothermic by as much as ~126 kJ/mol (in bare ZIF-8 structures).

231

Overall, topologically similar MOFs like BIFs, employing larger tetratopic linkers can display more energetically favorable CO_2 confinement compared to ZIFs employing ditopic linkers. These results indicate the possibility of general trends in the enhancement of guest-host interactions in MOF topologies from choice of metal and linker. This confirms strong interdependence between choice of constituents (metal, linker), porosity, and energetics of molecular confinement across MOF systems. Considering the decomposition of MOFs like ZIF-8 through carbonation reactions, upon long term exposure to CO_2 and moisture, the next chapter evaluates the energetic landscape for the formation of the decomposition product, mixed linker CO_3-ZIF-8.

REFERENCES

1. Cheng, S. & Logan, B. E. Increasing power generation for scaling up single-chamber air cathode microbial fuel cells. *Bioresour. Technol.* **102**, 4468–4473 (2011).

2. Mohareb, E. *et al.* Considerations for reducing food system energy demand while scaling up urban agriculture. *Environ. Res. Lett.* **12**, 125004 (2017).

3. Körner, Ch. Towards a better experimental basis for upscaling plant responses to elevated CO2 and climate warming. *Plant Cell Environ.* **18**, 1101–1110 (1995).

4. Pasupuleti, S. B., Sarkar, O. & Venkata Mohan, S. Upscaling of biohydrogen production process in semi-pilot scale biofilm reactor: Evaluation with food waste at variable organic loads. *Int. J. Hydrog. Energy* **39**, 7587–7596 (2014).

5. Urbain, F. *et al.* Upscaling high activity oxygen evolution catalysts based on CoFe2O4 nanoparticles supported on nickel foam for power-to-gas electrochemical conversion with energy efficiencies above 80%. *Appl. Catal. B Environ.* **259**, 118055 (2019).

6. Yue, Q., Xu, X., Hillier, J., Cheng, K. & Pan, G. Mitigating greenhouse gas emissions in agriculture: From farm production to food consumption. *J. Clean. Prod.* **149**, 1011–1019 (2017).

7. Herzog, H., Eliasson, B. & Kaarstad, O. Capturing Greenhouse Gases. *Sci. Am.* **282**, 72–79 (2000).

8. Hoefnagels, R., Smeets, E. & Faaij, A. Greenhouse gas footprints of different biofuel production systems. *Renew. Sustain. Energy Rev.* **14**, 1661–1694 (2010).

9. Wich-Konrad, T., Lüke, W., Oles, M. & Deerberg, G. Assessment of Industrial Greenhouse Gas Reduction Strategies Within Consistent System Boundaries. *Chem. Ing. Tech.* **92**, 1393–1402 (2020).

10. Singh, G. *et al.* Emerging trends in porous materials for CO2 capture and conversion. *Chem. Soc. Rev.* **49**, 4360–4404 (2020).

11. Lu, A.-H. & Hao, G.-P. Porous materials for carbon dioxide capture. *Annu. Rep. Sect. Inorg. Chem.* **109**, 484–503 (2013).

12. Siegelman, R. L., Kim, E. J. & Long, J. R. Porous materials for carbon dioxide separations. *Nat. Mater.* **20**, 1060–1072 (2021).

13. Gaikwad, S. & Han, S. Shaping metal-organic framework (MOF) with activated carbon and silica powder materials for CO2 capture. *J. Environ. Chem. Eng.* **11**, 109593 (2023).

14. Wang, J., Pu, Q., Ning, P. & Lu, S. Activated carbon-based composites for capturing CO2: a review. *Greenh. Gases Sci. Technol.* **11**, 377–393 (2021).

15. Introduction to Metal–Organic Frameworks. *Chem. Rev.* **112**, 673–674 (2012).

16. B. Lennox, C. *et al.* Simplifying and expanding the scope of boron imidazolate framework (BIF) synthesis using mechanochemistry. *Chem. Sci.* **12**, 14499–14506 (2021).

17. Novendra, N. *et al.* Linker Substituents Control the Thermodynamic Stability in Metal–Organic Frameworks. *J. Am. Chem. Soc.* **142**, 21720–21729 (2020).

18. Friščić, T., Mottillo, C. & Titi, H. M. Mechanochemistry for Synthesis. *Angew. Chem. Int. Ed.* **59**, 1018–1029 (2020).

19. Arhangelskis, M. *et al.* Theoretical Prediction and Experimental Evaluation of Topological Landscape and Thermodynamic Stability of a Fluorinated Zeolitic Imidazolate Framework. *Chem. Mater.* **31**, 3777–3783 (2019).

20. Furukawa, H., Cordova, K. E., O'Keeffe, M. & Yaghi, O. M. The Chemistry and Applications of Metal-Organic Frameworks. *Science* **341**, 1230444 (2013).

21. Czaja, A. U., Trukhan, N. & Müller, U. Industrial applications of metal–organic frameworks. *Chem. Soc. Rev.* **38**, 1284–1293 (2009).

22. Marco-Lozar, J. P., Juan-Juan, J., Suárez-García, F., Cazorla-Amorós, D. & Linares-Solano, A. MOF-5 and activated carbons as adsorbents for gas storage. *Int. J. Hydrog. Energy* **37**, 2370–2381 (2012).

23. Grünker, R. *et al.* A new metal–organic framework with ultra-high surface area. *Chem. Commun.* **50**, 3450–3452 (2014).

24. Farha, O. K. *et al.* Metal–Organic Framework Materials with Ultrahigh Surface Areas: Is the Sky the Limit? *J. Am. Chem. Soc.* **134**, 15016–15021 (2012).

25. Akimbekov, Z. *et al.* Experimental and Theoretical Evaluation of the Stability of True MOF Polymorphs Explains Their Mechanochemical Interconversions. *J. Am. Chem. Soc.* **139**, 7952–7957 (2017).

26. Mu, B. & Walton, K. S. Thermal Analysis and Heat Capacity Study of Metal–Organic Frameworks. *J. Phys. Chem. C* **115**, 22748–22754 (2011).

27. Åhlén, M. *et al.* Gas sorption properties and kinetics of porous bismuth-based metal-organic frameworks and the selective CO_2 and SF_6 sorption on a new bismuth trimesate-based structure UU-200. *Microporous Mesoporous Mater.* **329**, 111548 (2022).

28. Wells, B. A., Webley, P. A. & Chaffee, A. L. Simulations of model metal-organic frameworks for the separation of carbon dioxide. *Energy Procedia* **4**, 568–575 (2011).

29. Bingel, L. W. & Walton, K. S. Surprising Use of the Business Innovation Bass Diffusion Model To Accurately Describe Adsorption Isotherm Types I, III, and V. *Langmuir* **39**, 4475–4482 (2023).

30. Das, S., Ben, T., Qiu, S. & Valtchev, V. Two-Dimensional COF–Three-Dimensional MOF Dual-Layer Membranes with Unprecedentedly High H_2/CO_2 Selectivity and Ultrahigh Gas Permeabilities. *ACS Appl. Mater. Interfaces* **12**, 52899–52907 (2020).

31. Peng, Y.-W. *et al.* Nitrogen Coordination To Dramatically Enhance the Stability of In-MOF for Selectively Capturing CO_2 from a CO_2/N_2 Mixture. *Cryst. Growth Des.* **19**, 1322–1328 (2019).

32. Qasem, N. A. A., Ben-Mansour, R. & Habib, M. A. An efficient CO_2 adsorptive storage using MOF-5 and MOF-177. *Appl. Energy* **210**, 317–326 (2018).

33. Liu, Y., Liu, J. & Hu, J. Noble gas separation by a MOF with one-dimensional channels. *BMC Chem. Eng.* **1**, 3 (2019).

34. Wu, D. *et al.* Direct Calorimetric Measurement of Enthalpy of Adsorption of Carbon Dioxide on CD-MOF-2, a Green Metal–Organic Framework. *J. Am. Chem. Soc.* **135**, 6790–6793 (2013).

35. Pan, H., Ritter, J. A. & Balbuena, P. B. Examination of the Approximations Used in Determining the Isosteric Heat of Adsorption from the Clausius−Clapeyron Equation. *Langmuir* **14**, 6323–6327 (1998).

36. Czepirski, L. & JagieŁŁo, J. Virial-type thermal equation of gas—solid adsorption. *Chem. Eng. Sci.* **44**, 797–801 (1989).

37. Titi, H. M. *et al.* Metal–Organic Frameworks as Fuels for Advanced Applications: Evaluating and Modifying the Combustion Energy of Popular MOFs. *Chem. Mater.* **31**, 4882–4888 (2019).

38. Zhang, J., Zhang, T., Yu, D., Xiao, K. & Hong, Y. Transition from ZIF-L-Co to ZIF-67: a new insight into the structural evolution of zeolitic imidazolate frameworks (ZIFs) in aqueous systems. *CrystEngComm* **17**, 8212–8215 (2015).

39. M. Titi, H., Do, J.-L., J. Howarth, A., Nagapudi, K. & Friščić, T. Simple, scalable mechanosynthesis of metal–organic frameworks using liquid-assisted resonant acoustic mixing (LA-RAM). *Chem. Sci.* **11**, 7578–7584 (2020).

40. Ushakov, S. V. & Navrotsky, A. Direct measurements of water adsorption enthalpy on hafnia and zirconia. *Appl. Phys. Lett.* **87**, 164103 (2005).

41. Hulvey, Z. *et al.* Noble Gas Adsorption in Copper Trimesate, HKUST-1: An Experimental and Computational Study. *J. Phys. Chem. C* **117**, 20116–20126 (2013).

42. Hughes, J. T., Sava, D. F., Nenoff, T. M. & Navrotsky, A. Thermochemical Evidence for Strong Iodine Chemisorption by ZIF-8. *J. Am. Chem. Soc.* **135**, 16256–16259 (2013)

.

43. Guo, X., Zhang, P. & Navrotsky, A. The thermodynamics of gas absorption and guest-induced flexibility in zeolite Y. *Microporous Mesoporous Mater.* **294**, 109893 (2020).

44. Gouvêa, D., Ushakov, S. V. & Navrotsky, A. Energetics of CO2 and H2O Adsorption on Zinc Oxide. *Langmuir* **30**, 9091–9097 (2014).

45. Navrotsky, A., Mazeina, L. & Majzlan, J. Size-Driven Structural and Thermodynamic Complexity in Iron Oxides. *Science* **319**, 1635–1638 (2008).

46. Torres-Knoop, A., Poursaeidesfahani, A., Vlugt, T. J. H. & Dubbeldam, D. Behavior of the Enthalpy of Adsorption in Nanoporous Materials Close to Saturation Conditions. *J. Chem. Theory Comput.* **13**, 3326–3339 (2017).

47. Gensterblum, Y., Busch, A. & Krooss, B. M. Molecular concept and experimental evidence of competitive adsorption of H2O, CO2 and CH4 on organic material. *Fuel* **115**, 581–588 (2014).

48. Mayer, L. M. Extent of coverage of mineral surfaces by organic matter in marine sediments. *Geochim. Cosmochim. Acta* **63**, 207–215 (1999).

49. Mazeina, L. & Navrotsky, A. Enthalpy of Water Adsorption and Surface Enthalpy of Goethite (α-FeOOH) and Hematite (α-Fe2O3). *Chem. Mater.* **19**, 825–833 (2007).

CHAPTER 9

EXPERIMENTAL AND THEORETICAL EVALUATION OF THE

THERMODYNAMICS OF CARBONATION REACTION OF ZIF-8 AND ITS CLOSE-

PACKED POLYMORPH WITH CARBON DIOXIDE

Abstract: We report the first experimental and theoretical evaluation of the thermodynamic driving force for the reaction of metal organic framework (MOF) materials with carbon dioxide, leading to a metal organic carbonate phase. Carbonation upon exposure of MOFs to CO_2 is a significant concern for the design and deployment of such materials in carbon storage technologies, and this work shows that the formation of a carbonate material from the popular SOD-topology framework material ZIF-8, as well as its dense-packed *dia*-topology polymorph, are significantly exothermic. With knowledge of the crystal structure of starting and final phases in carbonation reaction, we have also identified periodic density-functional theory approaches that most closely reproduce the measured reaction enthalpies. This development now permits the use of advanced theoretical calculations to calculate the driving forces behind carbonation of zeolitic imidazolate frameworks with reasonable accuracy.

9.1 Introduction

Over the past three decades, the chemistry of metal organic frameworks (MOF) has become one of the central areas of advanced materials research,[1–3] with a wide range of

proposed applications, from gas storage, catalysis, and light harvesting, to extending shelf lives of vaccines and rocket propulsion.[4–7] The rapid development and high popularity of MOFs are to a large extent due to their inherently modular node-and-linker design, [8, 9] which permits the rational development of new materials that combine previously unimaginable surface area and microporosity with specific chemical or physical properties, such as color, luminescence, conductivity, sensing ability, and more.[6, 10–15] Whereas the development of new MOF designs is facilitated by concepts of reticular chemistry and, very recently, methodologies for *ab initio* crystal structure prediction (MOF-CSP),[16] the understanding and reliable design of thermodynamic stability in MOFs remains poorly explored. This is both a significant challenge and an opportunity for the further development of MOFs, as thermodynamic stability is the driving force underlying a wide range of environmental behaviors important for potential applications of MOFs, such as resistance to moisture, chemical reagents, temperature, etc.[17–21] Important insights into the relative stability of MOF polymorphs, as well as thermodynamic relationships with respect to metal precursors can be gained from computational methods, particularly periodic density-functional theory (DFT) calculations. In that context, our team has recently used a combination of solution calorimetry and periodic DFT to provide the first quantitative insights into how the thermodynamic stability of zeolitic imidazolate frameworks (ZIFs), a class of MOFs exhibiting zeolite-like topologies and based on imidazolate linkers and tetrahedral ions such as Zn^{2+}, Co^{2+}, or Cd^{2+}, is affected by changes in topology, polymorphism, and of substituents on the organic linker.[22–24] These studies have revealed that thermodynamic stability of ZIFs can be assessed through simple tabulated parameters, such as Hammett σ-constants, and even predicted from readily calculated linker parameters,

such as the electrostatic surface potential (ESP) of the linker substituent.[22] Moreover, the combined use of periodic DFT and solution calorimetry measurements enabled quantitative evaluation of the accuracy of the theoretical calculations and establish that dispersion-corrected provide more accurate energies for ZIF structures than pure semi-local functionals. This work mainly addressed thermodynamic stability of ZIFs with respect to the parent metal oxide plus linker, providing a measure of the sensitivity of the materials towards hydrolysis. It remains important to evaluate the stability of MOFs towards a wide range of environmental factors, such as the presence of reactive gases (CO_2, SO_2, etc).[25–28] Although one of the most prominent proposed applications of MOF materials (including ZIFs) is storage of CO_2, there have so far been no studies of their thermodynamic stability to reaction with CO_2. Reactivity with CO_2 is an important problem in MOF development and, indeed, our group has previously reported that exposure of diverse ZIFs to moist CO_2 environments leads to the formation of mixed-ligand carbonate-containing phases.[29]

We now provide the first experimental and theoretical study of the thermodynamics of the reaction of the popular, commercially-relevant framework ZIF-8 (Figure 1a), based on Zn^{2+} nodes and 2-methylimidazolate (MeIm⁻) linkers, to form the carbonate phase $Zn_2(MeIm)_2CO_3$ (Figure 1(c)) The reaction of ZIF-8 with moist CO_2 was previously reported to rapidly yield the $Zn_2(MeIm)_2CO_3$ phase,[29] which also forms as a side product upon mechanochemical synthesis of ZIF-8 if basic zinc carbonate is used as the metal precursor.[30]
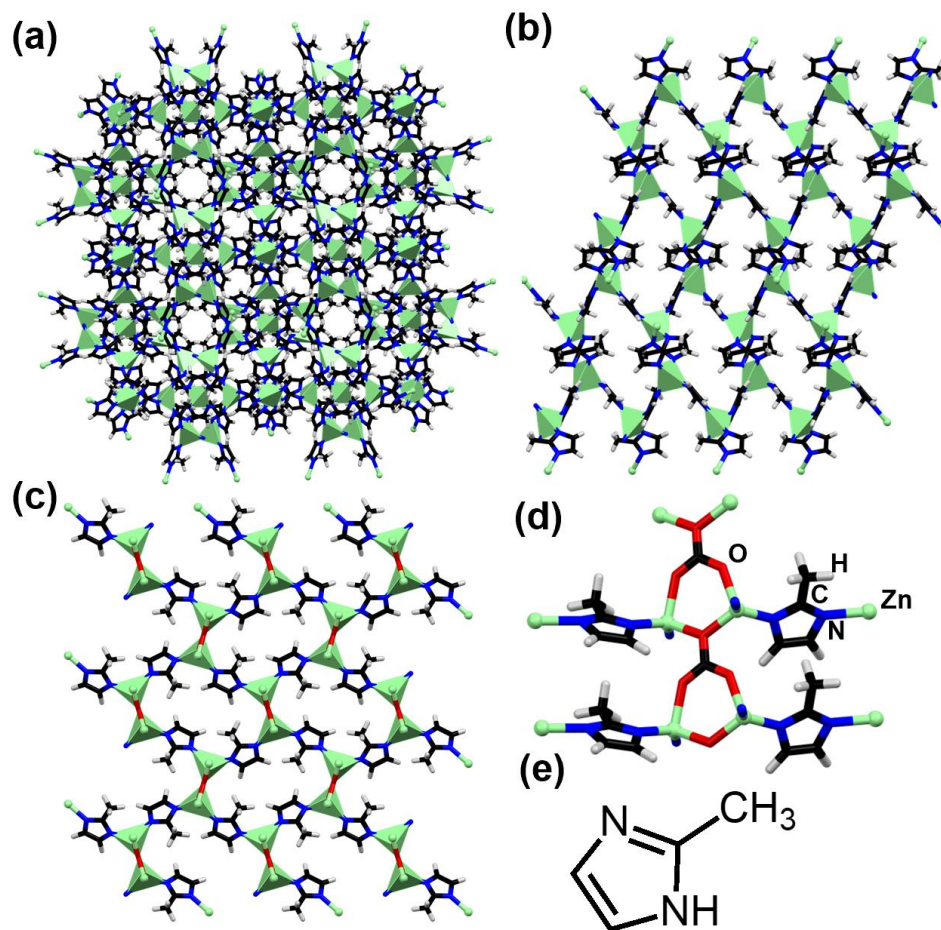
Figure 1. Structure of (a) SOD-Zn(MeIm)$_2$, (b) *dia*-Zn(MeIm)$_2$, (c) Zn$_2$(MeIm)$_2$CO$_3$, (d) carbonate and imidazolate linkers, and (e) 2-methylimidazole (HMeIm) ligand. Zn, oxygen, carbon, hydrogen, and nitrogen atoms are depicted by green, red, black, grey, and blue spheres, respectively.

The crystal structure of Zn$_2$(MeIm)$_2$CO$_3$ was previously determined from powder X-ray diffraction (PXRD)[30] and the data presents Zn^{2+} metal centers tetrahedrally coordinated to two imidazolate and two carbonate linkers (Figure 1c,d). Notably, the availability of crystallographic data for Zn$_2$(MeIm)$_2$CO$_3$ enabled us to develop and

compare different semi-empirical dispersion-corrected periodic density-functional (SEDC-DFT)[31–37] approaches to evaluate the driving force for the carbonation reaction of ZIF-8 and of *dia*-Zn(MeIm)$_2$.

To the best of our knowledge, this work presents the first experimental evaluation of the thermodynamics of the reaction of a MOF with carbon dioxide. Moreover, the high degree of agreement between experimentally determined enthalpies and theoretically calculated reaction energies demonstrates, for the first time, the ability to theoretically calculate with high accuracy the driving force for MOF carbonation using periodic DFT.

9.2 Experimental Methods

9.2.1 Materials and Methods

Unless otherwise indicated, all reagents and solvents were obtained from commercial sources and were used without further purification.

9.2.2 Thermal Analysis (TGA/DSC)

Thermogravimetric analysis (TGA) was performed utilizing approximately 5 mg of sample on a Mettler-Toledo TGA/DSC 1 system. The system was operated on a PC with STARe software. Samples were heated from 25 to 700 °C at a rate of 10 °C/min under constant air flow. The balance and purge flow were 40 mL/min and 25 mL/min respectively.

9.2.3 Powder X-ray Diffraction (PXRD)

Powder X-ray diffraction (PXRD) patterns were collected using a Bruker D2 Phaser powder diffractometer equipped with a Cu-Kα (λ = 1.5418 Å) source and Lynxeye detector. The patterns were collected in the angular region between 5° and 40° (2θ) with a step size of 0.05°.

9.2.4 Fourier-Transform Infrared Attenuated Total Reflectance (FTIR-ATR) Spectroscopy

Infrared spectra were obtained using a Bruker Platinum ATR spectrometer and are reported in wavenumber (cm^{-1}) units.

9.2.5 Synthetic Procedures

Synthesis of SOD-Zn(MeIm)$_2$ (ZIF-8):

A mixture of ZnO (1 mmol, 81 mg) was added to a 2.5 mL polypropylene vial along with HMeIm (2.1 mmol, 173 mg) and NH$_4$NO$_3$ (4 mg, 5 mol% Zn) and 75 µL of MeOH (η = 0.30 µL mg-1). The reaction mixture was mixed by Resonant Acoustic Mixing (RAM) at 95 g for 60 minutes to yield the microcrystalline product, confirmed by PXRD and FTIR. The ZIF was subsequently washed by stirring in EtOH (15 mL) and centrifugation at 4 500 rpm three times, and evacuated overnight at 80 °C and 165 mmHg.[38]

Synthesis of *dia*-Zn(MeIm)$_2$ (*dia*-ZIF-8):

A mixture of ZnO (1 mmol, 81 mg) was added to a 15 mL PMMA milling vessel along with HMeIm (2.1 mmol, 173 mg) and 29 µL of H$_2$O and 5 µL of acetic acid ($\eta = 0.10$ µL mg-1). The reaction mixture was ball milled at 30 Hz for 90 minutes to yield the microcrystalline product, confirmed by PXRD and FTIR. The ZIF was subsequently washed by stirring in EtOH (15 mL) and centrifugation at 4 500 rpm three times, and dried overnight at 80 °C and 165 mmHg.

Synthesis of CO$_3$-ZIF-8 (CO$_3$-ZIF-8):

A mixture of ZnO (1 mmol, 81 mg) was added to a 2.5 mL polypropylene vial along with HMeIm (2.1 mmol, 173 mg) and NH$_4$NO$_3$ (4 mg, 5 mol% Zn) and 75 µL of MeOH ($\eta = 0.30$ µL mg-1). The reaction mixture was mixed by Resonant Acoustic Mixing (RAM) at 95 g for 60 minutes to yield the microcrystalline product, confirmed by PXRD and FTIR. The ZIF was subsequently washed by stirring in EtOH (15 mL) and centrifugation at 4 500 rpm three times and evacuated overnight at 80 °C and 165 mmHg overnight. The ZIF was then added to 50 mL of EtOH under a CO$_2$ atmosphere and stirred for 2 hours.

9.2.6 Thermodynamic Measurements

Room temperature acid solution calorimetry (in 5 N HCl) measures heats of dissolution, from which heats of formation are calculated. Calorimetric measurements were performed in a CSC4400 isothermal microcalorimeter. The calorimeter was calibrated through the dissolution of KCl at room temperature (25 °C). The experimental procedure

is well-established.[39–41] The thermodynamic cycles employed in this study are shows in Tables 1-6

9.2.7 Theoretical Calculations of Reaction Thermodynamics

Periodic DFT geometry optimization calculations were used to compute the energies of all individual reaction components. All geometry optimizations were performed using plane-wave periodic DFT in the code CASTEP 19.11.[42] The input files were generated using the program cif2cell from the experimentally determined crystal structures.[43] For calculating the energies of gas molecules of CO_2 and H_2O using periodic DFT, a cell of dimension 20x20x20 Å^3 was created with one molecule of H_2O and CO_2 inside respectively to mimic the gaseous phase of these two species. Moreover, since the liquid phase water was involved in Equations 1-5, the experimentally measured enthalpy of water vaporization, which is 43.9 kJ/mol at 25 °C was the energy used to convert from gas- to liquid-phase water. Calculations were carried out with five different computational methods in order to investigate the effect of using different functionals and dispersion correction schemes on the resulting reaction energies: PBESOL functional; PBE functional with Grimme D3 dispersion correction; PBE with many-body dispersion (MBD*) correction scheme; PBE with Tkatchenko Scheffler (TS) dispersion correction scheme and PBESOL with TS dispersion correction scheme.[44–50] The plane-wave cutoff was set to 700 eV and the 1$^\text{st}$ electronic Brillion zone was sampled with a 2π x 0.07 Å^{-1} k-point grid spacing. The ultrasoft pseudopotentials from the default CASTEP internal library were used. For the convergence of geometry optimization, the criteria of maximum energy

change 2×10^{-5} eV/atom, maximum force on atom 0.05 eV/Å, maximum atom displacement 0.001 Å and residual stress 0.01 GPa were employed. The calculated energies of all reagent and product structures for each of the periodic DFT methods are shown in Table 7. These values were used to compute the theoretical energies for the reactions describing the formation of $Zn_2(MeIm)_2CO_3$ (Table 8).

Table 1. Thermodynamic cycle used to calculate enthalpy of formation (ΔH^o_f) of $Zn(MeIm)_2$ from ZnO and HMeIm.

ZnO (s, 298 K) + 2HMeIm (s, 298 K) →(dia/SOD)-$Zn(MeIm)_2$ (s, 298 K) + H_2O (l, 298) ΔH^o_f

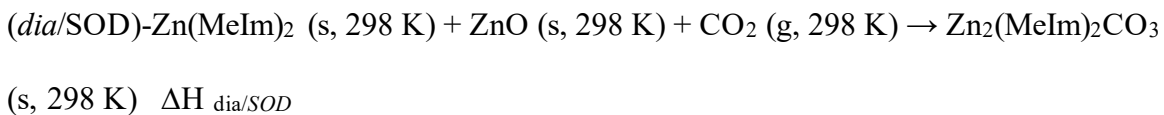| Reaction	ΔH (kJ/mol)
$Zn_2(MeIm)_2$ (s, 298 K) → Zn^{+2} (aq, 298 K) + 2$MeIm^{-1}$ (aq, 298 K)	ΔH^o_{ds}
ZnO (s, 298 K) +2H^+ (aq, 298 K) → Zn^{+2} (aq, 298 K) + H_2O (aq, 298 K)	ΔH_2
HMeIm (s, 298 K) → H^+ (aq, 298 K) + $MeIm^{-1}$ (aq, 298 K)	ΔH_3
H_2O (l, 298 K) → H_2O (aq, 298 K)	ΔH_4
$\Delta H^o_f = - \Delta H^o_{ds} + \Delta H_2 + 2\Delta H_3 - \Delta H_4$	

Table 2. Thermodynamic cycle used to calculate enthalpy of formation (ΔH^o_f) of $Zn(MeIm)_2CO_3$ relative to the ZnO, CO_2, and HMeIm.

$2ZnO$ (s, 298 K) + CO_2 (g, 298 K) + 2HMeIm (s, 298 K) → $Zn_2(MeIm)_2CO_3$ (s, 298 K) + H_2O (l, 298K) ΔH^o_f

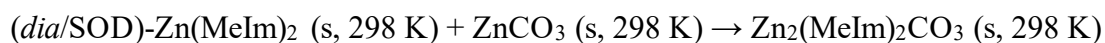| Reaction	ΔH (kJ/mol)
$Zn_2(MeIm)_2CO_3$ (s, 298 K) + $2H^+$→ $2Zn^{+2}$ (aq, 298 K) + $2MeIm^{-1}$. (aq, 298 K) + CO_2 (g, 298 K) + H_2O (aq, 298 K)	ΔH^o_{ds}
H_2O (l, 298 K) → H_2O (aq, 298 K)	ΔH_2
HMeIm (s, 298 K) → H^+ (aq, 298 K) + $MeIm^{-1}$ (aq, 298 K)	ΔH_3
ZnO (s,298 K) +$2H^+$ (aq, 298 K) → Zn^{+2} (aq, 298 K) + H_2O (aq, 298 K)	ΔH_4
$\Delta H^o_f = - \Delta H^o_{ds} - \Delta H_2 + 2\Delta H_3 + 2\Delta H_4$	

Table 3. Thermodynamic cycle used to calculate change in enthalpy for formation of $Zn_2(MeIm)_2CO_3$ from $Zn(MeIm)_2$, ZnO, and CO_2.

(*dia*/SOD)-$Zn(MeIm)_2$ (s, 298 K) + ZnO (s, 298 K) + CO_2 (g, 298 K) → $Zn_2(MeIm)_2CO_3$ (s, 298 K) $\Delta H_{dia/SOD}$

Reaction	ΔH (kJ/mol)
$Zn_2(MeIm)_2CO_3$ (s, 298 K) + $2H^+$→ $2Zn^{+2}$ (aq, 298 K) + $2MeIm^{-1}$. (aq, 298 K) + CO_2 (g, 298 K) + H_2O (aq, 298 K)	ΔH_1
(*dia*/SOD)-$Zn(MeIm)_2$ (s, 298 K) → Zn^{+2} (aq,298) + $2MeIm^{-1}$ (aq, 298 K)	ΔH_2

ZnO (s, 298 K) +2H$^+$ (aq, 298 K) → Zn^{+2} (aq, 298 K) + H$_2$O (aq, 298 K)	ΔH_3
$\Delta H_{dia/SOD}$ = - ΔH_1 + ΔH_2 + ΔH_3	

Table 4. Thermodynamic cycle used to calculate change in enthalpy for formation of Zn$_2$(MeIm)$_2$CO$_3$ from Zn(MeIm)$_2$, and ZnCO$_3$.

(*dia*/SOD)-Zn(MeIm)$_2$ (s, 298 K) + ZnCO$_3$ (s, 298 K) → Zn$_2$(MeIm)$_2$CO$_3$ (s, 298 K)

$\Delta H_{dia/SOD}$

Reaction	ΔH (kJ/mol)
Zn$_2$(MeIm)$_2$CO$_3$ (s, 298 K) + 2H$^+$→ 2Zn^{+2} (aq, 298 K) + 2MeIm^{-1} (aq, 298 K) + CO$_2$ (g, 298 K) + H$_2$O (aq, 298 K)	ΔH_1
Zn(MeIm)$_2$ (s, 298 K) → Zn^{+2} (aq,298) + 2MeIm^{-1} (aq, 298 K)	ΔH_2
ZnCO$_3$ (s, 298 K) +2H$^+$ (aq, 298 K) → Zn^{+2} (aq, 298 K) + CO$_2$ (g, 298 K)+ H$_2$O (aq, 298 K)	ΔH_3
ΔH^o_f = - ΔH_1 + ΔH_2 + ΔH_3	

Table 5. Thermodynamic cycle used to calculate change in enthalpy for formation of Zn$_2$(MeIm)$_2$CO$_3$ from HMeIm, and ZnO, and ZnCO$_3$.
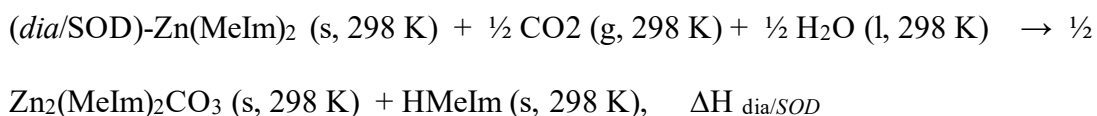
ZnO (s, 298 K) + ZnCO$_3$ (s, 298 K) + 2HMeIm (s, 298 K) → Zn$_2$(MeIm)$_2$CO$_3$ (s, 298 K) + H$_2$O (l, 298K) $\Delta H_{dia/SOD}$

Reaction	ΔH (kJ/mol)

$Zn_2(MeIm)_2CO_3$ (s, 298 K) + $2H^+ \rightarrow 2Zn^{+2}$ (aq, 298 K) + $2MeIm^{-1}$ (aq, 298 K) + CO_2 (g, 298 K) + H_2O (aq, 298 K)	ΔH_1
H_2O (l, 298 K) $\rightarrow H_2O$ (aq, 298 K)	ΔH_2
ZnO (s ,298 K) +$2H^+$ (aq, 298 K) $\rightarrow Zn^{+2}$ (aq, 298 K) + H_2O (aq, 298 K)	ΔH_3
$ZnCO_3$ (s, 298 K) +$2H^+$ (aq, 298 K) $\rightarrow Zn^{+2}$ (aq, 298 K) + CO_2 (g, 298 K)+ H_2O (aq ,298 K)	ΔH_4
$HMeIm$ (s, 298 K) $\rightarrow H^+$ (aq, 298 K) + $MeIm^{-1}$ (aq, 298 K)	ΔH_5
$\Delta H^o_f = - \Delta H_1 - \Delta H_2 + \Delta H_3 + \Delta H_4 + 2\Delta H_5$	

Table 6. Thermodynamic cycle used to calculate change in enthalpy for formation of $Zn_2(MeIm)_2CO_3$ from (Sod/dia)-Zn(MeIm)$_2$, CO_2, and H_2O. this is an true linker exchange reaction that does not incorporate extra ZnO

(*dia*/SOD)-Zn(MeIm)$_2$ (s, 298 K) + ½ CO2 (g, 298 K) + ½ H_2O (l, 298 K) → ½ $Zn_2(MeIm)_2CO_3$ (s, 298 K) + HMeIm (s, 298 K), $\Delta H_{dia/SOD}$

Reaction	ΔH (kJ/mol)
$Zn_2(MeIm)_2CO_3$ (s, 298 K) + $2H^+ \rightarrow 2Zn^{+2}$ (aq, 298 K) + $2MeIm^{-1}$ - (aq, 298 K) + CO_2 (g, 298 K) + H_2O (aq, 298 K)	ΔH_1
$HMeIm$ (s, 298 K) $\rightarrow H^+$ (aq, 298 K) + $MeIm^{-1}$ (aq, 298 K)	ΔH_2
H_2O (l, 298 K) $\rightarrow H_2O$ (aq, 298 K)	ΔH_3

Zn(MeIm)$_2$ (s, 298 K) $\rightarrow$ Zn $^{+2}$ (aq, 298 K) + 2MeIm $^{-1}$ (aq, 298 K)	ΔH_4
ΔH^o_f = - ½ ΔH_1 - ΔH_2 + ½ ΔH_3 + ΔH_4	

- s=solid; l=liquid; g= gas; aq= aqueous

Table 7. Calculated energies in eV per formula unit of crystallographic primitive cell for all reactants and products in Equation 1-5. The periodic DFT calculations were performed using the CASTEP code with the following methods: PBE+D3, PBESOL, PBE+MBD*, PBE+TS and PBESOL+TS.

method	H**MeIm**	CO$_2$	H$_2$O (g)	ZnO	ZnCO$_3$
PBE+D3	-1281.32	-1036.34	-471.56	-2227.89	-3264.78
PBESOL	-1277.10	-1034.02	-470.14	-2225.38	-3260.06
PBE+MBD*	-1281.43	-1036.36	-471.56	-2227.87	-3264.82
PBE+TS	-1281.41	-1036.34	-471.56	-2227.84	-3264.73
PBESOL+TS	-1277.59	-1034.02	-470.14	-2225.65	-3260.51

9.3 Results and Discussion

XRD patterns are shown in Figures 2-4. The experimental patterns are consistent with those calculated using CCDC Mercury software based on published crystallographic data for the structures.[51] The measured Fourier-transform infrared attenuated total reflectance (FTIR-ATR) spectra (see Figure 5) are consistent with the expected framework bonds. Thermogravimetric analysis (TGA) enabled quantitation of metal

content in the frameworks, the results are consistent with the expected stoichiometry (see Figure 6).
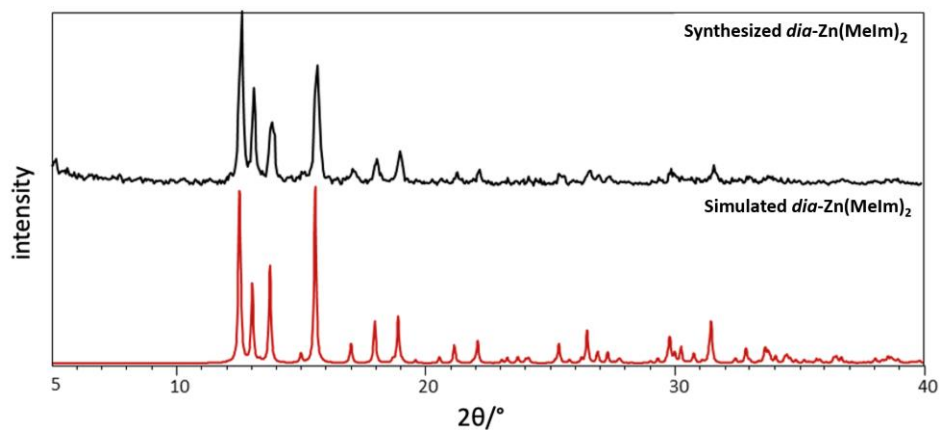

Figure 2: Powder X-ray diffractograms (PXRD) of (top) *dia*-Zn(MeIm)$_2$ following activation and (bottom) simulated powder diffraction pattern from crystal structure (CSD: OFERUN01).

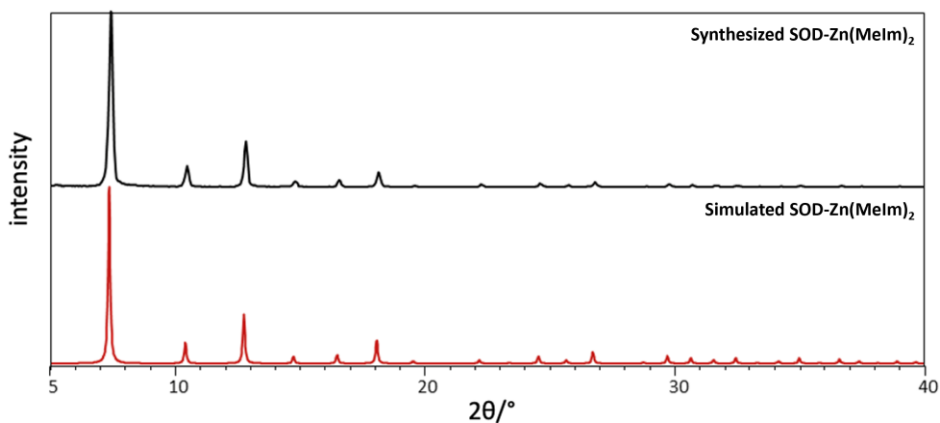
Figure 3: Powder X-ray diffractograms (PXRD) of (top) synthesized SOD-Zn(MeIm)$_2$ following activation and (bottom) simulated powder diffraction pattern from crystal structure (CSD: OFERUN08).
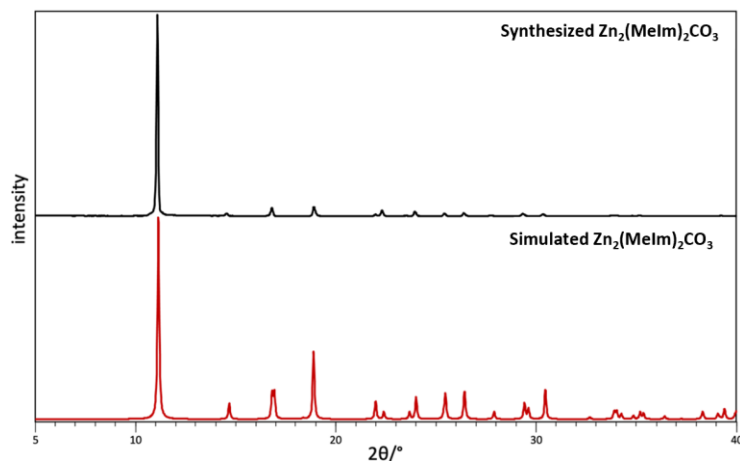
Figure 4: Powder X-ray diffractograms (PXRD) of (top) synthesized $Zn_2(MeIm)_2CO_3$ and (bottom) simulated powder diffraction pattern from crystal structure (CSD: HOYQAP01).
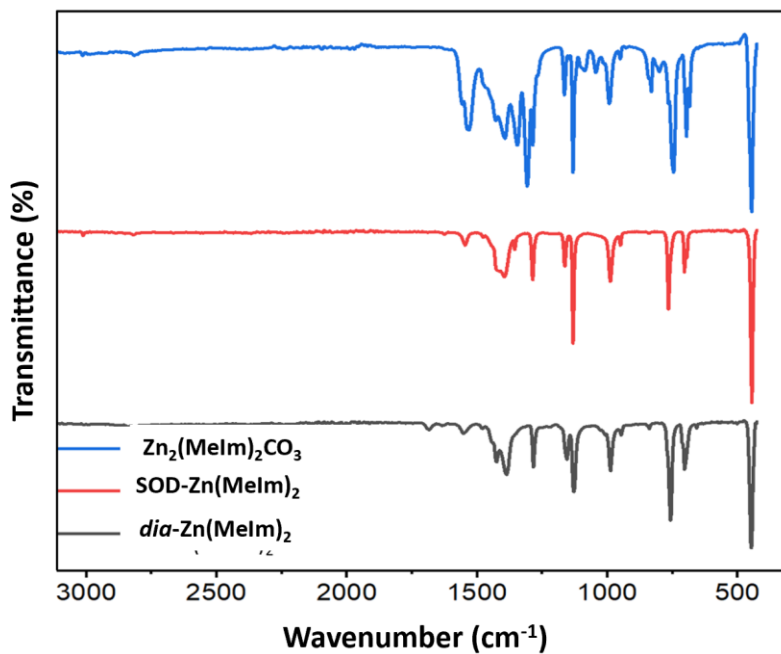

Figure 5: FTIR spectra, from top to bottom, synthesized $Zn_2(MeIm)_2CO_3$, SOD-$Zn(MeIm)_2$, and *dia*-$Zn(MeIm)_2$.
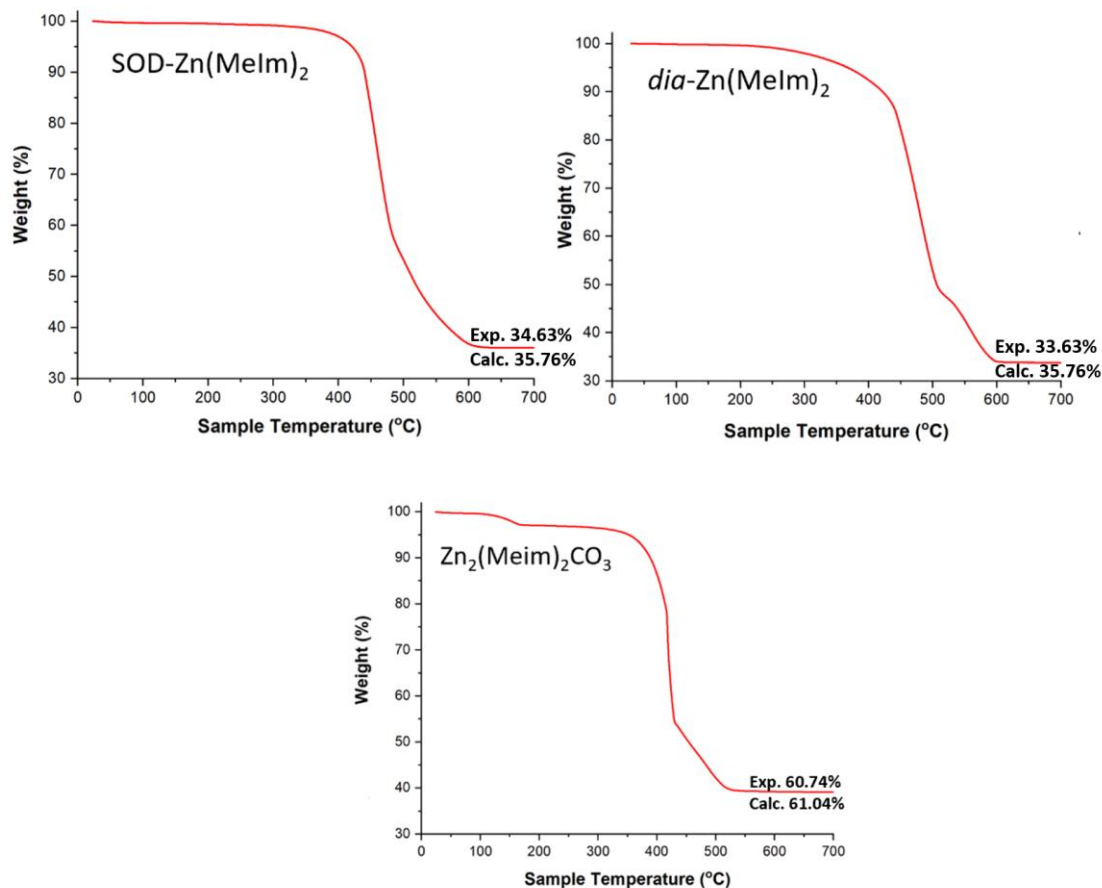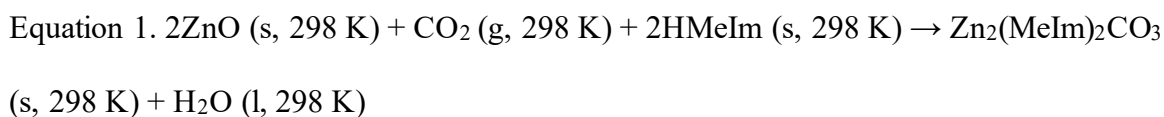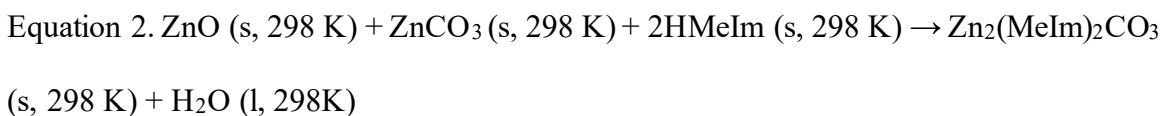
Figure 6: TGA of synthesized MOFs in air.

The results from calorimetric experiments (Table 9) are consistent with previous measurements for ZIF-8 and its close-packed polymorph *dia*-Zn(MeIm)$_2$, and show that formation of the Zn$_2$(MeIm)$_2$CO$_3$ is highly exothermic with respect to ZnO. Specifically, the measured enthalpy of formation (ΔH°_f) for Zn$_2$(MeIm)$_2$CO$_3$ of ca. -88 kJ/mol corresponds to the enthalpy of the reaction involving ZnO, HMeIm, H$_2$O and CO$_2$ as precursors (Equation 1).

Equation 1. 2ZnO (s, 298 K) + CO$_2$ (g, 298 K) + 2HMeIm (s, 298 K) → Zn$_2$(MeIm)$_2$CO$_3$ (s, 298 K) + H$_2$O (l, 298 K)

Compared to the ΔH^o_f values for ZIF-8 and dia-Zn(MeIm)$_2$ (-21 kJ/mol and -31 kJ/mol, respectively), the new calorimetric data indicate a significantly higher enthalpic driving force for the formation of the carbonate phase Zn$_2$(MeIm)$_2$CO$_3$ from ZnO plus linker than for the formation of the ZIF without carbonate. The driving force for the formation of the Zn$_2$(MeIm)$_2$CO$_3$ phase becomes smaller, but still exothermic (-15 kJ/mol, Table 9), if the reaction proceeds through a modified route (Equation 2), with CO$_2$ being delivered in the form of ZnCO$_3$.

Equation 2. ZnO (s, 298 K) + ZnCO$_3$ (s, 298 K) + 2HMeIm (s, 298 K) → Zn$_2$(MeIm)$_2$CO$_3$ (s, 298 K) + H$_2$O (l, 298K)

This less exothermic enthalpy simply reflects the stability of ZnCO3 relative to ZnO + CO$_2$.

Table 8. Enthalpies of dissolution (ΔH_{dis}, in kJ/mol) in 5 N HCl at 25 °C and formation from endmembers (metal oxide and linker). For Zn$_2$(MeIm)$_2$CO$_3$, enthalpy of formation (ΔH^o_f, in kJ/mol) is calculated relative to metal oxide, linker, and CO$_2$.

Sample	ΔH_{dis} (kJ/mol)	ΔH^o_f (kJ/mol)
HMeIm	-43.75 ± 0.59	-
ZnO[52]	-72.29 ± 0.17	-
H$_2$O[53]	-0.5	-

ZnCO$_3$	0.71	-
SOD-Zn(MeIm)$_2$	-138.25± 0.5	-21.04 ± 0.79
dia-Zn(MeIm)$_2$	- 127.86 ± 1.08	-31.09 ± 1.10
Zn$_2$(MeIm)$_2$CO$_3$ (CO$_3$-ZIF-8)	-143.68 ± 0.43	-87.88 ± 0.74

Besides establishing the enthalpies of formation for Zn$_2$(MeIm)$_2$CO$_3$, the obtained thermodynamic data enable the evaluation of the thermodynamic driving force (Equation 3) for the carbonation reaction of Zn(MeIm)$_2$ frameworks ZIF-8 and dia-Zn(MeIm)$_2$.

Equation 3. Zn(MeIm)$_2$ (s, 298 K) + ½ CO$_2$ (g, 298 K) + ½ H$_2$O (l, 298 K) → ½ Zn$_2$(MeIm)$_2$CO$_3$ (s, 298 K) + HMeIm (s, 298 K)
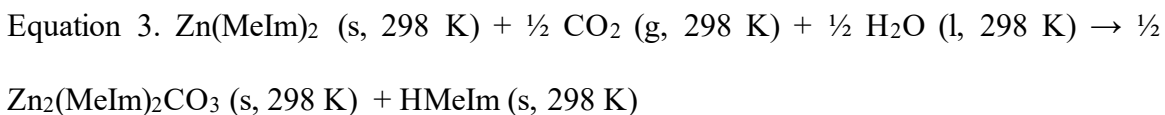
The obtained values (Table 9) show that the conversion of ZIF-8 to Zn$_2$(MeIm)$_2$CO$_3$ is exothermic by ca. 23 kJ/mol, which is consistent with the observed rapid transformation either in moist CO$_2$, or upon exposure of an aqueous suspension of ZIF-8 to a flow of CO$_2$ gas. The reaction enthalpy is less exothermic (-13 kJ/mol), but still significant for the dia-Zn(MeIm)$_2$ phase. Having demonstrated strong enthalpic driving force for the reaction of ZIF carbonation, we also explored the thermodynamics of other routes for the formation of Zn$_2$(MeIm)$_2$CO$_3$. In particular, we envisage the formation of Zn$_2$(MeIm)$_2$CO$_3$ from SOD- and dia-Zn(MeIm)$_2$ frameworks could also take place by reaction with ZnCO$_3$ (Equation 4) or a combination of equimolar amounts of ZnO and CO$_2$ as the source of carbonate (Equation 5)

Equation 4. Zn(MeIm)$_2$ (s, 298 K) + ZnCO$_3$ (s, 298 K) → Zn$_2$(MeIm)$_2$CO$_3$ (s, 298 K)

Equation 5. $Zn(MeIm)_2$ (s, 298 K) + ZnO (s, 298 K) + CO_2 (g, 298 K)) $\rightarrow$ $Zn_2(MeIm)_2CO_3$ (s, 298 K)
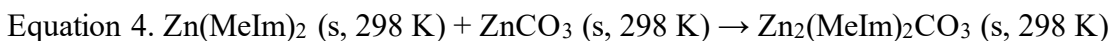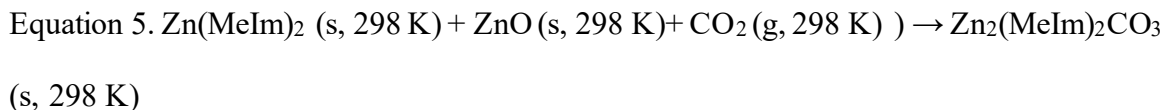
The thermodynamic cycles for these alternative pathways show that the reaction of $Zn(MeIm)_2$ and $ZnCO_3$ to form a carbonated ZIF phase is endothermic by ca. 6 kJ/mol (for ZIF-8) and 16 kJ/mol (for dia-$Zn(MeIm)_2$). This means that, considering the enthalpic driving force for the reaction, the carbonate phase $Zn_2(MeIm)_2CO_3$ may be metastable towards dissociating into an equimolar mixture of $ZnCO_3$ and the corresponding ZIF. Although the entropy associated with this reaction is not known, it is likely to be small in magnitude for the reaction involving only solid phases and the sign of the free energy change for the reaction is probably determined by the endothermic enthalpy term. In contrast, the reaction of Equation 5, where the source of additional zinc and carbonate is a combination of ZnO and CO_2, is exothermic by -67 kJ/mol and -57 kJ/mol for ZIF-8 and dia-$Zn(MeIm)_2$ as reactants, respectively. The entropy of reaction is almost certainly negative since CO_2 gas is consumed, but the sign of the free energy change is likely to be dominated by the strongly exothermic enthalpy term.[53]

Table 9. Measured and calculated thermodynamic data for the reactions leading to the formation of $Zn(MeIm)_2CO_3$ carbonate phase, including enthalpies of formation (ΔH^o_f, in kJ/mol), and enthalpies of reaction starting from ZIF-8 ($\Delta H^o_{f,ZIF-8}$, in kJ/mol) and *dia*-$Zn(MeIm)_2$ ($\Delta H^o_{f,dia}$, in Kj/mol), as well as corresponding energies based on periodic SEDC-DFT calculations.

Reaction from equation number	Reference framework	Experimental (kJ/mol)	PBE+D3 (kJ/mol)	PBESOL (kJ/mol)	PBE+MBD* (kJ/mol)	PBE+TS (kJ/mol)	PBESOL+TS (kJ/mol)
1		-87.88 ± 0.74	-78.06	-101.37	-88.21	-83.58	-96.79
2		-14.88 ±0.70	-26.05	-38.14	-30.80	-30.76	-15.51
3	*dia*	-12.53 ± 0.70	-39.86	-36.66	-37.30	-38.30	-53.07
3	SOD	-22.92 ± 0.44	-55.13	-29.05	-52.70	-61.96	-77.74
4	*dia*	16.53 ± 1.16	-26.88	-24.12	-23.99	-27.27	-20.19
4	SOD	6.14 ± 0.66	-42.15	-16.51	-39.40	-50.93	-44.85
5	*dia*	-56.47 ± 1.17	-78.89	-87.35	-81.41	-80.09	-101.47
5	SOD	-66.86 ± 0.68	-94.16	-79.74	-96.81	-103.75	-126.13

With the established experimental enthalpies for the formation of $Zn_2(MeIm)_2CO_3$ via five reaction pathways, we explored the possibility to theoretically calculate the energy differences for the reactions described by Equations 1-5. Whereas we have previously demonstrated high accuracy of periodic DFT for calculating energy differences between compositionally similar crystalline solids, the calculation of energies for reactions in Equations 1-5 are additionally challenged by the physical and chemical differences between the reaction components. For the periodic DFT calculations, we have tested the

performance of DFT functionals with and without dispersion semiempirical dispersion corrections (SEDCs).[47, 50, 54, 55] The use of SEDCs has been found essential to correctly reproduce the energy ranking of ZIF polymorphs, but it is not clear whether they will perform equally well when modelling solid state transformations involving at the same time crystalline metal organic phases (SOD- and *dia*-$Zn(MeIm)_2$, $Zn_2(MeIm)_2CO_3$), inorganic crystalline phases (ZnO, $ZnCO_3$) and non-crystalline components CO_2 (g) and H_2O (l). Modelling the thermodynamics of such reactions, therefore, requires treatment of three states of aggregation, as well as balancing the interconversions between organic and inorganic phases, where the former typically require treatment with dispersion corrections, while the latter generally do not. We have previously highlighted the challenge of modelling such processes, in the context of decomposition of putative metal pentazolate frameworks and of ZIF combustion.[4, 56, 57] In order to achieve the best possible understanding of the performance of periodic DFT calculations for calculating reaction energies involving such diverse components, we decided to employ a wider range of methods. Besides the previously used PBE[45] functional, we also introduced its modified version PBESOL,[58] which is specifically tailored to the calculations for solid materials. Alongside these functionals, we have tested the effect of various available dispersion correction approaches, namely Grimme D3,[46] Tkatchenko Scheffler (TS)[50] and many body dispersion (MBD*).[48–50] Since not all combinations of functionals and dispersion corrections are available in CASTEP,[42] we performed the calculations with the following methods: PBESOL, PBE+D3, PBE+MBD*, PBE+TS and PBESOL+TS. Comparison of the calculated and experimental reaction energies revealed that the PBESOL functional without any dispersion corrections provides the best overall agreement with experiment

(R^2=0.92, Figure 7), superior to any of the dispersion-corrected methods. However, this overall trend misses one important consideration, namely that PBESOL incorrectly ranks the energies of the two polymorphs of Zn(MeIm)$_2$, placing the *dia* polymorph 7.61 kJ/mol above the SOD polymorph, while experimentally the *dia* structure is found to be 10.39 kJ/mol lower in energy than ZIF-8. The dispersion-corrected methods, on the other hand, have all ranked the stability of the polymorphs of Zn(MeIm)$_2$ correctly, with the best overall match between theory and experiment displayed by the PBE+MBD* method (R^2=0.88). The PBE+MBD* that was previously found to offer the best agreement with the calorimetrically-measured energies of ZIF polymorphs,[23] is therefore shown to also reliably characterize the energetics of the carbonation reactions of ZIFs.
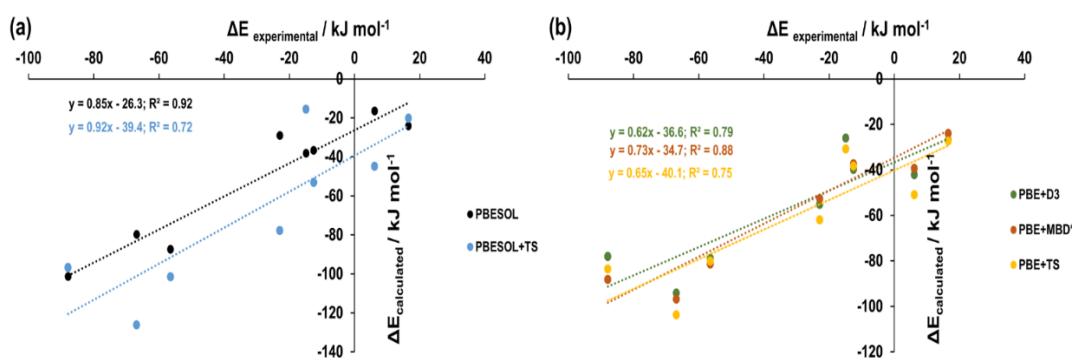

Figure 7. Linear regression plots showing the comparison between experimental and calculated reaction energies, for the different periodic DFT methods: (a) PBESOL and PBESOL+TS, (b) PBE+D3, PBE+MBD*, and PBE+TS.

Typically, the formation of higher density frameworks is energetically preferred (Figure 8), suggesting that the higher density of the carbonated framework Zn$_2$(MeIm)$_2$CO$_3$ compared to parent ZIFs may contribute to its energetically favorable

formation, perhaps pointing to increase in density as a plausible driving force for the reaction. [59–61] The results from this work might help explain previously observed facile carbonation of other ZIF materials,[29] since the structures proceed towards thermodynamically much more stable frameworks.
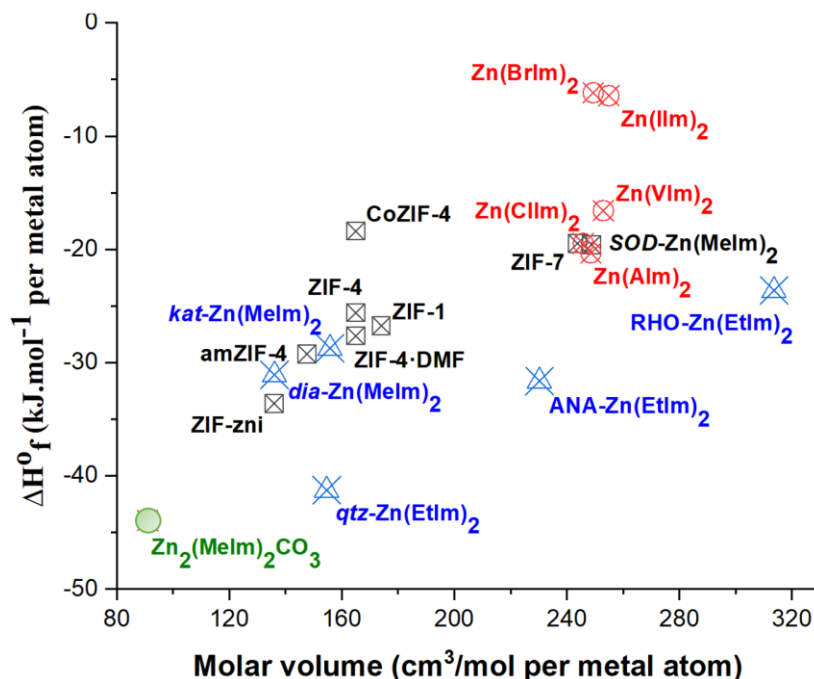

Figure 8. Change in enthalpy for the formation of ZIFs relative to their endmembers (metal oxide and linker). Note that $Zn_2(MeIm)_2CO_3$ employs additional CO_2 as endmember. This is adapted with permission for reference 52.

9.4 Conclusions

We have provided the first experimental evaluation of the thermodynamic force underlying a MOF carbonation reaction, and also investigated the dependence of this driving force on the polymorphic form of the reacting framework. With experimental

enthalpies at hand, we have also been able to conduct a unique study of how different theoretical approaches can evaluate the energies of the targeted MOF carbonation reaction. Our periodic DFT results match the trends for formation of $Zn_2(MeIm)_2CO_3$ via five reaction pathways in a challenging system which includes organic, metal organic and inorganic crystalline materials as reactants or products. Despite these challenges, the calculated reaction energies show a strong correlation with the corresponding experimental values, with the best overall performance shown by the dispersion-corrected PBE+MBD* method. This work provides an opportunity to not only understand the behavior of a single system, but also to begin exploring and potentially even predicting different pathways through which MOFs in general might react with CO_2.

REFERENCES

1. Ockwig, N. W., Delgado-Friedrichs, O., O'Keeffe, M. & Yaghi, O. M. Reticular Chemistry: Occurrence and Taxonomy of Nets and Grammar for the Design of Frameworks. *Acc. Chem. Res.* **38**, 176–182 (2005).

2. O'Keeffe, M. Design of MOFs and intellectual content in reticular chemistry: a personal view. *Chem. Soc. Rev.* **38**, 1215–1217 (2009).

3. Chen, Z. *et al.* Reticular chemistry in the rational synthesis of functional zirconium cluster-based MOFs. *Coord. Chem. Rev.* **386**, 32–49 (2019).

4. Jobin, O. *et al.* Metal–organic frameworks as hypergolic additives for hybrid rockets. *Chem. Sci.* **13**, 3424–3436 (2022).

5. Na, K., Choi, K. M., Yaghi, O. M. & Somorjai, G. A. Metal Nanocrystals Embedded in Single Nanocrystals of MOFs Give Unusual Selectivity as Heterogeneous Catalysts. *Nano Lett.* **14**, 5979–5983 (2014).

6. So, M. C., Wiederrecht, G. P., Mondloch, J. E., Hupp, J. T. & Farha, O. K. Metal–organic framework materials for light-harvesting and energy transfer. *Chem. Commun.* **51**, 3501–3510 (2015).

7. Singh, R. *et al.* Biomimetic metal-organic frameworks as protective scaffolds for live-virus encapsulation and vaccine stabilization. *Acta Biomater.* **142**, 320–331 (2022).

8. Li, M., Li, D., O'Keeffe, M. & Yaghi, O. M. Topological Analysis of Metal–Organic Frameworks with Polytopic Linkers and/or Multiple Building Units and the Minimal Transitivity Principle. *Chem. Rev.* **114**, 1343–1370 (2014).

9. Kalaj, M. & Cohen, S. M. Postsynthetic Modification: An Enabling Technology for the Advancement of Metal–Organic Frameworks. *ACS Cent. Sci.* **6**, 1046–1057 (2020).

10. Shen, Y., Tissot, A. & Serre, C. Recent progress on MOF-based optical sensors for VOC sensing. *Chem. Sci.* **13**, 13978–14007 (2022).

11. Li, C. *et al.* Recent development and applications of electrical conductive MOFs. *Nanoscale* **13**, 485–509 (2021).

12. Cui, Y., Yue, Y., Qian, G. & Chen, B. Luminescent Functional Metal–Organic Frameworks. *Chem. Rev.* **112**, 1126–1162 (2012).

13. Allendorf, M. D., Bauer, C. A., Bhakta, R. K. & Houk, R. J. T. Luminescent metal–organic frameworks. *Chem. Soc. Rev.* **38**, 1330–1352 (2009).

14. Lee, C. Y. *et al.* Light-Harvesting Metal–Organic Frameworks (MOFs): Efficient Strut-to-Strut Energy Transfer in Bodipy and Porphyrin-Based MOFs. *J. Am. Chem. Soc.* **133**, 15858–15861 (2011).

15. Ettlinger, R. *et al.* Toxicity of metal–organic framework nanoparticles: from essential analyses to potential applications. *Chem. Soc. Rev.* **51**, 464–484 (2022).

16. Darby, J. P. *et al.* Ab Initio Prediction of Metal-Organic Framework Structures. *Chem. Mater.* **32**, 5835–5844 (2020).

17. Ding, M., Cai, X. & Jiang, H.-L. Improving MOF stability: approaches and applications. *Chem. Sci.* **10**, 10209–10230 (2019).

18. Howarth, A. J. *et al.* Chemical, thermal and mechanical stabilities of metal–organic frameworks. *Nat. Rev. Mater.* **1**, 1–15 (2016).

19. Rieth, A. J., Wright, A. M. & Dincă, M. Kinetic stability of metal–organic frameworks for corrosive and coordinating gas capture. *Nat. Rev. Mater.* **4**, 708–725 (2019).

20. Nguyen, J. G. & Cohen, S. M. Moisture-Resistant and Superhydrophobic Metal−Organic Frameworks Obtained via Postsynthetic Modification. *J. Am. Chem. Soc.* **132**, 4560–4561 (2010).

21. Carter, K. P., Ridenour, J. A., Kalaj, M. & Cahill, C. L. A Thorium Metal-Organic Framework with Outstanding Thermal and Chemical Stability. *Chem. – Eur. J.* **25**, 7114–7118 (2019).

22. Novendra, N. *et al.* Linker Substituents Control the Thermodynamic Stability in Metal–Organic Frameworks. *J. Am. Chem. Soc.* **142**, 21720–21729 (2020).

23. Arhangelskis, M. *et al.* Theoretical Prediction and Experimental Evaluation of Topological Landscape and Thermodynamic Stability of a Fluorinated Zeolitic Imidazolate Framework. *Chem. Mater.* **31**, 3777–3783 (2019).

24. Friščić, T. & Jones, W. Recent Advances in Understanding the Mechanism of Cocrystal Formation via Grinding. *Cryst. Growth Des.* **9**, 1621–1637 (2009).

25. Bhattacharyya, S. *et al.* Acid Gas Stability of Zeolitic Imidazolate Frameworks: Generalized Kinetic and Thermodynamic Characteristics. *Chem. Mater.* **30**, 4089–4101 (2018).

26. Cui, K., Nair, S., Sholl, D. S. & Schmidt, J. R. Kinetic Model of Acid Gas Induced Defect Propagation in Zeolitic Imidazolate Frameworks. *J. Phys. Chem. Lett.* **13**, 6541–6548 (2022)
.

27. Bhattacharyya, S., Sholl, D. S. & Nair, S. Quantitative Correlations for the Durability of Zeolitic Imidazolate Frameworks in Humid SO2. *Ind. Eng. Chem. Res.* **59**, 245–252 (2020).

28. Bhattacharyya, S. *et al.* Stability of Zeolitic Imidazolate Frameworks in NO2. *J. Phys. Chem. C* **123**, 2336–2346 (2019).

29. Mottillo, C. & Friščić, T. Carbon Dioxide Sensitivity of Zeolitic Imidazolate Frameworks. *Angew. Chem.* **126**, 7601–7604 (2014).

30. Brekalo, I. *et al.* Manometric real-time studies of the mechanochemical synthesis of zeolitic imidazolate frameworks. *Chem. Sci.* **11**, 2141–2147 (2020).

31. Evans, J. D. *et al.* Computational Chemistry Methods for Nanoporous Materials. *Chem. Mater.* **29**, 199–212 (2017).

32. Duarte Rodrigues, A. *et al.* Joint Experimental and Computational Investigation of the Flexibility of a Diacetylene-Based Mixed-Linker MOF: Revealing the Existence of Two Low-Temperature Phase Transitions and the Presence of Colossal Positive and Giant Negative Thermal Expansions. *Chem. – Eur. J.* **24**, 1586–1605 (2018).

33. Baburin, I. A. & Leoni, S. The energy landscapes of zeolitic imidazolate frameworks (ZIFs): towards quantifying the presence of substituents on the imidazole ring. *J. Mater. Chem.* **22**, 10152–10154 (2012).

34. Witman, M. *et al.* Rational Design of a Low-Cost, High-Performance Metal–Organic Framework for Hydrogen Storage and Carbon Capture. *J. Phys. Chem. C* **121**, 1171–1181 (2017).

35. Nazarian, D., Camp, J. S., Chung, Y. G., Snurr, R. Q. & Sholl, D. S. Large-Scale Refinement of Metal−Organic Framework Structures Using Density Functional Theory. *Chem. Mater.* **29**, 2521–2528 (2017).

36. Tan, J.-C., Civalleri, B., Erba, A. & Albanese, E. Quantum mechanical predictions to elucidate the anisotropic elastic properties of zeolitic imidazolate frameworks: ZIF-4 vs. ZIF-zni. *CrystEngComm* **17**, 375–382 (2014).

37. Lewis, D. W. *et al.* Zeolitic imidazole frameworks: structural and energetics trends compared with their zeolite analogues. *CrystEngComm* **11**, 2272–2276 (2009).

38. M. Titi, H., Do, J.-L., J. Howarth, A., Nagapudi, K. & Friščić, T. Simple, scalable mechanosynthesis of metal–organic frameworks using liquid-assisted resonant acoustic mixing (LA-RAM). *Chem. Sci.* **11**, 7578–7584 (2020).

39. Huskić, I. *et al.* Functionality in metal–organic framework minerals: proton conductivity, stability and potential for polymorphism. *Chem. Sci.* **10**, 4923–4929 (2019).

40. Huskić, I. *et al.* Proton Conductivity, Stability and Potential for Polymorphism in Metal-Organic Framework Minerals. (2018).

41. Bhunia, M. K., Hughes, J. T., Fettinger, J. C. & Navrotsky, A. Thermochemistry of Paddle Wheel MOFs: Cu-HKUST-1 and Zn-HKUST-1. *Langmuir* **29**, 8140–8145 (2013).

42. Clark, S. J. *et al.* First principles methods using CASTEP. *Z. Für Krist. - Cryst. Mater.* **220**, 567–570 (2005).

43. Björkman, T. CIF2Cell: Generating geometries for electronic structure programs. *Comput. Phys. Commun.* **182**, 1183–1186 (2011).

44. *C. Spink, I. Wadsö D. Glick (Ed.), Methods of Biochemical Analysis, Vol. 23, Wiley, Oxford (1976), p. 123*. vol. 1.

45. Perdew, J. P., Burke, K. & Ernzerhof, M. Generalized Gradient Approximation Made Simple. *Phys. Rev. Lett.* **77**, 3865–3868 (1996).

46. Grimme, S., Antony, J., Ehrlich, S. & Krieg, H. A consistent and accurate ab initio parametrization of density functional dispersion correction (DFT-D) for the 94 elements H-Pu. *J. Chem. Phys.* **132**, 154104 (2010).

47. Tkatchenko, A., DiStasio, R. A., Car, R. & Scheffler, M. Accurate and Efficient Method for Many-Body van der Waals Interactions. *Phys. Rev. Lett.* **108**, 236402 (2012).

48. Ambrosetti, A., Reilly, A. M., DiStasio, R. A., Jr. & Tkatchenko, A. Long-range correlation energy calculated from coupled atomic response functions. *J. Chem. Phys.* **140**, 18A508 (2014).

49. Reilly, A. M. & Tkatchenko, A. van der Waals dispersion interactions in molecular materials: beyond pairwise additivity. *Chem. Sci.* **6**, 3289–3301 (2015).

50. Tkatchenko, A. & Scheffler, M. Accurate Molecular Van Der Waals Interactions from Ground-State Electron Density and Free-Atom Reference Data. *Phys. Rev. Lett.* **102**, 073005 (2009).

51. B. Lennox, C. *et al.* Simplifying and expanding the scope of boron imidazolate framework (BIF) synthesis using mechanochemistry. *Chem. Sci.* **12**, 14499–14506 (2021).

52. Hughes, J. T., Bennett, T. D., Cheetham, A. K. & Navrotsky, A. Thermochemistry of Zeolitic Imidazolate Frameworks of Varying Porosity. *J. Am. Chem. Soc.* **135**, 598–601 (2013).

53. Akimbekov, Z. *et al.* Experimental and Theoretical Evaluation of the Stability of True MOF Polymorphs Explains Their Mechanochemical Interconversions. *J. Am. Chem. Soc.* **139**, 7952–7957 (2017).

54. Grimme, S. Semiempirical GGA-type density functional constructed with a long-range dispersion correction. *J. Comput. Chem.* **27**, 1787–1799 (2006).

55. Ehrlich, S., Moellmann, J., Reckien, W., Bredow, T. & Grimme, S. System-Dependent Dispersion Coefficients for the DFT-D3 Treatment of Adsorption Processes on Ionic Surfaces. *ChemPhysChem* **12**, 3414–3420 (2011).

56. Arhangelskis, M., Katsenis, A. D., Morris, A. J. & Friščić, T. Computational evaluation of metal pentazolate frameworks: inorganic analogues of azolate metal–organic frameworks. *Chem. Sci.* **9**, 3367–3375 (2018).

57. Titi, H. M. *et al.* Hypergolic zeolitic imidazolate frameworks (ZIFs) as next-generation solid fuels: Unlocking the latent energetic behavior of ZIFs. *Sci. Adv.* **5**, eaav9044 (2019).

58. Perdew, J. P. *et al.* Restoring the Density-Gradient Expansion for Exchange in Solids and Surfaces. *Phys. Rev. Lett.* **100**, 136406 (2008).

59. Tan, J. C., Bennett, T. D. & Cheetham, A. K. Chemical structure, network topology, and porosity effects on the mechanical properties of Zeolitic Imidazolate Frameworks. *Proc. Natl. Acad. Sci. U. S. A.* **107**, 9938–9943 (2010).

60. Katsenis, A. D. *et al.* In situ X-ray diffraction monitoring of a mechanochemical reaction reveals a unique topology metal-organic framework. *Nat. Commun.* **6**, 6662 (2015).

61. Basnayake, S. A., Su, J., Zou, X. & Balkus, K. J. Carbonate-Based Zeolitic Imidazolate Framework for Highly Selective CO2 Capture. *Inorg. Chem.* **54**, 1816–1821 (2015).

CHAPTER 10

SUMMARY

10.1 Conclusions

This dissertation investigates structure-stability relations in PDCs and MOFs. The results from thermodynamic analyses of SiC fibers confirm that in PDCs more mixed bonding is consistent with greater thermodynamic stability. This work enables identification of key factors for the stabilization of SiOC systems: (1) between 1200-1500 $^{\circ}$C the PDCs evolve towards thermodynamically much more stable microstructures, (2) greater stability is consistent with more $SiOC_3$ and/or SiO_2C_2 (relative to SiO_3C) mixed bonds, and (3) more ordering of the free carbon phase corresponds to greater energetic stabilization. The investigation of SiC(N)(O) PDCs shows: (1) addition of N to SiC(O) systems can stabilize the structures by as much as 60 kJ/mol, (2) SiN_XC_{4-X} may promote greater stabilization compared to SiO_XC_{4-X} mixed bonds, and (3) unlike seen in SiOCs, in SiOCNs greater stability (> 12 kJ/mol) is consistent with increasing disorder of the free carbon phase. Lastly, the investigation of metal incorporation to SiOCs (SiO(M)C) shows: (1) SiO(M)C display similar temperature-stability trends seen in SiOCs (higher synthesis temperature forms more stable materials), (2) of the metals (Ta. Hf, Nb) incorporated, Ta promotes stabilization of otherwise unstable SiO_3C mixed bonds, and (3) incorporation of metal carbide instead of metal or metal oxide fillers may be thermodynamically preferred.

The work on ZIFs shows that: (1) dense *dia* polymorphs are more stable than the more porous SOD analogues, independent of choice of metal, and (2) 2-dimensional structures present much greater stability than 3-dimensional analogues in the SOD and *dia* configuration. The study of metal substitution in BIFs indicates an increase in framework density and metallic character of the metal nodes as unifying descriptors for increased stabilization of MOF structures. Evaluation of the energetics of CO_2 sorption using MOFs shows that: (1) in ZIFs greater porosity corresponds to most favorable incorporation of CO_2, and (2) binding energetics can be enhanced by use of larger/bulkier linkers, as in BIFs. Lastly, Investigation of carbonation reactions in MOFs suggests: (1) carbonation reactions proceed towards thermodynamically more stable structures, (2) beyond the carbonation of ZIFs there exist multiple other energetically favorable pathways for the formation of carbonate MOFs like CO_3-ZIF-8, (3) increase in density is a major driving force for the carbonation of ZIFs, and (4) we can now predict different pathways through which MOFs in general might react with CO_2.

These results indicate enhancement of thermodynamic stability and more favorable guest-host interactions in hybrid materials like MOFs, tailored by choice of metal and linker. Results from the PDCs work point to strong interdependence between the chemistry, structure, and thermodynamic stability of hybrid ceramics. The systematics provide an initial framework for the prediction and development of PDCs and MOFs with enhanced thermodynamic stability and desired functionality.

10.2 Future work

The structure-stability relations herein reported are a valuable addition to the current thermodynamic database, nonetheless, more work remains for the development of a predictive framework for thermodynamic stabilization in these hybrid systems. Beyond the effect of bonding, in PDCs it is important to understand how thermodynamic stability corelates with the size of individual mixed bonding and stoichiometric domains. The assessment of nanodomain size in these ceramics is challenging but can be done by use of X-ray techniques, including small angle X-ray scattering (SAX), as seen previously, as well as by neutron studies.[1] Future work comparing analysis of bonding from XPS and NMR would be valuable. This could provide important information of differences in the sensitivity of XPS and NMR to different bonds (stoichiometric and mixed bonds) in PDC microstructures. Lastly, this work only investigates the incorporation of Nb, Hf, and Ta metal fillers. Future work could systematically investigate the incorporation of many other metals (p and f-block) and their corresponding effect on the structural evolution and thermodynamic stability of the PDCs.

Similarly, the work on MOFs provides a starting point for assessment of the stabilizing effect resulting from metal substitution in BIFs and ZIFs. In the ZIFs study, Cu(II) metal atoms only formed structures in the diamondoid (*dia*) topology. For greater confidence in the trends herein reported it would be valuable to experimentally investigate the thermodynamics of Cu(II)-ZIFs in the sodalite (SOD) and ZIF-L configurations as well. Additionally, in the future, the energetic landscape for carbonation reactions in other MOFs systems, beyond ZIF-8 could be investigated. This

may permit the identification of trends in the energetic drive for the formation of mixed-linker carbonate frameworks through carbonation reaction of the parent structure. Lastly, it could be beneficial to systematically explore the trends for thermodynamic stabilization in other MOFs as well, perhaps in systems employing oxygen instead of nitrogen (azolates) based linkers. This could enable determination of the effect of linker environment on the stabilization trends (from choice of metal substitution or linker substituent) in MOFs. Following these recommendations could provide valuable addition to the current understanding of thermodynamic stabilization in PDCs, MOFs, and similar hybrid systems.

REFERENCES

1. Mera, G., Tamayo, A., Nguyen, H., Sen, S. & Riedel, R. Nanodomain Structure of Carbon-Rich Silicon Carbonitride Polymer-Derived Ceramics. *J. Am. Ceram. Soc.* **93**, 1169–1175 (2010).

LIST OF REFERENCES

1.   Roser, M., Ritchie, H. & Ortiz-Ospina, E. World Population Growth. *Our World Data* (2013).

2.   World Population Clock: 7.9 Billion People (2022) - Worldometer. https://www.worldometers.info/world-population/.

3.   *Economics of Natural Resource Scarcity: The State of the Debate*. (2005).

4.   Holdren, J. P. & Ehrlich, P. R. Human Population and the Global Environment: Population growth, rising per capita material consumption, and disruptive technologies have made civilization a global ecological force. *Am. Sci.* **62**, 282–292 (1974).

5.   Hallegatte, S., Fay, M. & Vogt-Schilb, A. *Green Industrial Policies : When and How*. \

6.   Siegelman, R. L., Kim, E. J. & Long, J. R. Porous materials for carbon dioxide separations. *Nat. Mater.* **20**, 1060–1072 (2021).

7.   Arakawa, H. *et al.* Catalysis Research of Relevance to Carbon Management: Progress, Challenges, and Opportunities. *Chem. Rev.* **101**, 953–996 (2001).

8.   Tranchemontagne, D. J., Ni, Z., O'Keeffe, M. & Yaghi, O. M. Reticular Chemistry of Metal–Organic Polyhedra. *Angew. Chem. Int. Ed.* **47**, 5136–5147 (2008).

9.   Yaghi, O. M. Reticular Chemistry in All Dimensions. *ACS Cent. Sci.* **5**, 1295–1300 (2019).

10.   Colombo, P. *Polymer Derived Ceramics: From Nano-structure to Applications*. (DEStech Publications, Inc, 2010).

11.   Colombo, P., Mera, G., Riedel, R. & Sorarù, G. D. Polymer-Derived Ceramics: 40 Years of Research and Innovation in Advanced Ceramics. *J. Am. Ceram. Soc.* **93**, 1805–1837 (2010).

12. Nagabhushana, G. P., Shivaramaiah, R. & Navrotsky, A. Thermochemistry of Multiferroic Organic–Inorganic Hybrid Perovskites [(CH3)2NH2][M(HCOO)3] (M = Mn, Co, Ni, and Zn). *J. Am. Chem. Soc.* **137**, 10351–10356 (2015).

13. Vasileiadou, E. S. *et al.* Insight on the Stability of Thick Layers in 2D Ruddlesden–Popper and Dion–Jacobson Lead Iodide Perovskites. *J. Am. Chem. Soc.* **143**, 2523–2536 (2021).

14. Wei, J. *et al.* Highly Stable Hybrid Perovskite Solar Cells Modified with Polyethylenimine via Ionic Bonding. *ChemNanoMat* **4**, 649–655 (2018).

15. Voskanyan, A. A., Goncharov, V. G., Novendra, N., Guo, X. & Navrotsky, A. Thermodynamics Drives the Stability of the MOF-74 Family in Water. *ACS Omega* **5**, 13158–13163 (2020).

16. Akimbekov, Z. *et al.* Experimental and Theoretical Evaluation of the Stability of True MOF Polymorphs Explains Their Mechanochemical Interconversions. *J. Am. Chem. Soc.* **139**, 7952–7957 (2017).

17. Hughes, J. T., Bennett, T. D., Cheetham, A. K. & Navrotsky, A. Thermochemistry of Zeolitic Imidazolate Frameworks of Varying Porosity. *J. Am. Chem. Soc.* **135**, 598–601 (2013).

18. Leonel, G. J., Mujib, S. B., Singh, G. & Navrotsky, A. Thermodynamic stabilization of crystalline silicon carbide polymer-derived ceramic fibers. *Int. J. Ceram. Eng. Sci.* 4, 315–326 (2022).

19. Ren, Z., Mujib, S. B. & Singh, G. High-Temperature Properties and Applications of Si-Based Polymer-Derived Ceramics: A Review. *Materials* **14**, 614 (2021).

20. Lin, Z.-J., Lü, J., Hong, M. & Cao, R. Metal–organic frameworks based on flexible ligands (FL-MOFs): structures and applications. *Chem. Soc. Rev.* **43**, 5867–5895 (2014).

21. Almáši, M., Király, N., Zeleňák, V., Vilková, M. & Bourrelly, S. Zinc(ii) and cadmium(ii) amorphous metal–organic frameworks (aMOFs): study of activation process and high-pressure adsorption of greenhouse gases. *RSC Adv.* **11**, 20137–20150 (2021).

22. Furukawa, H. *et al.* Ultrahigh Porosity in Metal-Organic Frameworks. *Science* **329**, 424–428 (2010).

23. Yeon, S.-H. *et al.* Carbide-derived-carbons with hierarchical porosity from a preceramic polymer. *Carbon* **48**, 201–210 (2010).

24. Xue, D.-X. *et al.* Topology meets MOF chemistry for pore-aperture fine tuning: ftw -MOF platform for energy-efficient separations via adsorption kinetics or molecular sieving. *Chem. Commun.* **54**, 6404–6407 (2018).

25. 25. Lale, A. *et al.* Polymer-Derived Ceramics with engineered mesoporosity: From design to application in catalysis. *Surf. Coat. Technol.* **350**, 569–586 (2018).

26. Vakifahmetoglu, C., Presser, V., Yeon, S.-H., Colombo, P. & Gogotsi, Y. Enhanced hydrogen and methane gas storage of silicon oxycarbide derived carbon. *Microporous Mesoporous Mater.* **144**, 105–112 (2011).

27. Yang, K. *et al.* Preparation of high surface area activated carbon from coconut shells using microwave heating. *Bioresour. Technol.* **101**, 6163–6169 (2010).

28. Leonel, G. J., Lennox, C. B., Marrett, J. M., Friščić, T. & Navrotsky, A. Crystallographic and Compositional Dependence of Thermodynamic Stability of [Co(II), Cu(II), and Zn(II)] in 2-Methylimidazole-Containing Zeolitic Imidazolate Frameworks. *Chem. Mater.* (2023).

29. Mottillo, C. & Friščić, T. Carbon Dioxide Sensitivity of Zeolitic Imidazolate Frameworks. *Angew. Chem.* **126**, 7601–7604 (2014).

30. Eddaoudi, M., F. Sava, D., F. Eubank, J., Adil, K. & Guillerm, V. Zeolite-like metal–organic frameworks (ZMOFs): design, synthesis, and properties. *Chem. Soc. Rev.* **44**, 228–249 (2015).

31. Mollick, S., Fajal, S., Mukherjee, S. & Ghosh, S. K. Stabilizing Metal–Organic Polyhedra (MOP): Issues and Strategies. *Chem. – Asian J.* **14**, 3096–3108 (2019).

32. Arhangelskis, M. *et al.* Theoretical Prediction and Experimental Evaluation of Topological Landscape and Thermodynamic Stability of a Fluorinated Zeolitic Imidazolate Framework. *Chem. Mater.* **31**, 3777–3783 (2019).

33. Novendra, N. *et al.* Linker Substituents Control the Thermodynamic Stability in Metal–Organic Frameworks. *J. Am. Chem. Soc.* **142**, 21720–21729 (2020).

34. Julien, P. A. & Friščić, T. Methods for Monitoring Milling Reactions and Mechanistic Studies of Mechanochemistry: A Primer. *Cryst. Growth Des.* **22**, 5726–5754 (2022).

35. Calvin, J. J. *et al.* Heat capacity and thermodynamic functions of crystalline and amorphous forms of the metal organic framework zinc 2-ethylimidazolate, Zn(EtIm)2. *J. Chem. Thermodyn.* **116**, 341–351 (2018).

36. Calvin, J. J., Rosen, P. F., Smith, S. J. & Woodfield, B. F. Heat capacities and thermodynamic functions of the ZIF organic linkers imidazole, 2-methylimidazole, and 2-ethylimidazole. *J. Chem. Thermodyn.* **132**, 129–141 (2019).

37. Bhunia, M. K., Hughes, J. T., Fettinger, J. C. & Navrotsky, A. Thermochemistry of Paddle Wheel MOFs: Cu-HKUST-1 and Zn-HKUST-1. *Langmuir* **29**, 8140–8145 (2013).

38. Hughes, J. T. & Navrotsky, A. MOF-5: Enthalpy of Formation and Energy Landscape of Porous Materials. *J. Am. Chem. Soc.* **133**, 9184–9187 (2011).

39. Wu, D. & Navrotsky, A. Thermodynamics of metal-organic frameworks. *J. Solid State Chem.* **223**, 53–58 (2015).

40. Akimbekov, Z., Wu, D., Brozek, C. K., Dincă, M. & Navrotsky, A. Thermodynamics of solvent interaction with the metal–organic framework MOF-5. *Phys. Chem. Chem. Phys.* **18**, 1158–1162 (2015).

41. Huskić, I., Pekov, I. V., Krivovichev, S. V. & Friščić, T. Minerals with metal-organic framework structures. *Sci. Adv.* **2**, e1600621 (2016).

42. 42. Li, S. *et al.* Mechanochemical Synthesis, Accelerated Aging, and Thermodynamic Stability of the Organic Mineral Paceite and Its Cadmium Analogue. *ACS Omega* **4**, 5486–5495 (2019).

43. Petrovic, I., Navrotsky, A., Davis, M. E. & Zones, S. I. Thermochemical study of the stability of frameworks in high silica zeolites. *Chem. Mater.* **5**, 1805–1813 (1993).

44. Navrotsky, A. Energetics of nanoparticle oxides: interplay between surface energy and polymorphism†. *Geochem. Trans.* **4**, 34 (2003).

45. Piccione, P. M. *et al.* Thermochemistry of Pure-Silica Zeolites. *J. Phys. Chem. B* **104**, 10001–10011 (2000).

46. Valenzano, L. *et al.* Computational and Experimental Studies on the Adsorption of CO, N2, and CO2 on Mg-MOF-74. *J. Phys. Chem. C* **114**, 11185–11191 (2010).

47. Huskić, I. *et al.* Functionality in metal–organic framework minerals: proton conductivity, stability and potential for polymorphism. *Chem. Sci.* **10**, 4923–4929 (2019).

48. Rosen, P. F. *et al.* Thermodynamic Evidence of Structural Transformations in CO2-Loaded Metal–Organic Framework Zn(MeIm)2 from Heat Capacity Measurements. *J. Am. Chem. Soc.* **142**, 4833–4841 (2020).

49. Zhang, Y., Yin, X., Ye, F. & Kong, L. Effects of multi-walled carbon nanotubes on the crystallization behavior of PDCs-SiBCN and their improved dielectric and EM absorbing properties. *J. Eur. Ceram. Soc.* **34**, 1053–1061 (2014).

50. Saha, A. & Raj, R. Crystallization Maps for SiCO Amorphous Ceramics. *J. Am. Ceram. Soc.* **90**, 578–583 (2007).

51. Leonel, G. J., Guo, X., Singh, G., Gervais, C. & Navrotsky, A. Energetics and structure of SiC(N)(O) polymer-derived ceramics. *J. Am. Ceram. Soc.* **106**, 5086–5101 (2023).

52. Sasikumar, P. V. W. *et al.* Polymer derived silicon oxycarbide ceramic monoliths: Microstructure development and associated materials properties. *Ceram. Int.* **44**, 20961–20967 (2018).

53. Ionescu, E. *et al.* Polymer-Derived Ultra-High Temperature Ceramics (UHTCs) and Related Materials. in *Ceramics, Glass and Glass-Ceramics: From Early Manufacturing Steps Towards Modern Frontiers* (eds. Baino, F., Tomalino, M. & Tulyaganov, D.) 281–323 (Springer International Publishing, 2021).

54. Sugie, C., Navrotsky, A., Lauterbach, S., Kleebe, H.-J. & Mera, G. Structure and Thermodynamics of Silicon Oxycarbide Polymer-Derived Ceramics with and without Mixed-Bonding. *Materials* **14**, 4075 (2021).

55. Niu, M. *et al.* Structure and energetics of SiOC and SiOC-modified carbon-bonded carbon fiber composites. *J. Am. Ceram. Soc.* **100**, 3693–3702 (2017).

56. Tavakoli, A. H., Golczewski, J. A., Bill, J. & Navrotsky, A. Effect of boron on the thermodynamic stability of amorphous polymer-derived Si(B)CN ceramics. *Acta Mater.* **60**, 4514–4522 (2012).

57. Leonel, G. J., Guo, X., Singh, G. & Navrotsky, A. Compositional Analysis of SiOC(H) Powders: A Comparison of X-ray Photoelectron Spectroscopy (XPS) and Combustion Analysis. *Ceramics* **6**, 74–85 (2023).

58. Widgeon, S. *et al.* Nanostructure and Energetics of Carbon-Rich SiCN Ceramics Derived from Polysilylcarbodiimides: Role of the Nanodomain Interfaces. *Chem. Mater.* **24**, 1181–1191 (2012).

59. Mera, G., Navrotsky, A., Sen, S., Kleebe, H.-J. & Riedel, R. Polymer-derived SiCN and SiOC ceramics – structure and energetics at the nanoscale. *J. Mater. Chem. A* **1**, 3826–3836 (2013).

60. Michelle Morcos, R. et al. Enthalpy of Formation of Carbon-Rich Polymer-Derived Amorphous SiCN *Ceramics. J. Am. Ceram. Soc*. 91, 3349–3354 (2008).

61. Tavakoli, A. H., Armentrout, M. M., Narisawa, M., Sen, S. & Navrotsky, A. White Si–O–C Ceramic: Structure and Thermodynamic Stability. *J. Am. Ceram. Soc.* **98**, 242–246 (2015).

62. Tavakoli, A. H. *et al.* Energetics and Structure of Polymer-Derived Si–(B–)O–C Glasses: Effect of the Boron Content and Pyrolysis Temperature. *J. Am. Ceram. Soc.* **97**, 303–309 (2014).

63. Morcos, R. M. et al. Thermodynamically Stable SiwCxNyOz Polymer-Like, Amorphous Ceramics Made from Organic Precursors. J. Am. Ceram. Soc. 91, 2391–2393 (2008).

64. Morcos, R. M. *et al.* Energetics of SixOyCz Polymer-Derived Ceramics Prepared Under Varying Conditions. *J. Am. Ceram. Soc.* **91**, 2969–2974 (2008).

65. Widgeon, S. *et al.* Effect of Precursor on Speciation and Nanostructure of SiBCN Polymer-Derived Ceramics. *J. Am. Ceram. Soc.* **96**, 1651–1659 (2013).

66. Ionescu, E., Sen, S., Mera, G. & Navrotsky, A. Structure, energetics and bioactivity of silicon oxycarbide-based amorphous ceramics with highly connected networks. *J. Eur. Ceram. Soc.* **38**, 1311–1319 (2018).

67. Varga, T. *et al.* Thermodynamically Stable SixOyCz Polymer-Like Amorphous Ceramics. *J. Am. Ceram. Soc.* **90**, 3213–3219 (2007).

68. Tavakoli, A. H., Armentrout, M. M., Sen, S. & Navrotsky, A. Hydrogenated Si–O–C nanoparticles: Synthesis, structure, and thermodynamic stability. *J. Mater. Res.* **30**, 295–303 (2015).

69. Chen, J. *et al.* Thermodynamic Stability of Low-k Amorphous SiOCH Dielectric Films. *J. Am. Ceram. Soc.* **99**, 2752–2759 (2016).

70. Colombo, P. Engineering porosity in polymer-derived ceramics. *J. Eur. Ceram. Soc.* **28**, 1389–1395 (2008).

71. Brinckmann, S. A. *et al.* Stereolithography of SiOC Polymer-Derived Ceramics Filled with SiC Micronwhiskers. *Adv. Eng. Mater.* **20**, 1800593 (2018).

72. Walsh, C., An, L., Kapat, J. S. & Chow, L. C. Feasibility of a High-Temperature Polymer-Derived-Ceramic Turbine Fabricated Through Micro-Stereolithography. in 1073–1080 (American Society of Mechanical Engineers Digital Collection, 2009).

73. Flores, O., Bordia, R. K., Nestler, D., Krenkel, W. & Motz, G. Ceramic Fibers Based on SiC and SiCN Systems: Current Research, Development, and Commercial Status. *Adv. Eng. Mater.* **16**, 621–636 (2014).

74. Idrees, M. *et al.* Polyborosilazane derived ceramics - Nitrogen sulfur dual doped graphene nanocomposite anode for enhanced lithium ion batteries. *Electrochimica Acta* **296**, 925–937 (2019).

75. Duan, W. *et al.* A review of absorption properties in silicon-based polymer derived ceramics. *J. Eur. Ceram. Soc.* **36**, 3681–3689 (2016).

76. Prasad, R. M. *et al.* Thermal decomposition of carbon-rich polymer-derived silicon carbonitrides leading to ceramics with high specific surface area and tunable micro- and mesoporosity. *J. Eur. Ceram. Soc.* **32**, 477–484 (2012).

77. Huang, K., Elsayed, H., Franchin, G. & Colombo, P. 3D printing of polymer-derived SiOC with hierarchical and tunable porosity. *Addit. Manuf.* **36**, 101549 (2020).

78. Ionescu, E., Kleebe, H.-J. & Riedel, R. Silicon-containing polymer-derived ceramic nanocomposites (PDC-NCs): preparative approaches and properties. *Chem. Soc. Rev.* **41**, 5032–5052 (2012).

79. Hotza, D. *et al.* Tape casting of preceramic polymers toward advanced ceramics: A review. *Int. J. Ceram. Eng. Sci.* **1**, 21–41 (2019).

80. Mera, G., Gallei, M., Bernard, S. & Ionescu, E. Ceramic Nanocomposites from Tailor-Made Preceramic Polymers. *Nanomaterials* **5**, 468–540 (2015).

81. Saha, A., Raj, R., Williamson, D. L. & Kleebe, H.-J. Characterization of Nanodomains in Polymer-Derived SiCN Ceramics Employing Multiple Techniques. *J. Am. Ceram. Soc.* **88**, 232–234 (2005).

82. Papendorf, B. *et al.* High-Temperature Creep Behavior of Dense SiOC-Based Ceramic Nanocomposites: Microstructural and Phase Composition Effects. *J. Am. Ceram. Soc.* **96**, 272–280 (2013).

83. Sujith, R., Jothi, S., Zimmermann, A., Aldinger, F. & Kumar, R. Mechanical behaviour of polymer derived ceramics – a review. *Int. Mater. Rev.* **66**, 426–449 (2021).

84. Gu, J., Lee, S.-H., Lee, H.-S. & Kim, J.-S. Fast pyrolysis of a SiC-based polymer precursor using a spark plasma sintering apparatus – Effects of heating methods and pyrolysis atmosphere. *J. Eur. Ceram. Soc.* **41**, 2297–2305 (2021).

85. Chauhan, P. K., Sujith, R., Parameshwaran, R. & Prasad, A. V. S. S. Role of polysiloxanes in the synthesis of aligned porous silicon oxycarbide ceramics. *Ceram. Int.* **45**, 8150–8156 (2019).

86. Sorarù, G. D., Pederiva, L., Latournerie, J. & Raj, R. Pyrolysis Kinetics for the Conversion of a Polymer into an Amorphous Silicon Oxycarbide Ceramic. *J. Am. Ceram. Soc.* **85**, 2181–2187 (2002).

87. Kulkarni, A., Pearce, J., Yang, Y., Motta, A. & Sorarù, G. D. SiOC(N) Cellular Structures with Dense Struts by Integrating Fused Filament Fabrication 3D Printing with Polymer-Derived Ceramics. *Adv. Eng. Mater.* **n/a**, 2100535.

88. Vashisth, A. *et al.* Mechanical size effects of amorphous polymer-derived ceramics at the nanoscale: experiments and ReaxFF simulations. *Nanoscale* **11**, 7447–7456 (2019).

89. Ishikawa, T., Kajii, S., Hisayuki, T. & Kohtoku, Y. New Type of SIC-Sintered Fiber and its Composite Material. in *22nd Annual Conference on Composites, Advanced Ceramics, Materials, and Structures: A: Ceramic Engineering and Science Proceedings* 283–290 (John Wiley & Sons, Ltd, 1988).

90. Ishikawa, T., Kohtoku, Y., Kumagawa, K., Yamamura, T. & Nagasawa, T. High-strength alkali-resistant sintered SiC fibre stable to 2,200 °C. *Nature* **391**, 773–775 (1998).

91. Ichikawa, H. Recent advances in Nicalon ceramic fibres including Hi-Nicalon type S. *Ann. Chim. Sci. Matér.* **25**, 523–528 (2000).

92. Sauder, C., Brusson, A. & Lamon, J. Influence of Interface Characteristics on the Mechanical Properties of Hi-Nicalon type-S or Tyranno-SA3 Fiber-Reinforced SiC/SiC Minicomposites. *Int. J. Appl. Ceram. Technol.* **7**, 291–303 (2010).

93. Yajima, S., Hasegawa, Y., Okamura, K. & Matsuzawa, T. Development of high tensile strength silicon carbide fibre using an organosilicon polymer precursor. *Nature* **273**, 525–527 (1978).

94. Yajima, S., Hayashi, J. & Omori, M. Continuous silicon carbide fiber of high tensile strength. *Chem. Lett.* **4**, 931–934 (1975).

95. Peng, C.-H. & Hwang, C.-C. Synthesis and characteristics of polycarbomethylsilane via a one-pot approach. *J. Mater. Res. Technol.* **9**, 15838–15848 (2020).

96. Sarkar, S. & Zhai, L. Polymer-Derived Non-Oxide Ceramic Fibers—Past, Present and Future. *Mater. Express* **1**, 18–29 (2011).

97. David, L., Bhandavat, R., Barrera, U. & Singh, G. Silicon oxycarbide glass-graphene composite paper electrode for long-cycle lithium-ion batteries. *Nat. Commun.* **7**, 10998 (2016).

98. Dong, S. M. *et al.* Characterization of nearly stoichiometric SiC ceramic fibres. *J. Mater. Sci.* **36**, 2371–2381 (2001).

99. Luo, Q. & Yang, S. Uncertainty of the X-ray Diffraction (XRD) sin2 ψ Technique in Measuring Residual Stresses of Physical Vapor Deposition (PVD) Hard Coatings. *Coatings* **7**, 128 (2017).

100. Mukaida, H. *et al.* Raman scattering of SiC: Estimation of the internal stress in 3C-SiC on Si. *J. Appl. Phys.* **62**, 254–257 (1987).

101. Rufino, B. *et al.* The effect of particle size on the formation and structure of carbide-derived carbon on β-SiC nanoparticles by reaction with chlorine. *Carbon* **49**, 3073–3083 (2011).

102. Patil, N. *et al.* Rapid Heating of Silicon Carbide Fibers under Radio Frequency Fields and Application in Curing Preceramic Polymer Composites. *ACS Appl. Mater. Interfaces* **11**, 46132–46139 (2019).

103. Ciftyürek, E., Šmíd, B., Li, Z., Matolín, V. & Schierbaum, K. Spectroscopic Understanding of SnO2 and WO3 Metal Oxide Surfaces with Advanced Synchrotron Based; XPS-UPS and Near Ambient Pressure (NAP) XPS Surface Sensitive Techniques for Gas Sensor Applications under Operational Conditions. *Sensors* **19**, 4737 (2019).

104. Seah, M. P. A review of the analysis of surfaces and thin films by AES and XPS. *Vacuum* **34**, 463–478 (1984).

105. NIST X-ray Photoelectron Spectroscopy Database. In NIST Standard Reference Database Number 20, National Institute of Standards and Technology: Gaithersburg MD, 20899, 2000.

106. DiCarlo, J. A. & Yun, H.-M. Non-oxide (Silicon Carbide) Fibers. in *Handbook of Ceramic Composites* (ed. Bansal, N. P.) 33–52 (Springer US, 2005).

107. Ustundag, E. & Fischman, G. S. *23nd Annual Conference on Composites, Advanced Ceramics, Materials, and Structures - A, Volume 20, Issue 3*. (John Wiley & Sons, 2009).

108. Youngblood, G. E., Lewinsohn, C., Jones, R. H. & Kohyama, A. Tensile strength and fracture surface characterization of Hi-Nicalon^{TM} SiC fibers. *J. Nucl. Mater.* **289**, 1–9 (2001).

109. Callaway, E. B. & Zok, F. W. Strengths of ceramic fiber bundles: Theory and practice. *J. Am. Ceram. Soc.* **100**, 5306–5317 (2017).

110. Ikarashi, Y. *et al.* Direct comparison between monofilament and multifilament tow testing for evaluating the tensile strength distribution of SiC fibers. *J. Eur. Ceram. Soc.* **42**, 1928–1937 (2022).

111. Morimoto, T. & Ogasawara, T. Potential strength of Nicalon^{TM}, Hi Nicalon^{TM}, and Hi Nicalon Type S^{TM} monofilaments of variable diameters. *Compos. Part Appl. Sci. Manuf.* **37**, 405–412 (2006).

112. Bunsell, A. R. & Piant, A. A review of the development of three generations of small diameter silicon carbide fibres. *J. Mater. Sci.* **41**, 823–839 (2006).

113. Sha, J. J., Nozawa, T., Park, J. S., Katoh, Y. & Kohyama, A. Effect of heat treatment on the tensile strength and creep resistance of advanced SiC fibers. *J. Nucl. Mater.* **329–333**, 592–596 (2004).

114. Hartman, D. R., Greenwood, M. E. & Miller, D. M. High strength glass fibers. *Mov. Forw. 50 Years Leadersh. Adv. Mater.* **39**, 521–533 (1994).

115. Chi, Z., Chou, T.-W. & Shen, G. Determination of single fibre strength distribution from fibre bundle testings. *J. Mater. Sci.* **19**, 3319–3324 (1984).

116. Coleman, B. D. On the strength of classical fibres and fibre bundles. *J. Mech. Phys. Solids* **7**, 60–70 (1958).

117. Martin, D. M., Akinc, M. & Oh, S. M. Effect of Forming and Aging Atmospheres on E-Glass Strength. *J. Am. Ceram. Soc.* **61**, 308–311 (1978).

118. Yajima, S., Hayashi, J., Omori, M. & Okamura, K. Development of a silicon carbide fibre with high tensile strength. *Nature* **261**, 683–685 (1976).

119. Bernard, S., Weinmann, M., Gerstel, P., Miele, P. & Aldinger, F. Boron-modified polysilazane as a novel single-source precursor for SiBCN ceramic fibers: synthesis, melt-spinning, curing and ceramic conversion. *J. Mater. Chem.* **15**, 289–299 (2005).

120. Shard, A. G. Chapter 4.3.1 - X-ray photoelectron spectroscopy. in *Characterization of Nanoparticles* (eds. Hodoroaba, V.-D., Unger, W. E. S. & Shard, A. G.) 349–371 (Elsevier, 2020).

121. Kroke, E. *et al.* Silazane derived ceramics and related materials. *Mater. Sci. Eng. R Rep.* **26**, 97–199 (2000).

122. Navrotsky, A. Progress and new directions in high temperature calorimetry revisited. *Phys. Chem. Miner.* **24**, 222–241 (1997).

123. Steyer, T. E. Shaping the Future of Ceramics for Aerospace Applications. *Int. J. Appl. Ceram. Technol.* **10**, 389–394 (2013).

124. Monteverde, F., Bellosi, A. & Scatteia, L. Processing and properties of ultra-high temperature ceramics for space applications. *Mater. Sci. Eng. A* **485**, 415–421 (2008).

125. Savino, R., Mungiguerra, S. & Di Martino, G. D. Testing ultra-high-temperature ceramics for thermal protection and rocket applications. *Adv. Appl. Ceram.* **117**, s9–s18 (2018).

126. Saccone, G., Gardi, R., Alfano, D., Ferrigno, A. & Del Vecchio, A. Laboratory, on-ground and in-flight investigation of ultra high temperature ceramic composite materials. *Aerosp. Sci. Technol.* **58**, 490–497 (2016).

127. Jia, Y. *et al.* Thermal properties of polymer-derived ceramic reinforced with boron nitride nanotubes. *J. Am. Ceram. Soc.* **102**, 7584–7593 (2019).

128. Zhao, Z., Xiang, H., Dai, F.-Z., Peng, Z. & Zhou, Y. (TiZrHf)P2O7: An equimolar multicomponent or high entropy ceramic with good thermal stability and low thermal conductivity. *J. Mater. Sci. Technol.* **35**, 2227–2231 (2019).

129. Wei, G. C. Beta Sic Powders Produced by Carbothermic Reduction of Silica in a High-Temperature Rotary Furnace. *J. Am. Ceram. Soc.* **66**, c111–c113 (1983).

130. Moshtaghioun, B. M. *et al.* Rapid carbothermic synthesis of silicon carbide nano powders by using microwave heating. *J. Eur. Ceram. Soc.* **32**, 1787–1794 (2012).

131. Carassiti, L. *et al.* Ultra-rapid, sustainable and selective synthesis of silicon carbide powders and nanomaterials via microwave heating. *Energy Environ. Sci.* **4**, 1503–1510 (2011).

132. Taylor, A. & Laidler, D. S. The Formation and Crystal Structure of Silicon Carbide. *Br. J. Appl. Phys.* **1**, 174 (1950).

133. Ren, R., Yang, Z. & Shaw, L. L. Synthesis of Nanostructured Silicon Carbide through an Integrated Mechanical and Thermal Activation Process. *J. Am. Ceram. Soc.* **85**, 819–827 (2002).

134. Moshtaghioun, B. M., Monshi, A., Abbasi, M. H. & Karimzadeh, F. A study on the effects of silica particle size and milling time on synthesis of silicon carbide nanoparticles by carbothermic reduction. *Int. J. Refract. Met. Hard Mater.* **29**, 645–650 (2011).

135. Hagelüken, L. *et al.* Multiscale 2D/3D microshaping and property tuning of polymer-derived SiCN ceramics. *J. Eur. Ceram. Soc.* **42**, 1963–1970 (2022).

136. Chaudhary, R. P. *et al.* Additive manufacturing of polymer-derived ceramics: Materials, technologies, properties and potential applications. *Prog. Mater. Sci.* **128**, 100969 (2022).

137. Ren, Z., Gervais, C. & Singh, G. Fabrication and characterization of silicon oxycarbide fibre-mats via electrospinning for high temperature applications. *RSC Adv.* **10**, 38446–38455 (2020).

138. Mujib, S. B. *et al.* Electrospun SiOC ceramic fiber mats as freestanding electrodes for electrochemical energy storage applications. *Ceram. Int.* **46**, 3565–3573 (2020).

139. Karakuscu, A., Guider, R., Pavesi, L. & Sorarù, G. D. Broad-band tunable visible emission of sol–gel derived SiBOC ceramic thin films. *Thin Solid Films* **519**, 3822–3826 (2011).

140. Mera, G., Tamayo, A., Nguyen, H., Sen, S. & Riedel, R. Nanodomain Structure of Carbon-Rich Silicon Carbonitride Polymer-Derived Ceramics. *J. Am. Ceram. Soc.* **93**, 1169–1175 (2010).

141. Yu, Y., Chen, Y., Xu, C., Fang, J. & An, L. Synthesis of Spherical Non-Oxide Silicon Carbonitride Ceramic Particles. *J. Am. Ceram. Soc.* **94**, 2779–2782 (2011).

142. Bhandavat, R., Pei, Z. & Singh, G. Polymer-derived ceramics as anode material for rechargeable Li-ion batteries: a review. *Nanomater. Energy* **1**, 324–337 (2012).

143. Kleebe, H.-J. & Blum, Y. D. SiOC ceramic with high excess free carbon. *J. Eur. Ceram. Soc.* **28**, 1037–1042 (2008).

144. Zank, G. A. Preceramic Polymer — Derived Silicon Oxycarbides. in *Silicon-Containing Polymers: The Science and Technology of Their Synthesis and Applications* (eds. Jones, R. G., Ando, W. & Chojnowski, J.) 697–726 (Springer Netherlands, 2000).

145. Bujalski, D. R., Grigoras, S., Lee, W. (nancy), Wieber, G. M. & Zank, G. A. Stoichiometry control of SiOC ceramics by siloxane polymer functionality. *J. Mater. Chem.* **8**, 1427–1433 (1998).

146. Barrios, E. & Zhai, L. A review of the evolution of the nanostructure of SiCN and SiOC polymer derived ceramics and the impact on mechanical properties. *Mol. Syst. Des. Eng.* **5**, 1606–1641 (2020).

147. Ricohermoso, E. I., Klug, F., Schlaak, H., Riedel, R. & Ionescu, E. Electrically conductive silicon oxycarbide thin films prepared from preceramic polymers. *Int. J. Appl. Ceram. Technol.* **19**, 149–164 (2022).

148. Eterigho-Ikelegbe, O., Trammell, R. & Bada, S. Preparation and characterization of ceramic composites from South Africa coal discard. *Constr. Build. Mater.* **302**, 124164 (2021).

149. Development of High Performance Hierarchical Multi-Functional Ceramic Nanocomposites Employing Carbon-Nanotube Nanoforest and Pre-ceramic Polymers - ProQuest (2020).

150. Bhandavat, R. & Singh, G. Stable and Efficient Li-Ion Battery Anodes Prepared from Polymer-Derived Silicon Oxycarbide–Carbon Nanotube Shell/Core Composites. *J. Phys. Chem. C* **117**, 11899–11905 (2013).

151. Torrey, J. D. & Bordia, R. K. Processing of Polymer-Derived Ceramic Composite Coatings on Steel. *J. Am. Ceram. Soc.* **91**, 41–45 (2008).

152. Navrotsky, A. Progress and New Directions in Calorimetry: A 2014 Perspective. *J. Am. Ceram. Soc.* **97**, 3349–3359 (2014).

153. Guo, X. *et al.* Thermodynamics of formation of coffinite, USiO4. *Proc. Natl. Acad. Sci.* **112**, 6551–6555 (2015).

154. Navrotsky, A. Progress and new directions in high temperature calorimetry. *Phys. Chem. Miner.* **2**, 89–104 (1977).

155. Benning, L. G., Phoenix, V. R., Yee, N. & Tobin, M. J. Molecular characterization of cyanobacterial silicification using synchrotron infrared micro-spectroscopy1 1Associate editor: J. P. Amend. *Geochim. Cosmochim. Acta* **68**, 729–741 (2004).

156. Osswald, J. & Fehr, K. T. FTIR spectroscopic study on liquid silica solutions and nanoscale particle size determination. *J. Mater. Sci.* **41**, 1335–1339 (2006).

157. Lubguban, J. *et al.* Low-k organosilicate films prepared by tetravinyltetramethylcyclotetrasiloxane. *J. Appl. Phys.* **92**, 1033–1038 (2002).

158. Mastalerz, M. & Marc Bustin, R. Electron microprobe and micro-FTIR analyses applied to maceral chemistry. *Int. J. Coal Geol.* **24**, 333–345 (1993).

159. Thomas, P. S., Guerbois, J.-P., Russell, G. F. & Briscoe, B. J. FTIR Study of the Thermal Degradation of Poly(vinyl Alcohol). *J. Therm. Anal. Calorim.* **64**, 501–508 (2001).

160. Chen, Y., Caro, L. d., Mastalerz, M., Schimmelmann, A. & Blandón, A. Mapping the chemistry of resinite, funginite and associated vitrinite in coal with micro-FTIR. *J. Microsc.* **249**, 69–81 (2013).

161. Mendelovici, E., Frost, R. L. & Kloprogge, J. T. Modification of Chrysotile Surface by Organosilanes: An IR–Photoacoustic Spectroscopy Study. *J. Colloid Interface Sci.* **238**, 273–278 (2001).

162. Wu, X. C., Cai, R. Q., Yan, P. X., Liu, W. M. & Tian, J. SiCN thin film prepared at room temperature by r.f. reactive sputtering. *Appl. Surf. Sci.* **185**, 262–266 (2002).

163. Canaria, C. A., Lees, I. N., Wun, A. W., Miskelly, G. M. & Sailor, M. J. Characterization of the carbon–silicon stretch in methylated porous silicon— observation of an anomalous isotope shift in the FTIR spectrum. *Inorg. Chem. Commun.* **5**, 560–564 (2002).

164. Li, H. *et al.* Polymer–ceramic conversion of a highly branched liquid polycarbosilane for SiC-based ceramics. *J. Mater. Sci.* **43**, 2806–2811 (2008).

165. Mahmoudi, M. *et al.* Processing and 3D printing of SiCN polymer-derived ceramics. *Int. J. Appl. Ceram. Technol.* **19**, 939–948 (2022).

166. Li, M., Cheng, L., Ye, F., Wang, Y. & Zhang, C. Tailoring dielectric properties of PDCs-SiCN with bimodal pore-structure by annealing combined with oxidation. *J. Eur. Ceram. Soc.* **40**, 5247–5257 (2020).

167. Sreeja, R., Jayalatha, T. & Devapal, D. Silicon oxycarbide (SiOC) foam from methylphenylpoly(silsesquioxane)(PS) by direct foaming technique. *J. Porous Mater.* (2022).

168. Sun, X., Yang, G., Tian, Z., Zhu, W. & Su, D. In-situ formation of titanium carbide in carbon-rich silicon oxycarbide ceramic for enhanced thermal stability. *J. Eur. Ceram. Soc.* **42**, 6935–6941 (2022).

169. Lee, A. Y. *et al.* Raman study of D* band in graphene oxide and its correlation with reduction. *Appl. Surf. Sci.* **536**, 147990 (2021).

170. Bin Mujib, S., Ribot, F., Gervais, C. & Singh, G. Self-supporting carbon-rich SiOC ceramic electrodes for lithium-ion batteries and aqueous supercapacitors. *RSC Adv.* **11**, 35440–35454 (2021).

171. Sang, Z. *et al.* SiOC nanolayer wrapped 3D interconnected graphene sponge as a high-performance anode for lithium ion batteries. *J. Mater. Chem. A* **6**, 9064–9073 (2018).

172. Greczynski, G. & Hultman, L. C 1s Peak of Adventitious Carbon Aligns to the Vacuum Level: Dire Consequences for Material's Bonding Assignment by Photoelectron Spectroscopy. *ChemPhysChem* **18**, 1507–1512 (2017).

173. Morgan, D. J. Comments on the XPS Analysis of Carbon Materials. *C* **7**, 51 (2021).

174. Zhao, H. *et al.* Synthesis, pyrolysis of a novel liquid SiBCN ceramic precursor and its application in ceramic matrix composites. *J. Eur. Ceram. Soc.* **37**, 1321–1329 (2017).

175. Wang, H., Zhu, W., Sun, X. & Su, D. Preparation of aerogel-like SiOC ceramic with honeycomb structure and its high-temperature performance. *J. Alloys Compd.* **937**, 168438 (2023).

176. Zhang, X. *et al.* Stable high-capacity and high-rate silicon-based lithium battery anodes upon two-dimensional covalent encapsulation. *Nat. Commun.* **11**, 3826 (2020).

177. Kollep, M. *et al.* Tomographic Volumetric Additive Manufacturing of Silicon Oxycarbide Ceramics. *Adv. Eng. Mater.* **24**, 2101345 (2022).

178. Key, T. S., Wilks, G. B. & Cinibulk, M. K. Effect of pendant groups on the mass yield and density of polycarbosilanes during pyrolysis. *J. Am. Ceram. Soc.* **105**, 2403–2410 (2022).

179. Luo, X., Wang, J., Dooner, M. & Clarke, J. Overview of current development in electrical energy storage technologies and the application potential in power system operation. *Appl. Energy* **137**, 511–536 (2015).

180. Eswarappa Prameela, S. *et al.* Materials for extreme environments. *Nat. Rev. Mater.* 1–8 (2022)

181. Davidovits, J. Geopolymers: Inorganic polymeric new materials. *J. Therm. Anal. Calorim.* **37**, 1633–1656 (2005).

182. Chauhan, S. S., Abraham, M. & Choudhary, V. Superior EMI shielding performance of thermally stable carbon nanofiber/poly(ether-ketone) composites in 26.5–40 GHz frequency range. *J. Mater. Sci.* **51**, 9705–9715 (2016).

183. Hamerton, I. & Mooring, L. 7 - The use of thermosets in aerospace applications. in *Thermosets* (ed. Guo, Q.) 189–227 (Woodhead Publishing, 2012).

184. Iqbal, A., Saeed, A. & Ul-Hamid, A. A review featuring the fundamentals and advancements of polymer/CNT nanocomposite application in aerospace industry. *Polym. Bull.* **78**, 539–557 (2021).

185. Keller, T. M. & Price, T. R. Amine-Cured Bisphenol-Linked Phthalonitrile Resins. *J. Macromol. Sci. Part - Chem.* **18**, 931–937 (1982).

186. Liu, C. *et al.* Synthesis, characterization, and ceramization of a carbon-rich SiCw-ZrC-ZrB2 preceramic polymer precursor. *Ceram. Int.* **45**, 16097–16104 (2019).

187. Xie, Z., Deng, X., Suo, X., Zhou, T. & Gou, Y. Synthesis and characterization of zirconium diboride precursor based on polycentric bridge bonds. *Mater. Chem. Phys.* **159**, 178–184 (2015).

188. Mansfield, B., Torres, S., Yu, T. & Wu, D. A Review on Additive Manufacturing of Ceramics. in (American Society of Mechanical Engineers Digital Collection, 2019).

189. Parikh, P. B. Alumina Ceramics: Engineering Applications and Domestic Market Potential. *Trans. Indian Ceram. Soc.* **54**, 179–184 (1995).

190. Zhao, W. *et al.* Ultralight polymer-derived ceramic aerogels with wide bandwidth and effective electromagnetic absorption properties. *J. Eur. Ceram. Soc.* **37**, 3973–3980 (2017).

191. Salles, V., Bernard, S., Brioude, A., Cornu, D. & Miele, P. A new class of boron nitride fibers with tunable properties by combining an electrospinning process and the polymer -derived ceramics route. *Nanoscale* **2**, 215–217 (2010).

192. Wang, B. *et al.* Polymer derived SiBCN(O) ceramics with tunable element content. *Ceram. Int.* **48**, 10280–10287 (2022).

193. Mazo, M. A., Tamayo, A., Caballero, A. C. & Rubio, J. Electrical and thermal response of silicon oxycarbide materials obtained by spark plasma sintering. *J. Eur. Ceram. Soc.* **37**, 2011–2020 (2017).

194. Yu, S., Tu, R. & Goto, T. Preparation of SiOC nanocomposite films by laser chemical vapor deposition. *J. Eur. Ceram. Soc.* **36**, 403–409 (2016).

195. Vasudev, M. C., Anderson, K. D., Bunning, T. J., Tsukruk, V. V. & Naik, R. R. Exploration of Plasma-Enhanced Chemical Vapor Deposition as a Method for Thin-Film Fabrication with Biological Applications. *ACS Appl. Mater. Interfaces* **5**, 3983–3994 (2013).

196. Rajagopalan, T. *et al.* Low temperature deposition of nanocrystalline silicon carbide films by plasma enhanced chemical vapor deposition and their structural and optical characterization. *J. Appl. Phys.* **94**, 5252–5260 (2003).

197. Jonas, S., Ptak, W. S., Sadowski, W., Walasek, E. & Paluszkiewicz, C. FTIR In Situ Studies of the Gas Phase Reactions in Chemical Vapor Deposition of SiC. *J. Electrochem. Soc.* **142**, 2357 (1995).

198. Goerke, O., Feike, E., Heine, T., Trampert, A. & Schubert, H. Ceramic coatings processed by spraying of siloxane precursors (polymer-spraying). *J. Eur. Ceram. Soc.* **24**, 2141–2147 (2004).

199. Greil, P. Polymer Derived Engineering Ceramics. *Adv. Eng. Mater.* **2**, 339–348 (2000).

200. Lücke, J., Hacker, J., Suttor, D. & Ziegler, G. Synthesis and Characterization of Silazane-Based Polymers as Precursors for Ceramic Matrix Composites. *Appl. Organomet. Chem.* **11**, 181–194 (1997).

201. Hurwitz, F. I. Filler/Polycarbosilane Systems as CMC Matrix Precursors. in *22nd Annual Conference on Composites, Advanced Ceramics, Materials, and Structures: A: Ceramic Engineering and Science Proceedings* 267–274 (John Wiley & Sons, Ltd, 1988).

202. Grossenbacher, J., Gullo, M. R., Grandjean, R., Kiefer, T. & Brugger, J. Sub micrometer ceramic structures fabricated by molding a polymer-derived ceramic. *Microelectron. Eng.* **97**, 272–275 (2012).

203. Chen, Z. *et al.* 3D printing of ceramics: A review. *J. Eur. Ceram. Soc.* **39**, 661–687 (2019).

204. Zhao, L., Wang, X., Xiong, H., Zhou, K. & Zhang, D. Optimized preceramic polymer for 3D structured ceramics via fused deposition modeling. *J. Eur. Ceram. Soc.* **41**, 5066–5074 (2021).

205. Chen, H. *et al.* 3D printing of SiC ceramic: Direct ink writing with a solution of preceramic polymers. *J. Eur. Ceram. Soc.* **38**, 5294–5300 (2018).

206. Schiavon, M. A., Gervais, C., Babonneau, F. & Soraru, G. D. Crystallization Behavior of Novel Silicon Boron Oxycarbide Glasses. *J. Am. Ceram. Soc.* **87**, 203–208 (2004).

207. Tavakoli, A. H., Gerstel, P., Golczewski, J. A. & Bill, J. Effect of boron on the crystallization of amorphous Si–(B–)C–N polymer-derived ceramics. *J. Non-Cryst. Solids* **355**, 2381–2389 (2009).

208. Terauds, K. & Raj, R. Limits to the Stability of the Amorphous Nature of Polymer-Derived HfSiCNO Compounds. *J. Am. Ceram. Soc.* **96**, 2117–2123 (2013).

209. Kleebe, H.-J., Suttor, D., Müller, H. & Ziegler, G. Decomposition-Crystallization of Polymer-Derived Si-C-N Ceramics. *J. Am. Ceram. Soc.* **81**, 2971–2977 (1998).

210. Soraru, G. D., Babonneau, F. & Mackenzie, J. D. Structural evolutions from polycarbosilane to SiC ceramic. *J. Mater. Sci.* **25**, 3886–3893 (1990).

211. Nazari, K. A. *et al.* Preceramic polymer composite: Fabrication process and mechanical performance. *Mater. Lett.* **318**, 132218 (2022).

212. Nabat Al-Ajrash, S. M., Browning, C., Eckerle, R. & Cao, L. Initial development of preceramic polymer formulations for additive manufacturing. *Mater. Adv.* **2**, 1083–1089 (2021)

213. Jana, P., Santoliquido, O., Ortona, A., Colombo, P. & Sorarù, G. D. Polymer-derived SiCN cellular structures from replica of 3D printed lattices. *J. Am. Ceram. Soc.* **101**, 2732–2738 (2018).

214. Apostolov, Z. D., Heckman, E. P., Key, T. S. & Cinibulk, M. K. Effects of low-temperature treatment on the properties of commercial preceramic polymers. *J. Eur. Ceram. Soc.* **40**, 2887–2895 (2020).

215. Bernard, S., Fiaty, K., Cornu, D., Miele, P. & Laurent, P. Kinetic Modeling of the Polymer-Derived Ceramics Route: Investigation of the Thermal Decomposition Kinetics of Poly[B-(methylamino)borazine] Precursors into Boron Nitride. *J. Phys. Chem. B* **110**, 9048–9060 (2006).

216. Key, T. S., Patel, D. K., Wilks, G. B. & Cinibulk, M. K. Modeling the pyrolysis of preceramic polymers: A kinetic study of the polycarbosilane SMP-10. *J. Eur. Ceram. Soc.* **41**, 6356–6365 (2021).

217. Key, T. S. *et al.* Process modeling of the low-temperature evolution and yield of polycarbosilanes for ceramic matrix composites. *J. Am. Ceram. Soc.* **101**, 2809–2818 (2018).

218. Massiot, D. *et al.* Modelling one- and two-dimensional solid-state NMR spectra. *Magn. Reson. Chem.* **40**, 70–76 (2002).

219. Deepa, M., Sharma, N., Agnihotry, S. A. & Chandra, R. FTIR investigations on ion–ion interactions in liquid and gel polymeric electrolytes: LiCF3SO3-PC-PMMA. *J. Mater. Sci.* **37**, 1759–1765 (2002).

220. Zhang, G. Y. & Peak, D. Studies of Cd(II)–sulfate interactions at the goethite–water interface by ATR-FTIR spectroscopy. *Geochim. Cosmochim. Acta* **71**, 2158–2169 (2007).

221. Bruzzoniti, M. C. *et al.* Polymer-derived ceramic aerogels as sorbent materials for the removal of organic dyes from aqueous solutions. *J. Am. Ceram. Soc.* **101**, 821–830 (2018).

222. Santhosh, B. *et al.* Processing and thermal characterization of polymer derived SiCN(O) and SiOC reticulated foams. *Ceram. Int.* **46**, 5594–5601 (2020).

223. Zhao, W. *et al.* Facile preparation of ultralight polymer-derived SiOCN ceramic aerogels with hierarchical pore structure. *J. Am. Ceram. Soc.* **102**, 2316–2324 (2019).

224. Liu, X. *et al.* Enhanced microwave-absorption properties of polymer-derived SiC/SiOC composite ceramics modified by carbon nanowires. *Ceram. Int.* **46**, 20742–20750 (2020).

225. Hung, I., Ionescu, E., Sen, J., Gan, Z. & Sen, S. Structure and Connectivity in an Amorphous Silicon Oxycarbide Polymer-Derived Ceramic: Results from 2D 29Si NMR Spectroscopy. *J. Phys. Chem. C* **125**, 4777–4784 (2021).

226. Bae, S.-G. *et al.* Effect of carbon and oxygen on the high-temperature properties of silicon carbide–hafnium carbide nanocomposite fiber. *J. Eur. Ceram. Soc.* (2022)

227. Rau, A. V., Knott, K. & Lu, K. Porous SiOC/SiC ceramics via an active-filler-catalyzed polymer-derived method. *Mater. Chem. Front.* **5**, 6530–6545 (2021).

228. Wang, K., Wang, H. & Cheng, Y.-B. Synthesis of nanostructured silicon carbide spheres from mesoporous C–SiO2 nanocomposites. *Chem. Commun.* **46**, 303–305 (2009).

229. Poerschke, D. L., Braithwaite, A., Park, D. & Lauten, F. Crystallization behavior of polymer-derived Si-O-C for ceramic matrix composite processing. *Acta Mater.* **147**, 329–341 (2018).

230. Zybill, C., Handwerker, H. & Friedrich, H. Silaorganometallic Chemistry on the Basis of Multiple Bonding. in *Advances in Organometallic Chemistry* (eds. Stone, F. G. A. & West, R.) vol. 36 229–281 (Academic Press, 1994).

231. Farnan, I., Cho, H. & Weber, W. J. Quantification of actinide α-radiation damage in minerals and ceramics. *Nature* **445**, 190–193 (2007).

232. Berger, F., Müller, A., Aldinger, F. & Müller, K. Solid-state NMR Investigations on Si-B-C-N Ceramics derived from Boron-Modified Poly(allylmethylsilazane). *Z. Für Anorg. Allg. Chem.* **631**, 355–363 (2005).

233. Widgeon, S. J. *et al.* 29Si and 13C Solid-State NMR Spectroscopic Study of Nanometer-Scale Structure and Mass Fractal Characteristics of Amorphous Polymer Derived Silicon Oxycarbide Ceramics. *Chem. Mater.* **22**, 6221–6228 (2010).

234. Xue, J. *et al.* Enhanced microwave absorbing properties of Y2O3 modified PDC SiCN ceramics with heterogeneous amorphous interface. *J. Alloys Compd.* **931**, 167499 (2023).

235. Jia, Y., Chowdhury, M. A. R. & Xu, C. Complex impedance spectra of polymer-derived SiC annealed at ultrahigh temperature. *J. Am. Ceram. Soc.* **103**, 6860–6868 (2020).

236. Feng, Y., Feng, N., Wei, Y. & Bai, Y. Preparation and improved electrochemical performance of SiCN–graphene composite derived from poly(silylcarbondiimide) as Li-ion battery anode. *J. Mater. Chem. A* **2**, 4168–4177 (2014).

237. Petry, N.-C. *et al.* Oxidation resistance of ZrB2-based monoliths using polymer-derived Si(Zr,B)CN as sintering aid. *J. Am. Ceram. Soc.* **105**, 5380–5394 (2022).

238. Miele, P., Bernard, S., Cornu, D. & Toury, B. Recent Developments in Polymer-Derived Ceramic Fibers (PDCFs): Preparation, Properties and Applications – A Review. *Soft Mater.* **4**, 249–286 (2007).

239. Duperrier, S. *et al.* Design of a Series of Preceramic B-Tri(methylamino)borazine-Based Polymers as Fiber Precursors: Architecture, Thermal Behavior, and Melt-Spinnability. *Macromolecules* **40**, 1018–1027 (2007).

240. Luan, X., Gu, S., Zhang, Q., Cheng, L. & Riedel, R. An electrically conductive SiBCN film prepared via polymer-derived ceramic and chemical vapor deposition methods. *Sens. Actuators Phys.* **330**, 112824 (2021).

241. Soboyejo, W. O. *et al.* Review of High Temperature Ceramics for Aerospace Applications. *Adv. Mater. Res.* **1132**, 385–407 (2016).

242. Barroso, G. S., Krenkel, W. & Motz, G. Low thermal conductivity coating system for application up to 1000°C by simple PDC processing with active and passive fillers. *J. Eur. Ceram. Soc.* **35**, 3339–3348 (2015).

243. Parcianello, G., Bernardo, E. & Colombo, P. Cordierite ceramics from silicone resins containing nano-sized oxide particle fillers. *Ceram. Int.* **39**, 8893–8899 (2013).

244. Sarkar, S., Gan, Z., An, L. & Zhai, L. Structural Evolution of Polymer-Derived Amorphous SiBCN Ceramics at High Temperature. *J. Phys. Chem. C* **115**, 24993–25000 (2011).

245. Zhou, S., Mei, H., Chang, P., Lu, M. & Cheng, L. Molecule editable 3D printed polymer-derived ceramics. *Coord. Chem. Rev.* **422**, 213486 (2020).

246. Scheffler, M., Greil, P., Berger, A., Pippel, E. & Woltersdorf, J. Nickel-catalyzed in situ formation of carbon nanotubes and turbostratic carbon in polymer-derived ceramics. *Mater. Chem. Phys.* **84**, 131–139 (2004).

247. Wang, X., Wang, J. & Wang, H. Performance and structural evolution of high-temperature organic adhesive for joining Al2O3 ceramics. *Int. J. Adhes. Adhes.* **45**, 1–6 (2013).

248. Hernández-Rodríguez, P. & López-Honorato, E. Polymer derived SiC environmental barrier coatings with superwetting properties. *Ceram. Int.* **43**, 11289–11295 (2017).

249. Niu, M. *et al.* Radiation Effects in the Crystalline–Amorphous SiOC Polymer-Derived Ceramics: Insights from Experiments and Molecular Dynamics Simulation. *ACS Appl. Mater. Interfaces* **13**, 40106–40117 (2021).

250. Zlotnik, S., Sahu, S. K., Navrotsky, A. & Vilarinho, P. M. Pyrochlore and Perovskite Potassium Tantalate: Enthalpies of Formation and Phase Transformation. *Chem. – Eur. J.* **21**, 5231–5237 (2015).

251. Thomas C. Allison. NIST-JANAF Thermochemical Tables - SRD 13. (2013)

252. Kornilov, A. N., Ushakova, I. M., Huber, E. J. & Holley, C. E. The enthalpy of formation of hafnium dioxide. *J. Chem. Thermodyn.* **7**, 21–26 (1975).

253. Mah, A. D. *Heats of Formation of Zirconium Carbide and Hafnium Carbide*. (U.S. Department of the Interior, Bureau of Mines, 1964).

254. Ikezawa, Y., Sawatari, T. & Terashima, H. In situ FTIR study of pyridine adsorbed on Au(111), Au(100) and Au(110) electrodes. *Electrochimica Acta* **46**, 1333–1337 (2001).

255. Yelil Arasi, A., Juliet Latha Jeyakumari, J., Sundaresan, B., Dhanalakshmi, V. & Anbarasan, R. The structural properties of Poly(aniline)—Analysis via FTIR spectroscopy. *Spectrochim. Acta. A. Mol. Biomol. Spectrosc.* **74**, 1229–1234 (2009).

256. Castro, D. C. *et al.* Synthesis and Characterization of Mesoporous Nb_2O_5 and Its Application for Photocatalytic Degradation of the Herbicide Methylviologen. *J. Braz. Chem. Soc.* (2015)

257. Ramadoss, A., Krishnamoorthy, K. & Kim, S. J. Novel synthesis of hafnium oxide nanoparticles by precipitation method and its characterization. *Mater. Res. Bull.* **47**, 2680–2684 (2012).

258. Zhang, N., Li, L. & Li, G. Nanosized amorphous tantalum oxide: a highly efficient photocatalyst for hydrogen evolution. *Res. Chem. Intermed.* **43**, 5011–5024 (2017).

259. Babar, Z. U. D. *et al.* Magnetic phase transition from paramagnetic in Nb 2 AlC-MAX to superconductivity-like diamagnetic in Nb 2 C-MXene: an experimental and computational analysis. *RSC Adv.* **10**, 25669–25678 (2020).

260. Tressler, R. E. Recent developments in fibers and interphases for high temperature ceramic matrix composites. *Compos. Part Appl. Sci. Manuf.* **30**, 429–437 (1999).

261. Duan, W. *et al.* Synthesis and microwave absorption properties of SiC nanowires reinforced SiOC ceramic. *J. Eur. Ceram. Soc.* **34**, 257–266 (2014).

262. Blum, Y. D., MacQueen, D. B. & Kleebe, H.-J. Synthesis and characterization of carbon-enriched silicon oxycarbides. *J. Eur. Ceram. Soc.* **25**, 143–149 (2005).

263. Jafari, B. *et al.* Development of a new composite ceramic membrane from mullite, silicon carbide and activated carbon for treating greywater. *Ceram. Int.* **47**, 34667–34675 (2021).

264. Alper, J. P. *et al.* Silicon carbide nanowires as highly robust electrodes for micro-supercapacitors. *J. Power Sources* **230**, 298–302 (2013).

265. Kwon, H., Kim, W. & Kim, J. Stability Domains of NbC and Nb(CN) During Carbothermal Reduction of Niobium Oxide. *J. Am. Ceram. Soc.* **98**, 315–319 (2015).

266. Sacks, M. D., Wang, C.-A., Yang, Z. & Jain, A. Carbothermal reduction synthesis of nanocrystalline zirconium carbide and hafnium carbide powders using solution-derived precursors. *J. Mater. Sci.* **39**, 6057–6066 (2004).

267. Réjasse, F., Trolliard, G., Rapaud, O., Maître, A. & David, J. TEM study of the reaction mechanisms involved in the carbothermal reduction of hafnia. *RSC Adv.* **5**, 45341–45350 (2015).

268. Paprocki, K. *et al.* The comparative studies of HF CVD diamond films by Raman and XPS spectroscopies. *Opt. Mater.* **95**, 109251 (2019).

269. Mera, G., Navrotsky, A., Sen, S., Kleebe, H.-J. & Riedel, R. Polymer -derived SiCN and SiOC ceramics – structure and energetics at the nanoscale. *J. Mater. Chem. A* **1**, 3826–3836 (2013).

270. Lahoz, R., Espinós, J. P., Yubero, F., González-Elipe, A. R. & Fuente, G. F. de la. "In situ" XPS studies of laser-induced surface nitridation and oxidation of tantalum. *J. Mater. Res.* **30**, 2967–2976 (2015).

271. Lee, S., Yun, D.-J., Rhee, S.-W. & Yong, K. Atomic layer deposition of hafnium silicate film for high mobility pentacene thin film transistor applications. *J. Mater. Chem.* **19**, 6857–6864 (2009).

272. Hans, K., Latha, S., Bera, P. & Barshilia, H. C. Hafnium carbide based solar absorber coatings with high spectral selectivity. *Sol. Energy Mater. Sol. Cells* **185**, 1–7 (2018).

273. Gupta, A., Mittal, M., Singh, M. K., Suib, S. L. & Pandey, O. P. Low temperature synthesis of NbC/C nano-composites as visible light photoactive catalyst. *Sci. Rep.* **8**, 13597 (2018).

274. Chang, Y.-Y. *et al.* Biological Characteristics of the MG-63 Human Osteosarcoma Cells on Composite Tantalum Carbide/Amorphous Carbon Films. *PLOS ONE* **9**, e95590 (2014).

275. Hellwig, M. *et al.* Stabilization of Amide-Based Complexes of Niobium and Tantalum Using Malonates as Chelating Ligands: Precursor Chemistry and Thin Film Deposition. *Chem. Mater.* **19**, 6077–6087 (2007).

276. Mullapudi, G. S. R. *et al.* Low-Temperature Deposition of Inorganic–Organic HfO2–PMMA Hybrid Gate Dielectric Layers for High-Mobility ZnO Thin-Film Transistors. *ACS Appl. Electron. Mater.* **1**, 1003–1011 (2019).

277. Aubry, D. *et al.* Molecular functionalization of tantalum oxide surface towards development of apatite growth. *Appl. Surf. Sci.* **255**, 4765–4772 (2009).

278. Lyu, Y., Tang, H. & Zhao, G. Effect of Hf and B incorporation on the SiOC precursor architecture and high-temperature oxidation behavior of SiHfBOC ceramics. *J. Eur. Ceram. Soc.* **40**, 324–332 (2020).

279. A. Abass, M., A. Syed, A., Gervais, C. & Singh, G. Synthesis and electrochemical performance of a polymer-derived silicon oxycarbide/boron nitride nanotube composite. *RSC Adv.* **7**, 21576–21584 (2017).

280. Ionescu, E. *et al.* Polymer-Derived SiOC/ZrO2 Ceramic Nanocomposites with Excellent High-Temperature Stability. *J. Am. Ceram. Soc.* **93**, 241–250 (2010).

281. Okamura, H. & Bowen, H. K. Preparation of alkoxides for the synthesis of ceramics. *Ceram. Int.* **12**, 161–171 (1986).

282. Yang, S. *et al.* Preparation of high-purity tantalum ethoxide by vacuum distillation. *Trans. Nonferrous Met. Soc. China* **18**, 196–201 (2008).

283. Bickmore, C. R., Waldner, K. F., Treadwell, D. R. & Laine, R. M. Ultrafine Spinel Powders by Flame Spray Pyrolysis of a Magnesium Aluminum Double Alkoxide. *J. Am. Ceram. Soc.* **79**, 1419–1423 (1996).

284. Yaghi, O. M. Reticular Chemistry: Molecular Precision in Infinite 2D and 3D. *Mol. Front. J.* **03**, 66–83 (2019).

285. Kim, H. & Seop Hong, C. MOF-74-type frameworks: tunable pore environment and functionality through metal and ligand modification. *CrystEngComm* **23**, 1377–1387 (2021).

286. Liu, J. *et al.* A Tunable Bimetallic MOF-74 for Adsorption Chiller Applications. *Eur. J. Inorg. Chem.* **2018**, 885–889 (2018).

287. Wei, R. *et al.* Tuning the Properties of Zr6O8 Nodes in the Metal Organic Framework UiO-66 by Selection of Node-Bound Ligands and Linkers. *Chem. Mater.* **31**, 1655–1663 (2019).

288. Wade, C. R., Corrales-Sanchez, T., Narayan, T. C. & Dincă, M. Postsynthetic tuning of hydrophilicity in pyrazolate MOFs to modulate water adsorption properties. *Energy Environ. Sci.* **6**, 2172–2177 (2013).

289. Titi, H. M. *et al.* Hypergolic zeolitic imidazolate frameworks (ZIFs) as next-generation solid fuels: Unlocking the latent energetic behavior of ZIFs. *Sci. Adv.* **5**, eaav9044 (2019).

290. Titi, H. M. *et al.* Metal–Organic Frameworks as Fuels for Advanced Applications: Evaluating and Modifying the Combustion Energy of Popular MOFs. *Chem. Mater.* **31**, 4882–4888 (2019).

291. Metzger, E. D. *et al.* Highly Selective Heterogeneous Ethylene Dimerization with a Scalable and Chemically Robust MOF Catalyst. *ACS Sustain. Chem. Eng.* **7**, 6654–6661 (2019).

292. Liu, J. *et al.* MOF-enabled confinement and related effects for chemical catalyst presentation and utilization. *Chem. Soc. Rev.* **51**, 1045–1097 (2022).

293. Smoljan, C. S. *et al.* Engineering Metal–Organic Frameworks for Selective Separation of Hexane Isomers Using 3-Dimensional Linkers. *J. Am. Chem. Soc.* **145**, 6434–6441 (2023).

294. Wang, H., Pei, X., Kalmutzki, M. J., Yang, J. & Yaghi, O. M. Large Cages of Zeolitic Imidazolate Frameworks. *Acc. Chem. Res.* **55**, 707–721 (2022).

295. Huang, X.-C., Lin, Y.-Y., Zhang, J.-P. & Chen, X.-M. Ligand-Directed Strategy for Zeolite-Type Metal–Organic Frameworks: Zinc(II) Imidazolates with Unusual Zeolitic Topologies. *Angew. Chem. Int. Ed.* **45**, 1557–1559 (2006).

296. Huang, X., Zhang, J. & Chen, X. [Zn(bim)2] · (H2O)1.67: A metal-organic open-framework with sodalite topology. *Chin. Sci. Bull.* **48**, 1531–1534 (2003).

297. Zhang, J.-P., Zhang, Y.-B., Lin, J.-B. & Chen, X.-M. Metal Azolate Frameworks: From Crystal Engineering to Functional Materials. *Chem. Rev.* **112**, 1001–1033 (2012).

298. Park, K. S. *et al.* Exceptional chemical and thermal stability of zeolitic imidazolate frameworks. *Proc. Natl. Acad. Sci.* **103**, 10186–10191 (2006).

299. R. Redfern, L. & K. Farha, O. Mechanical properties of metal–organic frameworks. *Chem. Sci.* **10**, 10666–10679 (2019).

300. B. Lennox, C. *et al.* Simplifying and expanding the scope of boron imidazolate framework (BIF) synthesis using mechanochemistry. *Chem. Sci.* **12**, 14499–14506 (2021).

301. Wang, J. *et al.* Metal organic framework-based nanostructure materials: applications for non-lithium ion battery electrodes. *CrystEngComm* **24**, 2925–2947 (2022).

302. A. Pearson, M., Bhagchandani, S., Dincă, M. & A. Johnson, J. Mixing ligands to enhance gas uptake in polyMOFs. *Mol. Syst. Des. Eng.* **8**, 591–597 (2023).

303. Zheng, Z., Hanikel, N., Lyu, H. & Yaghi, O. M. Broadly Tunable Atmospheric Water Harvesting in Multivariate Metal–Organic Frameworks. *J. Am. Chem. Soc.* **144**, 22669–22675 (2022).

304. Luo, J. *et al.* Hydrogen Adsorption in a Highly Stable Porous Rare-Earth Metal-Organic Framework: Sorption Properties and Neutron Diffraction Studies. *J. Am. Chem. Soc.* **130**, 9626–9627 (2008).

305. Gao, S. *et al.* Improving the Acidic Stability of Zeolitic Imidazolate Frameworks by Biofunctional Molecules. *Chem* **5**, 1597–1608 (2019).

306. Yuan, S. *et al.* Stable Metal–Organic Frameworks: Design, Synthesis, and Applications. *Adv. Mater.* **30**, 1704303 (2018).

307. Kouser, S., Hezam, A., Khadri, M. J. N. & Khanum, S. A. A review on zeolite imidazole frameworks: synthesis, properties, and applications. *J. Porous Mater.* **29**, 663–681 (2022).

308. Mo, Z., Tai, D., Zhang, H. & Shahab, A. A comprehensive review on the adsorption of heavy metals by zeolite imidazole framework (ZIF-8) based nanocomposite in water. *Chem. Eng. J.* **443**, 136320 (2022).

309. W. Lewis, D. *et al.* Zeolitic imidazole frameworks: structural and energetics trends compared with their zeolite analogues. *CrystEngComm* **11**, 2272–2276 (2009).

310. Katsenis, A. D. *et al.* In situ X-ray diffraction monitoring of a mechanochemical reaction reveals a unique topology metal-organic framework. *Nat. Commun.* **6**, 6662 (2015).

311. Al Obeidli, A., Ben Salah, H., Al Murisi, M. & Sabouni, R. Recent advancements in MOFs synthesis and their green applications. *Int. J. Hydrog. Energy* **47**, 2561–2593 (2022).

312. Howarth, A. J. *et al.* Chemical, thermal and mechanical stabilities of metal–organic frameworks. *Nat. Rev. Mater.* **1**, 1–15 (2016).

313. Rieth, A. J., Wright, A. M. & Dincă, M. Kinetic stability of metal–organic frameworks for corrosive and coordinating gas capture. *Nat. Rev. Mater.* **4**, 708–725 (2019).

314. Saliba, D., Ammar, M., Rammal, M., Al-Ghoul, M. & Hmadeh, M. Crystal Growth of ZIF-8, ZIF-67, and Their Mixed-Metal Derivatives. *J. Am. Chem. Soc.* **140**, 1812–1823 (2018).

315. Shi, Q., Chen, Z., Song, Z., Li, J. & Dong, J. Synthesis of ZIF-8 and ZIF-67 by Steam-Assisted Conversion and an Investigation of Their Tribological Behaviors. *Angew. Chem. Int. Ed.* **50**, 672–675 (2011).

316. Xu, Y. *et al.* Experimentally Validated Ab Initio Crystal Structure Prediction of Novel Metal–Organic Framework Materials. *J. Am. Chem. Soc.* **145**, 3515–3525 (2023).

317. Deacon, A. *et al.* Understanding the ZIF-L to ZIF-8 transformation from fundamentals to fully costed kilogram-scale production. *Commun. Chem.* **5**, 1–10 (2022).

318. Zhang, J., Zhang, T., Yu, D., Xiao, K. & Hong, Y. Transition from ZIF-L-Co to ZIF-67: a new insight into the structural evolution of zeolitic imidazolate frameworks (ZIFs) in aqueous systems. *CrystEngComm* **17**, 8212–8215 (2015).

319. M. Titi, H., Do, J.-L., J. Howarth, A., Nagapudi, K. & Friščić, T. Simple, scalable mechanosynthesis of metal–organic frameworks using liquid-assisted resonant acoustic mixing (LA-RAM). *Chem. Sci.* **11**, 7578–7584 (2020).

320. Qian, J., Sun, F. & Qin, L. Hydrothermal synthesis of zeolitic imidazolate framework-67 (ZIF-67) nanocrystals. *Mater. Lett.* **82**, 220–223 (2012).

321. Xu, W. *et al.* Entropy-Driven Mechanochemical Synthesis of Polymetallic Zeolitic Imidazolate Frameworks for CO2 Fixation. *Angew. Chem. Int. Ed.* **58**, 5018–5022 (2019).

322. Speight, I. R. *et al.* Disappearing Polymorphs in Metal–Organic Framework Chemistry: Unexpected Stabilization of a Layered Polymorph over an Interpenetrated Three-Dimensional Structure in Mercury Imidazolate. *Chem. – Eur. J.* **26**, 1811–1818 (2020).

323. Fu, H., Wang, Z., Wang, X., Wang, P. & Wang, C.-C. Formation mechanism of rod-like ZIF-L and fast phase transformation from ZIF-L to ZIF-8 with morphology changes controlled by polyvinylpyrrolidone and ethanol. *CrystEngComm* **20**, 1473–1477 (2018).

324. Lee, S., Oh, S. & Oh, M. Atypical Hybrid Metal–Organic Frameworks (MOFs): A Combinative Process for MOF-on-MOF Growth, Etching, and Structure Transformation. *Angew. Chem.* **132**, 1343–1349 (2020).

325. Low, Z.-X. *et al.* Crystal Transformation in Zeolitic-Imidazolate Framework. *Cryst. Growth Des.* **14**, 6589–6598 (2014).

326. Cheng, C.-C. *et al.* Gold nanocrystal decorated trimetallic metal organic frameworks as high performance electrocatalysts for oxygen evolution reaction. *Appl. Catal. B Environ.* **286**, 119916 (2021).

327. Gao, K., Guo, X., Zheng, B., Wang, J. & Wang, L. Investigation of interface compatibility in stiff polymer/metal–organic frameworks. *Mater. Today Chem.* **20**, 100458 (2021).

328. Hartmann, M. J., Häkkinen, H., Millstone, J. E. & Lambrecht, D. S. Impacts of Copper Position on the Electronic Structure of [Au25-xCux(SH)18]– Nanoclusters. *J. Phys. Chem. C* **119**, 8290–8298 (2015).

329. Hao, J. *et al.* Unraveling the electronegativity-dominated intermediate adsorption on high-entropy alloy electrocatalysts. *Nat. Commun.* **13**, 2662 (2022).

330. Kamdar, M. H. The occurrence of liquid-metal embrittlement. *Phys. Status Solidi A* **4**, 225–233 (1971).

331. Timofeeva, M. N. *et al.* Tuning the catalytic properties for cycloaddition of CO2 to propylene oxide on zeolitic-imidazolate frameworks through variation of structure and chemical composition. *Mol. Catal.* **529**, 112530 (2022).

332. Zaręba, J. K., Nyk, M. & Samoć, M. Co/ZIF-8 Heterometallic Nanoparticles: Control of Nanocrystal Size and Properties by a Mixed-Metal Approach. *Cryst. Growth Des.* **16**, 6419–6425 (2016).

333. Sahu, S. K. & Navrotsky, A. Thermodynamics of copper-manganese and copper-iron spinel solid solutions. *J. Am. Ceram. Soc.* **100**, 3684–3692 (2017).

334. Fu, L., Yang, H., Hu, Y., Wu, D. & Navrotsky, A. Tailoring Mesoporous γ-Al2O3 Properties by Transition Metal Doping: A Combined Experimental and Computational Study. *Chem. Mater.* **29**, 1338–1349 (2017).

335. Shivaramaiah, R., Tallapragada, S., Nagabhushana, G. P. & Navrotsky, A. Synthesis and thermodynamics of transition metal oxide based sodium ion cathode materials. *J. Solid State Chem.* **280**, 121011 (2019).

336. E. Casco, M. *et al.* Gate-opening effect in ZIF-8: the first experimental proof using inelastic neutron scattering. *Chem. Commun.* **52**, 3639–3642 (2016).

337. Krokidas, P. *et al.* ZIF-67 Framework: A Promising New Candidate for Propylene/Propane Separation. Experimental Data and Molecular Simulations. *J. Phys. Chem. C* **120**, 8116–8124 (2016).

338. Nijem, N. *et al.* Tuning the Gate Opening Pressure of Metal–Organic Frameworks (MOFs) for the Selective Separation of Hydrocarbons. *J. Am. Chem. Soc.* **134**, 15201–15204 (2012).

339. Du, L. *et al.* Hierarchically Self-Assembled MOF Network Enables Continuous Ion Transport and High Mechanical Strength. *Adv. Energy Mater.* **12**, 2200501 (2022).

340. Liu, J. *et al.* Electric Transport Properties of Surface-Anchored Metal–Organic Frameworks and the Effect of Ferrocene Loading. *ACS Appl. Mater. Interfaces* **7**, 9824–9830 (2015).

341. Zhao, Z., Ma, X., Li, Z. & Lin, Y. S. Synthesis, characterization and gas transport properties of MOF-5 membranes. *J. Membr. Sci.* **382**, 82–90 (2011).

342. Feng, X. *et al.* Series d–f Heteronuclear Metal–Organic Frameworks: Color Tunability and Luminescent Probe with Switchable Properties. *Inorg. Chem.* **56**, 1713–1721 (2017).

343. Liu, W., Erol, O. & Gracias, D. H. 3D Printing of an In Situ Grown MOF Hydrogel with Tunable Mechanical Properties. *ACS Appl. Mater. Interfaces* **12**, 33267–33275 (2020).

344. Aguilera-Sigalat, J. & Bradshaw, D. Synthesis and applications of metal-organic framework–quantum dot (QD@MOF) composites. *Coord. Chem. Rev.* **307**, 267–291 (2016).

345. Chen, W. & Wu, C. Synthesis, functionalization, and applications of metal–organic frameworks in biomedicine. *Dalton Trans.* **47**, 2114–2133 (2018).

346. Llabrés i Xamena, F. X., Corma, A. & Garcia, H. Applications for Metal−Organic Frameworks (MOFs) as Quantum Dot Semiconductors. *J. Phys. Chem. C* **111**, 80–85 (2007).

347. Su, J. & Chen, J. MOFs of Uranium and the Actinides. in *Lanthanide Metal-Organic Frameworks* (ed. Cheng, P.) 265–295 (Springer, 2015).

348. Lv, K., Fichter, S., Gu, M., März, J. & Schmidt, M. An updated status and trends in actinide metal-organic frameworks (An-MOFs): From synthesis to application. *Coord. Chem. Rev.* **446**, 214011 (2021).

349. A. Dolgopolova, E., M. Rice, A. & B. Shustova, N. Actinide-based MOFs: a middle ground in solution and solid-state structural motifs. *Chem. Commun.* **54**, 6472–6483 (2018).

350. Ni, Z. & Masel, R. I. Rapid Production of Metal−Organic Frameworks via Microwave-Assisted Solvothermal Synthesis. *J. Am. Chem. Soc.* **128**, 12394–12395 (2006).

351. DeSantis, D. *et al.* Techno-economic Analysis of Metal–Organic Frameworks for Hydrogen and Natural Gas Storage. *Energy Fuels* **31**, 2024–2032 (2017).

352. Stolar, T. & Užarević, K. Mechanochemistry: an efficient and versatile toolbox for synthesis, transformation, and functionalization of porous metal–organic frameworks. *CrystEngComm* **22**, 4511–4525 (2020).

353. Głowniak, S., Szczęśniak, B., Choma, J. & Jaroniec, M. Mechanochemistry: Toward green synthesis of metal–organic frameworks. *Mater. Today* **46**, 109–124 (2021).

354. Friščić, T. New opportunities for materials synthesis using mechanochemistry. *J. Mater. Chem.* **20**, 7599–7605 (2010).

355. López-Cabrelles, J. *et al.* Multivariate sodalite zeolitic imidazolate frameworks: a direct solvent-free synthesis. *Chem. Sci.* **13**, 842–847 (2022).

356. Mu, B. & Walton, K. S. Thermal Analysis and Heat Capacity Study of Metal–Organic Frameworks. *J. Phys. Chem. C* **115**, 22748–22754 (2011).

357. Lu, P. *et al.* What can pKa and NBO charges of the ligands tell us about the water and thermal stability of metal organic frameworks? *J. Mater. Chem. A* **2**, 16250–16267 (2014).

358. Zou, J.-P. *et al.* Two Novel Metal−Organic Frameworks (MOFs) with (3,6)-Connected Net Topologies: Syntheses, Crystal Structures, Third-Order Nonlinear Optical and Luminescent Properties. *Cryst. Growth Des.* **10**, 2613–2619 (2010).

359. Wang, C. *et al.* New Strategies for Novel MOF-Derived Carbon Materials Based on Nanoarchitectures. *Chem* **6**, 19–40 (2020).

360. Nandy, A., Duan, C. & Kulik, H. J. Audacity of huge: overcoming challenges of data scarcity and data quality for machine learning in computational materials discovery. *Curr. Opin. Chem. Eng.* **36**, 100778 (2022).

361. Leong, C. F., Usov, P. M. & D'Alessandro, D. M. Intrinsically conducting metal–organic frameworks. *MRS Bull.* **41**, 858–864 (2016).

362. Taddei, M. *et al.* Mixed-linker UiO-66: structure–property relationships revealed by a combination of high-resolution powder X-ray diffraction and density functional theory calculations. *Phys. Chem. Chem. Phys.* **19**, 1551–1559 (2017).

363. Tong, M., Yang, Q., Xiao, Y. & Zhong, C. Revealing the structure–property relationship of covalent organic frameworks for CO 2 capture from postcombustion gas: a multi-scale computational study. *Phys. Chem. Chem. Phys.* **16**, 15189–15198 (2014).

364. Nagabhushana, G. P., Shivaramaiah, R. & Navrotsky, A. Direct calorimetric verification of thermodynamic instability of lead halide hybrid perovskites. *Proc. Natl. Acad. Sci.* **113**, 7717–7721 (2016).

365.   Matsunaga, T. *et al.* Magnesium borohydride: A new hydrogen storage material. *Renew. Energy* **33**, 193–196 (2008).

366. Teo, B. K. & Zhang, H. Molecular Machines: Molecular Structure of [(p-Tol3P)10Au13Ag12Cl8](PF7)—a Cluster with a Biicosahedral Rotorlike Metal Core and an Unusual Arrangement of Bridging Ligands. *Angew. Chem. Int. Ed. Engl.* **31**, 445–447 (1992).

367. Majzlan, J., Navrotsky, A. & Evans, B. J. Thermodynamics and crystal chemistry of the hematite–corundum solid solution and the FeAlO3 phase. *Phys. Chem. Miner.* **29**, 515–526 (2002).

368. Ngene, P., Longo, A., Mooij, L., Bras, W. & Dam, B. Metal-hydrogen systems with an exceptionally large and tunable thermodynamic destabilization. *Nat. Commun.* **8**, 1846 (2017).

369. Lilova, K. *et al.* A Synergistic Approach to Unraveling the Thermodynamic Stability of Binary and Ternary Chevrel Phase Sulfides. *Chem. Mater.* **32**, 7044–7051 (2020).

370. Aspinall, H. C. *et al.* Pinwheel-Shaped Heterobimetallic Lanthanide Alkali Metal Binapholates: Ionic Size Matters! *Organometallics* **19**, 5416–5423 (2000).

371. Rakhsha, A. H. *et al.* Ag and Cu doped ZnO nanowires: A pH-Controlled synthesis via chemical bath deposition. *Materialia* **5**, 100212 (2019).

372. Liu, A. *et al.* High-performance p-channel transistors with transparent Zn doped-CuI. *Nat. Commun.* **11**, 4309 (2020).

373. Peng, H. *et al.* Simultaneous realization of broad temperature stability range and outstanding dielectric performance in (Ag+, Ta5+) co–doped TiO2 ceramics. *J. Alloys Compd.* **783**, 423–427 (2019).

374. Wen, T. *et al.* A boron imidazolate framework with mechanochromic and electrocatalytic properties. *Mater. Horiz.* **5**, 1151–1155 (2018).

375. Zheng, S. *et al.* Porous Metal Carboxylate Boron Imidazolate Frameworks. *Angew. Chem. Int. Ed.* **49**, 5362–5366 (2010).

376. Zhang, H.-X., Liu, M., Wen, T. & Zhang, J. Synthetic design of functional boron imidazolate frameworks. *Coord. Chem. Rev.* **307**, 255–266 (2016).

377. Wang, T. C. *et al.* Ultrahigh Surface Area Zirconium MOFs and Insights into the Applicability of the BET Theory. *J. Am. Chem. Soc.* **137**, 3585–3591 (2015).

378. Hu, Z. & Srinivasan, M. P. Mesoporous high-surface-area activated carbon. *Microporous Mesoporous Mater.* **43**, 267–275 (2001).

379. Liu, G. *et al.* Mixed matrix formulations with MOF molecular sieving for key energy-intensive separations. *Nat. Mater.* **17**, 283–289 (2018).

380. Hu, Z. *et al.* Combination of Optimization and Metalated-Ligand Exchange: An Effective Approach to Functionalize UiO-66(Zr) MOFs for CO2 Separation. *Chem. – Eur. J.* **21**, 17246–17255 (2015).

381. Park, C., Lee, K., Koo, M. & Park, C. Soft Ferroelectrics Enabling High-Performance Intelligent Photo Electronics. *Adv. Mater.* **33**, 2004999 (2021).

382. Fu, D.-W., Zhang, W. & Xiong, R.-G. The first metal–organic framework (MOF) of Imazethapyr and its SHG, piezoelectric and ferroelectric properties. *Dalton Trans.* 3946–3948 (2008)

383. Cheng, S. & Logan, B. E. Increasing power generation for scaling up single-chamber air cathode microbial fuel cells. *Bioresour. Technol.* **102**, 4468–4473 (2011).

384. Mohareb, E. *et al.* Considerations for reducing food system energy demand while scaling up urban agriculture. *Environ. Res. Lett.* **12**, 125004 (2017).

385. Körner, Ch. Towards a better experimental basis for upscaling plant responses to elevated CO2 and climate warming. *Plant Cell Environ.* **18**, 1101–1110 (1995).

386. Pasupuleti, S. B., Sarkar, O. & Venkata Mohan, S. Upscaling of biohydrogen production process in semi-pilot scale biofilm reactor: Evaluation with food waste at variable organic loads. *Int. J. Hydrog. Energy* **39**, 7587–7596 (2014).

387. Urbain, F. *et al.* Upscaling high activity oxygen evolution catalysts based on CoFe2O4 nanoparticles supported on nickel foam for power-to-gas electrochemical conversion with energy efficiencies above 80%. *Appl. Catal. B Environ.* **259**, 118055 (2019).

388. Yue, Q., Xu, X., Hillier, J., Cheng, K. & Pan, G. Mitigating greenhouse gas emissions in agriculture: From farm production to food consumption. *J. Clean. Prod.* **149**, 1011–1019 (2017).

389. Herzog, H., Eliasson, B. & Kaarstad, O. Capturing Greenhouse Gases. *Sci. Am.* **282**, 72–79 (2000).

390. Hoefnagels, R., Smeets, E. & Faaij, A. Greenhouse gas footprints of different biofuel production systems. *Renew. Sustain. Energy Rev.* **14**, 1661–1694 (2010).

391. Wich-Konrad, T., Lüke, W., Oles, M. & Deerberg, G. Assessment of Industrial Greenhouse Gas Reduction Strategies Within Consistent System Boundaries. *Chem. Ing. Tech.* **92**, 1393–1402 (2020).

392. Singh, G. *et al.* Emerging trends in porous materials for CO2 capture and conversion. *Chem. Soc. Rev.* **49**, 4360–4404 (2020).

393. Lu, A.-H. & Hao, G.-P. Porous materials for carbon dioxide capture. *Annu. Rep. Sect. Inorg. Chem.* **109**, 484–503 (2013).

394. Gaikwad, S. & Han, S. Shaping metal-organic framework (MOF) with activated carbon and silica powder materials for CO2 capture. *J. Environ. Chem. Eng.* **11**, 109593 (2023).

395. Wang, J., Pu, Q., Ning, P. & Lu, S. Activated carbon-based composites for capturing CO2: a review. *Greenh. Gases Sci. Technol.* **11**, 377–393 (2021).

396. Introduction to Metal–Organic Frameworks. *Chem. Rev.* **112**, 673–674 (2012).

397. Friščić, T., Mottillo, C. & Titi, H. M. Mechanochemistry for Synthesis. *Angew. Chem. Int. Ed.* **59**, 1018–1029 (2020).

398. Furukawa, H., Cordova, K. E., O'Keeffe, M. & Yaghi, O. M. The Chemistry and Applications of Metal-Organic Frameworks. *Science* **341**, 1230444 (2013).

399. Czaja, A. U., Trukhan, N. & Müller, U. Industrial applications of metal–organic frameworks. *Chem. Soc. Rev.* **38**, 1284–1293 (2009).

400. Marco-Lozar, J. P., Juan-Juan, J., Suárez-García, F., Cazorla-Amorós, D. & Linares-Solano, A. MOF-5 and activated carbons as adsorbents for gas storage. *Int. J. Hydrog. Energy* **37**, 2370–2381 (2012).

401. Grünker, R. *et al.* A new metal–organic framework with ultra-high surface area. *Chem. Commun.* **50**, 3450–3452 (2014).

402. Farha, O. K. *et al.* Metal–Organic Framework Materials with Ultrahigh Surface Areas: Is the Sky the Limit? *J. Am. Chem. Soc.* **134**, 15016–15021 (2012).

403. Åhlén, M. *et al.* Gas sorption properties and kinetics of porous bismuth-based metal-organic frameworks and the selective CO2 and SF6 sorption on a new

bismuth trimesate-based structure UU-200. *Microporous Mesoporous Mater.* **329**, 111548 (2022).

404. Wells, B. A., Webley, P. A. & Chaffee, A. L. Simulations of model metal-organic frameworks for the separation of carbon dioxide. *Energy Procedia* **4**, 568–575 (2011).

405. Bingel, L. W. & Walton, K. S. Surprising Use of the Business Innovation Bass Diffusion Model To Accurately Describe Adsorption Isotherm Types I, III, and V. *Langmuir* **39**, 4475–4482 (2023).

406. Das, S., Ben, T., Qiu, S. & Valtchev, V. Two-Dimensional COF–Three-Dimensional MOF Dual-Layer Membranes with Unprecedentedly High H2/CO2 Selectivity and Ultrahigh Gas Permeabilities. *ACS Appl. Mater. Interfaces* **12**, 52899–52907 (2020).

407. Peng, Y.-W. *et al.* Nitrogen Coordination To Dramatically Enhance the Stability of In-MOF for Selectively Capturing CO2 from a CO2/N2 Mixture. *Cryst. Growth Des.* **19**, 1322–1328 (2019).

408. Qasem, N. A. A., Ben-Mansour, R. & Habib, M. A. An efficient CO2 adsorptive storage using MOF-5 and MOF-177. *Appl. Energy* **210**, 317–326 (2018).

409. Liu, Y., Liu, J. & Hu, J. Noble gas separation by a MOF with one-dimensional channels. *BMC Chem. Eng.* **1**, 3 (2019).

410. Wu, D. *et al.* Direct Calorimetric Measurement of Enthalpy of Adsorption of Carbon Dioxide on CD-MOF-2, a Green Metal–Organic Framework. *J. Am. Chem. Soc.* **135**, 6790–6793 (2013).

411. Pan, H., Ritter, J. A. & Balbuena, P. B. Examination of the Approximations Used in Determining the Isosteric Heat of Adsorption from the Clausius−Clapeyron Equation. *Langmuir* **14**, 6323–6327 (1998).

412. Czepirski, L. & JagieŁŁo, J. Virial-type thermal equation of gas—solid adsorption. *Chem. Eng. Sci.* **44**, 797–801 (1989).

413. Ushakov, S. V. & Navrotsky, A. Direct measurements of water adsorption enthalpy on hafnia and zirconia. *Appl. Phys. Lett.* **87**, 164103 (2005).

414. Hulvey, Z. *et al.* Noble Gas Adsorption in Copper Trimesate, HKUST-1: An Experimental and Computational Study. *J. Phys. Chem. C* **117**, 20116–20126 (2013).

415. Hughes, J. T., Sava, D. F., Nenoff, T. M. & Navrotsky, A. Thermochemical Evidence for Strong Iodine Chemisorption by ZIF-8. *J. Am. Chem. Soc.* **135**, 16256–16259 (2013).

416. Guo, X., Zhang, P. & Navrotsky, A. The thermodynamics of gas absorption and guest-induced flexibility in zeolite Y. *Microporous Mesoporous Mater.* **294**, 109893 (2020).

417. Gouvêa, D., Ushakov, S. V. & Navrotsky, A. Energetics of CO2 and H2O Adsorption on Zinc Oxide. *Langmuir* **30**, 9091–9097 (2014).

418. Navrotsky, A., Mazeina, L. & Majzlan, J. Size-Driven Structural and Thermodynamic Complexity in Iron Oxides. *Science* **319**, 1635–1638 (2008).

419. Torres-Knoop, A., Poursaeidesfahani, A., Vlugt, T. J. H. & Dubbeldam, D. Behavior of the Enthalpy of Adsorption in Nanoporous Materials Close to Saturation Conditions. *J. Chem. Theory Comput.* **13**, 3326–3339 (2017).

420. Gensterblum, Y., Busch, A. & Krooss, B. M. Molecular concept and experimental evidence of competitive adsorption of H2O, CO2 and CH4 on organic material. *Fuel* **115**, 581–588 (2014).

421. Mayer, L. M. Extent of coverage of mineral surfaces by organic matter in marine sediments. *Geochim. Cosmochim. Acta* **63**, 207–215 (1999).

422. Mazeina, L. & Navrotsky, A. Enthalpy of Water Adsorption and Surface Enthalpy of Goethite (α-FeOOH) and Hematite (α-Fe2O3). *Chem. Mater.* **19**, 825–833 (2007).

423. Ockwig, N. W., Delgado-Friedrichs, O., O'Keeffe, M. & Yaghi, O. M. Reticular Chemistry: Occurrence and Taxonomy of Nets and Grammar for the Design of Frameworks. *Acc. Chem. Res.* **38**, 176–182 (2005).

424. O'Keeffe, M. Design of MOFs and intellectual content in reticular chemistry: a personal view. *Chem. Soc. Rev.* **38**, 1215–1217 (2009).

425. Chen, Z. *et al.* Reticular chemistry in the rational synthesis of functional zirconium cluster-based MOFs. *Coord. Chem. Rev.* **386**, 32–49 (2019).

426. Jobin, O. *et al.* Metal–organic frameworks as hypergolic additives for hybrid rockets. *Chem. Sci.* **13**, 3424–3436 (2022).

427. Na, K., Choi, K. M., Yaghi, O. M. & Somorjai, G. A. Metal Nanocrystals Embedded in Single Nanocrystals of MOFs Give Unusual Selectivity as Heterogeneous Catalysts. *Nano Lett.* **14**, 5979–5983 (2014).

428. So, M. C., Wiederrecht, G. P., Mondloch, J. E., Hupp, J. T. & Farha, O. K. Metal–organic framework materials for light-harvesting and energy transfer. *Chem. Commun.* **51**, 3501–3510 (2015).

429. Singh, R. *et al.* Biomimetic metal-organic frameworks as protective scaffolds for live-virus encapsulation and vaccine stabilization. *Acta Biomater.* **142**, 320–331 (2022).

430. Li, M., Li, D., O'Keeffe, M. & Yaghi, O. M. Topological Analysis of Metal–Organic Frameworks with Polytopic Linkers and/or Multiple Building Units and the Minimal Transitivity Principle. *Chem. Rev.* **114**, 1343–1370 (2014).

431. Kalaj, M. & Cohen, S. M. Postsynthetic Modification: An Enabling Technology for the Advancement of Metal–Organic Frameworks. *ACS Cent. Sci.* **6**, 1046–1057 (2020).

432. Shen, Y., Tissot, A. & Serre, C. Recent progress on MOF-based optical sensors for VOC sensing. *Chem. Sci.* **13**, 13978–14007 (2022).

433. Li, C. *et al.* Recent development and applications of electrical conductive MOFs. *Nanoscale* **13**, 485–509 (2021).

434. Cui, Y., Yue, Y., Qian, G. & Chen, B. Luminescent Functional Metal–Organic Frameworks. *Chem. Rev.* **112**, 1126–1162 (2012).

435. Allendorf, M. D., Bauer, C. A., Bhakta, R. K. & Houk, R. J. T. Luminescent metal–organic frameworks. *Chem. Soc. Rev.* **38**, 1330–1352 (2009).

436. Lee, C. Y. *et al.* Light-Harvesting Metal–Organic Frameworks (MOFs): Efficient Strut-to-Strut Energy Transfer in Bodipy and Porphyrin-Based MOFs. *J. Am. Chem. Soc.* **133**, 15858–15861 (2011).

437. Ettlinger, R. *et al.* Toxicity of metal–organic framework nanoparticles: from essential analyses to potential applications. *Chem. Soc. Rev.* **51**, 464–484 (2022).

438. Darby, J. P. *et al.* Ab Initio Prediction of Metal-Organic Framework Structures. *Chem. Mater.* **32**, 5835–5844 (2020).

439. Ding, M., Cai, X. & Jiang, H.-L. Improving MOF stability: approaches and applications. *Chem. Sci.* **10**, 10209–10230 (2019).

440. Nguyen, J. G. & Cohen, S. M. Moisture-Resistant and Superhydrophobic Metal−Organic Frameworks Obtained via Postsynthetic Modification. *J. Am. Chem. Soc.* **132**, 4560–4561 (2010).

441. Carter, K. P., Ridenour, J. A., Kalaj, M. & Cahill, C. L. A Thorium Metal-Organic Framework with Outstanding Thermal and Chemical Stability. *Chem. – Eur. J.* **25**, 7114–7118 (2019).

442. Friščić, T. & Jones, W. Recent Advances in Understanding the Mechanism of Cocrystal Formation via Grinding. *Cryst. Growth Des.* **9**, 1621–1637 (2009).

443. Bhattacharyya, S. *et al.* Acid Gas Stability of Zeolitic Imidazolate Frameworks: Generalized Kinetic and Thermodynamic Characteristics. *Chem. Mater.* **30**, 4089–4101 (2018).

444. Cui, K., Nair, S., Sholl, D. S. & Schmidt, J. R. Kinetic Model of Acid Gas Induced Defect Propagation in Zeolitic Imidazolate Frameworks. *J. Phys. Chem. Lett.* **13**, 6541–6548 (2022).

445. Bhattacharyya, S., Sholl, D. S. & Nair, S. Quantitative Correlations for the Durability of Zeolitic Imidazolate Frameworks in Humid SO2. *Ind. Eng. Chem. Res.* **59**, 245–252 (2020).

446. Bhattacharyya, S. *et al.* Stability of Zeolitic Imidazolate Frameworks in NO2. *J. Phys. Chem. C* **123**, 2336–2346 (2019).

447. Brekalo, I. *et al.* Manometric real-time studies of the mechanochemical synthesis of zeolitic imidazolate frameworks. *Chem. Sci.* **11**, 2141–2147 (2020).

448. Evans, J. D. *et al.* Computational Chemistry Methods for Nanoporous Materials. *Chem. Mater.* **29**, 199–212 (2017).

449. Duarte Rodrigues, A. *et al.* Joint Experimental and Computational Investigation of the Flexibility of a Diacetylene-Based Mixed-Linker MOF: Revealing the Existence of Two Low-Temperature Phase Transitions and the Presence of Colossal Positive and Giant Negative Thermal Expansions. *Chem. – Eur. J.* **24**, 1586–1605 (2018).

450. Baburin, I. A. & Leoni, S. The energy landscapes of zeolitic imidazolate frameworks (ZIFs): towards quantifying the presence of substituents on the imidazole ring. *J. Mater. Chem.* **22**, 10152–10154 (2012).

451. Witman, M. *et al.* Rational Design of a Low-Cost, High-Performance Metal–Organic Framework for Hydrogen Storage and Carbon Capture. *J. Phys. Chem. C* **121**, 1171–1181 (2017).

452. Nazarian, D., Camp, J. S., Chung, Y. G., Snurr, R. Q. & Sholl, D. S. Large-Scale Refinement of Metal−Organic Framework Structures Using Density Functional Theory. *Chem. Mater.* **29**, 2521–2528 (2017).

453. Tan, J.-C., Civalleri, B., Erba, A. & Albanese, E. Quantum mechanical predictions to elucidate the anisotropic elastic properties of zeolitic imidazolate frameworks: ZIF-4 vs. ZIF-zni. *CrystEngComm* **17**, 375–382 (2014).

454. Lewis, D. W. *et al.* Zeolitic imidazole frameworks: structural and energetics trends compared with their zeolite analogues. *CrystEngComm* **11**, 2272–2276 (2009).

455. Huskić, I. *et al.* Proton Conductivity, Stability and Potential for Polymorphism in Metal-Organic Framework Minerals. (2018)

456. Clark, S. J. *et al.* First principles methods using CASTEP. *Z. Für Krist. - Cryst. Mater.* **220**, 567–570 (2005).

457. Björkman, T. CIF2Cell: Generating geometries for electronic structure programs. *Comput. Phys. Commun.* **182**, 1183–1186 (2011).

458. *C. Spink, I. Wadsö D. Glick (Ed.), Methods of Biochemical Analysis, Vol. 23, Wiley, Oxford (1976), p. 123*. vol. 1.

459. Perdew, J. P., Burke, K. & Ernzerhof, M. Generalized Gradient Approximation Made Simple. *Phys. Rev. Lett.* **77**, 3865–3868 (1996).

460. Grimme, S., Antony, J., Ehrlich, S. & Krieg, H. A consistent and accurate ab initio parametrization of density functional dispersion correction (DFT-D) for the 94 elements H-Pu. *J. Chem. Phys.* **132**, 154104 (2010).

461. Tkatchenko, A., DiStasio, R. A., Car, R. & Scheffler, M. Accurate and Efficient Method for Many-Body van der Waals Interactions. *Phys. Rev. Lett.* **108**, 236402 (2012).

462. Ambrosetti, A., Reilly, A. M., DiStasio, R. A., Jr. & Tkatchenko, A. Long-range correlation energy calculated from coupled atomic response functions. *J. Chem. Phys.* **140**, 18A508 (2014).

463. Reilly, A. M. & Tkatchenko, A. van der Waals dispersion interactions in molecular materials: beyond pairwise additivity. *Chem. Sci.* **6**, 3289–3301 (2015).

464. Tkatchenko, A. & Scheffler, M. Accurate Molecular Van Der Waals Interactions from Ground-State Electron Density and Free-Atom Reference Data. *Phys. Rev. Lett.* **102**, 073005 (2009).

465. Grimme, S. Semiempirical GGA-type density functional constructed with a long-range dispersion correction. *J. Comput. Chem.* **27**, 1787–1799 (2006).

466. Ehrlich, S., Moellmann, J., Reckien, W., Bredow, T. & Grimme, S. System-Dependent Dispersion Coefficients for the DFT-D3 Treatment of Adsorption Processes on Ionic Surfaces. *ChemPhysChem* **12**, 3414–3420 (2011).

467. Arhangelskis, M., Katsenis, A. D., Morris, A. J. & Friščić, T. Computational evaluation of metal pentazolate frameworks: inorganic analogues of azolate metal–organic frameworks. *Chem. Sci.* **9**, 3367–3375 (2018).

468. Perdew, J. P. *et al.* Restoring the Density-Gradient Expansion for Exchange in Solids and Surfaces. *Phys. Rev. Lett.* **100**, 136406 (2008).

469. Tan, J. C., Bennett, T. D. & Cheetham, A. K. Chemical structure, network topology, and porosity effects on the mechanical properties of Zeolitic Imidazolate Frameworks. *Proc. Natl. Acad. Sci. U. S. A.* **107**, 9938–9943 (2010).

470. Basnayake, S. A., Su, J., Zou, X. & Balkus, K. J. Carbonate-Based Zeolitic Imidazolate Framework for Highly Selective CO2 Capture. *Inorg. Chem.* **54**, 1816–1821 (2015).

APPENDIX A

SUPPORTING INFORMATION FOR CHAPTER 7

A.1 Powder X-ray diffraction (PXRD)

A Bruker D2 Phaser powder diffractometer, equipped with a Ni-filtered Cu-Kα (λ = 1.5418 Å) source and Lynxeye 1D detector (Bruker AXS, Madison, WI, USA) was used to obtain powder X-ray diffractograms.

A.2 Fourier-transform infrared attenuated total reflectance (FTIR-ATR) spectroscopy

Infrared spectra were obtained using a Bruker Alpha II FTIR spectrometer and are reported in wavenumber (cm^{-1}) units.

A.3 Thermogravimetric Analysis (TGA)

All products were recorded on a Setaram Labsys Evo DTA/DSC, with samples between 5 and 10 mg, loaded in a 100 µL platinum crucibles. The samples were heated from 25 to 800 °C at a rate of 10 °C/min, with a continuous flow of air at 20 mL/min.

APPENDIX B

STATEMENT OF PUBLISHER PERMISSION

CHAPTER 1

CHAPTER 2

CHAPTER 3

CHAPTER 4

CHAPTER 5

CHAPTER 6

CHAPTER 7

The work presented in chapters 8 is currently under review in the Journal Physical Chemistry C.

APPENDIX C

STATEMENT OF COAUTHORS' PERMISSIONS

I, Gerson Leonel, confirm that all co-authors have granted their permissions for the usage of previous publications in this dissertation.